A novel approach to Property driven design of Titanium alloys for Biomedical applications.

Paul Sunday Ugwu Nnamchi

A thesis submitted for the degree of Doctor of
Philosophy

2013

Department of Materials Science and Engineering

The University of Sheffield

Table of Contents

List of Tables

List of Figures

List of acronyms

The notable conventions adopted in this thesis will be discussed in detail in the body of the thesis, but the essential elements are grouped here for easy reference:

- The use of β-Ti in this thesis referes to alloys which contains sufficient beta stabilizers (such as molybdenum, niobium and vanadium) to allow them to mentain the beta phase when quenched, and which can also be solution treated and aged to improve strength.
- The α–Ti alloy reefres to alloys which contain neutral alloying elements (such as tin) and /or alpha stabilizers (such as aluminium or oxygen) only. These alloys.
- Acronyms for high purity (HP) and commercial pure (CP) are uised to refer to approximate compostion. The alloy designations bearing similar names such as body centered crystals (BCC) and hexagonal close-packed crystal (HCP) acronyms distinquish the crystal structure of alloys followed. When discussing theoretical or experimental results from this work or literatures, the total impurity content in atomic percent is given, where possible.
- Al. Eq: The term ‘aluminium equivalent’ (Al. Eq.) is used to quantify the α-stability given by the ratio of Al equivalent divided by the weighted averages of the aluminium equivalent of the elements.
- Mo. Eq: The molybdenum equivalent defined as Mo. Eq. is used to express the stability of β phase in a titanium alloy.

- Electron per atom ratio (e/a) (See Eqn.2.1), originally proposed in 1926 by Hume-Rothery denote average electron per atom ratio.
- All temperature will be given in degrees Celsius, where possible. When referring to graphs from literature thatr are in degrees Kelvin this value will be given in brackets for easy comparison.
- EBSD refers to the electron back-scatter diffraction
- ODF denote orientation distribution function
- Psuedoelasticity sometimes called superelasticity is an elastic (reversible) response to an applied stress, caused by a phase transformation between the austenitic and martensitic phases of a crystal. This comes from the reversible motion of domain boundaries during the phase transformation, rather than bond stretching or introduction of defects in the lattice.
- Stress induced martensite (SIM) alloy is refers to transformable alloys that exhibit psuedoelasticity transition from $\beta \leftrightarrow \alpha''$ (orthorhombic) phase, And the bases for the continued search for shape memory alloys in Ti alloys consisting of orthorhombic crystal structure. psuedoelastic behaviour of alloys
- Gum metal is an acronym that refers to a class of Ti-Nb-Zr-O alloys developed some years ago at the Toyota central R&D labouratory with multifunctional mechanical properties. The material endures significant plastic deformation with little or no evidence of dislocation motion.
- Cambridge Serial Total Energy Package CASTEP refers to the quantum mechanical modelling method developed within the frame work of Kohn-

Sham DFT in Cambridge University. It is used in this thesis to investigate the electronic structure (principally ground state) of atoms and alloys and their condensed phases. Kohn-Sham density functional theory would yield the exact ground state energy E, if the exact exchange –correlation energy functional were known. With this code, many properties of a many electron system such as ground state energy, density of state, elastic constant amogst others can be determined by using electron density functionals, such as GGA and LDA.

- The Generalised gradient approximation, (GGA) has improved many properties of materials that are governed by a realistic description of bond formation. In addition to decreasing the total energy of each atom, the generalized gradient approximation has been shown to remove much of the over binding that is present in the existing local approximations to DFT [20-29].
- Nearly free electron model(NFE) refers to the model used by Jones and Mott in their early band theory to express the energy of the valence electron in the neighbourhood of the centre of the zone boundary as defined in eqns. 2.2-2.4, [19].
- First Brillouin zone interactions (FsBz) as used in this thesis refer to a set of points in K- space that can be reached from the origin without crossing the Bragg plane.
- Interatomic bond length(IBL) denote the bonding distance between two similar or dissimilar atoms in a compound.

Glossary of symbols

The more farmiliar used symbols and symbols derived from disambiguation (e.g., d for grain size and d_{hkl} for lattice spacing) are described in the list below.

E: total energy of a system

N(E): density of states of electrons..

N: total number of electron per volume V

E_{XC}: exchange and correlation energy

D(E): ground state energy of the total density of state (DOS)

Kz: axis is chosen perpendicular to the Brillouin zone plane in the reciprocal space and passes through its centre (0, 0, Ko).

$E|\rho(r)|$: is the energy gap across the zone plane

$T_s(\rho)$: Kinetic energy of electron in non-interating system

$\rho(r)$: electron density at the position r.

$\Psi(r)$: wave function of electrons in a systemat position **r**.

V(r): effective one-electron potential consisting of the Hartree potential, and $U_{XC}(\rho(r)$.

$U_{XC}(\rho(r)$: chemical potential defined as $\delta\big(\rho\varepsilon_{XC}(\rho)\big)/\delta\rho$

α: lattice constant

ρ: density

U: internal energy

$|Bo|$: is related to the strength of the covalent bonding between Ti and an alloying element.

$|Md|$: is correlated with the electronegativity and metallic radius of elements.

Φ: Euler angle

Φ_1 : Euler angle 1

Φ_2 : Euler angle 2

λ: denote the secondary of a dendritic arm spacing used to define the relationship (eqn. 3.1) with alloy cooling rate

N: is the total number of atoms per supercell.

$\mathrm{E}_{\mathrm{tot}}^{0}(\mathrm{Ti}_{\mathrm{x}}\mathrm{X}_{1-\mathrm{x}})$: is the first principle calculated total energies of the respective alloys.

μ: is the chemical potential of the element Ti or Mo in its corresponding bulk phase.

$\mathrm{E}_{\mathrm{Form}}^{(\mathrm{Ti}_{\mathrm{x}}\mathrm{Mo}_{1-\mathrm{x}})}$: is the first principle calculated formation energies of the respective alloys.

$G_{\beta}^{E}(\mathrm{x},\mathrm{Ti})$: is the first principle calculated free energies of the respective alloys.

C_{ijkl}: is the local elastic constant tensor with $\langle\sigma_{ij}(\boldsymbol{r})\rangle$ and $\langle\epsilon_{kl}(\boldsymbol{r})\rangle$ as the local stress and strain field at a point $\mathbf{r}$, respectively, and the angular brackets denote ensemble averages.

T: T-matrix is given by $T = \delta C(1 - G\delta C)^{-1}$, $\boldsymbol{I}$: is equivalent to the unit tensor.

C_{44}: denote single crystal bulk modulus; $B^{o} = (C_{11}^{0} + 2C_{12}^{O})/3$,

$C^{\prime} = (C_{11-}\, C_{12})/2$ (tetragonal shear modulus)

$C_{44},\ \mu^* = C^*_{44} = \ \mu^0\ + \frac{\langle\tau_{44}\rangle}{1+G_{44}\tau_{44}}$ (Trigonal shear modulus)

$\widetilde{\mathrm{Y}}^*$: the homogenised polycrystalline Young's modulus.

$\tilde{\mu}^*$: homogenised polycrystalline Poisson's ratio.

G : the ratio of shearing stress τ to shearing strain γ within the proportional limit of a material

M_S: Martensite formation start temperature

M_F: Martensite finish temperature

ΔH: Enthalpy of formation

ΔE: Formation Energy gain in a system

ΔG: Gibss energy of formation

ε_f : Fermi energy.

K_β : the coefficient of β stabilisation.

β_{c_i}: is its critical concentration

V_L and V_S are the ultrasonic longitudinal and shear wave velocities respectively, and ρ is the density of the material.

Abstract

A metallic alloy for implant and/or other biomaterial applications ideally needs the following properties: excellent biocompatibility with no adverse tissue reactions, excellent corrosion resistance in body fluid, high mechanical strength and fatigue resistance, low modulus, low density and good wear resistance [1-6]. Since β-type or near β- Ti alloys exhibit a significantly lower modulus and also satisfy most of the other requirements for an ideal metallic biomaterial, they are especially suitable for orthopaedic implant applications — hence, the reason for the huge interest in the development of lower modulus β-Ti alloys.

Furthermore, in the case of β stability, past studies have shown the maximum concentration of biocompatible alloying elements, such as Mo, Nb, and Ta —to be retained in β after quenching from β phase field are 5, 15, and 20 atomic % respectively for binary Ti–Mo [22], Ti–Nb [23], and Ti–Ta alloys [24]. Accordingly, it can be expected that Mo is the most effective β stabiliser and the β type Ti–Mo alloys are more suitable than the other β Ti alloys for biomedical applications. Nonetheless, most previous studies have focused on Ti-Nb alloys.

In this thesis, we have employed this new concept of property design involving a bottom up combinatorial approach (DFT calculations and experiment verification) to predict the structural and energetic stability,

mechanical, electronic and elastic properties of binary and multicomponent Ti-Mo alloys for biomedical applications in a consistent way. Furthermore, with the aid of Blackman diagrams, we attest to using elastic constant systematics as an effective tool to define and analyse predicted properties with experimental data. The results were found to provide an excellent theoretical guide to the design of SIM (stressed induced martensitic) low Young's modulus biomedical Ti alloys.

Dedication

This work is dedicated to God and my late beloved parents, Mr Robert Ugwu Aneke Nnamchi (Agbowo oke ugwu na-eri Ebune) and Mrs Angelina Nnamchi (Izele nwanyi).

Mum, you stood by me through dark and dusk, rain and sunshine and gave me the reason to look into the future. Wherever you are, this is for you. May your souls rest in perfect peace.

Acknowledgements

The research presented in this doctoral dissertation was carried out at the University of Sheffield in the United Kingdom, and would not have been possible without the guidance and help of several individuals who, in one way or another, contributed their valuable assistance in the preparation and completion of this study. It is a pleasure to convey my gratitude to them all.

First and foremost, I offer my sincerest gratitude to my two supervisors, Prof. Iain Todd and Prof. Mark W. Rainforth; they mentored and guided me throughout my research with patience, expert knowledge and invaluable suggestions. Their encouragement and support from the initial to the final step enabled me to develop an understanding of the subject and finish my thesis. One simply could not wish for better or friendlier supervisors. I am indebted to them more than they know.

I am, as ever, especially indebted to my late parents, Mr and Mrs Robert Ugwu Aneke and Angelina Nnamchi, for their love and invaluable support and prayers throughout my life. I lack sufficient words to express my appreciation towards my parents whose dedication, love and persistent confidence in me has taken the loads from my shoulders. I could not have achieved all this in the absence of their prayers. I simply cannot thank my parents enough. I also wish to thank my sister for her continuous support and love during my studies.

I would like to thank in a special way my wife, Mrs Onyedikachi Chinonyelum and my children Kamsiyochukwu Chichetam, Chimdindu Paul (Jnr.) and Chizitelu Lotachukwu for their patience, love, understanding and bearing with my long absence during my studies.

I also would like to acknowledge in a very special way Prof. Iain Todd, the head of Mercury and Additive Manufacturing Centre, University of Sheffield, United Kingdom for providing financial support during my PhD studies and research works. I gratefully acknowledge Dr. Fatos for his support. I also wish to express my deep appreciation to all the departmental staff members and administrative staff of Mercury Centre for their support and valuable assistance in the completion of my thesis.

I also feel blessed by having wonderful colleagues — Andy Cunlif, John Plummer, Chen, Jake, Hussain, Zifu, Gael, Everth, Zhao and Laura — who created a very friendly environment in the office and provided me with support whenever I needed.

Lastly, I offer my regards and blessings to all my friends and everyone else who supported me in any respect (too many to mention) during the completion of this thesis. Thank you!

Paul Sunday U Nnamchi
Sheffield, United Kingdom

Chapter 1

Introduction and Problem Statement

5.2 Summary

This chapter details the motivation and scientific objectives leading to the present research work on design of Ti-based biomaterial alloys. Further, the obvious and useful link between solid-state phase transformation and electronic structure of metallic alloys and the justification for applying the theory–guided materials design (density functional theoretical) approach implemented using castep code are highlighted.

1.2 Motivation for the design of beta-Ti-based biomaterial alloys

There is a need to develop Ti alloys for implant application that is Ni free and biocompatible with matching modulus to the human bones. The aim of this work is to provide some guidance for the development of Ti alloys for biomedical and other structural applications. Titanium has been a valued metal and its main advantages when compared with other engineering alloys are its high specific strength and corrosion resistance at low and elevated temperatures. Aerospace structures such as airframes and engine components have benefitted from the introduction of titanium alloys since the 1950s. Other applications include: steam turbine blades, superconductors, condenser tubing for fuel plants and biomedical devices [1].

For biomedical applications however, there has been a concern about the stress shielding phenomenon, which occurs as a direct result of the stiffness mismatch between implant materials and the surrounding natural bone (i.e., insufficient loading of bone due to the large difference in modulus between the implant device and its surrounding bone). This phenomenon, more often observed in cementless hip and knee prostheses, can potentially lead to bone resorption and eventual failure of the arthroplasty [2-4]. It is therefore particularly important that the elastic mismatch between the bone replacement material and existing bone be minimised.

Recent complementary studies based on strain gauge analysis [4, 5-6] and finite element analysis [7, 8] have demonstrated that lower modulus (more flexible) femoral hip implant components result in stresses and strains that are closer to those of the intact femur, and a lower modulus hip prosthesis may better simulate the natural femur in distributing stress to the adjacent bone tissue [5, 6]. Canine and sheep implantation studies have shown significantly reduced bone resorption in animals with low modulus hip implants [7], and the bone loss commonly experienced by hip prosthesis patients may be reduced by a prosthesis having lower modulus [7, 8]. To minimise the existing mismatch between bone replacement material and existing bone is therefore a particularly important goal.

Two alternative methods of avoiding diverse tissue reactions are being investigated. One is Ti-oxide surface modification [9], and the other is a new Ni-free Ti-shape memory alloy [10-13].

For the latter, previous studies have shown that the most promising compromise are those alloys that present niobium, zirconium, molybdenum, and tantalum as alloying elements in titanium [4, 5, 10-12]. Recently, alloys containing β phase stabiliser elements (niobium, tantalum and molybdenum) with lower values of Young's modulus have been considered attractive for use as biomaterials, among which the Ti-Mo or Ti-Nb and their complex alloy systems are outstanding [3-13]. The antecedent is that a new era of bone replacing materials will likely be based on β phase Ti alloys. In consideration, profound intensive materials design studies will be essential.

Additionally, Ti and their alloys exhibit a number of other metastable and stable phases, including a non-close packed ω phase, the martensitic α or α′′ phases and intermetallic compounds [14, 15]. These multiple phases encountered in Ti alloys (or in general group IV elements) can be attributed to the competing structural and compositional instabilities inherent within the bcc β phase of these alloys, on quenching from high temperatures [16]. For example, deformation of metastable β-Ti alloys containing the aforementioned β stabilising elements can lead to the formation of stress induced martensite (SIM), α′′ phase, which has an orthorhombic unit cell.

Though previous studies have primarily focused on the pressure induced α to β transformation in Ti and their respective alloys, and the α to β transformation pathway have been probed via experimental [17, 18] and computational methods [19], the opposite has been the case for metastable α′′ phase. The property of this metastable α′′ phase has intrigued researchers, because they are the basis for shape memory and pseudoelastic effect [20, 21]. Furthermore, α′′ precipitates have typically been observed in alloys quenched from high temperature β phase fields, retaining the composition of the parent β matrix, and formed by a diffusionless, purely displacive, collapse of the {111} planes of the bcc phase via a shuffle mechanism [22]. Though this is the generic understanding of how the α′′ phase nucleates and transforms to β phase, conclusive experimental and theoretical evidence for the postulated mechanism is, to the best of our knowledge, still lacking. Since Ti alloys often exhibit low elastic moduli due to the presence of α″ and/or β phase [1, 23-26], which is preferred for ideal metallic biomaterials, there has been a growing trend toward the development of low modulus β type Ti alloys that retain a single β phase or α″ and β phase microstructure on rapid cooling from high temperatures. Such alloys are especially suited for orthopaedic applications.

Reliable design of structural components requires in-depth theoretical understanding of the underlying mechanism for properties. For this reason, the effect of alloying additions on the thermodynamics, stability mechanisms, microstructure and mechanical properties of homogenised α′′ and β Ti alloys are investigated in order to examine their potential use in biomedical applications; and these data can then be reconciled with the corresponding experimental results.

1.3 Motivation for ab initio electronic structure method

The mechanism of β phase transformation from the parent phase to the martensite phase in Ti alloys has been attributed to the peculiarity of their electronic structure [27-29] because of the obvious and useful link between solid-state phase transformation and the electronic structure of metallic alloys. Accordingly, when atoms come together to form a crystal, a redistribution of electron charge creates bonds that govern almost all of the crystal physical and chemical properties [30-31]. The heats of formation, elastic constants and phonon dispersion, and density of states (DOS) can be used to predict the stability of metal alloys. There is experimental evidence that links the theoretical electronic structure to the stability of a broad class of Ti-based shape memory alloys using DFT ab initio calculations [17, 18, 20-29].

In general, wave-function based ab-initio methods approach the atomistic interactions at the fundamental level — quantum physics is utilised by solving Schrodinger's equation for the many-body problem of the electronic structure. The complexity of this approach is obvious — in general the wavefunction of the many-particle system depends on the coordinates of each particle and, thus, the treatment of any system larger than a small number of electrons is not feasible. DFT provides some kind of compromise in the field of ab initio concepts, and can be applied to the fully interacting system of many electrons. Essentially, DFT is based on the theorems of Hohenberg and Kohn [32], who demonstrated that the total ground state energy E of a system of interacting particles is completely determined by the electron density ρ. E can therefore be expressed as a functional of the electron density and the functional E[ρ] satisfies the variational principle. Kohn and Sham [33] then rederived the rigorous functional equations in terms of a simplified wave function concept, separating the contributions to the total energy as,

$$E|\rho(r)| = T_S|\rho| + \int V(r)\,\rho(r)dr + \frac{1}{2}\int \frac{\rho(r)\rho(r')}{r-r'}dxdx' + E'_{XC}|\rho(r)|, \qquad (1.1)$$

— in which Ts represents the kinetic energy of a noninteracting electron gas, and V the external potential of the nuclei. The last term, E_{xc}, comprises the many-body quantum particle interactions, it describes the energy functional connected with the exchange and correlation interactions of the electrons as fermions. Introducing the Kohn-Sham orbitals, the solution of the variational Euler equation corresponds to the functional of equation 1.1, resulting in Schrodinger-like equation for the orbitals ψ1.

$$\left(-\frac{h^2}{2m}\nabla^2 + V_{eff}(r)\right)\ \psi(r) \approx \epsilon\psi(r) \qquad (1.2)$$

These are the renowned Kohn-Sham equations which are then actually solved (after introducing the approximations described below). Equation 1.2 transforms the many-particle problem into a problem of one electron moving in an effective potential.

$$V_{eff}(r) = V(r) + \int \frac{\rho(r')}{|r-r'|}dr' + \frac{\delta E_{XC}[\rho]}{\delta\rho}, \qquad (1.3)$$

This describes the effective field induced by the other quantum particles. The actual role of the auxiliary orbitals is to build up the true ground state density by summing all occupied states,

$$\rho(r) = \sum_{occ} \psi*(r)\,\psi(r). \qquad (1.4)$$

This therefore provides a suitable basis to transform the functional equation into a set of differential equations, where the variational Kohn-Sham orbital may be expressed as a linear combination of basis functions ψ obeying Bloch's theorem. This equation has to be diagonalised for obtaining the eigenvalues ε and eigenvectors c from which the electron density is constructed and — consequently — the total energy is derived.

The resulting equations can be solved in a self-consistent manner. The crucial point for actual applications is the functional Exc, which is not known (and therefore has no analytical expression) and therefore requires approximations. The function ε_{xc} (ρ) has to be partially approximated as well, though this can be done accurately by computer simulations.

Currently, the most widely used numerical methods for solving the Kohn-Sham equations are The Linear Muffin-Tin Orbitals Method (LMTOM) and The Full-potential Linearised Augmented Plane Wave Method (FLAPW) [34]. In the present thesis, the commercial version of Cambridge Serial Total Energy Package (CASTEP code) [35, 36] is applied, which is one of the most powerful ab initio DFT packages available at present. CASTEP is based on the pseudopotential concept. For the actual calculations, a generalisation in terms of the so-called projector augmented waves construction of the potential [37] is applied, which is known to give very accurate results as tested by comparison to FLAPW benchmarks. CASTEP has already been applied to a wide range of problems and materials, to bulk systems, surfaces, interfaces; e.g. Refs. [38-39]. CASTEP provides a framework for the bulk and surface phonon calculations as well [35].

Other specific computational and technical aspects (e.g. number of k-points, geometry of the unit cell etc.) are discussed later together with the results. The theory and parameters underlying the CASTEP code have been addressed in the aforementioned publications. It should be noted that CASTEP has also been applied to materials and systems which may be considered 'well-established' from the computational point of view. The CASTEP as implemented in the materials studio package served as a tool, which works reliably when handled with care and knowledge. Convergency aspects were carefully tested in several cases. As a consequence, it can be argued that the results as presented in following chapters do not depend on inherent technical parameters and are physically meaningful.

1.4 Scope and outline of the thesis

Over the last decade, experimental and theoretical investigations have shown that changes in electronic interactions play a main role in solid state phase transformation. Different processing steps were carried out in this thesis for the design and in predicting the properties of novel Ti based alloys for structural applications in medical implants for spinal fixation, technological applications like shape memory metals. The scheme shows that after identifying the properties to be optimised, a property search is done by a combination of experimental and empirical calculations. The alloy dependencies are verified by characterisation analyses. The behaviours are optimised via theory and an experimental adjustment before the final characterisation analyses are carried out. In the end, novel alloys of desired quality and properties are produced by this process.

Above all, this combinatorial approach involving first principle calculation steps with experimental works are very important; points needing significant changes are identified and adjusted to optimise the alloy properties and improve the final cast product. This has led to some insight into the alloy microstructure -property relationships, and on the effect of atomic variables on the microstructure. The important information derived from the calculation includes the precise identification of stability boundaries, lattice constants and energetic landscape for phase transformation. The main drawback is that some of the probing experimental characterisation techniques are very expensive. Performing several interrupted tests to analyse the properties is time consuming. Finally, the thesis has been arranged into eight chapters, namely: the introduction background/literature review; experimental and computational techniques (following this introduction); results presented in chapters 4, 5, 6 and 7; and the conclusions and further work are briefly summarised in chapter 8.

1.5 References

[1] Boyer R. R., Welsch G. and Collings E. W.; Materials Properties Handbook, "Titanium Alloys", ASM Handbook, Institute of Metals, Metals Park, OH, USA (1994).

[2] Navarro M., Michiardi A., Castaño O. and Planell J.; Biomaterials in orthopaedic, J. Royal Society, Interface 5 (2008), 1137-58.

[3] Qazi, J. I. and Rack, H. J.; Metastable Beta Titanium Alloys for Orthopedic Applications, Advanced Engineering Materials 5(2005), 993-998.

[4] Ho W. F., Ju C. P. and Lin J. H.; Structure and properties of cast binary Ti-Mo alloys, Biomaterials 20 (1999), 2115-22.

[5] Hao Y. L., Li S. J., Sun S. Y., Zheng C. Y. and Yang R.; Elastic deformation behaviour of Ti-24Nb-4Zr-7.9Sn for biomedical applications, Acta biomaterialia 3 (2007), 277-86.

[6] Niinomi M.; Mechanical biocompatibilities of titanium alloys for biomedical applications, Biomed Mater. 1(2008), 30–42.

[7] Cheal E., Spector M. and Hayes W.; Role of loads and prosthesis material properties on the mechanics of the proximal femur after total hip arthroplasty, J Orthop Res. 10 (1992), 405–22.

[8] Prendergast P. and Taylor D.; Stress analysis of the proximo-medial femur after total hip replacement. J Biomed. Eng. 5 (1990), 379–82.

[9] Slokar L., Matković T. and Matković P.; Alloy design and property evaluation of new Ti–Cr–Nb alloys, Materials & Design 33 (2012), 26-30.

[10] Miyazaki S., Kim H. Y. and Hosoda H.; Development and characterization of Ni-free Ti-base shape memory and superelastic alloys, Mat. Sci.& Eng. A 438-440 (2006), 18-24.

[11] Kim H. Y., Ikehara Y., Kim J. I., Hosoda H. and Miyazaki S.; Martensitic transformation, shape memory effect and superelasticity of Ti–Nb binary alloys, Acta Materialia 54 (2006), 2419-2429.

[12] Biesiekierski A., Wang A., Gepreel J., Abdel-Hady M. and Wen C.; A new look at biomedical Ti-based shape memory alloys, Acta biomaterialia 8 (2012), 1661-9.

[13] Al-Zain Y., Kim H. Y., Hosoda H., Nam T. H. and Miyazaki S.; Shape memory properties of Ti–Nb–Mo biomedical alloys, Acta Materialia 58 (2010), 4212-4223.

[14] Moffat, D. L. and Larbalestier D. C.; The competitions between martensite and omega in quenched Ti-Nb alloys, Metallurgical Transactions A 19 (1998), 1677-86.

[15] Elkin, A. V. and Dobromyslov V. A.; Martensitic transformation and metastable β-phase in binary titanium alloys with d-metals of 4–6 periods, Scripta Materialia 44 (2001), 905-12.

[16] Bowles, J. S. and Barrett C. S.; Crystallography of transformations, Progress in Metal Physics 3 (1952), 21-34.

[17] Ogi H., Kai S., Ledbetter H., Tarumi R., Hirao M. and Takashima K.; Titanium's high temperature elastic constants through the hcp-bcc phase transformation, Acta Met, 52 (2004), 2075-2080.

[18] Zhao X., Niinomi M. and Nakai M.; Relationship between various deformation-induced products and mechanical properties in metastable Ti-30Zr-Mo alloys for biomedical applications, J. Mech. Beh.Biomed. Materials 4 (2011), 2009-16.

[19] Raabe D., Sander B., Fria´k M., Ma D. and Neugebauer J.; Theory-guided bottom-up design of b-titanium alloys as biomaterials based on first principles calculations- Theory and experiments, Acta Materialia 55 (2007), 4475–4487.

[20] Wang, B. L., Zheng Y. F. and Zhao L. C.; Effects of Sn content on the microstructure, phase constitution and shape memory effect of Ti–Nb–Sn alloys, Materials Science and Engineering: A 486(2008), 146-151.

[21] Zhang, L. C., Zhou, T., Alpay, S. P., Aindow M. and Wu M. H.; Origin of pseudoelastic behavior in Ti–Mo-based alloys, Applied Physics Lett. 87 (2005), 241909.

[22] Hao Y., Li S., Sun B., Sui M. and Yang R.; Ductile Titanium Alloy with Low Poisson's Ratio, Physical Review Lett. 98 (2007), 1-4.

[23] Long M., Rack H. J.; Titanium alloys in total joint replacement- a materials science perspective. Biomaterials 19 (1998), 1621–39.

[24] Hanada S., Matsumoto H., Watanabe S.; Mechanical compatibility of titanium implants in hard tissues, 1284. International Congress Series ; (2005), 239-47.

[25] Matsumoto H., Watanabe S., Hanada S: Microstructures and mechanical properties of metastable β TiNbSn alloys cold rolled and heat treated, J. Alloy Compd. 439 (2007), 146–55.

[26] Matsumoto H., Watanabe S., Hanada S.: Beta TiNbSn alloys with low Young's modulus and high strength, Mater Trans 46 (2005), 1070‑8.

[27] Yogesh K. V. and Spencer P. T: Novel γ-Phase of Titanium Metal at Megabar Pressures, Physical Review Letts. 86 (2001), 3068-3071.

[28] Akahama Y., Kawamura H., Le Bihan T: New δ (Distorted-bcc) Titanium to 220 GPA, Physical Review Letts.87 (2001), 2-5.

[29] Dai J. H., Wu X., Song Y. and Yang R: Electronic structure mechanism of martensitic phase transformation in binary titanium alloys, J. Applied Phys.112 (2012), 123718-24.

[30] Midgley Paul. A: Electronic bonding revealed by electron diffraction, Nature Science 331 (2007), 1528-1529.

[31] Dai J. H., Wu X., Song Y. and Yang R: Electronic structure mechanism of martensitic phase transformation in binary titanium alloys, J. Applied Physics 112 (2012), 123718.

[32] P. Hohenberg and W. Kohn; Inhomogeneous Electron Gas, Phys. Rev. B 136, (1964), 864–871.

[33] Kohn W. and Sham J.; Self consistent equation including exchange and correlation, physics Rev A 140 (1965), 1133.

[34] Wagner M. F. and Windl W.; Lattice stability, elastic constants and macroscopic moduli of NiTi martensites from first principles, Acta Materialia 56 (2008), 6232-6245.

[35] Huang X., Ackland G., Raabe J. and Karin M.; Crystal structures and shape-memory behaviour of NiTi, Nature materials 2 (2003), 307-11.

[36] Segall M., Philip J., Lindan D., Probert M. J., Pickard C. J., Hasnip P. J., Clark S. J. and Payne M. C.; First-principles simulation: ideas, illustrations and the CASTEP code, J. Phys.: Condens. Matter 14 (2002), 2717–2744.

[37] Bloch, P. E.; Projected augmented — wave method, Physical Review B 50(1994), 953-978.

[38] Rodriguez J., Hanson J. C., Chaturvedi S. M., Amitesh B. and Joaquin L.; Phase transformations and electronic properties in mixed-metal oxides: Experimental and theoretical studies on the behavior of NiMoO and MgMoO, The Journal of Chemical Physics 112 (2000), 935.

[39] Tan C. L., Tian X. H., Ji G. J, Gui T. L. and Cai W.; Elastic property and electronic structure of TiNiPt high-temperature shape memory alloys, Solid State Communications 147 (2008), 8-10.

Chapter 2

Background and Literature Review

2.1 Summary

This research incorporates recent characterisation and alloy development techniques such as: use of (e/a) as a parameter for β-Ti alloy stability, Md-orbital DVX-calculation model, and electronic structure methods (DFT calculation). This chapter first presents and discusses some background and recent work in the literature regarding alloy development by density functional theory (DFT) and by means of electronic calculations. A short introduction to the metallurgy and psuedoelasticity of β Ti alloy is also given, along with discussion of major operating mechanisms and some background on the potential elastic modulus improving alloy additions used in this work.

2.2 Advances in electronic approach to materials design theory

In this subsection, the main historical landmarks of alloy design by electronic theory of metals are discussed, starting with the first systematic efforts to exploit the potency of using electronic phenomena to derive phase stability through the work of Hume-Rothery in the 1920s, to the modern density functional theory (DFT).

2.2.1 Hume-Rothery's electron per atom ratio (e/a) parameter

The earliest record of alloy theory is the advent of electron per atom ratio e/a rule (See Eqn.2.1), originally proposed in 1926 by Hume-Rothery while working in Oxford University [1].

$$\frac{e}{a}=\frac{\sum_{i=1}^{I}(X_i n(s+d)_i)}{\sum_{i=1}^{I}X_i} \qquad (2.1)$$

Where, X_i is the atomic fraction of the alloying elements, i^{th} component $=\{1 \ldots \ldots I\}$, of the individual outer s+d contributed by the metal atoms. As reported elsewhere [2], although electronic theory of metals has developed along with the development of quantum mechanics, in the period preceding 1926 metallurgy seemed to be in confusion due to the deviation of stoichiometric compositions from those expected of the valency rule of in organic chemistry. Although people were aware of a class of materials with apparently loosely bound electrons, no one was able to think of the style of metallic bonding before the conception of the Schrodinger equation in 1926 [3] or the establishment of metallic cohesion based on quantum mechanics in 1933 by Wigner and Seitz [4].

In this work, Hume-Rothery reported regularity in spite of little connection in composition in the synthesis of various intermetallic compounds of Cu with reactive alkaline and alkaline earth metals in binary systems. Further examination of these alloys [5, 6] showed that they possess one characteristic, which highlighted the connection between the observed crystal structures and the electron concentration (e/a). Westgren and Phragmen were among the early scientists stimulated by Hume-Rothery's proposal, and extended their x-ray studies to examine structures of Cu-Zn, Cu-Al, and Cu-Sn systems [7]. They were also the first to confirm experimentally the utility of e/a as an important parameter in materials research. These three gamma-brasses show the existence of such regularity in spite of little connection in composition between Cu_2Sn, Cu_3Al and CuZn, which crystallise into a common structure of the BCC phase with the possession of e/a equal to 21/13 (see Figure 2.1 as reproduced from [8, 9]), superimposing the copper rich portion of the phase diagram of Cu-Zn and Cu-Ga on to the electron concentration.

This work by Hume-Rothery is justifiably celebrated for turning the art of metallurgy into modern science. Although previously criticised for being too semi empirical in approach, and failing in some cases, Tiwari and Ramanujan [10] recent review surveyed the e/a relations with a range of properties including solid solubilities, intermetallic compound formation, liquidus temperature, axial ratio of hexagonal phases, formation of different phases, stacking fault energy, specific heat, flow stress, superconductivity and stress corrosion cracking, giving a good indication of the roles of e/a ratio. They noted that, within the framework of a model for stable zones of electronic theory for metals, quite a strict correlation between the concentrations of phase boundaries in phase stability of some binary alloy systems exists, and its influence on determining the physical properties has long being theoretically [9,11,12] and experimentally observed [13-14]. They argued that, in reality, a pattern emerges whenever the magnitude of a physical property is plotted against e/a ratio, and a breakdown in the regularity can be an indication of significant changes within the electronic structure of the alloy matrix.

Very recently, Saito and co-workers [16] employed e/a alongside Mo and Bo as a parameter to develop the β-type Ti-Nb-Ta-Zr-O alloy series with multifunctional capability, referred to as Gum metals. They reported that β Ti phase would be stable when e/a ≥ ~4.25 eV. The work of Hao *et al* [17] on Ti-24Nb-4Zr-7.9Sn alloy, however, showed the extent of such relationships, with e/a parameter being a tool for tuning compositional stability and properties that is dependent on the type of alloying additions.

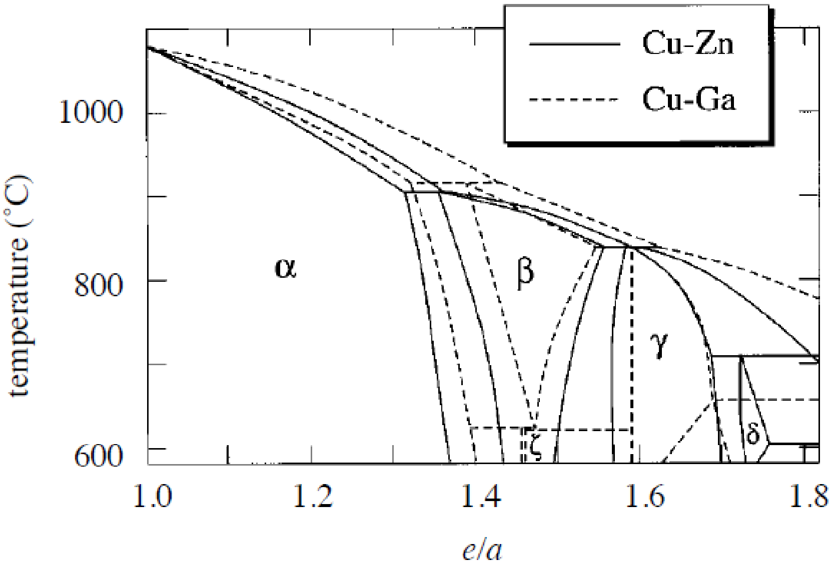

Figure 2.1 Cu-rich portions of the Cu–Zn and Cu–Ga phase diagram plotted against electron concentration rather than atom concentration, after Hume-Rothery (1961).

2.2.2 Jones and Mott early band theory

Not long after the publication by Hume-Rothery [1], Mott and Jones published their investigation into the theory of the properties of metals and alloys [18], in which they discussed different approaches to the Hume-Rothery electron concentration rule. They proposed that the critical electron concentration could be estimated from the Fermi surface Brillouin zone (FsBz) interaction for a given phase, referring to the gamma-brass phase, which occurs at the ratio of 21 valence electrons to 13 atoms with e/a equal to 21/13 for both Cu_3Zn_8 and Cu_9Al_4 gamma brasses as an example. Although, they conceded that no precise calculation had been done, they assumed that the free energy against solute concentration would suddenly increase as the concentration passes across a boundary of the phase, and that it would be most likely caused by an increase in the electronic energy at absolute zero.

They tried to explain the mechanism behind their argument using a density of state (DOS) curve, (see Figure 2. 2 (a) and (b) after [18]). In the DOS diagram, a round maximum A with a rapid declining slope in the DOS was attributed to the FsBz interaction. This suggests that when the Fermi surface approaches and touches the Brillouin zone phases, they assume that a small but naturally gradient E in the energy of dispersion would occur that would enable the DOS to be sharply enhanced. In effect, the electronic energy is considered to rise rapidly as soon as the electrons fill up the band to point A, in the form as shown shaded in Figure 2.2(c) [18]. The critical value of electron per atom ratio, (e/a), was simply calculated in the free electron model under the assumption that it was given by the electron filling a sphere inscribed to the Brillouin zone. The values of (e/a) for the alpha, beta, and gamma brasses are 1.362, 1.480 and 1.538, respectively, as illustrated in Figure 2.2b. Though their hypothesis did not stand the test of time — as it was not based on any calculation — surprisingly, the values of e/a are indeed not very far from the values of 1.4, 3.2, and 21/13 (=1.615) in the empirical Hume-Rothery electron rule. This is one of the most important conclusions advanced by them in 1936 [1, 5, 7].

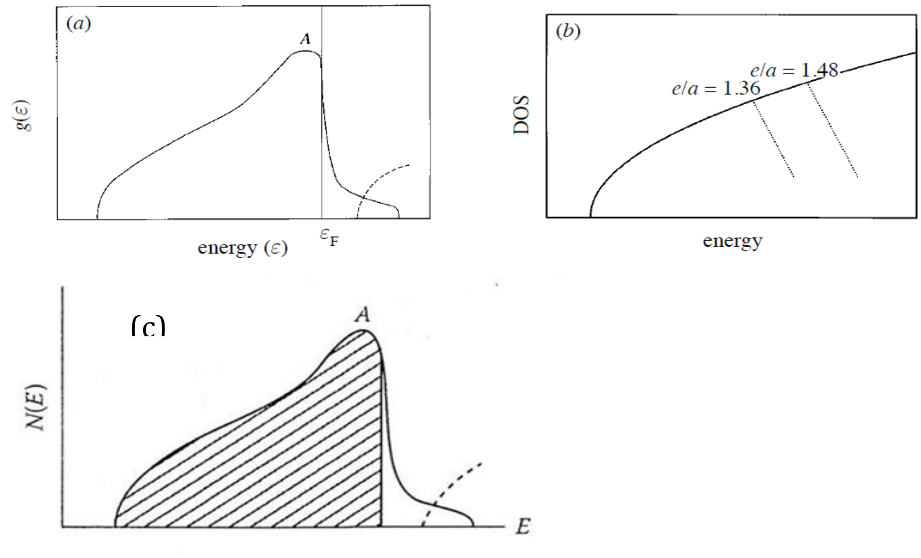

Figure 2.2: (a) Density of states in the Jones model. After Jones (1937); (b) Energy difference calculated by Jones from the density of states in (c) electrons fill up the band to just the point A just lower than the Fermi energy.

A year later, Jones [19, 20, 21] published his own theory. This became the first direct attempt at the application of quantum mechanics to analysing the stability of alloy phases by interpreting the phase competition between the FCC and BCC phases in the Cu-Zn system within the framework of the two-wave approximation in the nearly free electron (NFE) model [22]. By this model, Jones was able to introduce the energy of the valence electron in the neighbourhood of the centre of the zone boundary as defined in eqns. 2.2-2.4, [19]:

$$E = \left(\frac{h^2}{2m}\right)\left[k_x^2 + k_y^2 + k_0^2 + \alpha(k_z - k_\alpha^2)\right] - \frac{\Delta E}{2} \qquad (2.2)$$

$$= E_0[x^2 + y^2 + 1 + \alpha(z-1)^2] - \frac{\Delta \mathrm{E}}{2} \qquad (2.3)$$

$$= E_0\left[x^2 + y^2 + 1 + \alpha(z-1)^2 - 2\sqrt{(1-z)^2} + \frac{1}{(1-\alpha)^2}\right] \qquad (2.4)$$

Here, α =1-4Eo/E; m is the mass of the free electron and is the Planck's constant divided by 2; Kz- axis is chosen perpendicular to the Brillouin zone plane in the reciprocal space and passes through its centre (0, 0, Ko); E is the energy gap across the zone plane; and x, y and z are normalised variables with respect to Ko. The point (0, 0, Ko), refers to the principal symmetry points L and N at the centre of the 111 and 110 zone planes in the Brillouin zone of the FCC and BCC lattices, respectively. Using these equations, he indicated that the free electron behaviour is maintained as long as the electron states (x, y, z) are away from 0, 0, 1; but, as z approaches unity, the energy of the states associated with the points lying along a line in K space through the origin and perpendicular to a place of discontinuity would form a curve, as shown in Figure 2.3, where the dotted line represents the free electrons [19].

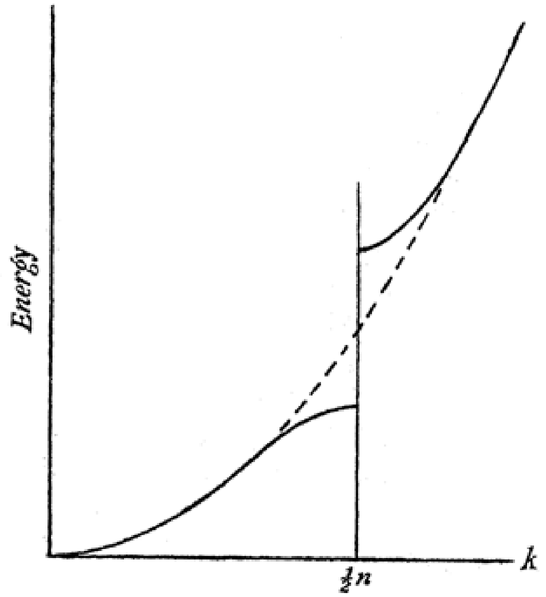

Figure 2.3: The energy of the states associated with the point lying along a line in K space through the origin, and perpendicular to a plane of discontinuity plotted against the distance from the origin. The dotted line represents energy of the free electron, after Jones (1934).

Jones essentially made a comparison of the valence band structural energies between the face-centred cubic (FCC) and body-centred cubic (BCC) Cu as a function of electron concentration (e/a) in the context of the rigid band model, when he assumes that the addition of Zn to increase e/a does not change the DOS of the parent Cu with the FCC and BCC structures, and the parameter e/a can be obtained from eqn. 2.5 [19]:

$$D(E) = \left(\frac{V_a}{2\pi^2}\right)\left(\frac{2m^{3/2}}{h^2}\right)\sqrt{E} \qquad (2.5)$$

Here, D (E) represents the DOS and Va is the volume per atom. A perfect coincidence of the two parabolas over the energy range below about 5 eV for the FCC and BCC-Cu indicate that Jones assumed, $V_a^{FCC} = V_a^{bcc}$ in Eqn. 2.5. The volumes per atom Va in FCC and BCC lattices are therefore obviously given by $\frac{a_{FCC}^3}{4} = \frac{a_{BCC}^3}{2}$ respectively, where a is the lattice constant. The DOS equation given by Jones therefore implicitly leads to the relation in eqn. 2.6. The energy difference calculated by Jones from the density of states in Figure 2.4(a) is displayed as Figure 2.4 b [20]:

$$a_{FCC} = 2a_{BCC}^{\frac{1}{3}} \tag{2.6}$$

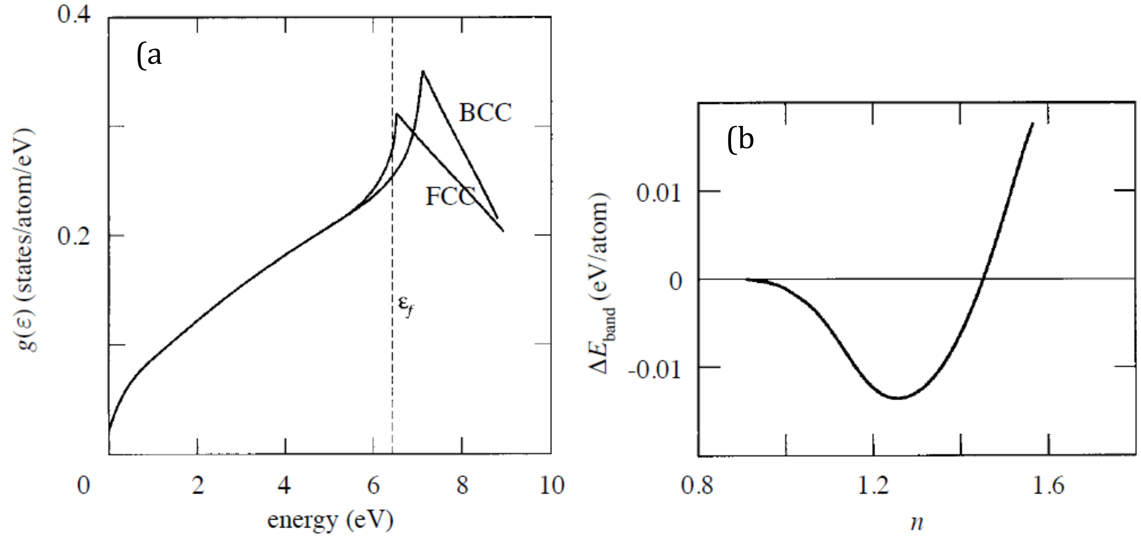

Figure 2.4: (a) Density of states in the Jones model. After Jones (1937); (b) Energy difference calculated by Jones from the density of states in (a).

The large kink found in the DOSs (see Figure 2.4(a)) represents the so-called ‘van Hove singularity’, which Jones believed to be responsible for the interpretation of the Hume-Rothery electron concentration rule [20]. To account for the e/a dependent stability of the α and β phases, Jones explained that the van Hove singularity in the BCC Cu in Figure 2.4 was caused by the contact of the Fermi surface with the 110 peak in the DOS of the BCC- Cu located about 1 eV higher than the 111 peak in the FCC-Cu e/a variation at different Fermi surface. Jones' work is displayed in Figure 2.5 [21].

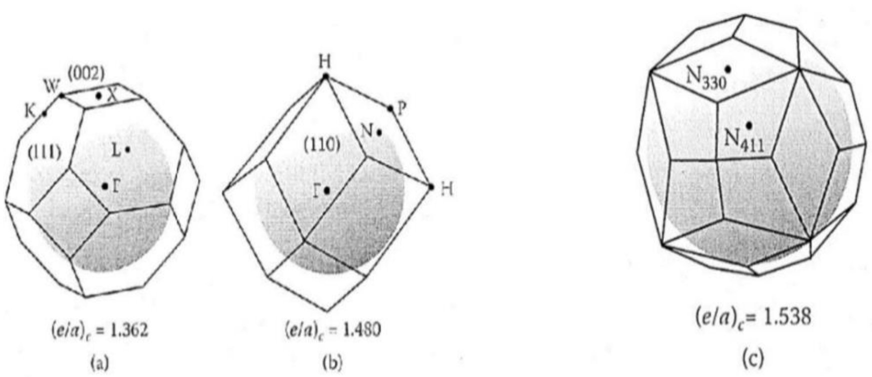

Figure 2.5: The FsBz interaction in the Mott and Jones theory, A critical vale of (e/a) is obtained when spherical Fermi surface touches the zone plane of the respective Brillouin zone (a) the principal symmetry point L in the FCC Brillouin zone, (b) the principal symmetry point N in the BCC Brillouin zone, and (c) the symmetry point N330 and N411 in the Brillouin zone for the gamma-brass structure from Mott and Jones 1936.

Similarly, Jones tried to use the valence band structure energy U of the respective phases to explain the α/β phase transformation. He found U by integrating the DOS multiplied by the energy E up to the energy corresponding to the highest occupied states. The valence-band structure energy difference between these two phases, U, is given as a function of e/a by eqn. 2.6:

$$\Delta E(e/a) = \int_0^{E_{fcc}} E D_{fcc}(E) dE - \int_0^{E_{bcc}} E D_{bcc}(E) dE \qquad (2.6)$$

Here, the upper limit of the integral E_{FCC} or E_{BCC} is the energy for FCC or BCC phases when the same number of electrons is filled into the respective DOSs. By this relation, it follows that the relative stability of an alloy phase will be enhanced if the DOS curve involves a large peak and a subsequent rapid declining slope like in Figure 2.4(a), while the competing phase is fairly monotonic for a given (e/a) range. It was not until 1957 that the error in Jones' model was recognised, when Pippard [23] discovered the flaws and inconsistency in the possession of neck in the Fermi surface contour of pure Cu. It was only then that people became aware of the many unjustified assumptions in the model, which had been made to conveniently account for the Hume-Rothery rule. Although the early theories as proposed by Mott and Jones in the 1930s were unfortunately far from being satisfactory, their work provided an inspiration for interpreting the Hume-Rothery electron concentration rule, which relates phase stability to the Fermi surface.

2.2.3 DV Xα and Md-parameter electronic calculation

The first theoretical approach to β-Ti alloys design was proposed by Morinaga *et al.* [24] using the d-electron method based molecular orbital calculation of electronic structures (called discrete variational Xα cluster method, DV-Xα cluster method). Figure 2.6 shows changes in Md-Bo relation of Ti by alloying. Two parameters were determined theoretically: namely, (i) the bond order number (Bo), which is a measure of the covalent bond strength between Ti and an alloying element; and (ii) the d-orbital energy level (Md), which correlates the electronegativity and the metallic radius of the elements. The values are defined for an alloy, the compositional average values of Bo and Md parameters is defined according to the following eqns. [24]:

$$|Bo| = \sum_{i=1}^{n} x_i \ (Bo) \tag{2.7}$$

$$|Md| = \sum_{i=1}^{n} x_i \ (Md) \tag{2.8}$$

In their calculation, the two parameters, Bo and Md, are defined, where Bo is related to the strength of the covalent bonding between Ti and an alloying element, and Md is correlated with the electronegativity and metallic radius of elements. According to the definition of the parameters, the average value of Bo for alloys should be between 2.86-2.92 eV and the average value of Md for alloys should be between 2.40-2.45 to attain low Young's modulus.

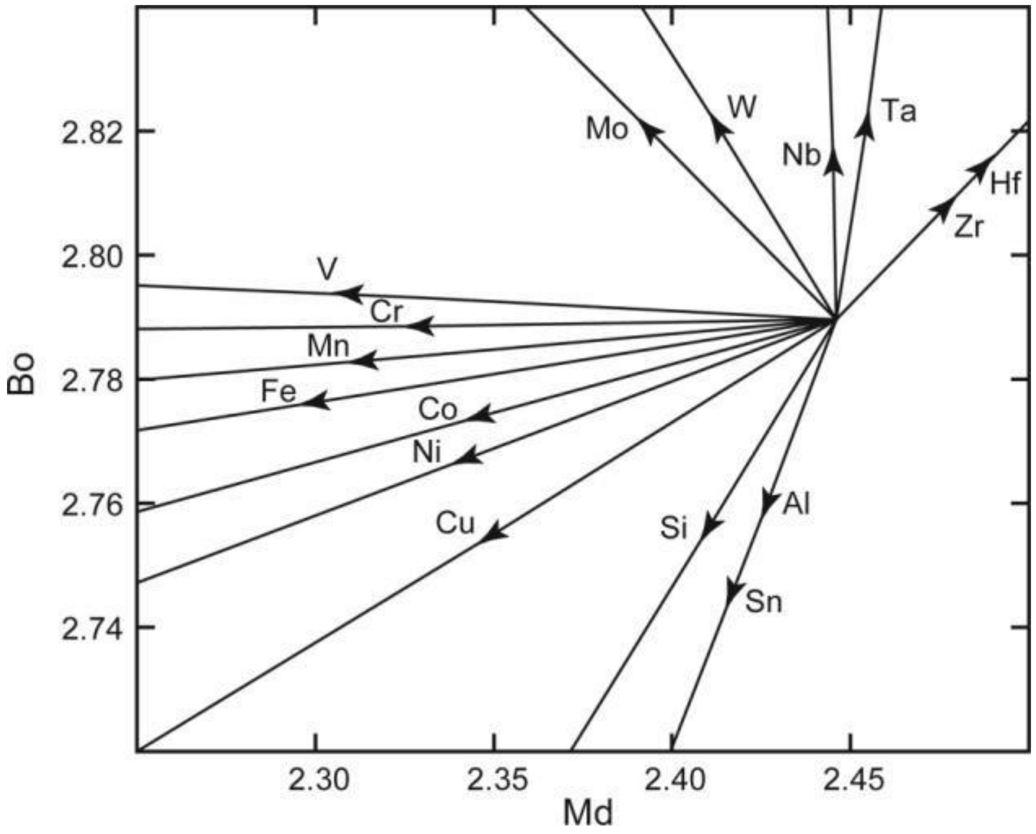

Figure 2.6: Bo-Md relations for various Ti binary alloys by Morinaga *et al.* [24] taken from Kuroda *et al.* [25].

Such a vector varies in direction and magnitude, depending on elements, as shown in the vector map in Figure 2.6. The alloy position moves in (Bo-Md) map as the alloy composition is altered. The areas for α; $\alpha + \beta$ Ti based alloys are labelled as shown in Figure 2.7. (Positions of Ti and its alloys are also shown in the Figure along with their Young's moduli.) The stability of elasticity of these alloys decreases with increasing Bo and Md and towards the stability limit of the β phases; i.e., at the β/β + ω boundary for mainly Ti-Nb alloy system.

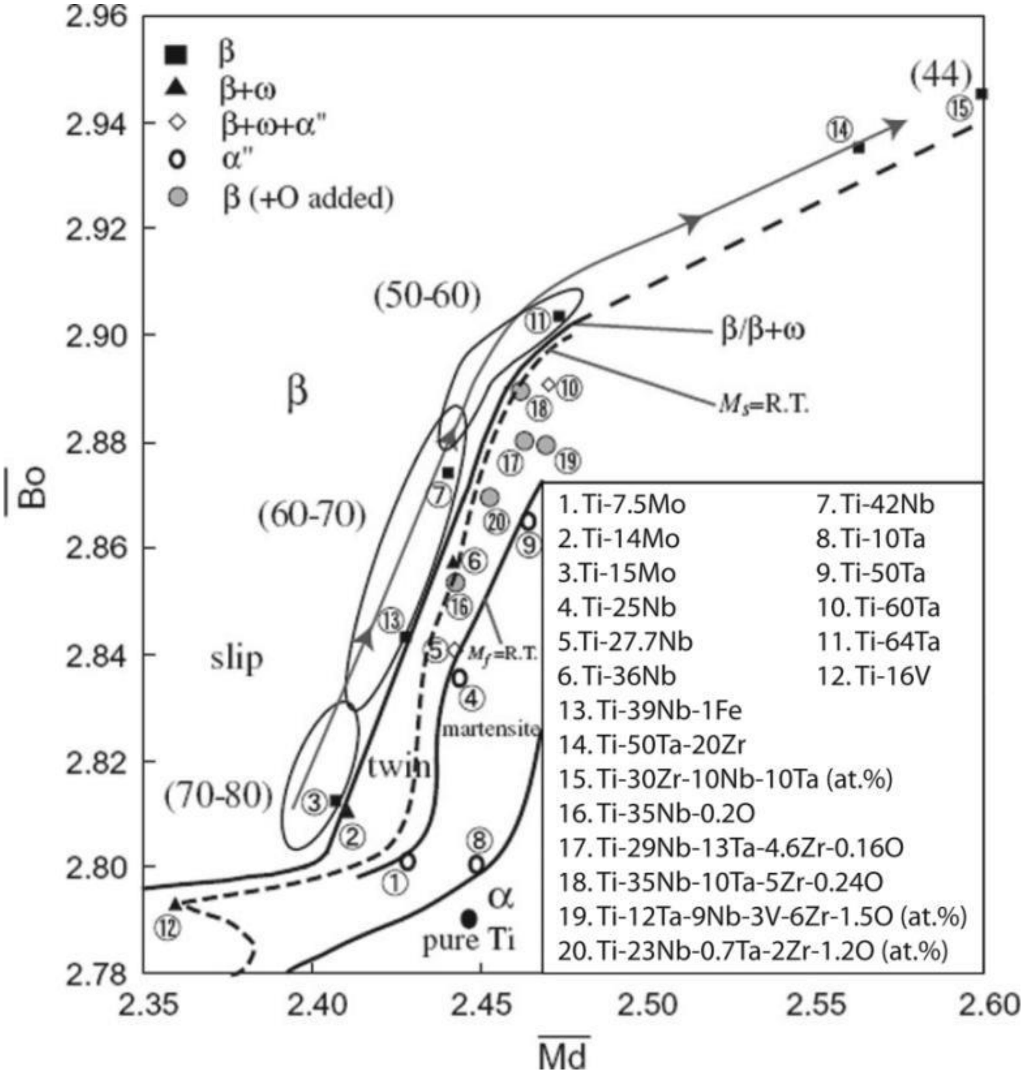

Figure 2.7: [Bo-Md] map in which β/β + ω phase boundary is shown together with the boundaries for Ms=RT and For Mf=RT. The value of the Young's modulus (GPa) is given in parentheses for typical alloys.

2.2.4 First principle (DFT) electronic structure methods

There is still a large step from the theoretical considerations outlined in the preceding section to a manageable form which can be run on a computer. As the solution for a solid is desired, a natural condition is translational symmetry for the observables, such as the potential,

$$\upsilon_{eff}(\mathbf{r} + \mathbf{R}) = \upsilon eff(r): \quad (2.9)$$

Here, R is a lattice translation vector. As a consequence of translational symmetry, the wave function must fulfil Bloch's theorem [26],

$$\psi\Psi\kappa(r + R) = e^{ikR}\,\psi k(r) \quad (2.10)$$

DFT is essentially based on the theorems of Hohenberg and Kohn [27], who demonstrated that the total ground state energy E of a system of interacting particles is completely determined by the electron density (ρ). E can therefore be expressed as a functional of the electron density and the functional E[ρ] that satisfies the variational principle. Kohn and Sham [28] then rederived the rigorous functional equations in terms of a simplified wave function concept, separating the contributions to the total energy as,

$$E|\rho(r)| = T_S|\rho| + \int V(r)\,\rho(r)dr + \frac{1}{2}\int \frac{\rho(r)\rho(r')}{r-r'}dxdx' + E'_{XC}|\rho(r)|, \quad (2.11)$$

The variational Kohn-Sham orbital may then be expressed as a linear combination of basis functions ψ obeying Bloch's theorem,

$$\psi_{nk}(r)=\sum c_{i,nk}\varphi_{ik}(r), \quad (2.12)$$

with band index n and k representing a vector of the first Brillouin zone. Building on energy functionals (i.e. the expectation value of the Hamiltonian) and applying the variational principle, the solution to the Kohn-Sham equations is transformed into a matrix eigenvalue problem,

$$\sum_t \langle \varphi_{jk} | H | \varphi_{ik} \rangle - \epsilon_{nk} \left\langle \phi_{jk} \middle| \phi_{ik} \right\rangle C_{i,nk} = 0 \tag{2.13}$$

This equation has to be diagonalised for obtaining the eigenvalues ε and eigenvectors c from which the electron density is constructed and — consequently — the total energy is derived.

Currently, the most widely used numerical methods for solving the Kohn-Sham equations are: pseudopotential (and related) methods, the linear muffin-tin orbitals method, the full-potential linearised augmented plane wave method (FLAPW) [29], VASP and CASTEP codes [30, 31] using either pseudopotential or the project augmented wave method, and a plane wave basis set. In the present thesis, the commercial version of Cambridge Serial Total Energy Package (CASTEP code) [31] is applied, which is one of the most powerful ab initio DFT packages available at present. CASTEP is based on the pseudopotential concept. For the actual calculations a generalised gradient approximation (GGA) construction of the potential [32] is self consistently applied, which is known to give very accurate results as tested by comparison to FLAPW benchmarks. CASTEP has been already applied to a wide range of problems and materials, to bulk systems, surfaces, interfaces, e.g. Refs. [32, 33, 34].

Other specific computational and technical aspects (e.g. number of k-points, geometry of the unit cell etc.) are discussed later, together with the results. The theory and parameters underlying the CASTEP code have been addressed in the abovementioned publications. It should be noted that CASTEP has also been applied to materials and systems which may be considered 'well-established' from the computational point of view. The CASTEP as implemented in the materials studio package served is a tool, which works reliably when handled with care and knowledge. Convergency aspects were carefully tested in several cases. Consequently, it can be argued that the results as presented in following chapters do not depend on inherent technical parameters and are physically meaningful.

2.3 Titanium metallurgy

Titanium metal is dominated by the allotropic transformation, but the exact transformation temperature is strongly influenced by interstitial and substitutional additions. A survey of the various phase transformations that take place are presented in this section.

2.3.1 Classification of phase transformation

Titanium metal, both in its pure and alloyed states, undergoes a series of allotropic phase transformations in equilibrium conditions from a high temperature body-centred cubic crystal structure (BCC) β phase with space group of the form Im3m (No 229), to the closed-packed hexagonal crystal structure (HCP) α phase of the form P63Immc, (No.194), (see Figure 2.8) at 1155.5 K (β -transus temperature). The exact transus point is dependent on the alloying composition and/or cooling rate regime [35, 36, 37, 38]. It can, however, be broadly classified as stable and metastable phases, depending on the mode of achieving steady state conditions, where the thermodynamics of phase stability is dominated by minimisation of Gibbs free energy (ΔG)[39]. When higher heating/cooling rates are applied, non-equilibrium or metastable phases possessing higher ΔG are formed through displacive transformation by shearing and shuffling mechanisms. In such circumstances, kinetics becomes the dominant driving force behind choosing the exact mechanism for transformation. The metastable phases might be temporal or permanent, depending on the final processing condition.

In describing the phenomenon that favours the formation of equilibrium phases, some metallic elements can be classified as being α, β or neutral stabilisers [35]. The illustrations of these crystal structures are presented in Figure 2.1(a) and 2.1(b).

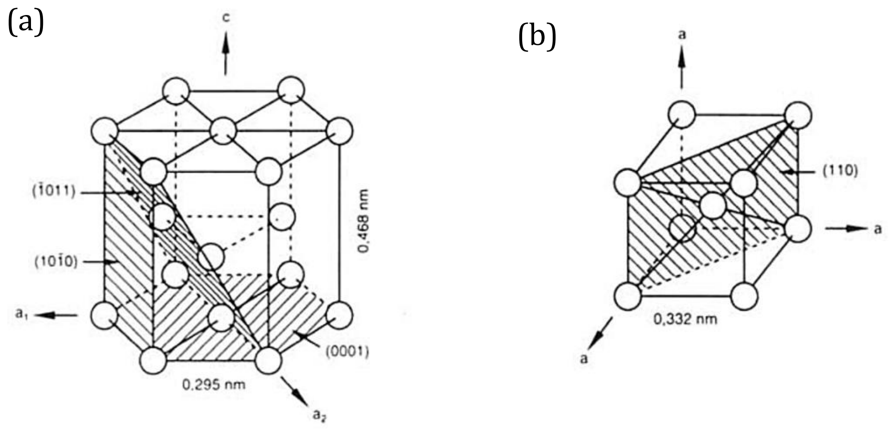

Figure 2.8: Schematic illustration of the unit cell of (**a**) HCP α- phase with the three most densely packed lattice planes and lattice parameters at room temperature, (**b**) the BCC β phase with one variant of the most densely packed [110] lattice planes, and the lattice parameter of pure β at ~ 1173 K.

2.4 Titanium alloys and the phases

The substitutional elements — such as Al and the interstitial elements, such as Al, B, Sc, Ga, La, Ce, Ge, O, N and C —extend the α phase field and are therefore referred to as α stabilisers. Aluminium is the most common alloying element to raise the transition temperature, while still having substantial solubilities in both α, and β phases. Oxygen is occasionally considered an alloying element, though only when it is used to obtain a desired property — such as increasing strength in commercially pure titanium [36, 40]. The term 'aluminium equivalent' (Al. Eq.) is used to quantify the α stability given by the ratio of Al equivalent divided by the weighted averages of the aluminium equivalent of the elements. The Al. Eq. is expressed as [36,37]:

$$(Al_{Eq}:) = Al + 13Sn + 16Zr + (O + C + 2N) \text{ per cent.} \qquad (2.14)$$

Elements which are classified as β stabilisers depress the phase field to a lower β phase transition field temperature [37, 38, 40, 41, 43]. They are classified as either β isomorphous or β eutectoid elements. The β-isomorphous additions are mainly the BCC elements V, Mo, Hf, Ta, and Nb. They are usually transition metals and noble metals in the periodic table which, similar to titanium, have unfilled d-electron bands. Previous investigations have shown that sufficient concentrations of these elements make it possible to stabilise the phase at room temperature. Other isomorphous elements include Ta and W, which are rarely used as alloying additions, because of density concerns. Elements that have limited solubility range in phase and are able to decompose via eutectoid reaction into plus a compounds are known as eutectoid elements. The most commonly used eutectoid elements are Cr, Fe, W, Pt, Pd and Si, Ni, Co, Au, Ag, Cu and Mn. The molybdenum equivalent defined as Mo. Eq. 2.15 is used to express the stability (or β stability) of a titanium alloy. In equation 2.15, the different variables are associated with the ratio of concentration for molybdenum divided by concentration for the particular element. The parameter seems fairly accurate for binary alloys, but it is not known how accurate it is in quantifying the β stability in a heavily alloyed multicomponent alloy. The Mo. Eq. is defined as:

$$[\mathrm{Mo}_{\mathrm{Eq}}) = 1.0\mathrm{Mo} + 0.67\mathrm{V} + 0.28\mathrm{Nb} + 0.22\mathrm{Ta} + 1.5\mathrm{Cr} + 2.9\mathrm{Fe} + 1.0\mathrm{Al}\% \quad (2.15)$$

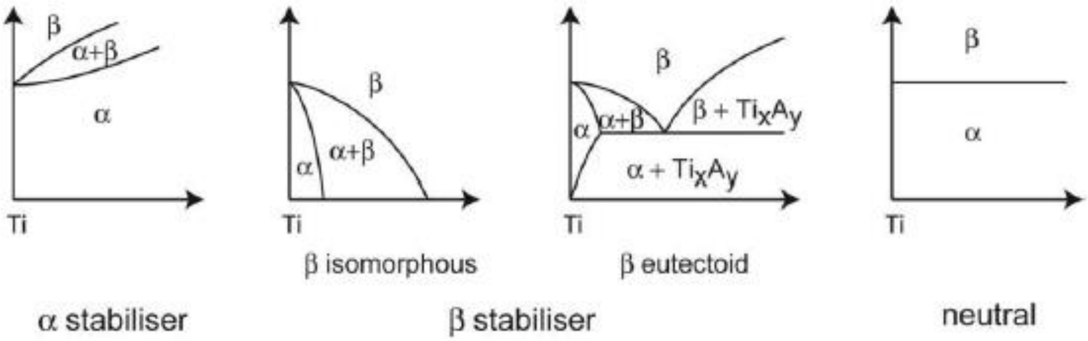

Figure 2.9: Schematic illustration of the relative effect of stabilising elements on a Ti alloy phase diagram after [35].

Although it might be that no metallic element is purely neutral, some elements are classified as neutral because they have a minor influence on the transus temperature. They can lower the β transus slightly, but again increase it at a higher concentration. These elements include Sn, Zr and Hf, which may slightly lower the α/β transformation temperatures after certain threshold concentrations. Zr and Sn are the commonly used neutral stabilising elements. Zr and Hf are isomorphous with titanium and therefore exhibit the same allotropic phase transformation from β to α and are completely soluble in both the α and β phases. Zr also substitutes titanium in a multicomponent alloy and thereby indirectly has a α stabilising effect [35-38]. Sn on the other hand belongs to β eutectoid elements and could have little or no effect on the α/β phase transformation temperature. Sn is considered α stabilising however, as it replaces Al in the hexagonal ordered Ti3 Al. The relative effects of stabilising elements on a Ti alloy phase diagram are schematically illustrated in Figure 2.9 after [35, 37, 38-43].

2.4.1 Equilibrium phases

Although the most common equilibrium phases are those of α and β, there are some intermetallic ordered phases that have been observed in titanium alloys. A brief description of them follows.

(a) H**exagonal phase called apha martensite** (α):

Titanium in its pure form exists as a hexagonal closed packed (HCP) structure at room temperature and pressure [38,40-43]. The HCP unit cell can be defined by placing two atoms at (0, 0, 0) and (1/3, 2/3, 1/2) positions of its unit cell, as shown in Figure 2.8(a), together with the three most densely packed lattice planes and lattice parameters at room temperature. The phase has a space group of P63mmc. The elastic moduli of single crystal of α are anisotropic in nature, varying between 145GPa (stress axis parallel to c-axis) and 100GPa (stress axis perpendicular to c-axis); while the shear modulus G ranges from 46GPa (stress applied in {1120} direction in (002) plane to 34GPa (stress applied in $(11\bar{2}0)$ direction in $(10\bar{1}0)$ plane) [37]. As expected, this is not the case in polycrystalline alpha. They appear as coarse grains while cooled from α phase region in nature; though a finer precipitate distribution in a β matrix can be observable in α/β after solution treatment with further coarsing of the previously precipitated α. The two scales of precipitations formed at different stages of heat treatment process are referred to as primary and secondary α by metallurgists. In addition, within the β matrix, another cluster laths forms of α belonging to one (colony) or multiple (basket weave) crystallographic variants growing together are formed, depending on the cooling or quenching rate evolving from the α phase field. In general, the morphology of this phase is dependent on factors such as parent morphology, cooling rate, thermomechanical treatment and alloy content.

During deformation, several slip systems operate within the α titanium alloys system. The most common slip direction is $\langle 11\bar{2}0\rangle$. The $\vec{a}$ direction slip occurs in one (0002) basal plane, three $\{10\bar{2}0\}$ prism planes, and six $\{10\bar{1}1\}$ pyramidal planes [38, 40-43]. They are therefore responsible for the four independent slip systems. The fifth slip system required for homogeneous deformation of polycrystals (Von-Mises criteria) is provided by the two basal slips that occur in the $\langle 112\bar{3}\rangle$ direction and in the $\{11\bar{2}2\}$ plane. If the slip systems are unable to operate, twinning occurs in α titanium. The main twinning modes are $\{10\bar{1}2\}$ and $\{11\bar{2}1\}$ in tension and {1122} in compression loading [37].

(b) Beta (β)

This is normally the high temperature phase, when pure titanium is heated above 1156K (known as the β transus), α allotropically transforms to β (BCC) structure, shown in Figure. 2.8. The BCC structure has two atoms per unit cell and could be defined by placing the atoms at (0, 0, 0) and (1/2, 1/2, 1/2) positions. The space group is 1m $\bar{3}$ m. As BCC is a more open structured crystal, it can accommodate higher entropy required at elevated temperatures, making BCC more stable at higher temperatures than HCP α phase. The elastic modulus E of β phase measured at these temperatures is about 58GPa and the shear modulus G is around 20GPa [36]. While the elastic constants — C11, C12 and C_{44} in β phase — seem to be almost independent of temperature [39], pure β mono-crystals at 173 K have C_{11}; C_{12} and C44 values to be 97.7 GPa, 82.7 GPa and 37.5 GPa respectively [39]. As BCC β is not a closed packed structure, the deformation occurs by slip via different slip systems. The [110] planes have the highest atomic density, but other planes — like [112] and [123] — come very close. [111] direction is, however, a closed packed direction, thus there are 48 slip systems operating in β materials. As slip can occur in multiple planes, the dislocation can readily cross-slip giving rise to wave slip bands [37]. When slipping is hindered, twinning occurs in β titanium alloys. The different twin systems observed are {332},⟨113⟩ and {112} ⟨111⟩ [40].

(c) Beta2 called (β2)

This phase has two interpenetrating simple cubic sublattices; one containing the corners of the BCC unit cell (0, 0, 0) and the other containing the body centred (1/2, 1/2, 1/2) sites. Thus, β2 is actually a simple cubic structure (space group Pm $\overline{1}$ m superlattices). Evidence of this is common in several binary and ternary titanium aluminates and Nickelides (shape memory alloy), and is confirmed by the presence of {100} superlattice spots in a [001] electron diffraction pattern. These spots are forbidden reactions according to the BCC structure factor calculations which would not normally show up in an ordinary disordered β2 structure. The nature of these {100} super reflections — ranging from strong, weak or diffuse streaks — bears information about the degree of ordering in a particular alloy. Quantitatively, the degree of ordering is defined in the crystal via a long-range parameter L, such that L=1 for fully ordered and L=0 is for completely random distribution [37, 43].

(d) α_2 (alpha 2):

This is otherwise an ordered hexagonal solid solution of chemical formula Ti_3M (where M are simple metals such as Al, Ga, In or Sn), formed instead of the disordered HCP α phase. It has a DO_{19} structure with a unit cell composed of four regular HCP cells seemingly supported by covalent-like directional bonds connecting titanium and the simple metal atoms [37, 38]. This form is mainly due to the addition of higher concentration of alpha stabilisers, as seen in the case of Ti3Al, α_2 in alloys containing more than 6 Wt.% Al.

(e) γ (Gamma):

This is an intermetallic structure formed at still higher additions of alpha stabilising elements. Predominantly, this phase occurs when about 50 at.% of Al has been added to titanium (TiAl). It has a L10 structure, with alternating (001) planes of Ti and Al. It is known for being the cause of increased embrittlement in Ti-Al alloys at 25 at.% Ti3 Al, 50 at.% TiAl and 70 at.% $TiAl_3$ [38].

(f) O phase:

This is an ordered ternary Ti_2AlNb phase that has been discovered in the Ti-Al-Nb systems that may have potential for use as a structural material for use at elevated temperatures [65]. This O phase has orthorhombic symmetry (Cmcm) which occurs by Ti/Nb ordering of the hexagonal DO19 phase, or by Al/Al ordering of the cubic B_2 phases. Alloys with microstructures consisting of the O (i.e. $\beta/\beta 2$ phases) have been shown to possess excellent combinations of low and high temperature mechanical properties. Commonly found in alloys consisting in atomic per cent ranging between 18-30% Al, 18-34% Nb, and balance Ti.

(g) β8₂

This is another ternary phase in the Ti-Al-Nb system that was discovered recently. This phase has a composition close to Ti_4Al_3Nb. It has been described as being in apparent equilibrium with the, γ, Li0, α_2, DO_{19} and O (orthorhombic) phases [38-41], and it has been observed that it has the $\beta 8_2$ structure of the omega phase. It forms readily at high temperatures from the cubic B_2 phase by the displacement of pairs of (111) and subsequent chemical ordering.

2.4.2 Non-equilibrium phases (metastable)

As stated earlier, the phase(s) formed are dependent on a number of conditions, including but not limited to the alloying composition and processing treatment. Metastable (non-equilibrium) Ti phase(s) can be formed due to varying alloy thermodynamic or kinetics, such as insufficient cooling time for long range diffusion of atoms needed to arrange from one stable phase to another (α to β and vice versa in the case of titanium). In general, the phase(s) form as a compromise between thermodynamics that favour minimisation of Gibbs free energy ΔG and kinetics which dictate how fast the transformation can occur. The following sections offer a brief description of some of the metastable phases encountered in titanium alloys.

(a) Alpha prime martensite α′

This martensitic phase forms instead of α as a result of an extreme rate of quenching in dilute titanium alloys from high temperature β phase. Its crystal structure is hexagonal ($P6_3mmc$). In dilute alloys, the morphology changes from colonies of lath to lenticular or a twinned structure, depending on the solute contents [44]. In Ti-Mo alloys, it is said to have orientation relationships between adjacent plates, consistent with the Burgers relationship. This further indicates that the plates are formed by a martensitic reaction. The microstructure is dominated by large plates of α′ and β precipitation (because both shear (martensitic) and diffusional growth mechanisms are involved) [44].

Many metallic and non-metallic materials undergo a first order transformation in the same fashion as in steel. For this reason, all other types of lattice transformation (other than steel) without atomic diffusion are known in physical metallurgy as a martensitic transformation [45]. In principle, however, all metallic bodies can be made to undergo diffusionless transformation, provided the cooling rate or stress rate is rapid enough to prevent transformation by alternative means. Martensite is named after eminent German metallurgist Adolf Martens, who was the first to observe the structure of martensite in a quenched steel sample. The name 'martensite' had been used mainly, and originally, to describe the structure formed in steel quenched from a temperature of, say 960°C, from face-centred austenite to martensitic phase (γ-α). The most familiar martensite formed in steel takes an irregular shaped plate, which, in three dimensions, is a hard lens body centred cubic described as acicular martensite [46]. Its formation is less likely as the β stabilising elements increase in a titanium alloy because the martensite start temperature decreases and thus the phase is less easily formed (as illustrated in Figure 2.8).

(b) Orthorhombic martensite α″:

This is also formed by martensitic transformation, but with higher solute concentration than α′ [45, 46]. Its crystal structure is orthorhombic (Cmcm) (no.63). The morphological structure is more or less an internal twinned structure and, unlike α′, which can form by quenching only (athermal), this can also form on application of external stress — hence the name. Stress or strain induced martensite is formed as the name suggests, upon the application of external stress or strain (see Figure 2,10).

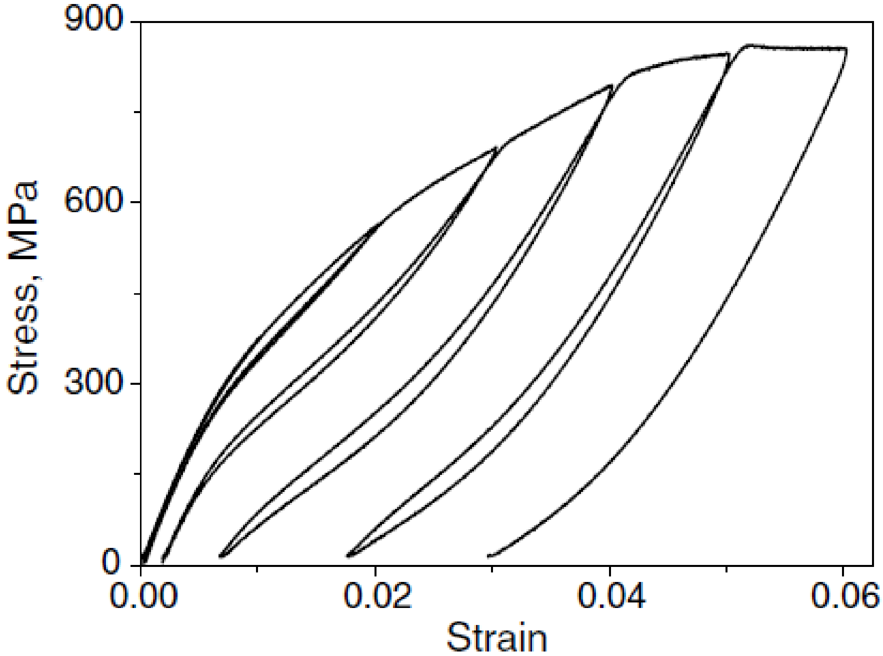

Figure 2.10: Elastic deformation behaviour of Ti-24Nb-4Zr-7.9Sn alloy: the figure displays the stress–strain curves resulting from cyclic loading–unloading deformation with 1% strain step of the as hot-rolled alloy, thus demonstrating the recovery of incipient Young's modulus after the work done by [76].

The detection of α" by x-ray diffraction (XRD) is relatively simple because its characteristic pattern has five low angle lines compared to three for α' [47]. A typical XRD pattern, showing reflections corresponding to the α" phase, is shown in Figure 2.11 [48]. If the β phase was present in this Figure, the first two reflections would occur at angles of ~38.5 (110β) and ~55.5 (200β).

Identifying α" by electron microscopy can be problematic, as other crystal forms of the martensite phase have mistakenly been observed. For example, a face centred cubic or tetragonal martensite has been detected in some Ti alloys [47]. This was reported on the basis of thin foil electron microscopy data. Evidence obtained by Williams [42], however, shows that this martensite is orthorhombic in its bulk form. For example: when Ti-14V-6Al is quenched from 900°C, XRD analysis of bulk samples shows that this alloy contains α", whereas TEM examination of thin foils prepared from the same sample shows evidence of a face-centred cubic martensite. Furthermore, light microscopy of the thin edge of the electron microscopy specimens shows marked rumpling, characteristic of shears resultant from mechanical instability along the thin edge of the foil. In other alloys which observe α" in bulk form, thin foil results show that α" reverts to the β phase along the thin edge of the foil during thinning. Based on this evidence, Williams [42] suggested that the reported face-centred cubic and/or face-centred tetragonal martensites are in fact thin foil artefacts.

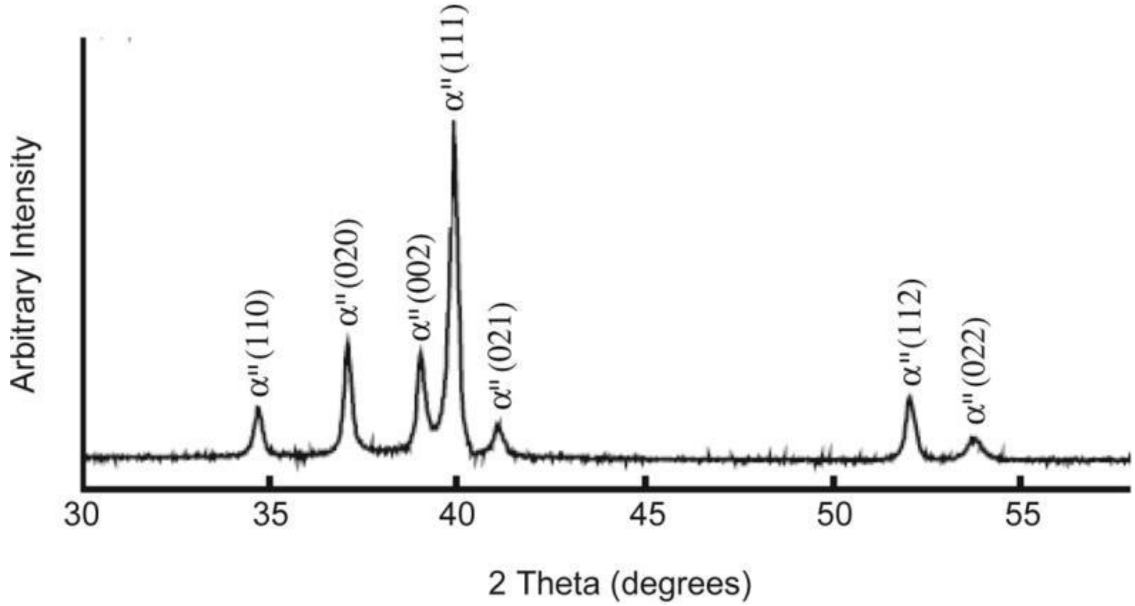

Figure 2.11: XRD pattern of Ti-50Ta alloy after solution treatment at 950°C for one hour, followed by ice water quenching, showing reflections due to α'', adapted from Zhou *et al.* [67].

The microstructures of the α′′ and α′ phase, however, have similar acicular textures, characteristic of all martensitic phases. The difference is that it is confined to higher compositional ranges. Considering that α′′ forms only at higher amounts of alloying, it is therefore not surprising that the deformation martensite is invariably of the orthorhombic variety, which is halfway between the BCC β and the HCP α Ti- phases [49]. This appears justifiable as HCP is just a special type of orthorhombic structure with a/c =√3; and for higher alloy content when the constraints of hexagonal structure cannot be met, martensite with orthorhombic structure are formed [50, 51] (see Figure 2.12).

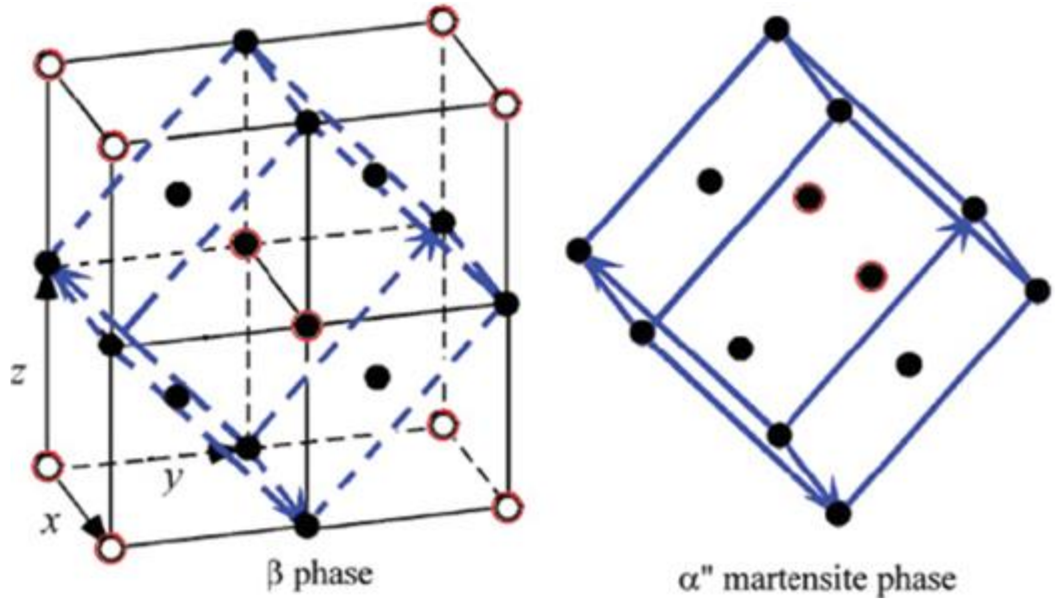

Figure 2.12: A schematic illustration showing the lattice correspondence between the β and α" phases, taken from Kym *et al.* [52].

It is surprising that the hardness of α′′ is much lower than α′ and α or even β [52b]. This would have an influence on the elastic modulus. Though the real reason behind it is not well known, one can guess that stretching of the BCC lattice along two of its orthogonal pairs by contraction in the "c" axis and expansion on the "a" and "b" axes leading to the formation of rectangular prism such as that of ∡ a, b and c are distinct. Thus changing the coordination might play a part (see Figure 2.12).

The effect of some of these microstructural phases on the Young's modulus of binary Ti –Nb alloy is illustrated in Figure 2.13, after the work by [53]. The Figure displays the correlation between Young's modulus and e/a ratio, which is similar for most Ti TM alloys. At low values of e/a, the β Ti phase is unstable and the formation of the α′ phase or α′ martensite corresponds to high modulus and high e/a; the β phase is stabilised and the Young's modulus increases with alloying contents. With the intermediate range of e/a, a local maximum in Young's modulus is caused by the formation of the metastable ω phase [53, 54]. The true minimum of Young's modulus of the β phase can only be realisable (as indicated by the broken line) if the metastable phases can be suppressed through appropriate alloying.

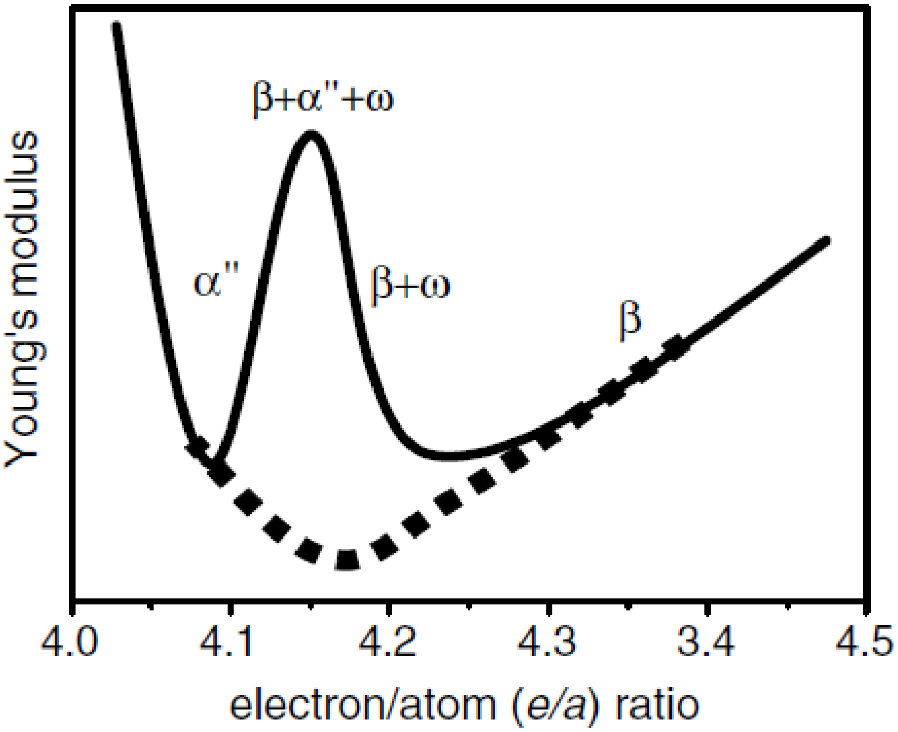

Figure 2.13: Schematic variation of Young's modulus with (e/a) ratio in binary Ti–TM system. The β stability increases with increasing e/a, but is challenged by the formation of metastable α'' and ω above a certain e/a value that corresponds to the peak in Young's modulus. If these metastable phases could be suppressed, a minimum in Young's modulus might be obtained (the broken line), after [55].

Over a broader compositional range, the actual concentration limit for this phase has not been very clear. In the past, Bagariatsky and his co-workers tried to determine some α''/ α' composition boundaries for a few of the binary titanium alloys [55]. In this work, they showed that with increasing amounts of

Nb, Ti-Nb binary alloys undergo martensitic transformation upon quenching from the high-temperature β- phase field to hexagonal α′ or to orthorhombic α′ phases (these α′ and α″ martensites can be analogous to the high-pressure γ and δ phases in pure iron respectively). The high temperature BCC structure of titanium can be stabilised by alloying with TM elements to its right in the periodic table. The border line between α′ and α″ has been linked to a certain critical value of the e/a ratio discussed earlier. For many binary Ti-TM (TM = metallic elements) alloys, the critical e/a ratio of 4.15 corresponds to compositions that fall into the stability range of the α″ martensite, with the martensite start temperature (Ms) estimated to be ≈ 473 K [53, 55]. If the Ms can be suppressed to below room temperature by further alloying additions, the reversible β to α″ transformation can be induced by applied stress at room temperature. This idea formed the basis of continued efforts towards developing shape memory and super-elastic titanium alloys of the β type [56, 57, 58, 59].

(c) Omega Phase (ω)

Perhaps the most studied among all metastable phases in titanium metallurgy is ω. It is a submicroscopic precipitate that is supposed to be a transition phase formed during the β to α transformation. Probably because the complex morphology causes the most substantial change in the physical and mechanical properties of the alloys (such as ductility and superconductivity), the kinetics of its formation, as well as the nature of its diffuse X-ray and neutron scattering, its mechanism of formation from the parent β phase [60], and its formation are characterised by a series of special features. The first reports of this phase were made in 1954 by Frost *et al.* [61], who observed it in binary alloys of titanium with chromium and manganese. Later, the ω phase was found in many other titanium alloys as well. The compositional windows within which the ω phase will form, however, varies according to the alloy system [62].

Over a broader composition range, the ω phase will occur as a precipitation product of β decomposition during moderate temperature (300-550°C) isothermal aging (ω_{iso}). The formation of the ω_{ath} phase occurs by a diffusionless, or compositionally invariant, transformation [42, 63]. This transformation cannot be suppressed, no matter how rapid the quench rate [49].

The detection of the ω phase, like the detection of α", can often be difficult. In a recent study [64], the alloys Ti-30Nb-5Zr and Ti-30Nb-5Ta-5Zr were both found to contain the ω_{ath} phase after solution heat treatment. The presence of the ω phase, however, could mostly be precisely detected under TEM, therefore suggesting that the particle size of the ω phase was very small. When detectable by XRD, diffraction peaks of the ω_{ath} phase are typically broad and of low intensity. In addition, because many of the ω peaks overlap with the positions of the β peaks, typically only one or two singular ω peaks are present. The ω_{iso} phase is typically easier to identify with stronger reflections in XRD. An example of an XRD pattern of a β+ω_{iso} microstructure is shown in

Figure 2.14, for the recently developed biomedical alloy Ti-29Nb-13Ta-4.6Zr [65].

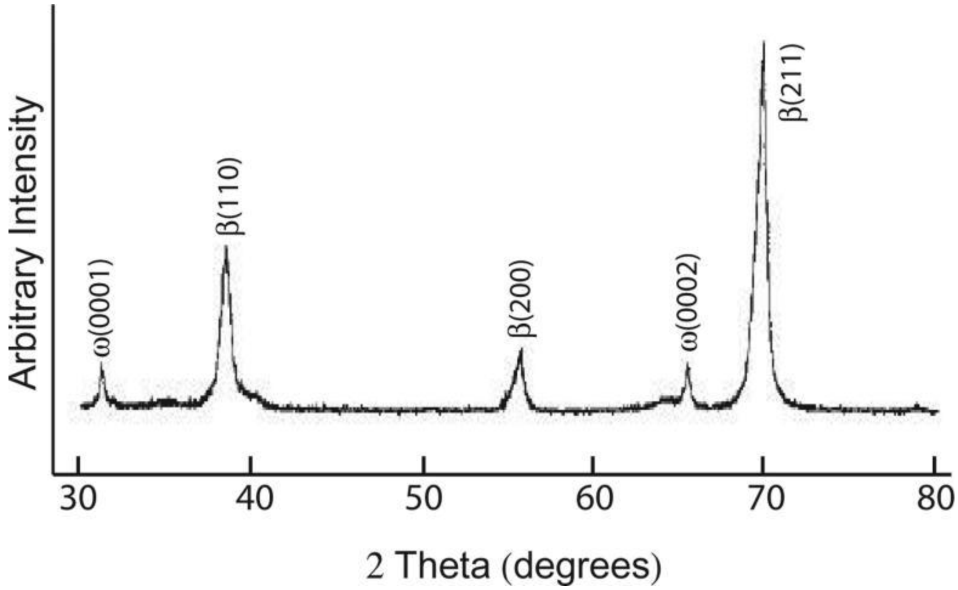

Figure 2.14: X-ray diffraction pattern of Ti-29Nb-13Ta-4.6Zr alloy after solution treatment at 790°C for one hour, followed by water quenching, then aged for two days at 350^{o}C, adapted from Li *et al*. [65].

It is well known that ω phase is related to the *BCC* parent phase according to the <000l>*ω*||<111>β;{11 0}ω||{1 0}β orientation relationship, implying the existence of four variants of the ω, with respect to the *BCC* lattice. The ω lattice is obtained by collapse of neighbouring (111)β planes of a *BCC* structure, leaving every third plane in place. The atomic movements required are ± $a\beta\ \sqrt{3}/12$, where $a\beta$ is the β lattice parameter or equivalently ± $c_{\omega}/6$ where c_{ω} is the c axis of the ω phase. Complete plane collapse will produce the ideal ω structure with $a_{\omega} = \sqrt{2}a\beta$ and $c_{\omega} = \sqrt{3}/2a\beta$. For a partial collapse (< $a\beta\sqrt{3}/12$), the trigonal ω crystal structure is obtained [63]. Most ω crystal detected by XRD is found to bear the hexagonal crystal structure.

Like the α phase, it forms in all alloys of titanium with transition metals, but only at a definite "critical" concentration of the alloying element. An indirect proof of the two-stage occurrence of the process of ω phase transformation in low alloys of titanium and in titanium itself is by volume changes. By analogy with the volume effect in a β to ω transformation, one should expect that the occurrence of the first stage of the β to α transformation should be accompanied by an increase in density (i.e. a decrease in volume), and that the occurrence of the second stage (ω to α′) should be associated with a decrease in density. The understanding of the mechanism of omega formation in titanium systems is mainly under these conditions [66].

(i) The ω phase is the product of transformation of the metastable β solid solution. Experimental evidence suggests that the process of the β to ω transformation never reaches completion; i.e. the disappearance of the complete β solid solution — the ω phase always coexists with the metastable β phase.

(ii) The lattice constants of the ω phase are practically independent of the conditions of formation (hardening or tempering) and of the type of alloying elements.

(iii) The process of β to ω transformation on hardening alloys from the "critical" concentration takes place at approximately the same or neighbouring martensite temperatures Ms, which are relatively low (≈573-890K), independently of the alloying elements. This can be distinguished from the athermal by its large size and a composition gradient along ω /β interface.

(iv) The temperature of formation of the ω phase during the tempering of more highly alloyed metastable solid solutions is approximately 180–500°C, which is practically equal to the temperature of formation of the ω phase during hardening (Ms).

(v) The formation of the ω phase is always accompanied by an increase in the density of the alloys.

(vi) As was noted above, a characteristic feature of the ω phase is that it does not show up under the optical microscope and the difficulties arise in the interpretation of its crystal structure.

(vii) Its deformation at room temperature and application of higher pressure has also shown to stabilise ω phase under certain circumstances. Studies on Ti-Cr and on Ti-V alloys by Bagariatski *et al.* [54b] have shown an increase in ω phase on deformation.

In a similar move with α′′, a link was made by Luke *et al.* [54a] concerning the occurrences and stability of ω phase and e/a ratio of ≈4.06-4.14eV for ω-Ti phase formation from experimental data. This was disputed by authors such as Hickman, however, who noted that the stability of the ω phase in alloys could not be predicted from the e/a ratio alone [67]. The position of alloying element in the periodic table is also an important factor; this is thought to be because of the d-band and s-d band hybridisation influence on the electron density of state.

Blackburn and Williams tried to gain an insight into the composition of the ω phases, estimating its volume faction in Ti-Mo alloys by electron microscopy [68]. Their findings seem to be in an agreement with the work of Silcock *et al.* [69] on the structure of ω phase in titanium alloys. They both agreed that the structure was hexagonal with a=4.60Å A and c=2.82 Å (c/a= 0.613). They differed, however, on the type of structure they found: while Silcock *et al.* believed the atomic position to be (0,0,0) and (2/3, 1/3, 1/2) belonging to P6mmm space group as HCP, Bagariatski and co. [70] thought it to be at (0, 0, 0) and (2/3, 1/3, μ), where μ is equal to 0.48 0.01Å — therefore possessing P3 ml space group, which is a trigonal structure instead.

In reality they are both correct, as it can be either hexagonal or trigonal depending on whether the transformation is complete or in the initial stages [62]. This was later clarified by Sass, who observed that ω SAD patterns have straight or curvilinear lines of diffuse intensity instead of sharp spot [71]. The latter, referred to as the “diffuse ω phase", relates to the early stages of ω formation.

As a result, Blackburn and Williams devoted a lot of effort to their groundbreaking work relating to the ω phase morphology with misfit strains. Here, the authors studied Ti-Mo and Ti-V alloys at various stages of aging and found a similar ellipsoidal morphology of ω with a major to minor axis ratio of about 2.2. In Ti-V alloy however, the ω precipitates were approximately cube-shaped with sides of the cube parallel to (2021) ω [72, 73]. They observed that, for all Ti-(3d) transition metal alloys with unfilled 3d electronic shells (like Ti-V, Ti-Cr, Ti-Mn and Ti-Fe), the ω phase is cubic-shaped when visualised on the TEM microscope; whereas for Ti-(4d)Tm alloys (i.e. transition metals with unfilled 4d electronic shells — like Ti-Nb and Ti-Mo), the ω phase is ellipsoidal in shape [74, 75]. They inferred that the precipitation morphology is related to the Ti/transition Metal atomic volume ratios or their lattice misfits. In Ti-Nb and Ti-Mo alloy systems, the misfit was small and the ellipsoidal particle shape seemed dominated by the minimisation of the anisotropic surface energy. In Ti-V, Ti-Mn, Ti-Fe and Ti-Cr systems, the misfit was greater and the precipitate morphology cubic-shaped and determined by minimisation of the matrix elastic strains. A value of 0.5% misfit was quoted, below which the precipitate would be ellipsoidal in nature, and above which would yield cubic ω morphology [74, 75].

(d) β′: we commented earlier on how increasing the beta alloying additions to pure titanium martensitic and omega phases formed on quenching. At still higher β stabilising alloying additions, however, (i.e. the solute rich β) Ti alloys undergo a phase separation reaction to form β1 and β2. This could occur either by classical nucleation and growth or a less observed spinodal reaction. A number of criteria determine which of these two mechanisms would be predominant. From a pure kinetic aspect, for spinodal reaction to occur the quenching rate should be optimal: neither too fast to prevent short-range diffusion of atoms, nor too slow to form the equilibrium β and α phases. It is important to note that β1 and β2 are just a convention referring to the two phases as having the same crystal structure as the parent β phase (BCC), but with different solute content and lattice parameters. Conventionally, β1 is assumed to be the solute lean phase and β2 the solute rich phase. Sometimes, in the literature, the β1 is referred to as β′ and β2 as simple β [42]. This β′ usually remains as coherent and distributed in the β isomorph matrix. The above description may not be exhaustive in terms of some of the equilibrium and non-equilibrium phases observed in titanium alloys; but the most important ones, and the influence of alloy properties that are useful for engineering applications, have been mentioned. The following section will explain some aspects of martensitic transformation from the high temperature β phase that is peculiar to some of our main work on beta isomorphs Ti alloys (Ti-Nb and Ti-Mo).

2.5 Some aspects of α″ transformations in βTi – (Mo, Nb) alloys

As discussed earlier, phase transformation occurs whenever a materials system is not at equilibrium, or changes its microstate, as a result of external constraints such as pressure or temperature. In effect, these materials adopt different crystal structures favourable for the minimisation of their free energy. In general, the microstructural features and the order in the system changes, leading to variations in most of the important properties. By so doing, phase transformation provides an effective way to modify the microstructure of solids. If it can be activated by a mechanical or other physical force, it becomes part of the deformation process and directly affects the properties of materials as well [76].

There is possibly satisfaction to be derived from possessing an understanding of phenomena such as martensitic transformation in metals and alloys. The present work, however, deals with the basic mechanisms of phase stabilities, therefore providing insight into the mechanical and chemical properties of materials which are necessary for the design of new materials. In this section, some of the structural, crystallographic and morphological characteristic changes that take place as a result of phase transformations in titanium alloys are briefly described.

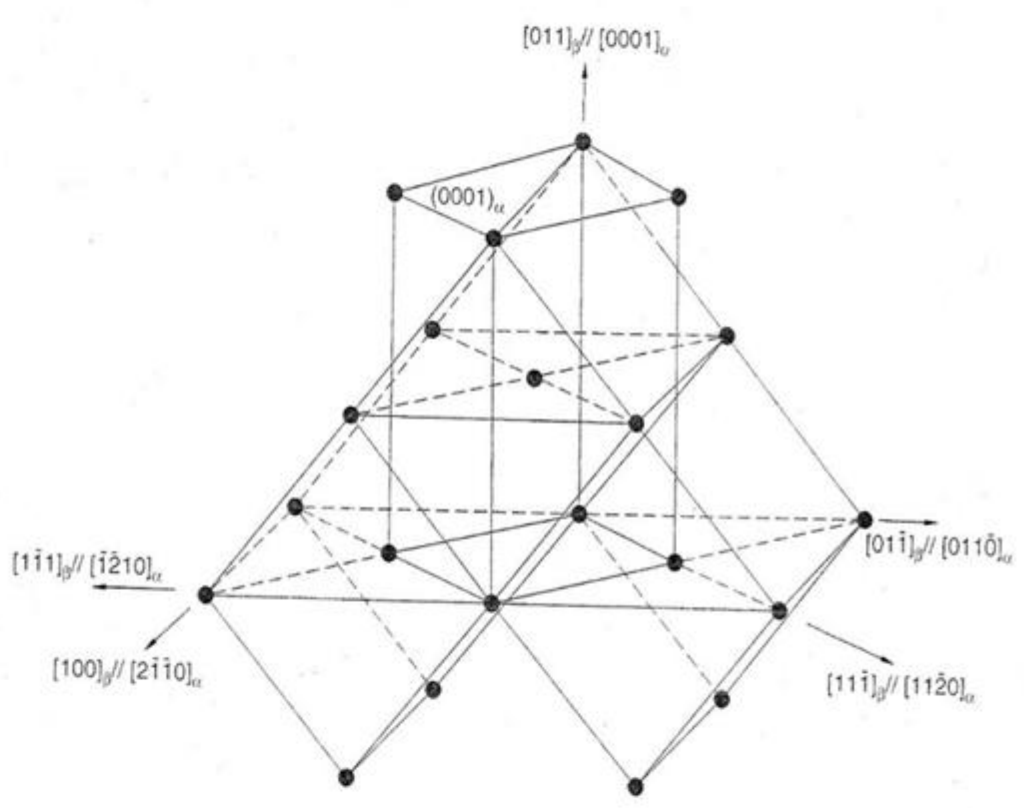

Figure 2.15: Schematic illustration of the distorted closed-packed hexagonal cell (HCP), as derived from the parent BCC lattice after Burgers [82].

2.5.1 Shear transformations of β to (α′/α″)

As explained earlier, a martensitic transformation involves homogeneous movement of atoms. Ideally, such a process is not involve thermally activated and takes place at an extraordinary speed [45]; but in practice a clear cut separation of transformation process into nucleation and growth and martensite is generally not possible [77]. Based on such a premise, we assume that diffusion does not occur and atomic correspondence is maintained during such transformation. Independent theories to this effect have been put forward by others [78]. Although in pure titanium metal a simple athermal martensitic transformation is conceivable, in an alloy the situation is more complicated for the following reasons.

The long-range effect of alloying, described, for example, in terms of changes to the elastic parameter, may simply be to change the conditions under which athermal transformation takes place. The local effect of alloying, on the other hand, is to inhibit the movement of atomic, and thereby, (1) reduce the distance over which atomic regions can cooperate, thus perturbing the microstructure of the transformation product; and (2) reduce the speed of the transformation, thus bringing it into completion with nucleation and growth mechanisms [62]. This could inhibit the necessary microstructure of the transformed product and rate at which such a reaction takes place [62]. The diffusion coefficient of the solute species in Ti was also thought to play a large role in the evolution of crystallographic texture and during phase transformations, which has a direct effect on the internal microstructure and properties of retained phases of the alloy while quenching. For example: the work of Jepson *et al.* [79] on the kinetics of transformation in Ti-Nb alloys found the critical cooling rate at which martensite always formed (equivalent to reaching the Ms temperature in terms of the TTT diagram of the alloy) decreasing with increasing Nb content [80]. From these findings, the influence of alloy content on crystallographic orientation in different Ti based systems was made very apparent. Previous investigations [76, 80] have shown that such a cubic β to hexagonal α transformation occurs via a habit plane near $\{334\}_{\beta}$. One of these two different martensites would be formed, and β to α transformation process would be reducible to the activation of following shear systems that follow a well-established Burgers relation [81]: i.e. (110) ‖ (0001)α′; $[111]_{\beta}$‖ [110]α′ (see Figure 2.15). A study of the orientation relationship in zirconium Burgers [82] proposed that the martensite transformation of body centred cubic (BCC) to close-packed hexagonal (HCP) occurs by a heterogeneous shear on the system $(112)_{\beta}$BCC $[2\bar{1}10]_{\alpha}$. This distortion is illustrated in Figure 2.15. The crystallographic principle underlying this proposal is that the configuration of atoms in the (112) plane of a body-centred cubic structure is exactly the same as that in the (1010) plane of a close-packed hexagonal structure based on the same atom radius. The pattern on both of these planes is a rectangle $d\ x\ \sqrt[2]{2}/\sqrt{2)}d$, where d is the atom diameter. Thus a hexagonal close-packed structure can be built up from a body-centred cubic structure by displacing the (112) planes relative to each other. It should be noted, however, that the array on the $(110)_{\beta}$ planes (see

Figure 2.15) cannot be converted into an exact hexagonal array merely by the pure shear proposed by Burgers, since the spacings of the $(ll2)_{\beta}$ planes and $[10\bar{1}0]_{\alpha}$ planes into which they transform are not equal. Nevertheless, this mechanism leads to approximately the observed orientation relationship. Accordingly, the orientation relationship between the β and the (α′/α″) were found to be same as the burger orientation relationship between the β to α type [49, 60, 83, 84]. This was schematically illustrated in Figure 2.16, after [84], the basal plane of α is derived from the $[011]_{\beta}$-type plane and those of $[011]_{\beta}$ and $[100]_{\beta}$ directions transform into $[01\bar{1}0]_{\alpha}$and $[2\bar{1}\bar{1}0]_{\alpha}$ directions, respectively. The closed packed direction $[1\bar{1}1]_{\beta}$ and $[\bar{1}1\bar{1}]_{\beta}$ lying on the $\{110\}_{\beta}$ plane transformed to closed packed $\langle 12\bar{2}0\rangle$ directions. The other $\langle 1120\rangle$ directions are derived from $\langle 100\rangle$ directions. Based on this orientation relationship and the symmetries of the cubic and hexagonal structures, a total of 12 crystallographically distinct variants of the alpha phase can result from the transformation of a single beta grain. It is not surprising that, to maintain such orientation, a relationship has to be achieved via a series of contraction and expansion of the β lattice in order to form (α′/α″). This is listed, according to [78], here:

- a 10 % contraction of $[001]_{\beta}$ corresponds to $\langle 2\bar{1}10\rangle\alpha'$
- a 10% expansion along $[011]_{\beta}$ correspond to $\langle 01\bar{1}0\rangle\alpha'$
- a 1% contraction $[011]_{\beta}$ corresponds to $\langle 0001\rangle\alpha'$

The orthorhombic α″ crystal structure can be described as a slightly distorted hexagon with the same atomic positions as in hexagonalα′, but distorted so that the lattice parameter is in between the α′ phase and β phase. It is said to form by a degeneration of the hexagonal structure in form of a compromise between the two. This is better illustrated when the Burgers orientation is written in terms of the orientation crystal lattice. Hatt *et al.* deduced that, in quenched Ti-Nb alloy, the following crystallographic adjustments have to be made to get the observed orientation relationship [85]:

- $[100]_{\alpha''}$ is 2° from $\langle 011\rangle\beta$
- $[010]_{\alpha''}$ is 2° from $\langle 110\rangle\beta$
- $[001]_{\alpha''}$ is 2° from $\langle 1\bar{1}0\rangle\beta$

This orientation relationship outlined above and in Figure 2.16 shows the interrelationship between the three lattices as represented in the orthorhombic system [63]. It is no surprise that as more and more β stabilisers are added, the orthorhombic parameters change and become closer to the BCC dimensions [84, 85, 86]. In the past, several quenched binary titanium alloys (including Al, Mo, Nb, V, Au and Ag) were investigated for the presence of martensites. Apart from Ti-Al, alloys were β to α was impossible to suppress [80]; all the other alloy additions are β formers, though — by definition — they do not promote martensitic formation. The size and the cooling rate of the specimen were, however, quite rigid and a bit confusing to understand. As a consequence, even when thin slices of these alloys typically would not form martensite, thicker ones would do due to the thermal shock experienced while quenching.

Also, in lean Ti-Mo alloys, Davis and co-workers did find martensite on quenched and un-quenched conditions [86]. They observed that with the increase in Mo concentration, the structure changed from α′ to α″ and then to completely retained β. So, at less than 4wt. %, α′ formed; and above it, there was the presence of α″ martensite. It was indicated that, at low Mo concentrations, the critical cooling rate for 1005°C/min transformation to α′ was not achieved on water quenching and thus there was a competition between shear and diffusional transformations. At a higher Mo content (> 4wt. %), the martensite start temperature, Ms and the critical cooling rate decreased and thus a complete shear transformation occurred [87]. This was similar to what Ho *et al.* [88] observed with 6-20 wt. % Mo titanium alloys. At 7.5 wt. % Mo, α″ phase was seen to form with the lowest hardness; but at about 10-12.5 wt.% Mo, the alloys showed increased hardness values due to retained β.

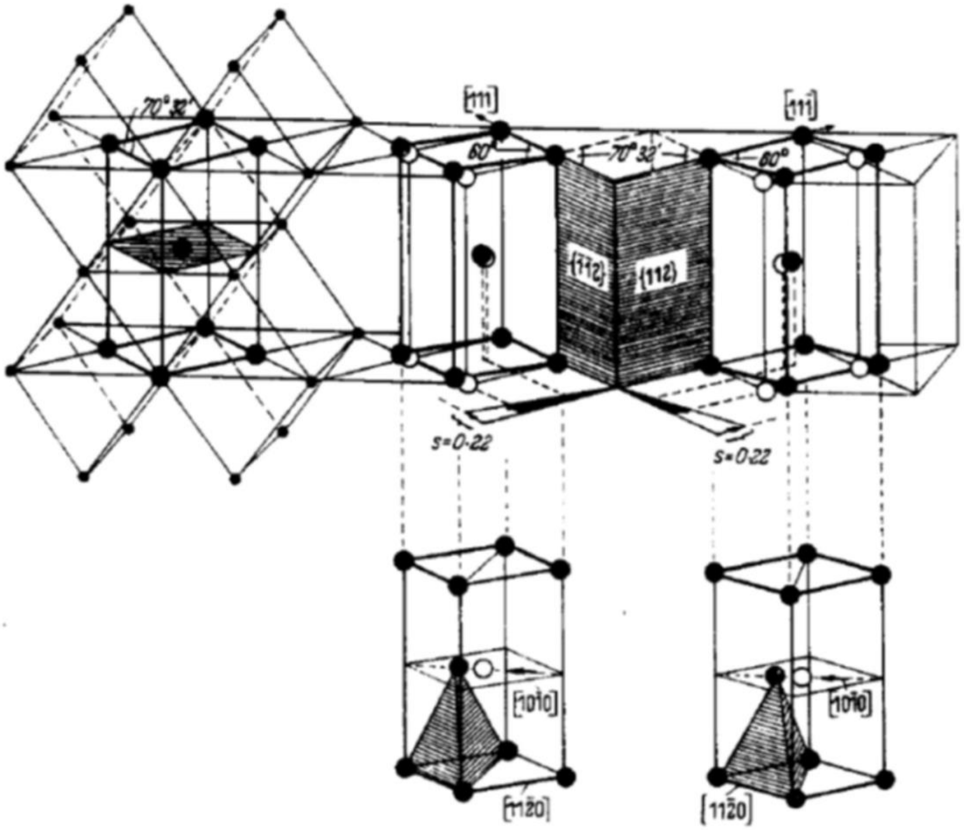

Figure 2.16: Atom movements postulated by Burgers for the body-centred cubic to close packed hexagonal transformation in zirconium. On the left are body-centred cubic cells, and in heavy lines a cell having $(1\bar{1}0)_\beta$ as a base and $(112)_\beta$ as vertical sides, the latter serving as shear planes when the two hexagonal cells at the lower right are produced.

In the Ti-Nb systems, these effects have been studied by several other groups [88]. It has been found that at < 13wt. % Nb, α' was formed while higher concentration yielded α'' [89]. The evolution of α' and α'' in some Ti-Nb and Ti-V alloys were studied by some others including [90]. Similar investigations on titanium based on eutectoid systems (Hypoeutectoids, such as T-Ag and Ti-Si, and hypereutectoids, such as Ti-Au) by Menon *et al.* confirmed the identification of massive β to α_m transformation [91, 92].

Stress-induced α'' martensite (SIM) can be triggered in quenched metastable β alloys by application of an external stress [93]. The triggering stress (σ_{SIM}) inducing the formation of α" rises with an increase in the stability of the metastable β phase. Some alloy compositions, e.g. Ti-24Nb-4Zr-7.9Sn [94, 95] (wt. %) exhibit both types of martensitic transformation; i.e. α" can be induced athermally or by the application of an external stress [62]. The thermoelastic reversibility of SIM is responsible for the observed shape memory effect and superelasticity in some β Ti alloys. Athermally, evidence of stress induced martensite transformation in deformed samples is revealed through the cusp (kinks) present in their tensile stress strain curves. The sudden jump in strain occurs usually to accommodate the β to α′′ transformation and from lattice invariant during deformation. The physical basis for transformation to the α′′ to occur in Ti–Nb and Ti-Mo based alloys is that Nb or Mo stabilises the BCC structure with respect to HCP titanium, but destabilises it with respect to the α′′ martensite by reducing its elastic shear modulus. The composition of our alloy corresponds to small elastic shear modulus [38, 54], $\acute{C} = (C_{11} - C_{12})/2$, and, as such, {110} shear or shear along [111] on {110}, {112} or {123} will be particularly easy [121]. It was demonstrated that one of the three most probable mechanisms of the transformation to the α′′ in BCC titanium is accomplished partially [110] {110} atomic shuffles in opposite directions on every other {110} plane. The highly anisotropic slip may also produce defect configurations such as kink bands [53].

For high β content alloys too rich to undergo such transformations, deformation while undergoing tensile stress can be attributable to mechanical twinning. TEM images in Figure 2.17 reveal further details of the substructure associated with this transformation and the variation of martensite microstructure, including internal twins in Ti (20, 22, and 24) Nb alloys shown in Figure 2.17 [97].

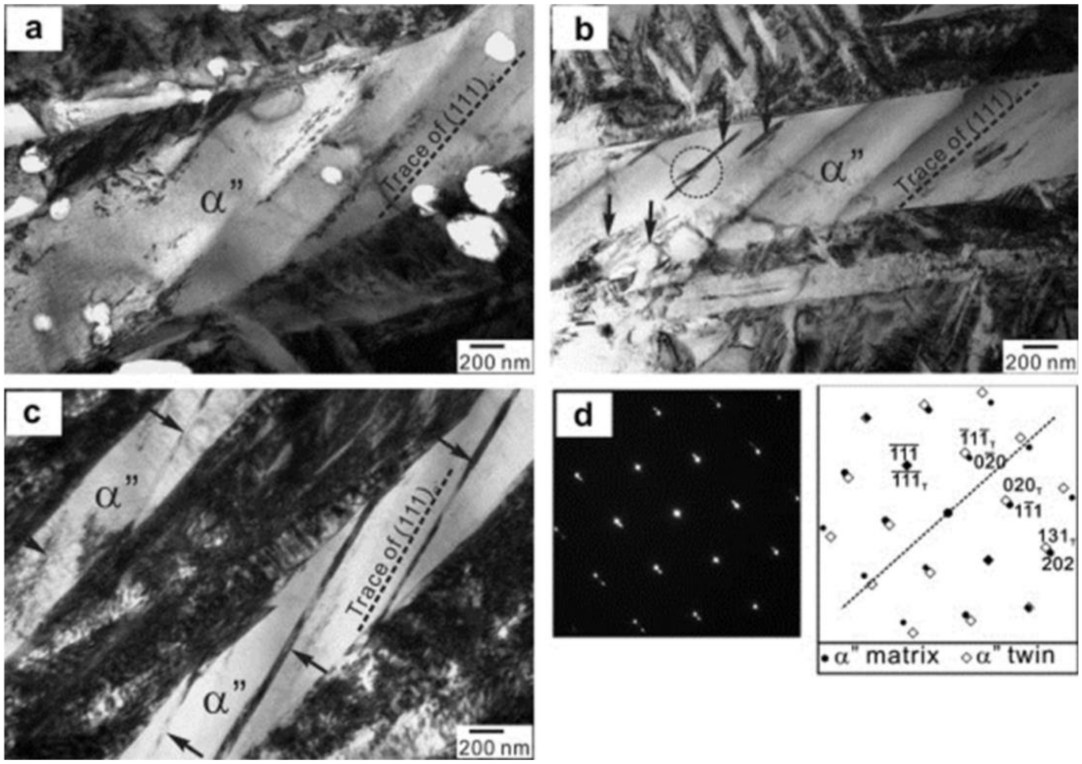

Figure 2.17: (a), (b) and (c) are TEM images showing the variation of martensite microstructure including internal twins in the Ti (20, 22, and 24) Nb alloys. (d) is [111] β SAD pattern and the index that were obtained from the circle in (b), and indicating that the internal twins are of Type 1 twinning on (111) β plane after [4]

Several deformation mechanisms have been studied in Ti-based alloys systems. It appears that the concentration and type of solute strongly influences whether the stress-induced product in a given alloy is twinning or α" [49]. In some alloys, clear evidence of mechanical twinning has been observed, while evidence of α" has been obtained in others, or both. Due to the difficulty involved in discerning between deformation products, it has been suggested that light microscopy is insufficient to identify the product since both the twin and martensite have a similar appearance (as shown in Figure 2.18). The existence of twinning in the microstructure points have been studied in Ti-Mo [98], T-V [99], Ti-Mn [100], Beta III [101] and Ti-15V-3Sn-3Cr-3Al [102] alloys. These alloys have shown to exhibit two twin systems: {332} [113] and {112} [113]. Both the {334} and the {344} martensite are found in Ti-Mo alloy systems, a transition occurring between 10.5 and 11.5% Mo. The {344} martensite found in the higher Mo alloys are usually formed by deformation of the quenched alloy [98]. It has been suggested, however, that light microscopy is insufficient to identify the product since both the twin and martensite have similar appearance (as shown in Figure 2.18). XRD patterns obtained from the samples in Figure 2.17(a) show no additional peaks, other than those from the β phase, indicating that the lenticular features in the figure are *BCC* twins. Electron microscopy has verified the formation of {112}<111> [49] and {332}<111> twinning during stressing of Beta III and many other metastable β alloys. The stress-induced product in Ti-14Mo-3Al in Figure 2.18(b) was identified as α". The evidence therefore suggests that high resolution XRD is the most reliable way to detect the crystal structure of the martensite phase [103].

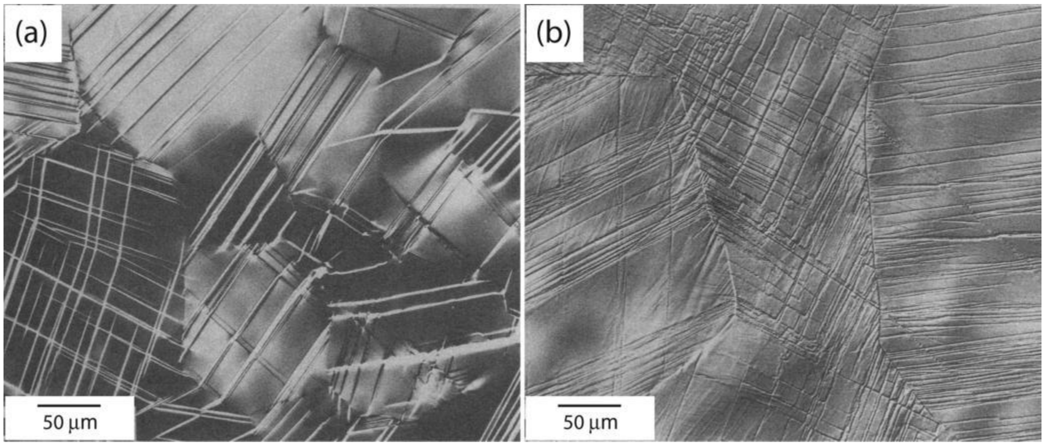

Figure 2.18; Light micrographs of lenticular stress-induced products in: (a) Ti-11.5Mo-4.5Sn-6Zr (Beta III), and (b) Ti-14Mo-3Al, taken from Williams [49].

2.5.2 The similarities between ω and α″transformation

Some close uniformity could be drawn between the shearing and shuffling transformations of β that could lead to respective formation of ω and α″. Some work has been done on compositional ranges and quench rates applicable for the formation of each of these phases. Mofiat *et al.* [90] investigated the Ti-Nb alloy system having between 20-70 atomic % Nb to understand the competition between ω and α″. They established that α″ and ω precipitation specifically in Ti-Nb systems was favoured by fast and slow quenching rates respectively, which confirmed the belief that, at slower quench rate, the collapse of the (111)β planes are more complete. This was similar to the result presented by Ohmori *et al.* [103], which showed that in Ti alloys with the progress of ω phase precipitation, the β to α″ transformation was quite largely suppressed.

In order to determine the underlying similarities between these metastable phases, the theory of localised soft phonon mode of transformation was introduced by de Fontaine [104, 105]. Cook [106, 107], Clapp *et al.* [109]

and Suzuki [110] compared martensitic transformation to spinodal decomposition, which in itself is related to the ω phase precipitation. It is well understood that while the spinodal reaction takes place through compositional fluctuations, the ω grows by displacement fluctuations. Similar to the spinodal mechanism, the martensitic transformation could therefore be triggered by strain fluctuations in the vicinity of a strain spinodal. In addition, from the neutron diffraction studies of Moss *et al.* [111] and the Mossbauer-effect measurements of Batterman *et al.* [112], it can be said that the ω also possesses strain fluctuations. This further narrows down the difference between martensite and ω, and one can safely say that they are manifestations of the same β instability phenomenon.

2.6 Evolution of β Ti alloy for orthopaedic implant

During the first part of the arthroplastic surgery development, stainless steel was considered as a one of the viable implant materials, mainly because of its availability and processing ease. Alloying additions of chromium (Cr), nickel (Ni) and molybdenum (Mo) were made to the ferrous (Fe) matrix to prepare alloys like 316L, also known as ASTM F-138 [113]. They were primarily used to make temporary devices such as fracture plates, screws and hip nails; but gradually, as TJR (total joint replacement) surgery became popular, it became evident that very high modulus of stainless steel (~200GPa) (Table 2.1) would be a deterrent. Researchers also started looking for alloys that were more biocompatible and corrosion and wear resistant.

Cobalt (Co) based alloys came into the picture, while wrought alloys were used to fabricate prosthetic stems and load bearing components. Even though they offered excellent corrosion resistance, wear resistance and fatigue strength, these Co-Cr-Mo alloys (ASTM F-75, ASTM F-799) still had higher modulus (~210GPa) [see Table 2.1] and inferior biocompatibility to that desired for implant materials [113]. As a consequence, after the early 1970s titanium alloys started to gain popularity due to their excellent specific strength, lower modulus, superior tissue compatibility and higher resistance [114].

The commercially pure titanium (ASTM F-67) was the first trial due to the fact that its oxide (titanium in the atmosphere readily forms an oxide coating around it) had excellent osseo-integration properties — i.e. human bone cells bonded and grew on the titanium-oxide layer quite effectively. Due to its limited strength however, the implants were confined to specific parts, such as hip cup shells, dental crown and bridges, endosseous dental implants, pacemaker cases and heart valve cage [115]. In order to improve the strength for load bearing applications — such as total joint replacements — the alloy Ti-6Al-4V ELI (ASTM F-136; the Extra Low Interstitial alloy composed of Titanium (Ti), 6 wt. % Aluminium (Al) and 4 wt. Vanadium (V) and Ti-6Al-4V), which was originally developed for the aviation industry. The elastic modulus of about 110GPa (See Table 2.1), which was about half of 316L stainless steel was chosen. As this was used for TJR surgery with modular femoral heads and long term devices like pacemakers, it was soon found out that the presence of vanadium caused cytotoxicity and adverse tissue reactions [202, 203]. Thus niobium (Nb) and iron (Fe) were introduced, replacing vanadium, to develop alloys such as Ti-6Al-7Nb [116] and Ti-5Al-2.5Fe [117]. Also other alloys with aluminium additions like Ti-15Mo-5Zr-3Al [118] and Ti-15Mo-2.8Nb-3Al [113] were tried out. Further studies, however, showed that the release of both V and Al ions from the alloys might cause long-term health problems, such as peripheral neuropathy, osteomalacia, and Alzheimer's [119,120]. Consequently, Ti-6Al-4V somewhat lost its importance as the most viable orthopaedic alloy.

Table 2.1: Comparison of mechanical properties of commonly-used orthopaedic alloys.

Alloy	**Modulus(GPa)**	**Yield Strength (MPa)**	**UTS**
Stainless steel	200	170	465-950
Co-Cr-Mo	200-230	275-1585	600-1795
c.p. Ti	105	692	785
Ti-6Al-4Al	110	850-900	960-970

Due to demographic changes and a worldwide increase in the average age of the older population, which has led to a rapidly increasing number of surgical procedures involving prosthesis implantation, there was an urgent need to develop newer and better orthopaedic metallic alloys. For this, the researchers first had to identify the metallic elements that were completely biocompatible as to alloy with titanium. The ideal recipe for an element to be used for implant application was excellent biocompatibility with no adverse tissue reactions effect, excellent corrosion resistance in bodily fluids, high mechanical strength and fatigue resistance, low elastic modulus, low density and good wear resistance. Regrettably, only a handful of elements will not cause harmful reactions when planted inside the human body [121]: titanium (Ti), molybdenum (Mo), niobium (Nb), tantalum (Ta), zirconium (Zr), iron (Fe) and tin (Sn). Out of these, only tantalum showed an osseo-compatibility similar to that of titanium; but its high atomic weight hindered it from being used as a primary alloying addition. In fact, biocompatibility of higher amounts of tantalum and palladium additions was only tested for dental and craniofacial prosthesis where implant weight would not be of much concern [122]. For other types of load bearing implants, several molybdenum and niobium based alloys were analysed. For example: investigations on ternary Ti-Mo-Fe alloys were carried out where the strengthening effect of Fe addition was studied in a Ti-7.5Mo alloy [123, 124]. Another time, Guillermot *et al.* conducted tests on Ti-Mo-Fe-Ta alloys with hafnium (Hf) additions [125]. Previous work by Feeney *et al.* considered one of the most promising quaternary molybdenum-based β-Ti alloys, Ti-11.5Mo-6Zr-4.5Sn, also known as βIII [126]. The phase transformations occurring in these alloys were found to be similar to those of binary Ti-Mo alloys. At room temperature the as quenched βIII alloy showed low yield strength, high ductility and high toughness. The effects of iron on Ti-Mo alloys [123] and the superior properties of βIII [126] were finally combined to develop Ti-12Mo-6Zr-2Fe [127, 128], which recorded superior yield strength and modulus values. As discussed earlier, it was believed that the ω phase precipitation had a great effect on the strength of these alloys. A parallel if not better effort was put in to develop niobium based β-Ti alloys. Karudo *et al.* [25] and Tang *et al.* [129] developed alloys based on the Ti-Nb-Ta, Ti-Nb-Ta-Zr, Ti-Nb-Ta-Mo and Ti-Nb-Ta-Sn systems. Of all the different alloys that were chosen, the tensile strength and elongation of Ti-29Nb-13Ta-4.6Zr alloy was found to be greater than, or equivalent to, those of conventional titanium alloys for implant materials [130, 133]. Upon comparing the hardness values of the quaternary alloys, it became evident that the homogenised samples had higher hardness than the air or water quenched samples. Finally the dynamic moduli was observed to be lowest at 5 at% Zr and Nb/Ta ratio of 12.0, which was attributed to the preferred site occupancy of Nb, Ta and Zr within the BCC unit cell and its effect on the nature of bonding [130]. The alloys that possessed the lowest moduli were Ti-35.5Nb-5.0Ta-6.9Zr and Ti-35.3Nb-5.7Ta-7.3Zr.

Consequently, based on this research, a number of contemporary and prospective alloys were developed. These included Ti-12Mo-6Zr-2Fe [127, 128] and Ti-15Mo-3Nb-0.3O [134]. Additional inclusion of Interstitial Oxygen (O) in the alloy, also referred as TIMETAL 21 SRX, Ti-13Nb-123Zr [135], Ti-25Nb-4Zr-7.9Sn [93] and Ti-35Nb-7Zr-5Ta [136]. Happily, all these alloys were primarily β or β+α′′ type Ti alloys. The change in the direction of the search for better biomaterials from α/β Ti to β and β+ α′′ could be explained by the fact that the latter fitted in very well with the tight mechanical properties requirements of orthopaedic alloys. The standard requirement on which such important properties decisions on modern day implants can be based will now be discussed.

(a) Yield strength: The yield strength would determine the load bearing capability of the implant. For TJR (total joint replacement) surgeries, where load-bearing capability is indispensable, ideally a high strength value of the alloy would be desirable. Hence, an alloy intended for orthopaedic use should combine a high strength value with adequate ductility (defined by percentage elongation or percentage reduction of area in a standard tensile test). Table 2.2 below lists the yield strength and ultimate tensile strength values of some of the common titanium alloys. One would see that some of the metastable β titanium alloys do show very high values in comparison to the α or α/β titanium alloys.

(b) Elastic Modulus: A number of experimental techniques have been used to determine the elastic properties of solids [137]. The relative elastic modulus of implant compared to that of the bone (~10-40 GPA) has always been a source of concern [113]. Long-term experiences indicate insufficient load transfer from artificial implant to the adjacent remodelling bone may result in bone re-absorption and eventual premature loosening of the prosthetic device [138, 139] due to the complex nature of compressive and tensile activities which they are exposed to when the implant is in service. This is termed the “stress shielding” effect, caused by the differences in flexibility and stiffness, dependent partly on elastic moduli difference between the natural bone and artificial implant material [140]. A reduction in the stiffness of the implant by using a lower modulus material would therefore definitely enhance the stress re-distribution of the adjacent bone tissue, ultimately minimise the stress shielding effect, and eventually prolong the service life of the implant device. In these terms, Ti6Al-4V and related α/β alloys have been considered to be inferior. The metastable β (i.e. microstructure predominantly consisting of α'' +β phase) and some fully transformed β phase exhibit lower overall moduli. Figure 2.13 shows the interrelationship of elastic moduli with microstructure; and Table 2.2 shows that Ti-15Mo-5Zr-3Al, Ti-12Mo-6Zr-2Fe, Ti-15Mo-2Nb-0.3O and Ti-13Nb-13Zr have an elastic moduli ranging from 74-88GPa, which is about 2-7 times higher than the modulus of bones.

There have been numerous previous attempts (some failed and some successful) and many more will probably be developed and tested in the near future. The Ti-33Nb-7Zr-5Ta and Ti-24Nb-4Zr-7.9Sn alloys, however, stand out as prospective alloys mainly because they had one of the lowest modulus to date (~55 GPa and 24 GPA respectively): almost 20-40% lower than those of other available alloys [106, 136, 93]. Ti-24Nb-4Zr-7.9Sn was developed by Hao *et al.* of Shenyang National Laboratory for Materials Science, Institute of Metal Research, Chinese Academy of Sciences, in China; while Ti-33Nb-7Zr-5Ta was developed by Dr. Henry Rack at Clemson University and is now commercially sold by Allvac ® as TiOsteum® and TiOstalloy®, and its low yield strength value (547 MPa) was increased by adding interstitial oxygen. Thus Ti-33Nb-7Zr-5Ta-0.4O showed the strength of 976 MPa and elastic modulus of 66GPa [136]. It has been suggested that a two-step aging (instead of one) — one at a low temperature and a second at a high temperature — could be a means of increasing the yield strength. This is because the first step might lead to nucleation of fine distribution of ω as a precursor for α nucleation, which would be coarsened to a desired strength in a relatively higher temperature at the second aging step [141, 142].

Table 2.2: Orthopaedic alloys developed and/or utilised as orthopaedic implants and their mechanical properties (E=Elastic Modulus, YS=Yield Strength, UTS-ultimate Tensile Strength [113, 93].

Alloys designations	Microstructure	E(GPa)	YS(MPa)	UTS(MPa)
c.p Ti	{α}	105	692	785
Ti-6Al-4V	{α/β}	110	850-900	960-970
Ti-6Al-7Nb	{α/β}	105	921	1024
Ti-5Al-2.5Fe	{α/β}	110	914	1033
Ti-12Mo-6Zr-2Fe	{Metastable β}	74-85	1000-1060	1060-1100
Ti-15Mo-5Zr-3Al	{Metastableβ} {aged α+β}	75 88-113	870-968 1087-1284	882-975 1099-1312
Ti-15Mo-2.8Nb-3Al	{Metastableβ} {aged α+β}	82 100	771-1215	812 1310
Ti-13Nb—13Zr	{α′/β}	79	900	1030
Ti-15Mo-3Nb-0.3O (21Srx)	{Metastableβ}+ Silicides	82	1020	1020
Ti-35Nb-7Zr-5Ta	{Metastable β}	55	530	590
Ti-35Nb-7Zr-5Ta-0.04O	{Metastable β}	66	976	1010
Ti-24Nb-4Zr-7.9Sn	{α″/β}	24	900	920

2.7 Summarising comments

In summary, one must appreciate the growing interest in Ti and its alloys and its ability to possess a range of property values depending on alloying additions and/or thermomechanical treatments adopted. Though significant advances have been made by alloying or micro-alloying as an effective means of improving those properties and exploiting their potential as materials for load-bearing components, these efforts are unfortunately still far from the final goal in terms of understanding the microstructural development, preventing poor ductility and toughness at ambient temperature. This work attempts to identify the effect alloying additions have on the mechanical behaviour and thermodynamic stability of α'' and β Ti phase and its dependence on initial β matrix instabilities. Chapters 3 to 7 discuss this approach and the results, which are then summed up in Chapter 8.

2.8 References

[1] Hume-Rothery W.; Research on the nature, properties and conditions of formation of intermetallic compounds, with special reference to certain compounds of tin, J. Inst. Metals, 35 (1926), 295-307.

[2] Mizutani U.; The Hume-Rothery rules for Structurally Complex Alloy Phases; CRS Press, Taylor and Francis, United States of America, 2011.

[3] Schrodinger E.: Quantification of the eigen-value problem, Ann. Physik, 79 (1926), 361-731.

[4] Wigner, E., and Seitz F.; On the Constitution of Metallic Sodium. Phys. Rev, 43(10), (1933), 804-810.

[5] Hume-Rothery W., Mabbot G. V., and Channel-Evans K. M.; The Structure of Metals and Alloys, Phil. Trans. R. Soc. Lond. A 233 (1934), 1.

[6] Reynolds P. W., and Hume-Rothery W.; The constitution of silver-rich antimony silver alloys, J. Inst. Metals 60 (1937), 365-374.

[7] Westgren A., and Phragmena G.; X-ray analysis of copper-zinc, silver-zinc and gold zinc alloys, Philo. Mag.50 (6), (1926), 311-341.

[8] Raynor G. V.; Progress in theory of alloys, Progr. Met. Phys. 1 (1949), 76.

[9] Paxton A., Methfessel M. T., and D. G.; Pettifor: A band structure view of the Rothery electron phases. Proceedings of the Royal Society A, Mathematical, Physical and Engineering Sciences, 453 (1997) 1493-1514.

[10] Tiwari G. P., and Ramanujan R. V.; The relation between the electrons to atom ratio and physical properties of materials, J. Mat. Sci. 6 (2001), 271-283.

[11] Mizutani U., Asahi U., Sato R., Noritake H., and Takeuchi T.; Mediated resonance effect of the vanadium 3d states on phase stability in the Al8V5 g-brass studied by first-principles FLAPW and LMTO-ASA electronic structure calculations. Phys. Rev. 74; (2006), 235119.

[12] Mizutani U., Asahi U., Sato R., Noritake H., and Takeuchi T.; Failure of the Hume-Rothery stabilization mechanism in the Ag5Li8 gamma-brass studied by first principles FLAPW electronic structure calculations, J. Phys. Condens; Mat, 20 (2008), 275228.

[13] Obrado E., Manosa L., and Planes A.; Stability of the bcc phase of Cu-Al-Mn shape-memory alloys. Phys. Rev. B, 56(1) (1997), 20-23.

[14] Pippard A. B.; An Experimental Determination of the Fermi Surface in Copper, Philos. Trans. R. Soc. London, Ser. A., (1957), 250-325.

[15] Moller C. P.; Note on an Approximation Treatment for Many-Electron Systems, Phys. Rev. 46, (1934), 618-622)

[16] Saito T. *et al.;* Science 300, (2003), 464; Kuramoto S et al., Mater. Sci. & Eng. A 442, (2006), 454; Gutkin M, Ishizaki T, Kuramoto S, and Ovid'ko I. A: Acta Mater. 54; 2489 (2006), 2489.

[17] Hao Y. L., Li S. J., Sun S. Y., Zheng C. Y., and Yang R.; Elastic deformation behaviour of Ti-24Nb-4Zr-7.9Sn for biomedical applications, Acta Biomaterialia 3 (2007), 277-86.

[18] Mott N. F., and Jones H.; Theory of the properties of metals and alloys, (Oxford University: Clarendon press, 1936.

[19] Jones H.; The Theory of Alloys in the gamma Phase, Proc. R. Soc. Lon 144(1934), 225-234.

[20] Jones H.; The phase boundaries in binary alloys, part 1: the equilibrium between liquid and solid phases, Proc. Phys. Soc.49 (1937), 243-250.

[21] Jones H.; The phase boundaries in binary alloys, part 2: the theory of the α, β phase boundaries, Proc. Phys. Soc.49 (1937), 250.

[22] Ashcroft Neil W., and Mermin N.; David (1976): Solid State Physics, Orlando, Harcourt; ISBN 0-03-083993-9; Kittel, Charles (1996): Introduction to Solid State Physics (7th ed.). New York: Wiley; ISBN 0-471-11181-3.

[23] Pippard A. B.; An Experimental Determination of the Fermi Surface in Copper, Phil.Trans. R. Soc. Lond. A, 250, (1957), 325.

[24] Morinaga M., Kato M., Kamimura T., Fukumoto M., Harada M., and Kubo K.; Titanium 1992, Science and Technology, Proc. 7th Int. Conf. on Titanium, San Diego, CA, USA, (1992), 276–283.

[25] Kuroda D., Niinomi M., Morinaga M., Kato Y., and Yashiro Y.; Design and mechanical properties of new β type titanium alloys for implant materials, Mater. Sci. & Eng. A, 243 (1998), 244-249.

[26] Bloch, P. E.; Projected augmented-wave method, Physical Review B 50(1994), 953-978.

[27] Hohenberg P., and Kohn W.; Inhomogeneous Electron Gas, Phys. Rev. B 136, (1964), 864–871.

[28] Kohn W. and Sham J.; Self consistent equation including exchange and correlation, Physics Rev A 140 (1965), 1133.

[29] Wagner M. F., and Windl W.; Lattice stability, elastic constants and macroscopic moduli of NiTi martensites from first principles, Acta Mater. 56 (2008), 6232-6245.

[30] Georg K.; (March 31, 2010), "VASP Group, Theoretical Physics Departments, Vienna.

[31] Segall M., Philip J., Lindan D., Probert M. J., Pickard C. J., Hasnip P. J., Clark S. J., and Payne M. C.; First-principles simulation: ideas, illustrations and the CASTEP code, J. Phys.: Condens. Matter 14 (2002), 2717–2744.

[32] Huang X., Ackland G., Raabe J. and Karin M.; Crystal structures and shape-memory behaviour of NiTi, Nature Materials 2 (2003), 307-11.

[33] Bautista-Hernández T., Rangel A., Romero H., Rignanese G. M., Salazar-Villanueva M. and Chigo-Anota E.; Structural and vibrational stability of M and Z phases of silicon and germanium from first principles, J. Appl. Phys. 113, (2013), 193504.

[34] Xiao H. B., Yang C. P., Wang R. L., Marchenkov V. V., and Bärner K.; Effect of alloying element Al substitution on Ni-Mn-Sn shape memory alloy by first-principle calculations, J. Appl. Phys. 112, (2012), 123723.

[35] Collings E. W., and Gegel H. L.; A physical basis for solid solution strengthening and phase stability in alloys of titanium, Scripta Metall 7; (1973), 437–43.

[36] Luetjering G., and Williams J. C.; "Titanium", Engineering Materials and Processes, Springer Publication, 2nd edition.

[37] Reedhill R. E., and Abbaschian R.; "Physical Metallurgy Principles", In the PWS-Kent Series in Engineering, (1991).

[38] Collings E. W., Ho J. C., Jaffee R. I.; Superconducting transition temperature, lattice instability and electron-to-atom ratio of transition-metal binary solid solutions, Phys. Rev. 5 (1972), 4435–49.

[39] Blanco M. A., Francisco E., and Luaña V.; GIBBS: isothermal-isobaric thermodynamics of solids from energy curves using a quasi-harmonic Debye model, Comp. Phys. Comm. 158 (2004), 57-72.

[40] Reedhill R. E., and Abbaschian R.; "Physical Metallurgy Principles", The Pws-Kent Series in Engineering, (1991).

[41] Hirao M., Ogi H., Kai S., Ledbetter H., Tarumi R. and Takashima K.; Titanium's high temperature elastic constants through the hcp-bcc phase transformation, Acta Met. 52 (2004), 2075-2080.

[42] Deurig T. W., and Williams J. C.; *Beta titanium alloys in the 1980s*. ed. by R. R. Boyer and H. W. Rosenberg, AIME, New York, USA, (1984), 19-67.

[41] Welsch G., Boyer R. R., and Collings E. W.; Materials Properties Handbook: Titanium Alloys, ASM Handbook, Institute of Metals, USA, 1994.

[42] Balcerzak A. T., and Sass S. L.; The Formation of ω phases in Ti-Nb Alloys. Metall. Trans. 3, (1972), 1601-1605.

[43] Biancaniello F. S., Bendersky L. A., Boettinger W. J., Burton B. P. and Shoemaker C.B: The Formation of Ordered Omega-related Phases in Alloys of Composition TiAlNb, Acta Metall Mater, 38(6)(1990),931-943.

[44] Banerjee D., and Muraleedharan K.; Substructure in titanium alloy martensite, Phil. Mag. A, 77(2)(1998), 299-323.

[45] Porter D. A. and Easterling K. E.; Phase Transformations in Metals and Alloys. Nelson Thornes Limited, 2nd edition, 2001.

[46] Patel J. R., and Cohen M.; Criterion for the action of applied stress in the martensitic transformation, Acta Metall. 1 (1953), 531-540.

[47] Kim S., Ledbetter H., Ogi H., Kai S., and Hirao M.; Elastic constants of body cantered cubic titanium mono crystals, J. Appl. Phys., 95(9) (2004), 4642.

[48] Zhou Y. L., Niinomi M., and Akahori T.; Decomposition of martensite α“ during aging treatments and resulting mechanical properties of Ti-Ta alloys, Mater. Sci. Eng., A, 384(1-2) (2004), 92-101.

[49] Williams J. C.; Critical review: Kinetics and phase transformations. Titanium 1973 Science and Technology, ed. by R. I. Jaffee and H. M. Burte, Plenum Press, New York, USA, (1973), 1433-1494.

[50] Duerig F., and Richter A.; Formation and Reversion of Stress Induced Martensite in formation and reversion of stress induced martensite in Ti10V2Fe3Al, Acta Metall. Mater, 30(1982), 2161-2172.

[51] Middleton R., Duerig T. W., Terlinde G. T., and Williams J. C.; Stress Assisted Transformation in Ti-10-2-3, Titanium 80 Science and Technology, (1980), 1503.

[52] Kim H. Y. *et al.*; Martensitic transformation, shape memory effect and superelasticity of Ti-Nb binary alloys, Acta Mater. 54(9)(2006), 2419-2429; (b) Nakai K Ohmori Y, Ogo T and Kaobayashi S: Effects of ω-phase precipitation on α′ and α′′ transformations in a metastable β titanium alloy, Met. Sc. & Eng. A 312; (2001), 182-188.

[53] Hao Y. L., Li S. J., Sun S. Y., Zheng C. Y., and Yang R.; Elastic deformation behaviour of Ti-24Nb-4Zr-7.9Sn for biomedical applications, Acta biomater. 3 (2007), 277-86.

[54] Luke C. A., Taggart R., Polonis D. H.; The metastable constitution of quenched titanium and zirconium-base alloys, Trans ASM 57(1964), 142–9.(b) Nosova G.I, Bagariatskii Y. A and Tagunova T.V: Factors in the Formation of Metastable Phases in Titanium-Base Alloys", Sov. Phys. Dokl. [transl. of Dokl. Akad. Nauk. SSSR, 122, (1958), 593-596.

[55] Hao Y. L. *et al.*; Young's modulus and mechanical properties of Ti-29Nb-13Ta-4.6Zr in relation to α'' Martensite. Metall, Mater. Trans. A, 33(2002), 3137-3144.

[56] Wu M. H., Zhou T., Aindow M., Ainow S. P., Alpay S. P. and Blackburn M. J.; Pseudoelastic deformation behaviour in a Ti/Mo based alloys, Script. Mater. 50 (2004), 243-248.

[57] Zhang L. C., Zhou T., Alpay S. P., Aindow M., and Wu M. H.; Origin of Pseudoelastic behaviour in TiMo-based alloys, App. Phys. Lett. 87; 24 (2005), 241909.

[58] Zhang S. Q. *et al.*; Fatigue properties of a multifunctional titanium alloy exhibiting nonlinear elastic deformation behaviours, Scr. Mater. 60; 8 (2009), 733-736.

[59] Xiaoli Z. *et al.*; Relationship between various deformation-induced products and mechanical properties in metastable Ti-30Zr- Mo alloys for biomedical applications. J.Mech. Beh. Biomed. Mater. 4; 8 (2011), 9-16.

[60] West D. F. R., Flower H. M. and Henry S. D.; The β-α transformation in dilute Ti-Mo. alloys, J. Mater. Sci. 9 (1974), 57-64.

[61] Frost P. D. *et al.*; Isothermal transformation of titanium-chromium alloys Trans. Am. Soc. Metals, 461954, 231-251.

[62] Collings E. W.; *The physical metallurgy of titanium alloys*. American Society of Metals, Metals Park, Ohio, USA, (1984), 75-110.

[63] Banerjee S., Tewari R. and Dey G. K.; Omega phase transformation — morphologies and mechanisms. Int. J. Mater. Res., 97 (2006), 963-977.

[64] Sakaguchi N. *et al.*; Relationships between tensile deformation behavior and microstructure in Ti-Nb-Ta-Zr system alloys, Mater. Sci. Eng., C, 25:3 (2005), 363-369.

[65] Li S. J. *et al.*; Phase transformation during aging and resulting mechanical properties of two Ti-Nb-Ta-Zr alloys, Mater. Sci. Technol., 21; 6(2005), 678-686.

[66] Schwartz C. M., Frost P. D., Parris W. M., Hirsch L. L., Doig J. R.; Isothermal transformation of titanium chromium alloys, Trans Am Soc. Met Trans, 46; (1954), 231-256.

[67] Hickman B. S.; Omega Phase Precipitation in Alloys of Titanium with Transition Metals, Trans. TMS-AIME, 245; (1969), 1329-1335.

[68] Blackburn M. J., and Williams J. C.; Phase Transformation in Ti-Mo and Ti-V alloys, Trans. TMS-AIME, 242; (1968), 2461-2469.

[69] Davies M. H., Silcock J. M. and Hardy H. K.; The Mechanism of Phase Transformations in Solids, Inst. of Metals 3; 93 (1956), 671-698.

[70] Bagariatskii Yu A., and Nosova G. I.; A more accurate determination of Atomic Coordinates of the Metastable ω-Phase in Ti-Cr Alloys, Sov. Phys. Crystallogr. [transl. of Kristallografiya, 3, (1958), 17-28.

[71] Sass S. L.; The Structure and Decomposition of Zr and Ti bcc Solid Solutions, J. Less-Common Met., 28; (1972), 157-173.

[72] Williams J. C., Hickman B. S. and Marcus H. L.; "The Effect of Omega Phase on the Mechanical Properties of Titanium Alloys", Met. Trans., 2, (1971), 1913-1919.

[73] Strychor R., Williams J. C., and Soffa W. A.; "Phase Transformations and Modulated Microstructures in Ti-Al-Nb Alloys", Metall. Trans., 19A, (1988), 225-234.

[74] Blackburn M. J.; Some Aspects of Phase Transformations in Titanium Alloys. In The Science, Technology and Application of Titanium, (1970), 633-643.

[75] Williams J. C. and Blackburn M. J.; The influence of Misfit on the Morphology and Stability of the Omega Phase in Titanium — Transition Metal alloys, Trans. (TMS-AIME) 245; (1969), 2352.

[76] Oka M., and Taniguchi Y.; Metall. Trans., 10 A (1979), 651.

[77] Collings E. W.; Magnetic investigations of Electronic Bonding and a through Phase Equilibria in the Titanium Aluminum System, In Titanium and Titanium Alloys Scientific and Technological Aspects, (1970), 1391-1402.

[78] Bowles J. S., and Mackenzie J. K.; Acta Met, 2 (1954), 129.

[79] Jepson K. S., Brown A. R. G., and Gray J. A: The Effect of Cooling Rate on the Beta Transformation in Titanium-Niobium and Titanium-Aluminium Alloys. The Science, Technology and Application of Titanium, (1970), 677-690.

[80] Cook H. E.; "A Theory of the Omega Transformation", *Acta Met*, **22**, (1974), 239-247.

[81] Otte H. M.; Mechanism of the Martensitic Transformation in Titanium and its alloys, In The Science, Technology and Application of Titanium, (1970), 645-657.

[82] Burgers W. G.; On the process of transformation of the cubic body centered modification into hexagonal close packed modification in Zirconium, Physica I, (1934), 561-586.

[83] Shibata M., and Ono K.; On the Minimization of Strain Energy in the Martensitic Transformation of Titanium, Acta Metal. Mater, 25 (1977) 35-42.

[84] Davis R., Flower H. M., and West D. R. F.; Martensitic transformations in Ti-Mo alloys, J. Mater. Sci. 14; (1979), 712-722.

[85] Sukedai E, Hashimoto H, and Tomita M: Investigation of omega-phase in Ti-Mo alloys by high resolution electron microscopy, image processing and dark field methods", Phil. Mag., 64A (6), (1991), 1201-1208.

[86] Davis R., Flower H. M., and West D. R. F.; Martensite Formation and Decomposition in Alloys of Titanium Containing β -Stabilizing Elements, Titanium and Titanium Alloys, In Scientific and Technological Aspects, {1982), 1703-1715.

[87] Kaneko H., Huang Y. C., Suzuki S., and Sato T.; Titanium 1970, Science and Technology, ed. by R. I. Jaffee and Promisel, Plenum Press, New York, USA, 1970: p. 691.

[88] Ho W. F., Ju C. P., and Lin J. H.; Structure and properties of cast binary Ti-Mo alloys, Biomat. 20; 22 (1999), 2115-22.

[89] Hatt B. A., and Rivlin V. G.; Phase Transformations in Superconducting Ti-Nb alloys, J. Phys. D, Appl. Phys. 1; (1968), 1145-1149.

[90] Mofiat D. L., and Larbalestier D. C: The Competition between Martensite and Omega in Quenched Ti-Nb Alloys, Met. Trans. 19A, (1988), 1677-1686.

[91] Williams J. C., Plichta M. R and Aaronson H. I: On the Existence of the β-α transformation in the alloy systems containing Ti-Ag, Ti-Au, and Ti-Si" Met. Trans. A, 8A ;(1977), 1885-1892.

[92] Plichta M. R. and Aaronson H. I.; The Thermodynamics and Kinetics of the β-α transformation in Three Ti-X Systems, Acta Metall. Mater. 26; (1978), 1293-1305.

[93] Hao Y. *et al.*; Ductile Titanium Alloy with Low Poisson's ratio, Phys. Rev. Lett. 98; 21 (2007), 1-4.

[94] Grosdidier T. *et al.*; The deformation mechanisms in the β-Metastable β-CEZ titanium alloy, Scr. Mater., 36; 1 (1997), 21-28.

[95] Zhang D. C. *et al.*; Effect of ternary alloying elements on microstructure and superelastictity of Ti-Nb alloys, Mater. Sci. & Eng. A 559(2013), 706-710.

[96] Rack H. J. *et al.*; Metastable Beta Titanium Alloys for Orthopaedic applications. Adv. Eng. Mater. 7; 11(2005)993-998.

[97] Miyazakia S. *et al.*; Interfacial defects in TiNb shape memory alloys, Acta Mater. 13 (2008), 3097-3088.

[98] Yokohari Y., Hida M., Sukedai E. and Nagakawa A.; Thermal Instability and Mechanical Properties of Beta Titanium-Molybdenum Alloys. Titanium 80, Science and Technology, ed. by R. I. Jaffee and Promisel, Plenum Press, New York, USA, (1980), 1327-1334.

[99] Paton N. E., and Williams J. C.; The Deformation of Body-Centred-Cubic Titanium-Vanadium Single Crystals, American Society of Metals, Metals Park, Ohio, USA, (1970), 108.

[100] Young A. P. *et al.*; Acta Metall Mater.11 (1963), 1097.

[101] Blackburn M. J. *et al.*; J. Inst. Met.99 (1971), 132.

[102] Kishimoto K., Furuhara T., and Maki T.; Transmission Electron Microscopy of [332]<113> Deformation Twin in Ti-15V-3Cr-3Sn-3Al Alloy, Mater Trans, JIM, 35; 12(1984), 843-850.

[103] Ohmori Y., Natsui H., Nakai K., and Ohtsubo H.; "Effects of ω Phase Formation on Decomposition of α''/β Duplex Phase Structure in a Metastable β Ti Alloy", Mater Trans, JIM, 39(1), (1998), 40-48.

[104] De Fontaine D.; Mechanical Instabilities in the BCC lattice and the Beta to Omega Phase Transformation, Acta Met, 18(1970), 275-279.

[105] Williams J. C., De Fontaine D., Paton N. E.; The Omega Phase Transformation in Titanium Alloys as an example of displacement controlled reactions, Acta Met. 19; (1971), 1153.

[106] Cook H. E.; On First-Order Structural Phase Transitions — II The Omega Transformation, Acta Met. 23, (1975), 1041-1054.

[107] Cook H. E.; On the nature of the Omega Transformation. Acta Met, 21, (1993), 1445-1449.

[108] Cook H. E.; A Theory of the Omega Transformation, Acta Met., 22(1974), 239-247.

[109] Clapp P. C.; A Localized Soft Mode Theory for Martensitic Transformations. Phys. Stat. Sol. (b), 57(1973), 561-569.

[110] Suzuki T., and Wuttig M.; Analogy between Spinodal Decomposition and Martensitic Transformation, Acta Met. 23 (1975), 1069-1076.

[111] Moss S. C., Keating D. T., and Axe J. D.; "Neutron Study of the Beta-to-Omega Instability in Zr0.80Nb0.20", Phase Transitions, (1973), 179-188.

[112] Batterman B. W., Maracci G., Merlini A. and Pace S.; Diffuse Mossbauer Scattering Applied to Dyanamics of Phase Transformations, Phys Rev Letter, 31, (1973), 227-230.

[113] Long M. J., and Rack H. J.; Titanium alloys in total joint replacement — a materials science perspective, Biomater. 19, (1998), 1621-1639.

[114] Dowson D.; "Friction and wear of medical implants and prosthetic devices, ASM Handbook, 18, (1992), 656-664.

[115] Lee C. M., Ho W. F., Ju C. P. and Chern Lin J. H.; Structure and properties of Titanium-20Niobium-xIron alloys, J. Mater. Sci.: Materials in Medicine, 13, (2002), 695-700.

[116] Semlitsch M. F., Weber H., Streicher R. M., and Schön R.; Joint replacement components made of hot-forged and surface-treated Ti-6Al-7Nb alloy, Biomater. 13; 11 (1992), 781-788.

[117] Borowy K. H., and Krammer K. H.; On the properties of a new Titanium alloy (Ti-5Al-2.5Fe) as implant material Titanium '84: Science and Technology 2, (1985), 1381-1386.

[118] Steinemann S. G., Mäusli P. A., Szmukler-Moncler S., Semlitsch M., Pohler O., Hintermann H. E., and Perren S. M.; "Beta-titanium alloy for surgical implants", Beta Titanium in the 1990s, (1993), 2689-2696.

[119] Rao S., Ushida T., Tateishi T., and Okazaki Y.; Bio-med. Mater. Eng., 6; 79 (1996); 208.

[120] Walker P. R., Leblanc J. and Sikorska M.; Biochemistry, 28 (1990), 3911.

[121] Cohen J.; Metal implants — Historical background and biological response to implantation, Biomaterials in reconstructive Surgery, (1979), 46-61.

[122] Ito Y., Okazaki Y., Ito A., and Tateishi T.; New Titanium alloys for medical implants", Titanium '95: Science and Technology, (1995), 1776-1783.

[123] Lin D. J., ChernLin J. H., and Ju C. P.; Structure and properties of Ti-7.5Mo-x Fe alloys, Biomater. 23, (2002), 1723-1730.

[124] Donache M. J. *et al.*; Titanium: a technical guide, (1989), 218.

[125] Guillermot F., Prima F., Bareille R., Gordin D., Gloriant T., Porté-Durrieu M. C., Ansel D., and Baquey Ch.; Design of new titanium alloys for orthopaedic applications, Medical & Biological Engg. & Computing 42, (2004), 137-141.

[126] Feeney J. A., and Blackburn M. J.; Effect of microstructure on the Strength, Toughness and Stress-Corrosion Cracking Susceptibility of a Metastable Beta Titanium Alloy (Ti-11.5Mo-6Zr-4.5Sn), Met. Trans. 1, (1970), 3309-3323.

[127] Wang K.; The use of titanium for medical applications in the USA, Mater. Sci. & Eng. A, 213, (1996), 134-137.

[128] Wang K., Gustavson L., and Dumbleton J; "The characterization of Ti-12Mo-6Zr-2Fe. A new biocompatible titanium alloy developed for surgical implants", Beta Titanium in the 1990's, (1993), 2697-2704.

[129] Tang X., Ahmed T. and Rack H. J.; Phase transformations in Ti-Nb-Ta and Ti-Nb-Ta-Zr alloys, J. Mat. Sc. Mats., in Medicine, (2000), 1805-1811.

[130] Niinomi M., and Williams J. C.; Ti-2003: Science and Technology, 95 (2004).

[131]Niinomi M., Hattori T., Kasuga T. and Fukui H.; Titanium and its Alloys, Dekker Encyclopaedia of Biomaterials and Biomedical Engineering, (2005).

[132] Akahori T., Niinomi M., Fukui H., Suzuki A., Hattori Y. and Niwa S.; Ti-2003: Science and Technology, (2004), 3181.

[133] Fanning J. C.; Properties and processing of a new metastable beta titanium alloy for surgical implant applications: TIMETAL™ 21SRx", Titanium 95': Science and Technology, (1996), 1800-1807.

[134] Mishra A. K., Davidson J. A., Kovacs P. and Poggie R. A.; Ti-13Nb-13Zr: a new low modulus, high strength, corrosion resistant near-beta alloy for orthopaedic implants, Beta Titanium in the 1990s, (1993), 61-72.

[135] Ahmed T. A., Long M., Silverstri J., Ruiz C., and Rack H. J.; "A new low modulus biocompatible titanium alloy", Titanium 95': Science and Technology, (1996), 1760-1767.

[136] Radovic M., Lara-Curzio E., and Riester L.; Comparison of different experimental techniques for determination of elastic properties of solids, Mater. Sci. & Eng. A, 368, (2004), 56-70.

[137] Dujovne A. R., Bobyn J. D., Krygier J. J., Miller J. E., and Brooks C. E.; Mechanical compatibility of noncemented hip prostheses with the human femur, J. Arthroplasty, 8:1, (1993), 7-22.

[138] Engh C. A., and Bobyn J. D.; The influence of stem size and extent of porous coating on femoral bone resorption after primary cementless hip arthroplasty, Clin Orthop Relat Res, 231, (1988), 7-28.

[139] Sumner D. R., and Galante J. O.; Determinants of stress shielding: design versus materials versus interface, Clin Orthop Relat Res, 274, (1992), 202-212.

[140] Qazi J. I., Tsakiris V., Marquard B., and Rack H. J.; Ti-2003, Science and Technology, (2004), 1651.

[141] Qazi J. I., and Rack H. J.; Adv. Eng. Mat. 7, (2005), 993.

Chapter 3

Experimental and Computational Techniques

3.1 Summary

This chapter itemises the experimental plan and process and computational techniques utilised individually and in relation to the whole work. The experimental techniques include alloy fabrication route, cold rolling process, texture and thermoelectric power method for assessing electronic behaviours. Explicit details of techniques such as microstructural, metallographic processing, cold rolling and mechanical testing are considered individually in the respective sections.

Computational technique is based on the CASTEP code simulation, which fully features first principles and, as such, its capabilities are numerous. The basic quantity is the total energy from which many other quantities are derived. For example, the derivative of total energy with respect to atomic positions results in the forces and derivatives with respect to cell parameters given stresses. These are then used to perform full geometry optimisation of structure calculations and interpretation of bulk electronics (such as electronic band structure, density of states) and mechanical properties (such as elastic parameters and ductility) are deduced. These techniques are appropriate for characterising, understanding, designing and predicting microstructure and electronic changes in the properties of alloys based on the aforementioned Ti systems.

3.2 Experimental schedule plan

There is a growing interest in Ti-Mo based alloys for biomedical materials, and their ability to possess a range of property values depending on alloying additions and/or thermomechanical treatments adopted. This work is divided into three phases: the research process is schematically shown in Figure 3.1. In the first phase, pure Ti-Mo binary alloys were melted into ingots and casted into cylindrical rods. These binary alloys were characterised as determining the phase and microstructural types. The results were correlated with semi empirical calculations based on the Md, Bo and the electron per atom ratio (e/a) discussed previously in chapter 3.

The ideal recipe for an element to be used for implant application was excellent biocompatibility with no adverse tissue reactions effect, excellent corrosion resistance in the body fluid, high mechanical strength and fatigue resistance, low elastic modulus, low density and good wear resistance. That limits the list to a small number: titanium (Ti), molybdenum (Mo), niobium (Nb), tantalum (Ta), zirconium (Zr), iron (Fe) and tin (Sn).

In the second and third phase respectively, we designed and investigated the properties of multicomponent alloys aimed at meeting the qualities expected of bio- implants materials; namely, Ti-Mo (Ti-Mo-Sn, Ti-Mo-Zr, Ti-Mo-Nb, Ti-Mo-Ta, Ti-Mo-Ta-Sn, Ti-Mo-Ta-Zr, Ti-Mo-Ta-Nb and Ti-Mo-Nb-Zr) and Ti-Nb (Ti-Nb-Zr, Ti-Nb-Sn, Ti-Nb-Ta, Ti-Nb-Mo, Ti-Nb-Zr-Sn, Ti-Nb-Ta-Sn, Ti-Nb-Mo-Zr, Ti-Nb-Ta-Zr and Ti-Nb-Mo-Zr). A rigorous experimental and DFT theoretical study of the properties of these alloys was undertaken. In this research, various mechanical, phase composition and microstructural properties were investigated.

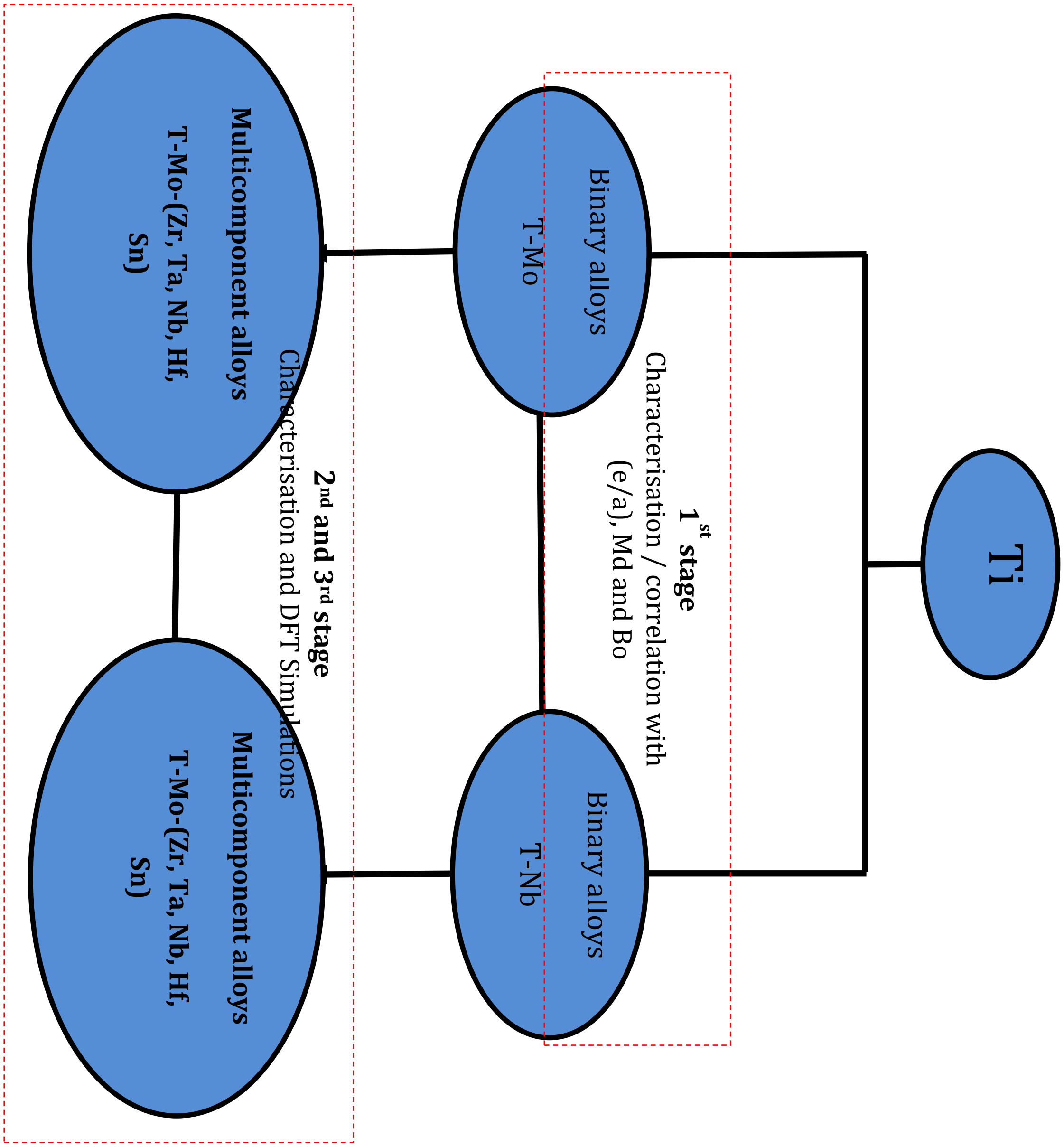

Figure 3.1: Schematic illustration of different stages of the work plan.

3.3 Fabrication process

3.3.1. Alloy preparation

The constituent elements of alloys were weighed out on a Precisa XB120A electronic balance (Precisa instruments) to an accuracy of ± 0.1 mg to obtain the required composition. The elements used, which were in solid bar, had purities >99.8%. Unalloyed titanium and other alloying elements were initially cold rolled to produce small pieces, before polishing and cleaning in an ultrasonic bath to remove surface grease or other impurities, particularly those that may have remained after cutting. This was to minimise and remove contaminants that might adversely influence the phase stability and other properties of the alloys.

3.3.2. Argon arc furnace

An argon arc furnace utilised for the preparation of alloy ingots is depicted in Figure 3.2. The chamber is usually evacuated to < 10-5 torr (10-3 Pa) before being back filled to 1/3 atm. (30 KPa) of high purity argon gas. A Ti button of mass 20 g was melted in the chamber prior to the melting of the alloy sample in order to minimise residual oxygen in the chamber, and thus minimise oxidation of the alloy (commonly known as oxygen gettering). The Ti button was normally used only 20 times, and then it was replaced with a clean unmelted piece of Ti. Fifteen gram buttons of each alloy were melted at least five times under argon atmosphere to ensure a low oxygen starting condition. They were re-melted at least five times, or until change in the solidification behaviour was not observed, in order to reduce the possibility of macrosegregation in the ingot. The ingots were cooled to room temperature in the chamber under the argon atmosphere. An average weight loss of 0.1 % was recorded.

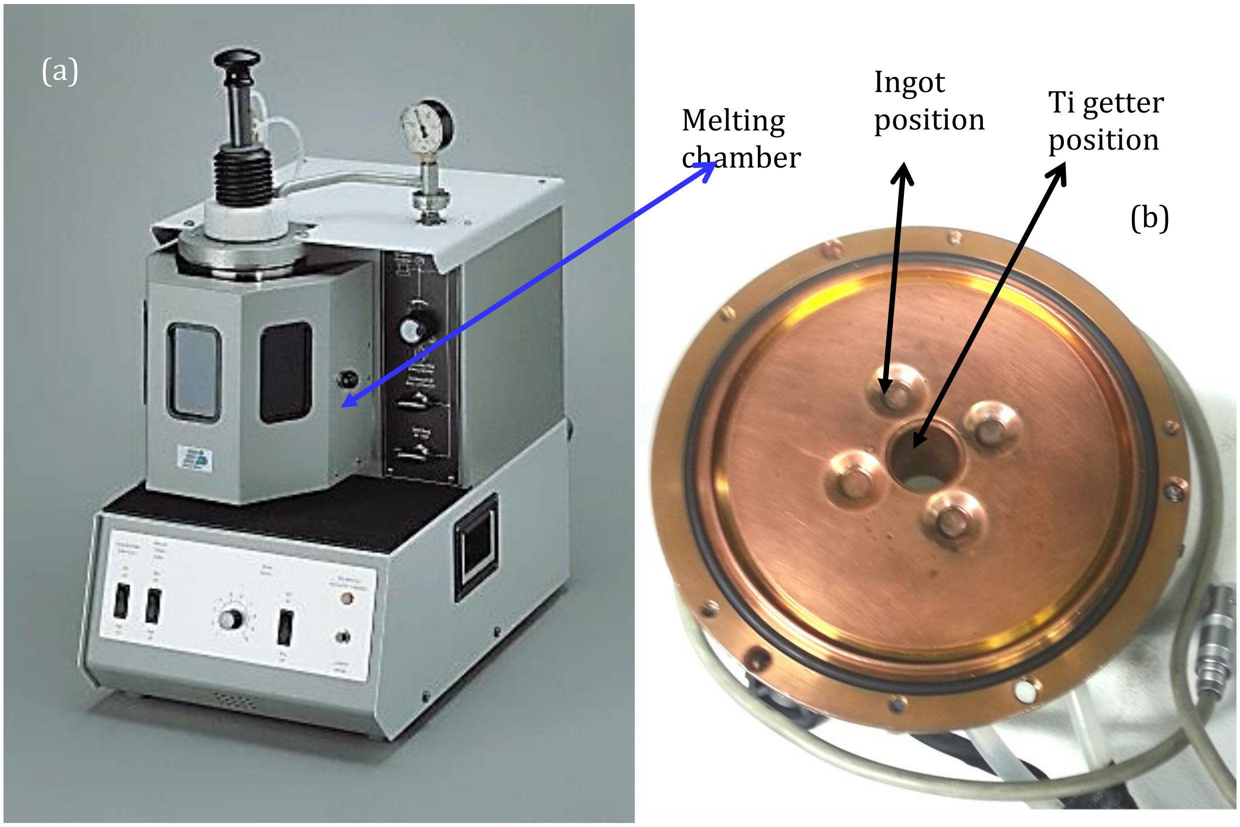

Figure 3.2: Schematic illustration of the argon arc melting furnace system; (b) Aerial view of the water cooled copper mould inside the chamber of the arc melter.

3.3.3. Copper die suction casting

The suction casting facility has been incorporated into the argon arc furnace as a part of the system. As the pre-alloyed ingot was melted in the argon arc furnace, the melted alloy was pressure induced to suck down onto a water-cooled copper die under the influence of a negative pressure differential between the copper die and the melting chamber. The process technique involves arc melting of 1-20g of the pre-alloyed ingots. This is followed by forcing superheated molten metallic alloys into the copper die using the excess pressure in the chamber. The pressure differential is generated by the use of a roughing pump connected to the secondary chamber at the base of the die cavity via a solenoid valve. Due to the design of the chamber it was not possible to measure the actual superheat of the sample, so a successful cast was strongly dependent on the operator's judgment. With insufficient superheat the melt did not completely fill the die cavity. If the sample superheat were excessive however, the molten metal would access the secondary chamber and damage or destroy the seal in the solenoid valve.

The chamber of the suction unit is divided in two — the upper and lower chamber. The upper chamber contains connections for vacuum pumps (roughing and diffusion), gas inlets (argon is normally used), vacuum gauges and a tungsten electrode. The lower chamber consists of a water-cooled copper hearth. The copper hearth has connections for water in and out and for the secondary chamber, which is controlled by the solenoid valve. The copper block with channels for water-cooling is placed into the copper hearth. In the copper hearth there is a space where the split die with connections to the secondary vacuum chamber is fitted. Fig. 3.3 is a photograph of the suction casting apparatus with a diagonal section of a cupper die in the figure. Several types of copper dies were employed in preparing the samples. The shapes and sizes depend on the operator's need. Stepped cylindrical dies with cavities ranged from 0.5 mm to 5 mm and a conical die with a length of 50 mm and cone base diameters in the range 2-10 mm were commonly used. The moulds surfaces were normally polished with 6 micron diamond paste and cleaned using acetone before use. This was done in order to enhance the thermal contact between the melt and mould wall and minimise any possible external contamination of the melt.

The cooling rates of the system had been estimated earlier using an aluminium composition (Al-4 wt. % Cu alloy). The alloy was suction cast into a 2/3/4 mm stepped die; the cooling rate was then calculated by measuring the secondary dendrite arm spacing (2) (m), which exhibits the following relationship with the cooling rate (likely to change with alloy type):

$$\lambda_2 = 50/\dot{T}^3 \qquad \text{eqn. 3.1}$$

where $\dot{T}$ is the cooling rate and λ_2 is the secondary arm spacing

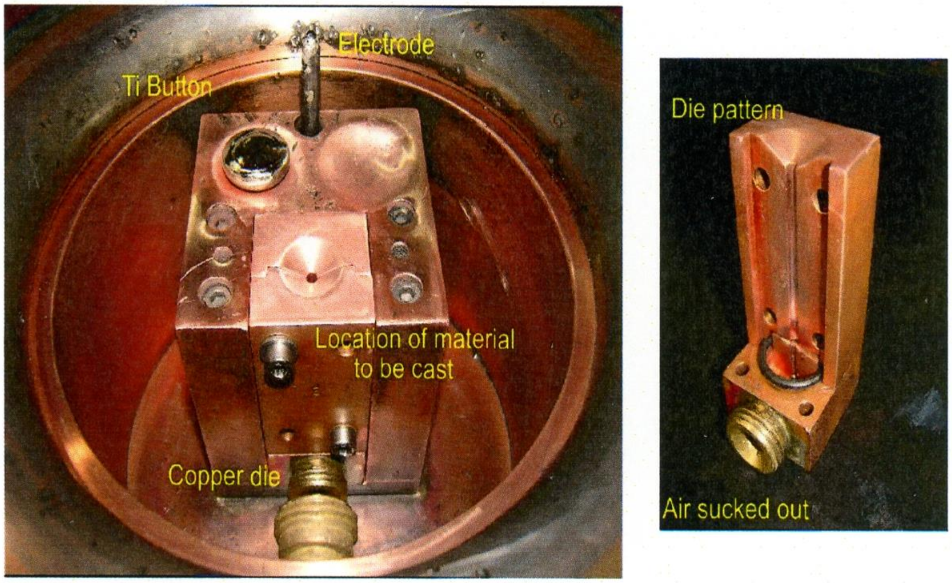

Figure 3.3: The lower half of the suction casting facility with adjoined picture of a section of a copper die.

3.4 Microtexture analysis by EBSD technique

In solid crystals, almost every property of interest in the whole spectrum — ranging from chemical resistance to mechanical properties such as strength and fracture toughness — is anisotropic.

Furthermore, almost all materials of engineering interest obtained by a non-specific solidification process (directional growth and single crystal growth) are polycrystals, which means that they are made up from aggregates of grains and/or phases.

Predicting the anisotropy of polycrystals from the multi grain/phase properties involves the fundamental ability to obtain information combining microstructure and crystallographic studies. This inter-correlated analysis of the microstructure and of texture, which is non-random distribution of crystallographic orientations, is called microtexture analysis and it is usually carried out using Electron Backscatter Diffraction (EBSD) technique.

The EBSD technique, also known as Backscattered Kikuchi Diffraction, was first developed by Alam and co-workers in 1954 [1], who described some diffraction patterns and called them “wide-angle back-scattered Kikuchi patterns” in recognition of related diffraction phenomena reported by Kikuchi in the 1920s. It was not until the 1970s however that Venerables and co-workers applied EBSD to metallurgical microcrystallography, paving the way for a more widespread application of EBSD to the materials science in the ensuing years [2].

Rapid developments in both hardware and software in the past 10 years have made EBSD an easy-to-use technique, ideal for the rapid analysis of microstructures in a range of crystalline materials.

3.4.1 Principle of EBSD

This technique allows crystallographic information to be obtained from samples in the scanning electron microscope (SEM).

In EBSD a stationary electron beam strikes a tilted crystalline sample and the diffracted electron forms a pattern on a florescent screen. The specimen tilt angle with respect to the horizontal axis is usually 70° because this provides the highest yield of backscattered primary electrons. The pattern obtained is characteristic of the crystal structure, and orientation of the sample region from which it was generated. The diffracted pattern can be used to measure the crystal orientation, measure grain boundary misorientations, discriminate between different materials, and provide information about local crystalline perfection [2-3].

When the beam is scanned in a grid across a polycrystalline sample and the crystal orientation measured at each point, the resulting map will reveal the constituent grains morphology, orientation and boundaries.

The principal components of an EBSD system are visible in the figure below and they can be listed as follows:

- SEM station: electronic hardware that controls the SEM, including the beam position, stage, focus and magnification;
- Sensitive charge couple device (CCD): video camera interfaced to a phosphor screen for viewing the orientation pattern;
- Camera control/diffraction pattern processor unit;
- Computer and dedicated software to control EBSD experiments analyse the diffraction pattern and process (data processing and pattern indexing) and display the results.

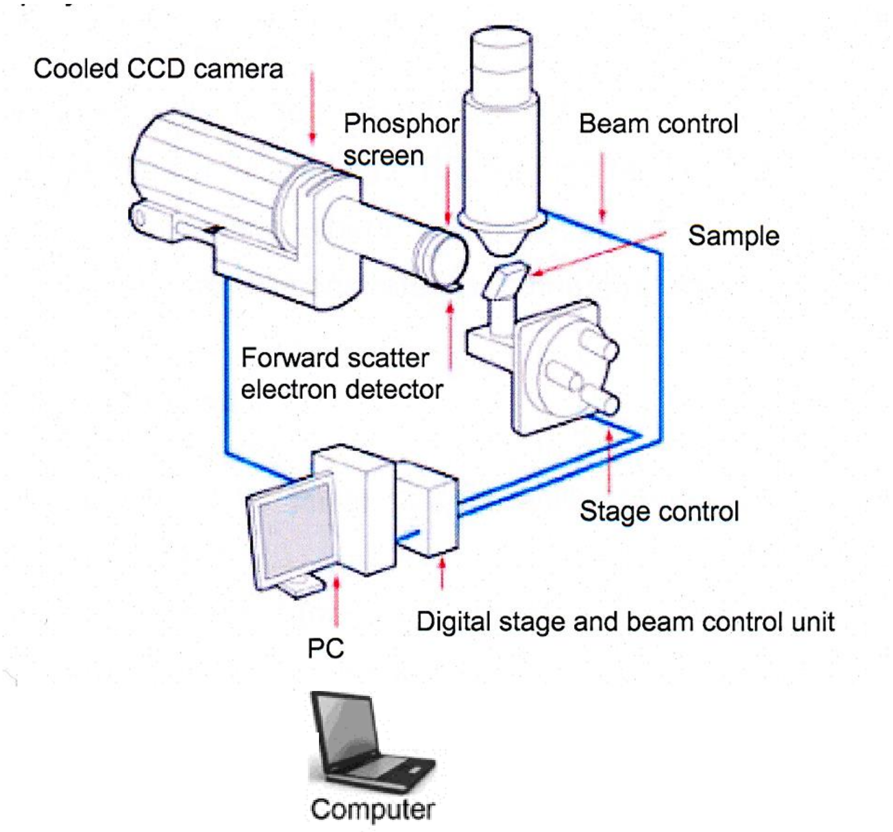

Figure 3.4: Schematic illustration of the components and assembly of a typical modern EBSD system.

3.4.2 EBSD data presentation

The main standard method of representing texture is by means of phase map (PM), pole figures (PFs) and orientation distribution functions.

3.4.2.1 Phase map

The sample population can be processed, displayed and quantified statistically in several ways. The EBSD data processing is usually carried out in two parts: the orientation map, which represents the more pictorial output, and the statistical distribution of the orientations.

Although the most used application of EBSD is for microtexture, this technique can also be used for the identification of the phases that compose the alloy under examination.

The orientation map is a visual portrayal of some orientation related aspect of the microstructure at each sampling point, accompanied by the crystallographic orientation. To compose an orientation map, the electron beam moves automatically in regular steps over a predefined region of stationary specimen, or, alternatively, the beam is kept stationary and the specimen is moved. Figure 3.5 is an illustration of an orientation map.

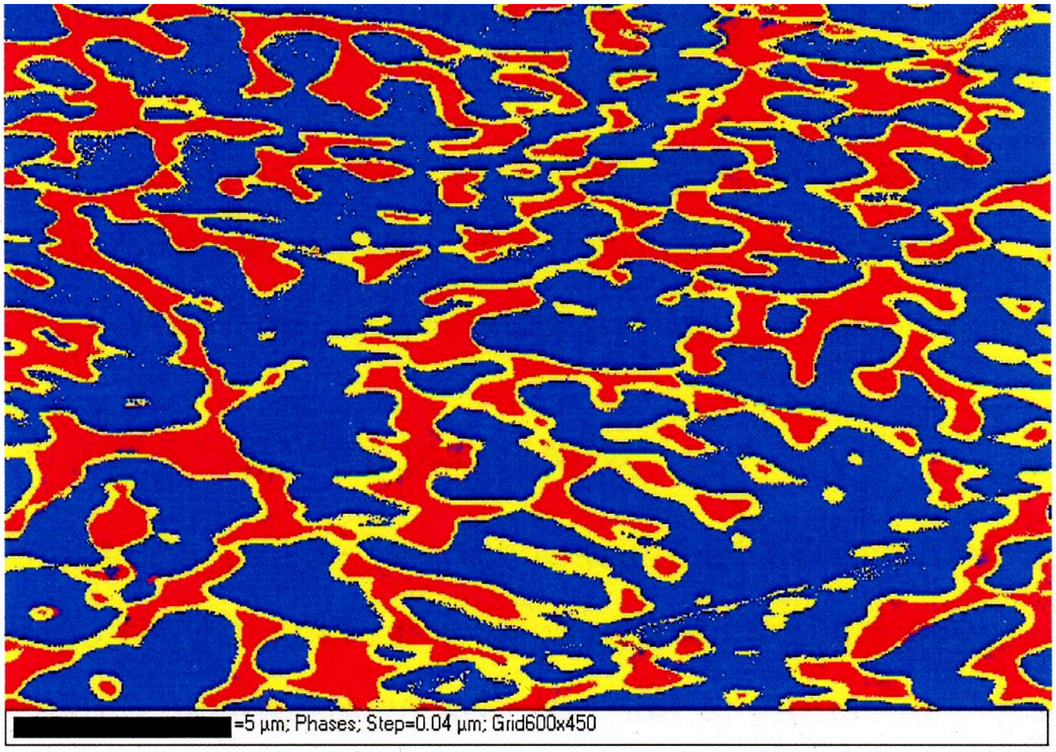

Figure 3.5: Orientation map of the phases which constitute a dual phase material. The zones coloured blue represent phase A; the red ones represent the intermetallic compound or phase B; and the yellow zones are the 'Zero solution' zones. In the left bottom angle the marker and the parameter used, for instance the step and the grid, are also indicated.

3.4.2.2 Pole figure

Another common method of representing a microtexture is a pole figure, which has the advantage that only a single graphic is required to embody the texture information. To construct a pole figure, the direction of the plane normal is projected onto a sphere around a crystallite. The point where the plane normal intersects the sphere is defined by two angles, a pole distance α and azimuthal angle β. The azimuthal angle is measured anti-clockwise from the point X (see Figure 3.6).

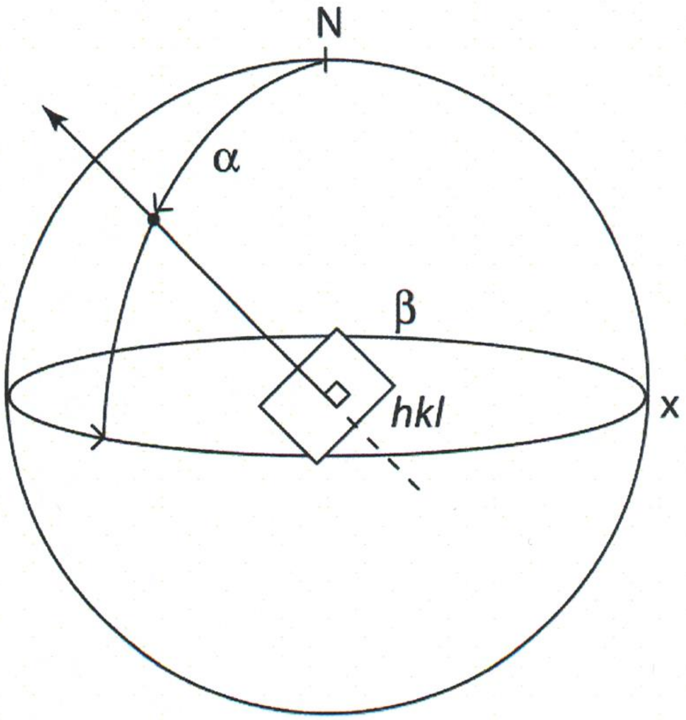

Figure 3.6: The basis of a pole figure showing the plane normal intersecting with the sphere.

As the sphere with its pole density is projected onto a plane, this projection is called a pole figure. A pole figure is scanned by measuring the diffraction intensity of a given reflection with constant 2θ at a large number of different angular orientations of a sample. Microtexture measurement in this thesis is performed on a Sirion 200 Field Emission Gun Scanning Electron Microscope (FEGSEM). A contour map of the intensity is then plotted as a function of the angular orientation of the specimen. The intensity of a given reflection is proportional to the number of (*hkl*) planes in reflecting condition; hence the pole figures gives the probability of finding a given (*hkl*) plane normal as a function of the specimen orientation. If the crystallites in the sample have random orientation, the contour map will have uniform intensity contours. The pole figure contains families of pole derived from all subset points in a data set of individual orientations in the grains of the phases considered.

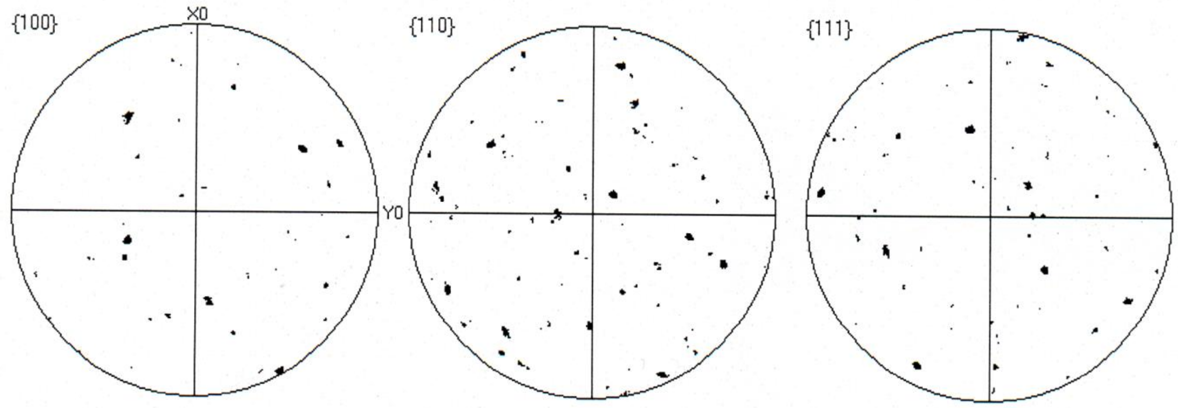

Figure 3.7: Pole figure or stereographic projection from the map of the dispersed phase or phases of the reference materials (for example in the case is Ni_3Al).

3.5 Density functional modelling

An important aspect of density functional theory (DFT) is that, while it is not possible to solve the N-electron Schrodinger equation [4] directly, DFT

[5-6] gives us, in principle, a method to determine the ground state electronic structure of a system. This enables materials engineers and scientists to understand how materials behave under certain physical processes by making it possible to predict important material properties. On the other hand, due to the complexities arising from inhomogeneous nature of material's microstructure, resulting in anisotropic properties, this problem is not trivial and an accurate solution is difficult to obtain.

Most metals used in engineering consist of an aggregate of phases. It is well known that alloy properties are governed by phase content and they depend additively on the ratio and properties of the constituent phases. The main difficulty in predicting material behaviour arises from types, sizes and variations of the phase content due to binary and multicomponent additions which can interact with each other in a non-linear manner to alter the material behaviour.

In the late 1980s and early 1990s, Payne and co-workers [7] developed the CASTEP code for electronic structure calculations. The development made further enhancement difficult to implement, because there were no modular structures or written code specifications on it. More accurate developments and new technologies to redesign CASTEP using a new modular Fortran 90 code were added by a large and disparate number of collaborators and researchers. Due to the new code re-design, new methods and technologies are quickly and easily added to CASTEP, allowing users to rapidly take advantage of such developments. The code can be used either in serial or parallel.

The methodology for electronic structure calculations was implemented in CASTEP by solving a set of one electron Schrödinger (Kohn-Sham) equations using the plane wave pseudopotential approach [7]. The wavefunctions were expanded in a plane wave basis set defined by the use of periodic boundary conditions and Bloch's Theorem. The electron-ion potential is described by means of ab initio pseudo potentials within both norm-conserving [8] and ultrasoft [9] formulations. Energy minimisation schemes were used to obtain, self-consistently, the electronic wavefunctions and corresponding charge density. In particular, the conjugate gradient [7] and density mixing [8-9] schemes were implemented. The robust electron ensemble DFT [10] can also be used for systems with partial occupancies (in particular metals).

Although the total energy is the total quantity, the response of that energy to external influences is extremely important and can lead to further direct comparison with experimental data through the calculation of experimental observables. If the system is perturbed in some way then the total energy can be expanded as a perturbation series. There is wide array of physical properties that then become accessible to us; for instance, when a second order energy is calculated with respect to a given perturbation (see Table 3.1).

CASTEP uses a free form file format so that only the specific commands required for a calculation need to be given. The set-up tab allows you to choose the type and quality of calculations that CASTEP will perform, along with other basic input options such as exchange correlation functional, spin polarisation, and total energy. The value of all input variables have defaults set, with an intelligent selection of the essential parameters such as basis size (plane wave cut off energy) and k- point sets.

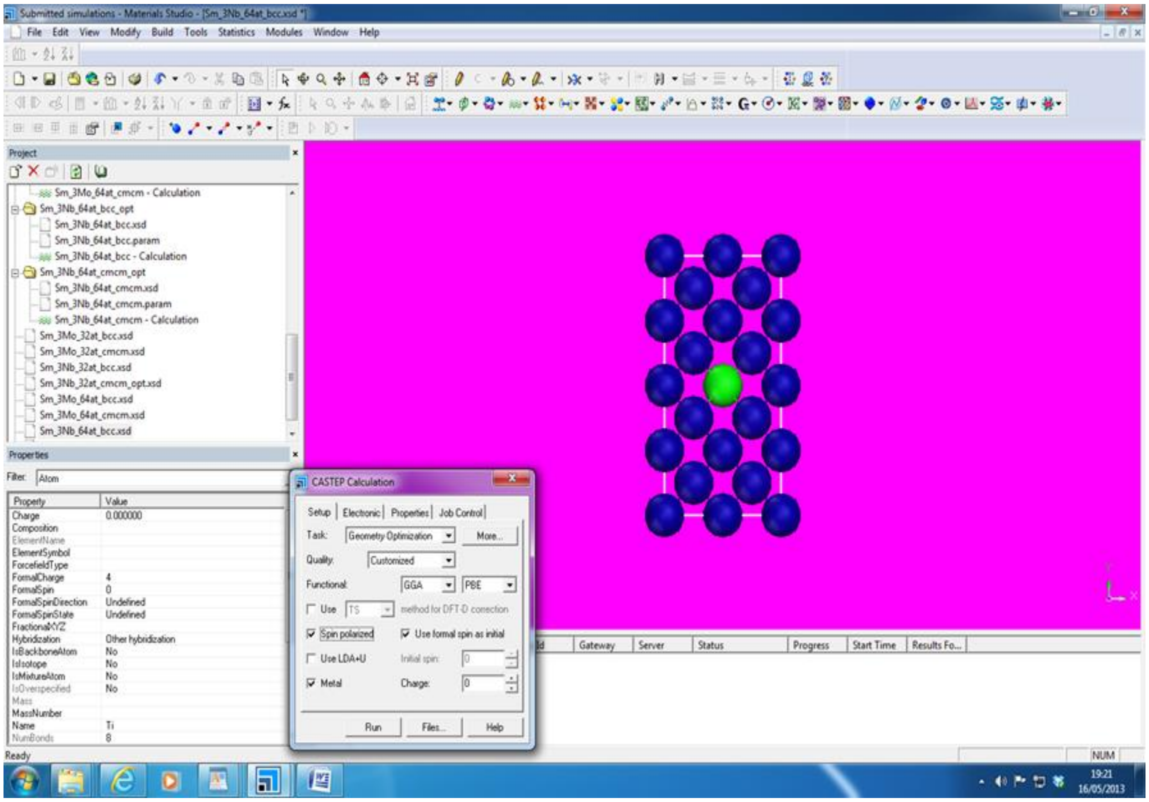

Filter: Atom

Property	Value
Charge	0.000000
Composition	
ElementName	
ElementSymbol	
ForcefieldType	
FormalCharge	4
FormalSpin	0
FormalSpinDirection	Undefined
FormalSpinState	Undefined
FractionalXYZ	
Hybridization	Other hybridization
IsBackboneAtom	No
IsIsotope	No
IsMixtureAtom	No
IsOverspecified	No
Mass	
MassNumber	
Name	Ti
NumBonds	8

Task: Geometry Optimization

Quality: Customized

Functional: GGA PBE

☐ Use TS method for DFT-D correction

☑ Spin polarized ☑ Use formal spin as initial

☐ Use LDA+U Initial spin: 0

☑ Metal Charge: 0

Figure 3.8: Graphical user interface of CASTEP available from Accelrys, Inc. namely the materials studio showing 2D pictorial view of a BCC super cell and run geometry optimisation setup.

The command line running of the code is simple, with an output file summarising the details — such as wave function coefficients and charge densities. This is in addition to the help features.

A graphical user interface is available from Accelrys, Inc.; namely, the materials studio package which can be used to build the initial structure, generate input files, run the calculation, and finally analyse the data (see Figure 3.8). It can be used to create supercells, charge densities, isosurface, to visualise band structures, and to analyse phonon data among other capabilities.

Some of the task and materials properties that can be calculated using CASTEP set-up tab include, but are not limited to, the following:

Total energies: Calculation of total energy, forces, stresses and elastic constants. Electric structure: electric charge densities, orbitals, electrostatic potentials, band structure, total and partial electronic density of states, Milliken population analysis, and optical properties (such as reflective, absorption, refractive index, dielectric, dielectric function) subject to usual band gap considerations. Previously, through the comparison of predictions to demonstrate the convergence by running different and larger simulations with atomic volume between 500 to 5000 Å^3 (16-160 atoms) for different configurations of binary Ti-Nb alloys, we found that an interesting consistency of linearity exists between the number of atoms per unit cell and the total energy (ev), as shown in Figure 3.9. Although most published works on metallic alloys using density functional theory have been based on data from 16 atoms [11-15], the trend from Figure 3.9 suggests that a 64 atoms per supercell adopted in the present study is a good approximation to predict the properties of alloys that is not likely to differ markedly from the actual ones. This volume is also reasonable enough to capture the basic physics of Ti-Mo system.

Geometry: Optimisation of atomic positions and unit cell parameters, either constrained or unconstrained and external pressure and stresses.

Elastic constant: Performs an elastic constant calculation.

Dynamics: Finite temperature molecular dynamics can be performed under various conditions such as constant temperature, energy, volume and pressure.

Properties: Calculates properties based on the results obtained from one of the other tasks; for example, using density functional perturbation theory, phonon frequencies and eigenvectors are calculated, which can be used to give the Gibbs free energy, entropy, enthalpy, Debye temperature, heat capacity and a measurement of phase stability.

Table 3.1: Some examples of perturbation series and physical quantities we can obtain using CASTEP.

Perturbation	**Physical quantity**
Atomic positions	phonons
Electric field	dielectric properties
Magnetic field	NMR
Lattice parameters	elastic constants and related mechanical properties
K-point	Born charges

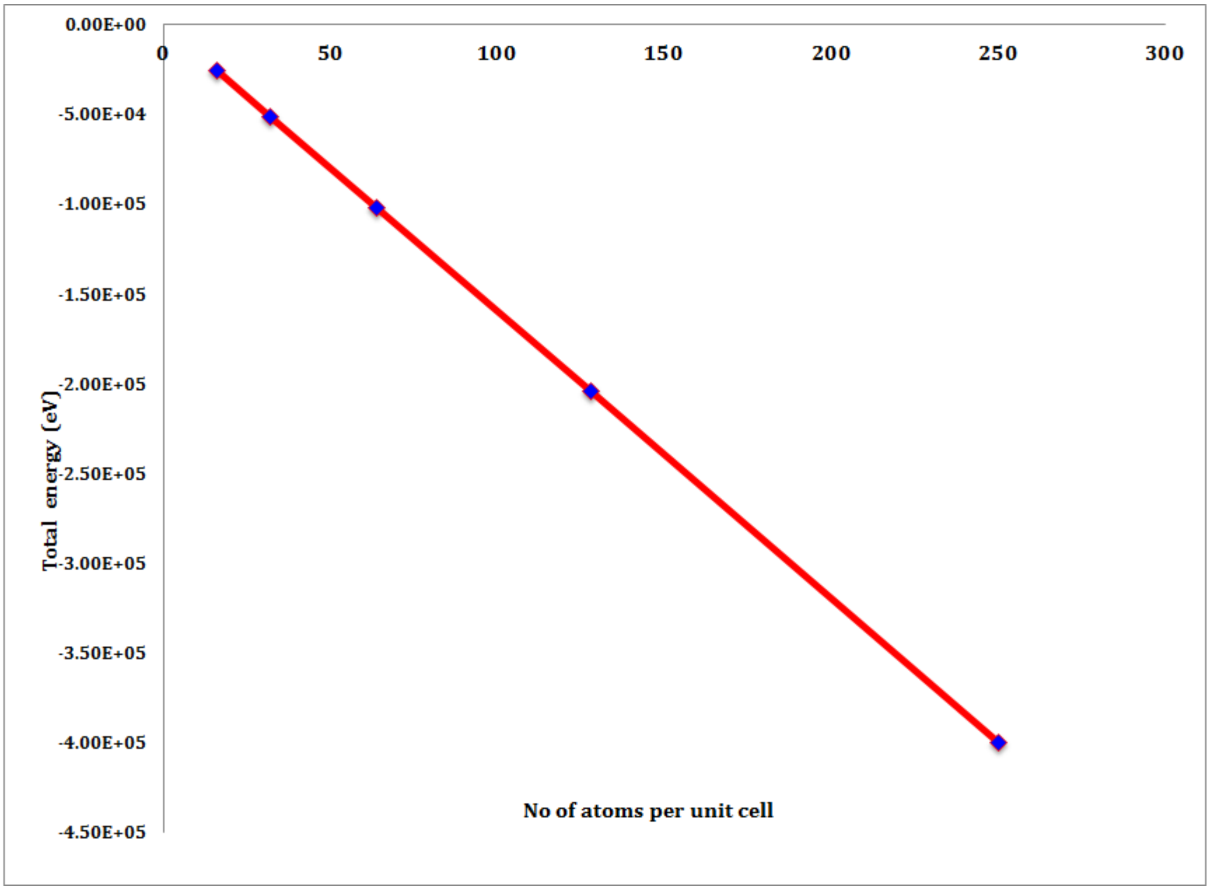

Figure 3.9: Plot of total energy (eV) as a function of number of atoms per unit cell for different configurations of binary Ti-Nb alloys, displaying the trend of relationship between them.

3.6 References

[1] Microtexture determination and its application, 2nd edition — V. Randle — The institute of materials, minerals and mining, Maney Publishing, London UK, 2003.

[2] Channel 5 users manual — HKL technology, 2001.

[3] http://www.ebsd.com/basicsofebsd 1.htp.

[4] Schrödinger E.; Quantisierung als Eigenwertproblem (Erste Mitteilung) Annalen der Physik, (4), 79, (1926), 361-376.

[5] Hohenberg, P., Kohn, W.; Inhomogeneous electron gas. Phys. Rev.136 (1964) B854.

[6] Kohn, W., Sham, L. J.; Self-consistent equations including exchange and correlation effects. Phys. Rev.140 (1965) A1133.

[7] Payne, M. C., Teter, M. P., Allan, D. C., Arias, T. A., Joannopoulos J. D.; Iterative minimization technique for abinitio total energy calculations-molecular-dynamics and conjugate gradient. Rev. Mod. Phys. 64 (1992) 1045-1097.

[8] Kleinman, L., Bystander, D. M.; Efficacious form for modelpsuedopotentials. Phys. Rev. Lett. 48 (1982) 1425-1428.

[9] Vanderbilt, D.; Soft self-consistent equations including exchange eigenvalue formalism. Phys. Rev. B41 (1990) 1425-1428.

[10] Kresse, G., Furthmuller, J.; Efficient iterative schemes for ab initio total energy calculations using a plane wave basis set. Phys. Rev. B54 (1996) 11169-11186.

[8] Alfe, D.; Ab initiomolecular dynamics, a simple algorithm for charge extrapolation. Comp. Phys. Commun. 118 (1999) 31-33.

[10] Marzari, N., Vanderbilt, D., Payne, M. C.; Ensemble dynsity-functional theory for ab initio moleculardynamic of metals and finite-temperature insulators. Phys. Rev. Lett. 79 (1997) 1337-1340.

[11] Chun-Mei Li *et al.*; First principles investigation of the composition dependent properties of Ni2+xMn1-xGa shape memory alloys, Physics. Rev.B 82(2010) 24201-9.

[12] Raabe D. *et al.*: Theory-guided materials design of multi-phase Ti-Nb alloys with bone-matching elastic properties, Materials 7(2012), 3390/1-19.

[13] Ikebata H. *et al.*; First principles calculations for development of low elastic modulus Ti alloys, Phys. Rev B 70 (2004) 174113/1-8.

[14] Dai J. H. *et al*,; Electronic structure mechanism of martensitic phase transformation in binary titanium alloys, Appl. Phys. 112 (2012) 123718/1-9.

[15] Rodriguez A. J., Mailti A., Brito L. J.; Phase transformations and electronic properties in mixed-metal oxides: Experimental and theoretical studies on the behaviour of $NiMoO_4$ and $MgMoO_4$, J. Chem. Phys. 112, (2000) 935; doi: 10.1063/1.480619.

Chapter 4

A Modelling Approach to Property Prediction in Metallic Alloys

4.1 Introduction

The phase transformations which can occur in binary titanium and other 3d (such as Zr and Hf) metals with elements such as Nb, V, Fe, Mo and Cr form an area of exploration for physical–chemical factors of structural stability. This is largely because, while they possess a BCC solid solution (called the β phase) extending over large composition ranges at high temperatures, metastable phases are formed during the decomposition of β phase, which has a marked effect on the physical properties of these alloys. For example: several forms of martensite have been observed in titanium alloys after transformation of the high-temperature BCC form of titanium to HCP (1-9), orthorhombic (9, 10), and FCC (8) or FCT (5, 6) structures.

In the Ti-Mo system specifically, it has been shown that hexagonal martensite is formed in alloys containing up to approximately 4% Mo and that orthorhombic martensite is formed in alloys containing between 4%- 8% Mo (9), which has a space group of Cmcm (No.63) and lattice parameters of a= 3.01Å, b=4.91 Å, and c=4.53 Å. The lattice parameters do, however, vary with alloy compositions [11]. The Ms is below room temperature for alloys that contain greater than 10% Mo and thus remain single-phase BCC on water quenching.

Traditionally, materials scientists have studied the structure of the metals and alloys relying mainly on phase stability phenomenon to account for the material properties. Early studies focused on the explanation of trends in the periodic table, such as the sequence of structures $HCP \rightarrow BCC \rightarrow HCP \rightarrow FCC$ that is observed when going from left to right across the transition metal (TM) series [11-16]. This is a formalism based on the thermodynamic description of trends in terms of energy difference of equilibrium structures as a function of electron per atom, (e/a) or in some literatues as Ne [14]. Following the trend, most theoretical [11-20] and experimental [21-23] studies on the development of engineering alloys that exist in the literature are usually based on the properties of the equilibrium phases such as BCC or HCP.

Interest in the study of complex and metastable phases and their relationship to materials properties has been rekindled by recent developments and an increasing complexity of industrial materials designed to meet the demand for high-tech applications. Such interest requires more than the aforementioned approach. Nevertheless, while there is a huge interest in equilibrium structures such as BCC, FCC and HCP of metals and alloys that are well understood, this specialisation, while no doubt necessary, carries the risk that more complex metastable phases that occur in binary and higher order metals and alloys have been neglected.

It should be noted that complex metallic alloys have come into increasingly widespread use and engineering and scientific interest in these materials is growing continuously. The physical essence of the processes that take place in these alloys is, however, still not well understood. Both an improvement in the mechanical properties of metallic materials and their physical stability are critical to further progress in the field of their research, development and use. It is therefore of great value to further explore the structural relationships of some of these alloys by examining for related phases and their corresponding properties. Ti–Mo alloys are most widely used as superconducting materials, and also find uses in aerospace applications [25, 26], petro-chemical and biomedical industries. It is therefore important that the relative phase stability in this system is understood properly. In titanium and related alloys, there has been a considerable amount of discussion concerning the unique physical and chemical properties of orthorhombic martensitic (α'') phase [25]. The role of α'' phase for the shape memory effect and psuedoelasticity phenomenon, as well as the reduction of Young's modulus for biomedical titanium based alloys, is well known [27-28], but the theoretical information including investigations pertaining to competing phase transformations between $\beta \rightarrow$ martensites (α', α''), thermodynamic stability, mechanophysical and electronic properties with respect to the usual TM structures such as Mo, Nb etc., is unknown. Certainly, this lack of information limits understanding of the general trends in the properties of Ti and other *3d*-TM alloys. This is why we consider orthorhombic martensitic (α'') in the present work a representative example of complex binary phases derived from or combining with the initial BCC structure to form a multiphase alloy.

The present study has three main objectives. The first is a general objective to build theoretical understanding of the metastable orthorhombic (α'') martensitic structure in the Ti-Mo alloy systems. To this end, first principle calculations based on the density-functional theory (DFT) and using the commercial version of Cambridge Serial Total Energy Package (CASTEP code) method will be performed, on the basis of which a detailed analysis of the predicted structural properties will be compared with some experimental data.

The second objective of the work is to study the thermodynamic stability of the orthorhombic (α'') martensitic relative to BCC structure (i.e. the structure from which α'' forms in the Ti-Mo alloy systems) by quenching in alloys. More specifically, we shall first construct and compare a Gibbs free energy ΔG obtained through the structural energy difference (SED) versus ne plot, and then use it to obtain information on the $\beta \rightarrow \alpha''$ phase transformation. Based on this, a microscopic picture of the α'' stability based on the band filling of electron bands will be developed.

The third objective of the work is to use information provided by homogenising the elastic constant BCC and orthorhombic crystal structures in the way described elsewhere [29] to predict the polycrystalline elastic property of the alloy. In this way a good comparison will be made with previous experimental data, and additional insight gained into the stability of the BCC phase in 3d-TM*S* alloy systems.

4.2 Experimental and theoretical methods

4.2.1 Calculation details

All the calculations in this study are based on the electronic density-functional theory (DFT) implemented using the commercial version of Cambridge Serial Total Energy Package (CASTEP code) method [30]. In this code, the Kohn-Sham [31] single electron equation model with periodic boundary conditions and the psuedopotential method as an approximation of the atomic core-valence electron interaction, as well as the electronic wave function with kinetic energy smaller than a specified cut-off energy cut-off, are expanded in a plane wave basis.

The exchange and correlation are treated using the generalised-gradient approximation (GGA) of Perdew, Burke and Ernzerhof (PBE) formalism [32] due to its computational efficiency. The motivation for our choice is that the (PBE) methods are efficient, due to their accuracy in describing the bulk properties of many materials, and flexible enough to describe the random distribution of the impurity of atoms on Ti lattice [28]. The PBE functional is designed to reproduce closely the PW91 results, but the PBE formulation is more robust to guarantee a high level of convergence, cut-off energy of 500 eV and the Methfessel and Paxton [19] Gaussian smearing method with 0.1 eV smearing of the electron levels.

We studied 16 different binary Ti-Mo materials (eight each for orthorhombic (α′′) and body-centred cubic (β) phases). For each structure, tests were carried out using different k-point meshes to ensure absolute convergence of the total energy to within a better than 1.0 meV/atom. For all structures considered, we calculated the total energies as a function of volume while optimising unit cell-external degree(s) of freedom (i.e. the unit-cell shape) and unit cell-internal degree(s) of freedom (i.e. Wyckoff positions) as permitted by the space-group symmetry of the crystal structure. Such structural optimisations were iterated until the Hellman–Feynman forces were less than 4 meV/Å in magnitude, ensuring a convergence of the energy with respect to the structural degrees of freedom to better than 1 meV/atom (~0.1 kJ/mol). In addition, all calculations were performed using the ‘‘accurate’’ setting within CASTEP code to avoid wrap-around errors. With the chosen plane-wave cut-off and k-point sampling, the reported formation energies are estimated to be converged to a precision of better than 2 meV/atom.

For alloying systems, one titanium atom was substituted by an alloying atom in each supercell, and the relative concentrations of alloying elements in the systems ranges from 3 to 23 at.%. A random distribution of the chemical species over the sites of the structures has been considered and studied by replacing Ti atoms by Mo atoms (as illustrated in Figures 4.1 and 4.2), representing different Mo concentrations for BCC and orthorhombic structures respectively.

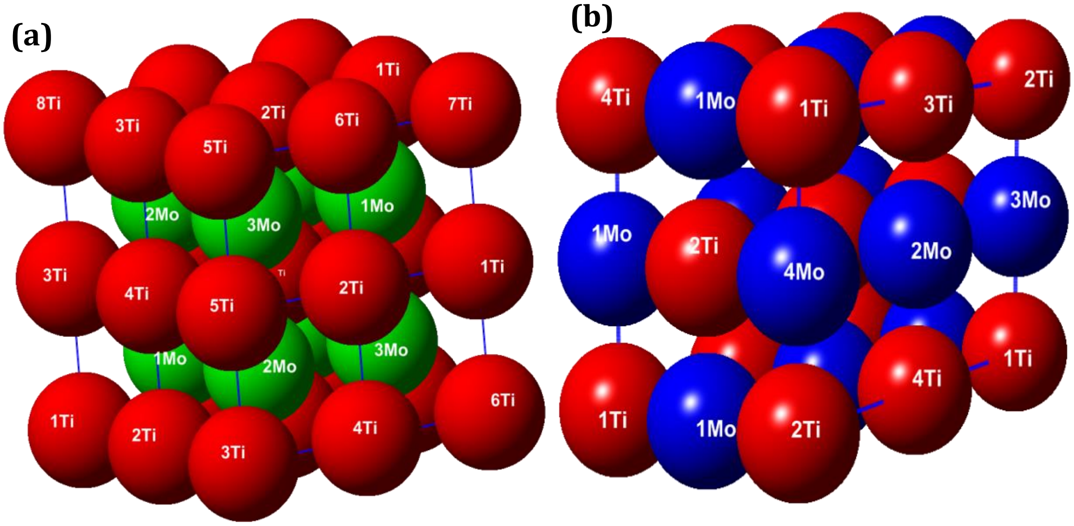

Figure 4.1: The 4x4 32 atomic supercell of (a) a BCC crystal structure; and a 2x2x2 32 atomic supercell of (b) an orthorhombic martensitic α″ crystal structure both from the closed packed [111] plane of (Ti-Mo) used in the calculation, with the atoms numbered (1-6) variably in the various atomic layers (depicted in two distinct colours for Ti and Mo in the two supercells by large spheres for the sake of clarity) in the [111]β and [0001] α″ directions.

The equilibrium phase boundaries and the phase transformations which occur in titanium systems can be rationalised using a thermodynamic approach. In particular, some insights can be gained into metastable transformations which can be expected where experimental data are lacking. It is known that the orthorhombic crystal structure is not stable in molybdenum, niobium and vanadium. The fundamental quantity expressing the thermodynamic stability of an alloy is the alloy formation energy. The formation energy (per atom) of α″ and β phases in binary Ti-χMo(where χ= 3,6,8,9,10,14,18,23) in configuration σ = BCC/HCP is defined as:

$$E_{\mathrm{Form}}^{(\mathrm{Ti_xMo_{1-x}})} = \frac{E_{\mathrm{tot}}^{\mathrm{bulk}}(\mathrm{Ti_xMo_{1-x}})}{\mathrm{N}} - \mathrm{x}\mu^{\mathrm{Ti}}\left(E_{\mathrm{N(i=1)}}^{\mathrm{Ti}} - \left(1 - x^{Ti}\right).\mu^{\mathrm{x}}(E_{N(i=1)}^{Mo})\right) \qquad (4.1)$$

Here, N is the total number of atoms per supercell, $E_{\mathrm{tot}}^{0}(\mathrm{Ti_xX_{1-x}})$ is the first principle calculated total energies of the respective alloys; μ is the chemical potential of the element Ti or Mo in its corresponding bulk phase, respectively, and x the alloy composition. In the above definition (Eqn.4.1), the alloy is thermodynamically stable for $\mathrm{E}_{\mathrm{T}}^{0} < 0$. From the point of view of thermodynamics, lower formation energy means better stability of a particular crystal structure over another.

Past studies [20-23] revealed deformation of metastable β Ti alloys can lead to the formation of stress-induced martensites (SIMs), and the reversion is the basis for the shape memory and pseudoelastic effects. **ΔG** is more descriptive than the total energy, which includes a large contribution from states that do not play a role in bonding. In order to gain some insight into the activation energy for SIM transformations in β Ti-Mo alloy, we performed total energy calculation using DFT-GGA implemented on the CASTEP code to determine the free energies **ΔG** of α′′ and β structures for Ti-Mo using Eqns. 4.2 and 4.3 respectively.

$$G^{E}_{\alpha''}(\mathrm{x, Ti}) = \langle (1-x)G^{Ti}_{\alpha''} + \mathrm{x}G^{Mo}_{\alpha''} + G^{E}_{\alpha''} + \mathrm{RT} * \mathrm{xInx} + (1-\mathrm{x})\mathrm{In}(1-\mathrm{x})\rangle \ (4.2)$$

$$G^{E}_{\beta}(\mathrm{x, Ti}) = \langle (1-x)G^{Ti}_{\beta} + \mathrm{x}G^{Mo}_{\beta} + G^{E}_{\beta} + \mathrm{RT} * \mathrm{xInx} + (1-\mathrm{x})\mathrm{In}(1-\mathrm{x})\rangle \, . (4.3)$$

Here $G^{Ti}_{\beta/\alpha''}$,x$G^{Mo}_{\beta/\alpha''}$, $G^{E}_{\beta}(\mathrm{x, T})$ and $G^{E}_{\alpha''}(\mathrm{x, T})$ represents the excess free energies of mixing in terms of the pure β / α′′ titanium element, pure β / α′′ Molybdenum element and the bulk with different phase configurations, but with the same concentration of Ti-Mo system and R=(8.314)/KMol. At equilibrium in the two phase (β + α′′) region of the phase diagram:

$$\frac{\delta G_\alpha}{\delta x}\Big|_{X_{\alpha''}} = \frac{\delta G_\beta}{\delta x}\Big|_{X_\beta} \qquad (4.4)$$

For a given alloy, $x_{\alpha''}$ and x_β are the atomic fractions of solute at the limit of solubility. This allows the determination of free energy of any composition.

For many applications, the study of elastic response is of critical importance. Not only does it provide the measures of the deformations under loading, but from a microscopic viewpoint the elastic constants provide an accurate measure of the strength of the average interatomic bonding and therefore insight into related expected such as hardness [3, 25].

In the present study, to obtain the integral elastic response of multiphase polycrystalline samples we followed the procedure originally applied by Zeller and Dederichs *et al.* [33] to determine elastic properties of single phase polycrystals with cubic symmetry. This work was later generalised and further extended by Midada and Basu *et al.* [33,34] and by Raabe *et al*. [20] to multiphase composites to determine: (i) the elastic single constants, and (ii) the volume fraction of the components within a self-consistent *T*-matrix solution for the effective medium. The T-matrix approach is based on the multiple scattering theory. It can be reviewed in terms of a macroscopic homogeneous effective medium consisting of microscopic fluctuation characterised by an effective stiffness C_{ijkl} defined by:

$$\langle \sigma_{ij}(\boldsymbol{r}) \rangle = C_{ijkl} \langle \epsilon_{kl}(\boldsymbol{r}) \rangle \qquad (4.4)$$

Here, C_{ijkl} is the local elastic constant tensor with $\langle \sigma_{ij}(\boldsymbol{r}) \rangle$ and $\langle \epsilon_{kl}(\boldsymbol{r}) \rangle$ as the local stress and strain field at a point **r**, respectively, and the angular brackets denote ensemble averages. A repeated index implies the usual summation convention. The effective stiffness C_{ijkl} is defined by:

$$\langle \sigma_{ij}(\boldsymbol{r}) \rangle = C^{*}_{ijkl} \langle \epsilon_{kl}(\boldsymbol{r}) \rangle \tag{4.5}$$

Since the aggregate represents a body in equilibrium, $\sigma_{ij}(r)|j = 0$, where $|j = \partial/\partial r_j$ and the local elastic constant tensor can be now be decomposed into an arbitrary constants part (C^{o}_{ijkl}) and a fluctuating part — $\delta C(\boldsymbol{r})$.

$$C_{ijkl}(r) = C^{o}_{ijkl} + \delta C_{ijkl}(r) \tag{4.6}$$

As shown in [33], an integral part of Eqn. 4.6 is the interactive equivalent solution representing the resulting local strain ϵ distribution (in a short notation) as

$$\epsilon = \epsilon^{0} + GT\epsilon^{0}, \tag{4.7}$$

Here, ϵ^{0} and G are the strain and modify Green's function of the medium defined by C^{O}, and the T-matrix is given by:

$$T = \delta C(1 - G\delta C)^{-1} \quad , \tag{4.8}$$

Here, $\boldsymbol{I}$ is equivalent to the unit tensor. Combining Eqns. 4.2 and 4.4, we get

$$C^{*} = C^{0} + \langle T \rangle / (1 + \langle GT \rangle)^{-1} \tag{4.9}$$

Although Eqn. 4.6 constitutes an exact solution for C^{*}, finding the exact solution of $\langle T \rangle$ and $\langle GT \rangle$ for realistic cases is impossible. By neglecting the intergranular scattering that may occur in some cases in the form of grain to grain position orientation correlation function however, the T-matrix can be written in terms of single-grain t –matrix (t_{α}) for each grain α

$$T \approx \textstyle\sum_{\alpha} t_{\alpha} = \tau. \tag{4.10}$$

where

$$t_{\alpha} = \delta C_{\alpha} + \delta C_{\alpha} G t_{\alpha} = \delta C_{\alpha}(1 - G\delta C_{\alpha})^{-1} \tag{4.11}$$

with

$\sum_{\alpha} \delta C_{\alpha} = \delta C = C - C^{0}$

Inserting Eqn. 4.7 into 4.6 leads to:

$$C^{*} = C^{0} + \langle \tau \rangle (1 + \langle G\tau \rangle)^{-1} \qquad (4.12)$$

For single phase polycrystal, the self–consistent solution of Eqn. 4.12 can be obtained by choosing a C^{*}that satisfies:

$$\langle \tau \rangle = 0 \qquad (4.13)$$

For a multiphase polycrystal, a solution to Eqn. 4 can be found by evaluating the volume fraction and τ of each phase i $(u^{2}\ and\ \tau^{2}$) respectively [33] via

$$\langle \sum_{i} v^{2} \tau^{2} \rangle = 0 \qquad (4.14)$$

The application of the method to both single-phase aggregates and multi-phase composites relevant to Ti-Mo alloys is as follows.

4.2.1.1 Single-β phase aggregate

For a single-phase polycrystal with cubic symmetry [33, 34] to the following expression for B^{*} and μ^{*}

$$B^{*} = B^{o}$$

$$8\mu^{*3} + \left(9B_{0} + 4C^{''}\right)\mu^{*2} - 3C_{44}(B_{O} + 4C^{''})\mu^{*} - 6B_{O}C_{44}C^{''}=0 \qquad (4.15)$$

In Eqn. 4.12, three independent single crystal elastic constants — C_{11}, C_{12}, C_{44} — define the single crystal bulk modulus $B^{o} = (C_{11}^{0} + 2C_{12}^{O})/3$, the tetragonal shear modulus $C^{'} = (C_{11-}\ C_{12})/2$ and trigonal shear modulus, C_{44}, $\mu^{*} = C_{44}^{*} = \mu^{0} + \frac{\langle \tau_{44} \rangle}{1+G_{44}\tau_{44}}$.

For polycrystals with orthorhombic symmetry, Eqn. 4.10 and 4.11 are reduced to a set of coupled equations for B^* and μ^* .

$$0 = 9(K_V - B^*) + 2\beta(d - c + e) + 3\beta^2\Delta^{'} \qquad (4.16)$$

$$0 = \frac{a - b + \beta(2d - 2c - e) + 3\gamma(d - c + e) + \eta\beta\Delta^{'}}{1 - \alpha\beta - 9\gamma(k_v - B_0) + \beta(\beta + 2\gamma)(c - d) - 2e\beta\gamma - \frac{1}{3}\eta\beta^2\Delta^{''}} + 3\left(\frac{C_{44} - \mu^O}{1 - 2\beta(C_{44} - \mu^O)} + \frac{C_{55} - \mu^O}{1 - 2\beta(C_{55} - \mu^O)} + \frac{C_{66} - \mu^O}{1 - 2\beta(C_{66} - \mu^O)}\right)$$

(4.17)

where

$$9K_v = C_{11} + C_{22} + C_{33} + 2(C_{12} + C_{13} + C_{23}), \qquad (4.18)$$

$$B = {}^1/_3\,(C_{11} + 2C_{12}) \qquad \mu^* = C_{44}$$

(4.19)

$$\gamma = {}^1/_9\,(\eta - 3\beta) \qquad (4.20)$$

$$a = \delta C_{11} + \delta C_{22} + \delta C_{33};\ b = \delta C_{12} + \delta C_{13} + \delta C_{23}; \qquad (4.21)$$

$$c = \delta C_{11}\delta C_{22} + \delta C_{11}\delta C_{33} + \delta C_{22}\delta C_{33};\ d = \delta C_{12}^2 + \delta C_{13}^2 + \delta C_{23}^2\ ; \qquad (4.22)$$

$$e = \delta C_{12}\delta C_{13} + \delta C_{12}\delta C_{23} + \delta C_{13}\delta C_{23} - \delta C_{11}\delta C_{23} - \delta C_{22}\delta C_{13} - \delta C_{33}\delta C_{12}\ ; \qquad (4.23)$$

$$\Delta^{'} = \delta C_{11}\delta C_{22}\delta C_{33} + 2\delta C_{12}\delta C_{13}\delta C_{23} - \delta C_{11}\delta C_{23}^2 - \delta C_{22}\delta C_{13}^2 - \delta C_{33}\delta C_{12}^2;$$

(4.24)

$$\delta C_{11} = C_{11} - C_{11}^O = C_{11} - K^0 - \tfrac{4}{3}\mu^0;\ \delta C_{22} = C_{22} = C_{22} - K^0 - \tfrac{4}{3}\mu^0; \qquad (4.25)$$

$$\delta C_{33} = C_{33} - K^0 - \tfrac{4}{3}\mu^0;\ \delta C_{12} = C_{12} - C_{12}^O = C_{12} - K^0 + \tfrac{4}{3}\mu^0; \qquad (4.26)$$

$$\delta C_{13} = C_{13} - K^0 + \tfrac{4}{3}\mu^0;\ \delta C_{23} = C_{23} - K^0 + \tfrac{4}{3}\mu^0; \qquad (4.27)$$

$$\beta = \frac{-3(B^* + 2\mu^*)}{5\mu^*(3B^* + 4\mu^*)}, \qquad (4.28)$$

$$\eta/3 = -1/3B^* + 4\mu^*, \qquad (4.29)$$

$$C_{66} = (1/2)(C_{11} - C_{12}) \tag{4.30}$$

and orthorhombic symmetry has nine of the single crystal elastic constant; namely, $C_{11}, C_{22,}C_{33}, C_{44}\ C_{55}, C_{66}C_{12}, C_{23}$ and C_{13} .

4.2.1.2 Multi-phase (β/α″) aggregate

The elastic constants of a multi-phase polycrystal can be determined directly by coupling 4.10 for τ_{44} and the $(\tau_{11} + 2\tau_{12})$ components of the T-matrix. For materials with cubic symmetry, the equation is defined by:

$$5\tau_{44} = \left(\frac{1}{C_{11}-C_{12}-\tilde{\mu}^*}^{-\beta}\right)^{-1} + 3\left(\frac{1}{C_{44}-\tilde{\mu}^*}^{-2\beta}\right)^{-1} \tag{4.31}$$

$$\tau_{11} + 2\tau_{12} = \frac{3(C_{11}+2C_{12})-9\tilde{B}^*}{3-(C_{11}+2C_{12})-3\tilde{B}^*} \tag{4.32}$$

where β is defined in Eqn. 4.25 with $\tilde{\mu}^*$ and $\tilde{B}^*$ replacing μ^* and B^*. For materials with orthorhombic symmetry, the equation reads:

$$15\tau_{44} = \frac{a - b + \beta(2d - 2c - e) + 3\gamma(d - c + e) + \eta\beta\Delta'}{1 - \alpha\beta - 9\gamma(K_v - \tilde{B}_0) + \beta(\beta + 2\gamma)(c - d) - 2e\beta\gamma - \frac{1}{3}\eta\beta^2\Delta''} + 3\left(\frac{C_{44} - \tilde{\mu}^O}{1 - 2k(C_{44} - \tilde{\mu}^O)} + \frac{C_{55} - \tilde{\mu}^O}{1 - 2k(C_{55} - \tilde{\mu}^O)} + \frac{C_{66} - \tilde{\mu}^O}{1 - 2\beta(C_{66} - \tilde{\mu}^O)}\right)$$

(4.33)

$$\tau_{11} + 2\tau_{12} = \frac{9(K_v - \tilde{B}^0) + 2\beta(d - c + e) + 3\beta^2\Delta'}{3\left[1 - \alpha\beta - 9\gamma(K_V - \tilde{B}^0) + \beta(\beta + 2\gamma)(c - d) - 2e\beta\gamma - \frac{1\eta\beta^2\Delta'}{3}\right]}$$

(4.34)

Here, β is defined in Eqn. 4.33, η is defined in 4.34, and Δ′ in Eqn. 4.33. Here, again $\tilde{\mu}^*$ and $\tilde{B}^*$ replaces μ^* and B^* in the equations for β, η, and Δ'.

4.2.1.3 Homogenised Young's modulus and Poisson's Ratio

As soon as $\tilde{\mu}^*$ and $\tilde{B}^*$ have been determined, the homogenised Young's modulus $(\tilde{Y})^*$ and Poisson's ratio $(\tilde{\eta})^*$ for (an elastically isotropic) polycrystal can be determined using standard elasticity relationships. The homogenised polycrystalline Young's is calculated using:

$$\tilde{Y}^* = \frac{9\tilde{B}^*\tilde{\mu}^*}{3\tilde{B}^* + \tilde{\mu}^*} \qquad (4.35)$$

— and the homogenised polycrystalline Poisson's ratio is calculated using

$$\tilde{\mu}^* = \frac{3\tilde{B}^* - 2\tilde{\mu}^*}{3(2\tilde{B}^* + \tilde{\mu}^*)} \qquad (4.36)$$

4.3 Experimental methods

4.3.1 Materials

In order to compare the prediction with experimental data, five different compositions of Ti-Mo alloys were made. The alloys were prepared from 99.9% pure titanium and pure molybdenum in an electric arc-melter under an argon atmosphere into buttons containing approximately 10 grams, at the Department of Materials Science and Engineering University in the United Kingdom. (The actual chemical compositions have been summarised in Table 4.1, and all compositions are in atomic percentage — hence percentage will be mentioned instead). The furnace was equipped with a water-cooled copper crucible. The temperature of the electric furnace amounted to about 3000^{0}C, while the melt was at the electrode centre-hold peak temperature that is above

2050^0C in order to ensure complete dissolution of the solid Ti and Mo metals.

To ensure optimal chemical and structural homogeneity, each button was remelted and turned over six times in order to eliminate dendritic structure, and the final ingot was cast into a cylindrical sample of ≈90 mm in length and 8mm in width. This led to rapid solidification and suppression of dendritic formation. The copper mould had a temperature of about 20^0C, which led to rapid solidification and suppression of dendritic formations. All the cast samples were subjected to homogenisation in quartz tubing at 1200°C in an argon atmosphere for five hours in to remove microsegregation. These samples were quenched in water. These samples were only superficially contaminated. Before characterisation of the microstructure, the surfaces were cleaned by mechanical polishing followed by electropolishing in a solution of five glacial acetic acid and acetone, since Ti alloys undergo strong chemical reaction with oxygen,

Table 4.1: Nominal chemical composition of Ti-(6-23) Mo alloys (unit: atomic %).

Alloys	Mo	O	N	Ti
Ti-6Mo	6.3	0.07	0.013	bal.
Ti-10Mo	10.2	0.05	0.005	bal.
Ti-14Mo	14.16	0.06	0.007	bal.
Ti-18Mo	18.08	0.07	0.002	bal.
Ti-20Mo	20.12	0.09	0.002	bal.
TI-23Mo	23.3	0.08	0.005	bal.

4.3.2 X-Ray measurements and Microstructure analysis

Phase constitution was investigated using XRD diffuse scattering measurements at room temperature with monochromatic CuK and radiation diffracted from a bent silicon crystal cut to the (111) orientation. The detecting assembly consisted of a proportional counter and a pulse height analyser arranged to eliminate the one-third wavelength of the white radiation (the one half component was eliminated by the silicon crystal), the cosmic background and the fluorescence radiation from titanium. Readings were recorded continuously on a horizontal spectrometer with the counter rotating at 0.25^0 in 2Θ/min, and measurements were made from 10 to 100^0 in 2Θ. Flat samples were used and the geometry of the system satisfied the usual focussing condition.

For the quantitative phase, an analysis was performed with an X'Pert Highscore software package. Chemical etching was done for optical microscopy using a solution of 15% HCl, 8% HNO3 and 77% H2O (distilled water). The microstructure was cross examined using electron backscatter diffraction (EBSD) after grinding on 400, 600, 1200 and 2400 paper with subsequent use of 6μm (35min), 3μm (20min), and 1μm (15min) polishing.

4.3.3 Measurement of modulus of elasticity

This basic material property is of interest in many manufacturing and research applications and is related to the atomic bonding of the materials. In the case of biomaterials for load bearing applications, the elastic modulus is an important parameter. The stiffness mismatch between implant material and surrounding bone leads to ‘stress shielding’ of the bone. Higher stiffness or Young’s modulus of the implant will result in a greater amount of bone loss, bone fracture and loss of bone interface. Loss of bone due to stress shielding effects also makes revision surgeries more difficult. Finite element analysis has suggested that a low elastic modulus hip prosthesis can stimulate better bone growth by distributing the stress to the adjacent bone tissue [20]. The elastic modulus of the materials can be determined by different methods, such as ultrasonic technique.

Velocity of the ultrasonic waves in a solid medium is directly related to the elastic properties and density of the material. The elasticity of the material delays the transmission of wave and introduces a time delay, i.e. a phase lag. When the frequency of the wave is higher than the audible range, it is called elastic wave or ultrasound. Two types of vibration-induced deformation resulting in compression or shear are generally possible in an infinite medium. These are associated with two modes of elastic wave propagation, i.e. longitudinal waves, where particles are displaced along the direction of propagation and transverse or shear waves, where the particles are displaced perpendicular to the direction of propagation. The velocity of propagation of the elastic waves in a body is characteristic of the material [32].

Ultrasonic waves are generated in the material by a transmitter oscillating at the desired waveform and frequency, with collection by a detector. Ultrasonic velocity changes have been determined by time-of-flight measurements using Olympus 6.2 ultrasonic equipment. The relationships between ultrasonic velocity and the elastic properties of materials are given below [33–35].

Young's modulus (E) is expressed as:

$$E = \frac{\rho V_S^2 (3V_L^2 - 4V_S^2)}{V_L^2 - V_S^2} \tag{4.37}$$

Shear modulus (G) is the ratio of shearing stress τ to shearing strain γ within the proportional limit of a material and is expressed as:

$$G = \rho V_S^2 \tag{4.38}$$

Poisson's ratio υ is the ratio of transverse contraction strain to longitudinal extension strain in the direction of stretching force and is expressed as:

$$\upsilon = \frac{\left(\frac{1}{2}\right)(V_L^2 - 2V_S^2)}{V_L^2 - V_S^2} \tag{4.39}$$

In the above set of equations, *V*L and *V*S are the ultrasonic longitudinal and shear wave velocities, respectively, and ρ is the density of the material. The elastic modulus of the samples was measured by ultrasonic method on an ultrasonic velocity gauge, Olympus 62, UK. A normal incident probe (model M110, 5MHz) and a shear probe (model V221, 5MHz) were used for the measurement of normal and shear velocities of the wave, respectively. The density of the samples was measured using an automatic meter; for each composition at least five samples were measured.

4.4 Results and discussion

4.4.1 Structure and interatomic bond distances

4.4.1.1 Definition and crystallographic considerations

The orthorhombic α′′ phase can be described as a type of martensitic structure formed by the stretching of the BCC lattice along two of its orthogonal pairs when the constraints to form hexagonal or body-centred cubic structures cannot be met. In essence there is a contraction of "c" axis and stretching of “a" and "b" axes with the collapsing of the inner atoms into the same plane with distinct angles a, b and c. This permits a continuous transformation of α′′ → β transformation, as the stability of the transforming matrix is increased. The atomic positions are (0, y, 1/4), (0,$\bar{y}$, 3/4), (1/2, y+1/2, 1/4) and (1/2, $\bar{y}$+1/2, ¾). In Figure 4.2 we see a partial view of the two structures along the “c” axis of the unit cell, further illustrating the transformation of both phases. The orientation relationship between the original β and the sheared α′′ orthorhombic phase has been established approximately as (0110) β|| (001)α″ and [111]β|| [101]α″.

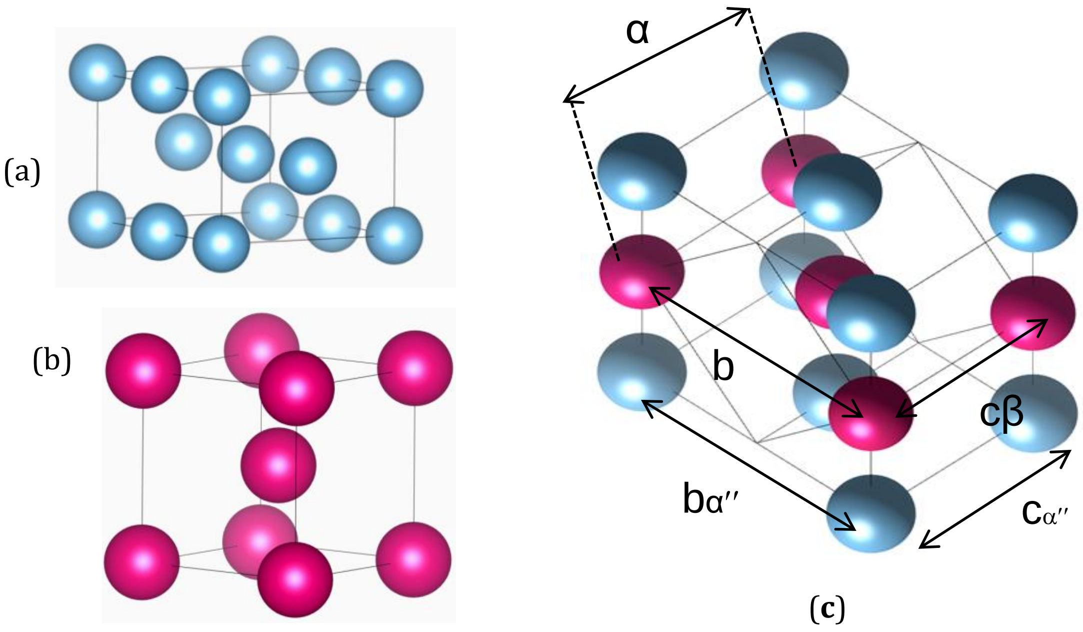

Figure 4.2:(a) Unit cell of (a) orthorhombic α′′ (b) BCC phase; and (c) scheme of the geometrical relations between the [001] projection of orthorhombic α′′ and BCC β phases, the atoms that are involved in the formation of the BCC phase are shown in red filled circles while the orthorhombic corner atoms are blue open circles.

4.4.1.2 Symmetry and bonding strength/length of α′′ and β phase

Ti-Mo is a compound based on elements in group IV and V of the periodic table. As Mo (2.16) is significantly more electronegative than Ti (1.54), the Ti-Mo bond is partially ionic. In effect, one of the main differences in the crystal structures of the BCC (β) and α′′ phases of Ti-Mo might be the changes in the interatomic bond distances with alloying additions. We performed ab initio calculation of the total energy and electronic structure in the present work using the DFT-GGA method [30, 32, 33] to determine the interatomic bond distances of the metastable α′′ and stable β phases for Ti-χMo alloys (where χ= 3, 6, 8, 10, 12, 14, 18) for a system with the external pressure P=0. Indeed, Table 4.1 shows that in the three interatomic bond lengths (IBLs) of the α′′ and β phases, two atomic types can be identified. The first corresponds to metal atoms that occupy mixed Ti-Mo-Ti or Mo-Ti-Mo rings. The second type includes metal atoms that are in pure Mo-Mo or Ti-Ti rings. Implicitly, Mo atoms can form two types of bonds: those that bridge the chain of rings and have only two Ti neighbours, and those that form part of the rings and have three or four neighbours. Within the rings, one can have metal bonds that are either parallel or perpendicular (Ti-Mo, or Mo-Mo, Ti-Ti). Essentially, one has a stack or column of three membered titanium-molybdenum rings.

From Table 4.1 (α′′ phase), we can see that the coordination of Mo-Mo (2.770 Å) is substantially longer than typical Mo-Mo bond length (2.725 Å) [37]; while in the Mo-Mo bond, distances in β-Ti-Mo are close enough to allow substantial Mo-Mo interactions. The indication of non-Mo-Mo bond interaction at Ti-3% and Ti-6% as observed in Table 4.1 can be ascribed to seemingly strong Ti-Ti bonds in the lean Mo concentration range [38] (see Table 4.1). These strong Ti-Ti interactions disappear, however, when the Mo-Mo distances are abridged to produce the β-phase.

Table 4.2: The ratios between interatomic bond lengths (IBLs) of α″ and β phases for Ti-Mo calculated by DFT-GGA calculations.

Initial crystallographic dimensions (Å)

$a_{\beta} = 3.2$ $a\alpha'' = 3.01$ $b\alpha'' = 4.91$ $c\alpha'' = 4.53$

Alloys [at.%]	$\frac{d_{Ti-Ti}}{x''}$	$\frac{d_{Ti-Ti}}{\beta}$	$\frac{d_{Ti-Mo}}{x''}$	$\frac{d_{Ti-Mo}}{\beta}$	$\frac{d_{Mo-Mo}}{x''}$	$\frac{d_{Mo-Mo}}{\beta}$
3	2.8679	2.8679	2.6948	2.6281	-	-
6	2.8733	2.8833	2.7029	2.6945	-	-
8	2.875	2.8750	2.7156	2.7156	2.7704	2.7704
10	2.8769	2.8799	2.7135	2.6848	2.5650	2.7435
12	2.881	2.8721	2.7006	2.7006	2.7870	2.7370
14	2.8819	2.8690	2.6971	2.6971	2.7084	2.7084
18	2.882	2.8679	2.7007	2.7007	2.6949	2.6949

In Figure 4.3, we plot the interatomic bond distances (IBD) of Ti-Ti for α″ and β phases as a function of compositions. For the α″ structure (black dots), we can see from figure 4.3 that the Ti-Ti bond distances in the α″ crystal structure increased in the lean Mo alloy where the occurance are highly probable, but were mainly unchanged in high Mo region. In the context , the distortion of β phase leading to α″ orthorhombic martensitic structure in the lean Mo region in Ti-Mo system can be interpreted as a way of keeping the Ti-Ti bond distance unchanged, in spite of the fact that the lattice parameter of the α″ structure varies with composition. A possible explanation of this result has been proposed [38], suggesting that certain sites might be fully occupied by Group 1V atoms, which due to seemingly strong Ti-Ti bonds keep the d_{B-B} in Ti alloy identical to that of pure elements [40]. They found that the Ti atoms are distributed amongst the A-type and B type sites in an essentially random fashion.

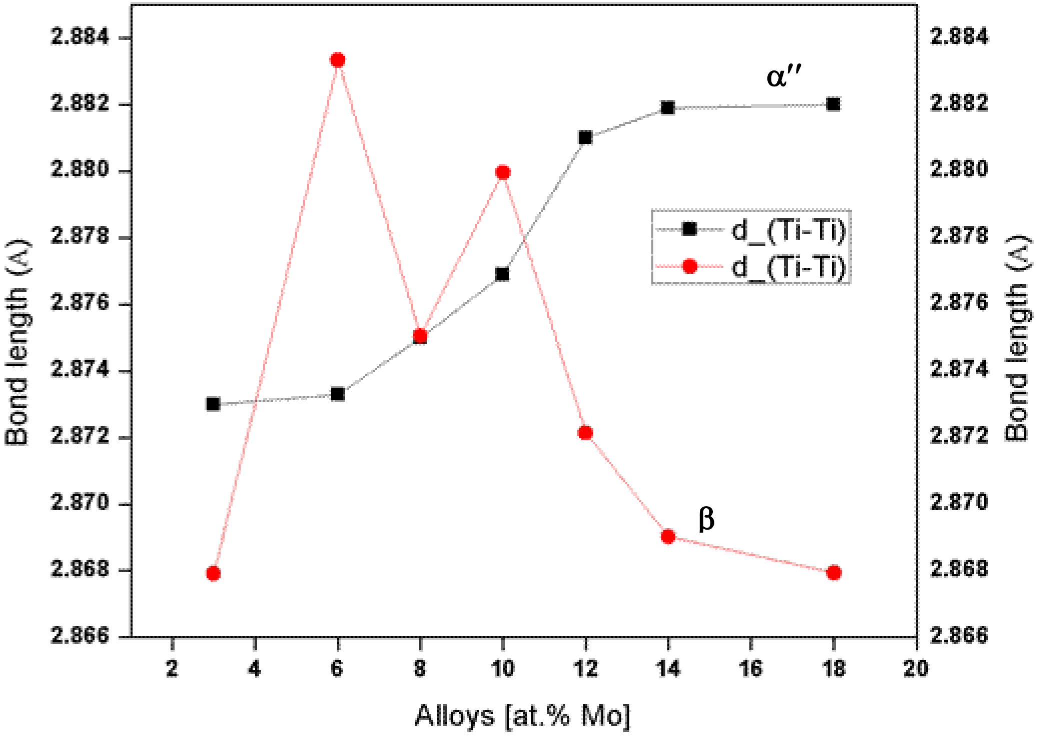

Figure 4.3: The composition dependence of Ti-Ti bond distance for α″ and β phase according to the present work. The lines are only to guide the eye.

For the β-phase, Figure 4.3 (the red line) clearly illustrates that the Ti-Mo interatomic bond remains essential for the change in the crystal structure of the Ti-Mo alloy. Molybdenum atoms produce major structural perturbation in the unit cell of Ti-Mo to force the breaking of the Ti-Ti bonds and the formation of β Ti-Mo alloy.

A possible explanation for the change in crystal structure from α″→β was offered by Brown *et al.* [9]. In the orthorhombic martensite of Ti-Nb system they found no evidence of segregation of niobium to special sites, and showed that the crystal structure gave an eightfold co-ordination around each (Ti, Nb) atom, with four additional neighbours at a slightly greater distance. Both atoms have a Goldschmidt atomic radius of 1.47Å and, therefore, difference in size is unlikely to account for the distortion to orthorhombic symmetry alone. It was suggested that the distortion was a reflection of a tendency for niobium to retain the eightfold co-ordination obtained in the BCC form.

Similarly, crystal structure transition in the Ti-Mo with rising Mo can be regarded as a change in the nearest neighbour co-ordination from twelve in the HCP structure to approximately eight in the orthorhombic structure and eight in BCC. The size of molybdenum (1.36Å) is very close to that of titanium, and size difference affects should again be small. This was noted by Dupouy [41] of Ti-Ti and Mo-Mo atomic bonds tending to approach the average distance in the solution at compositions of between 10 and 50 at.% molybdenum, and was taken to indicate an electron exchange in the solution.

The present results are consistent with the above suggestions for the change in α″→β symmetry. One can therefore believe that the maxima could be accidental or could be a clue to the role that Mo plays in stabilising β-Ti alloys. Thus, leading to the implicit transition states for α→α″ and α″→β structures respectively, where Ti-Mo bonds reorganise within the unit cell and the system gains stability by adopting the new phase, which corresponds to the new structures — as illustrated in Figure **4.2(c)**. Figure 4.4 is thought to be a successful illustration of the legitimacy of all the above statements.

4.4.1.3 Lattice parameter

An interesting conclusion follows from the comparison of the theoretically lattice constants of the optimised Ti-Mo alloy structures and the as water quenched Ti-Mo alloys experimental analysis of the X-ray diffraction patterns, shown in Figure 4.4(b). The calculated lattice parameter decreases linearly with the excess Mo concentration. The x dependence of the theoretical lattice constant can be fitted as $a = 3.235 - 0.02x(\text{Å})$, which is in good agreement with experimental relationship, $a = 3.276 - 0.022x(\text{Å})$. Note that the theoretical experimental is only about 0.1% smaller than experimental value.

The decrease in the lattice constant with increasing x can be attributed to two factors. One is that the atomic radius of the Mo (1.36 Å) is slightly smaller than that of Ti (1.46 Å). The replacement of Ti by Mo therefore induces the shrinkage of the crystal lattice. The second factor was a change in the nearest neighbour co-ordination from approximately eight in α'' to eightfold co-ordination in original BCC β cell, which means the distortion is a reflection of a tendency for molybdenum to break Ti bonds and retain the eightfold co-ordination obtained in the BCC form, resulting in a reduction in the lattice parameter.

The lattice contraction by about 5% that is reached in Ti-Mo in comparison with pure ≈ Ti initiates the $\alpha'' \rightarrow \beta$ transformation similar to the appearance of ω phase under pressure in Ti. Further lattice decrease in ternary alloys on the Ti-Mo basis favours β-phase and low Ms.

It is our belief that the α″ phase appearance in β phase alloys of Ti with Mo, Fe, Nb, Mn, Cr and V can also be considered the result of lattice parameter contraction. The analysis shows that α″ phase in Ti β-phase alloys appears at electronic concentrations 4.09~ 4.16 and lattice parameter 3.225 A. The analysis from theory was consistent with the experimental behaviour of more recent values for Ti-Mo alloys obtained [9], probably due to the large basis-set employed in the present work. The minor discrepancy between experimental results may be due to differences in temperatures, or probable approximations inherent to DFT-GGA [22, 23] may play a role.

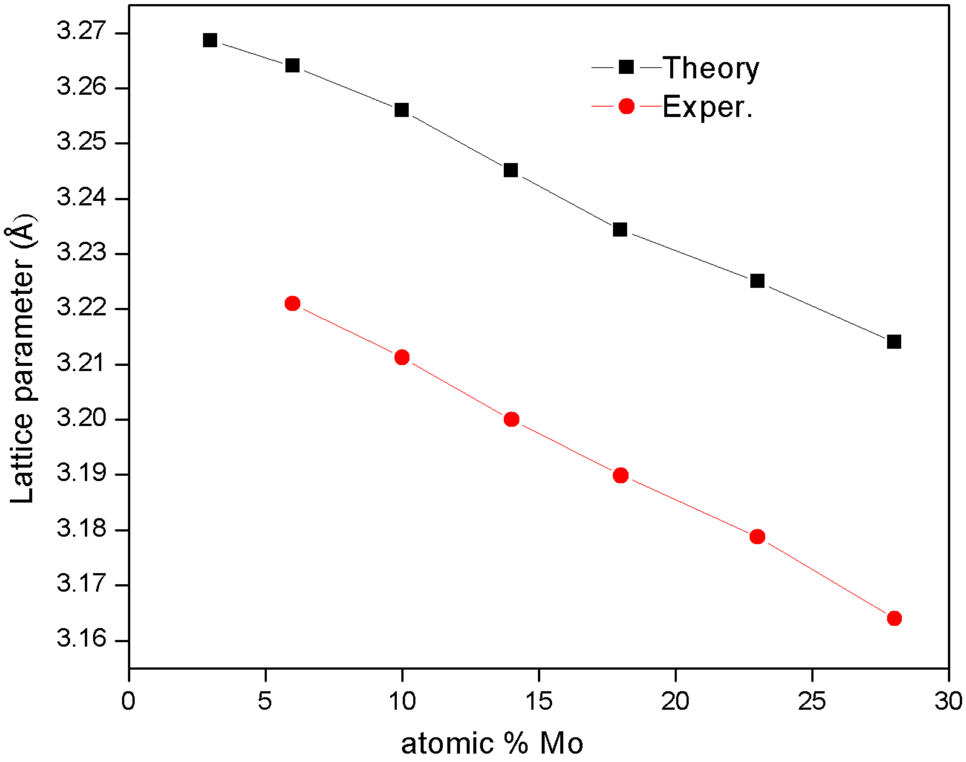

Figure 4.4: A comparison of the theoretical and experimental determined lattice parameter of the alloys in to the present work. The lines are only for guides to the eye.

4.4.2 Energetic analysis of thermodynamic stability – ab initio simulation

4.4.2.1 Thermodynamic analysis of β and α'' stability in Ti-Mo alloy: theory

In order to compare the relative stability of β phase with respect to α″ phase stability, the formation energies for α″ and β structures in Ti-Mo system, at T= 0K formation energies have been calculated based on Eqn. 4.1. The result of the relative stability between the two phases as functions of Mo content is shown in Figure 4.5. As can be seen in Figure 4.5(a), which shows formation energies of α″ and β phases, the two phases closely track one another. While the formation energy of α′′ phase is slightly more negative (exothermic) in low solute alloys (3 at.% to 8 at.% Mo), Mo destabilises the α″ phase (formation energy increases with compositions) but stabilises the β (the formation energy decreases with compositions). The present results are consistent with other studies [6, 9, 21-22] on β-Ti-Mo alloys, and this consistency in also obtained in the Ti-6% Mo alloy. The estimated energy difference is 3.5 eV between α″ and β phases, which is close to other theoretical reports of 2.9 eV [20, 23, 24], and slightly larger than another estimation [23]. The difference between the formation energies of the two phases, however, is ~ 3.5 eV/atom. This indicates their nearly equal probability to occur in the samples. Again, the process of β→α″ transformation is associated with small strain, which is less than β→α′ transformation. The small strain might account for the β→α″ transformation ahead of β→α′ or ω as explained elsewhere [24]. We found the influence of site occupancy rather weak.

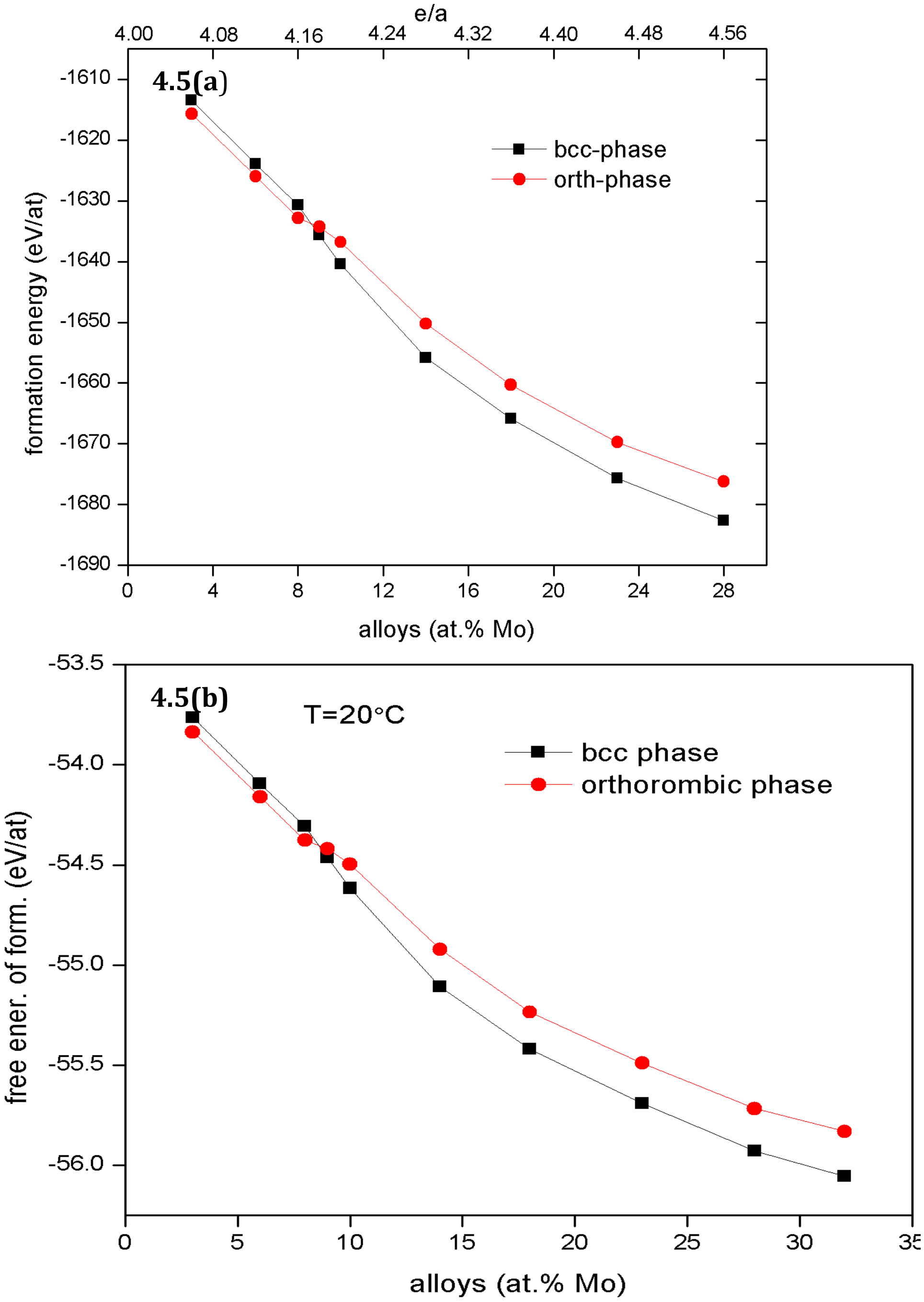

Figure 4.5: (**a**) Theoretical alloy formation energy at T=0K; and (**b**) free energies of formation at 20^0 C (293K). The results are displayed as a function of composition, the region in between the dotted lines depicts the most likely region of coexistence of both phases. The lines are to guide the eye.

On thermodynamic stability, it should be noted that these calculations found negative formation energy for both phases in agreement with calculations by Rudman [42], who determined values for the heat of mixing of Ti-Mo alloys using a bond-energy concept. For an alloy to be thermodynamically stable, its formation energy must be negative. According to Figure 4.5(a), α″ and β structures exhibit similar behavioural path ways in Ti-Mo alloys. For α′′ phase, the formation energy at temperature T=0K is more endothermic at a low Mo concentration of between 3 at.% — <8at. %. Mo is thermodynamically immiscible in α′′phase in a low concentration regime. It is only reasonable that α″ phase will be the more stable phase even without any entropy stabilisation effects.

In contrast, β phase at the T=0K is very stable beyond ≈ 8 at.% Mo. The significance of this result is that Mo is completely immiscible in β phase at ≈ 8 at.%. We can conclude from this result that α″ is very unstable at higher Mo as it promotes β stability at high concentration regimes even in the absence of any entropy driven temperature effect.

In view of the practical application of biomedical Ti alloys, we felt that ambient temperature is a more suitable choice as a reference temperature for the formation and stabilisation of both phases. The corresponding results are shown in Figure 4.5(b). The results as shown in Figures 4.5(a) and 4.5(b) confirm earlier reports [20] suggesting that the energy spread for given composition in Ti alloys and the different local configurations are weak, and that their dependence on energy of formation are also lacking. Hence, the small and negative interaction parameter obtained in the result is well justified.

Although the effect of temperature is less pronounced, evidently the finite temperature significantly reduced the formation energy, thus indicating the stability of the alloy is somewhat entropy driven. A direct comparison of the outcome of this theoretical result with experimental results based on the first occurrence of a stable fraction of α″ and β phases can now be done.

4.4.2.2 Thermodynamic analysis: comparison of the theoretical predictions and experimental data

The onset of β phase formation, its composition and volume fraction can be described using the hypothetical free energy composition, following the work by Raabe *et al*. [20] on HCP and BCC in T-Nb and Ti-Mo systems. We therefore predicted these by performing a Gibbs construction using the average formation energy to compare the experimentally determined onset and volume fraction of the β phase for the alloys. The Gibbs construction was performed by approximating third-order polynomial using a least-squares approach because of the important statistical interpretations. The actual Gibbs construction and the volume fraction of the α″/β phases are summarised in Figure 4.6(a). The Gibbs construction found ≈18 at.% Mo as the threshold concentrations where only β-phase exists. The result of calculated volume fractions of the phases are summarised in Table 4.3, shown in the blue circle in Figure 4.6(b).

In order to compare the experimentally determined volume fraction of the two phases, we conducted x-ray wide angle diffraction experiments on the Ti-Mo alloys associated with the region of interest — see Figure 4.6(c). The splitting of the diffraction profile lines for the Ti-6% and Ti-7% alloys as a result of an increased orthorhombic distortion is in agreement with the theoretical prediction α'' phase regions for this system. To further verify this prediction, the phase content of as quenched Ti-18 at.% Mo alloy determined by x-ray diffraction was further cross-examined by the EBSD measurement (see Figure 4.6d). The indexing of this EBSD image reveals a random texture of almost complete BCC structure with an isotropic grain shape.

As expected, because Mo is a high β stabiliser, the results of the Gibbs free energy detailed in the present work entails that the alloy has a narrow two-phase ($\alpha''+\beta$) window. Furthermore, application of the lever rule to the tangent of the α'' and β curves shows that, in agreement with Hickman's findings [44], the volume fraction of α'' decreases with increasing alloy content. The overall form of the Gibbs construction from formation energies suggested here, however, indicates the existence of a metastable orthorhombic α'' martensite in Ti-Mo system, and the phase diagram should include either a monotectoid reaction or a metastable miscibility gap within the ($\alpha+\beta$) phase region.

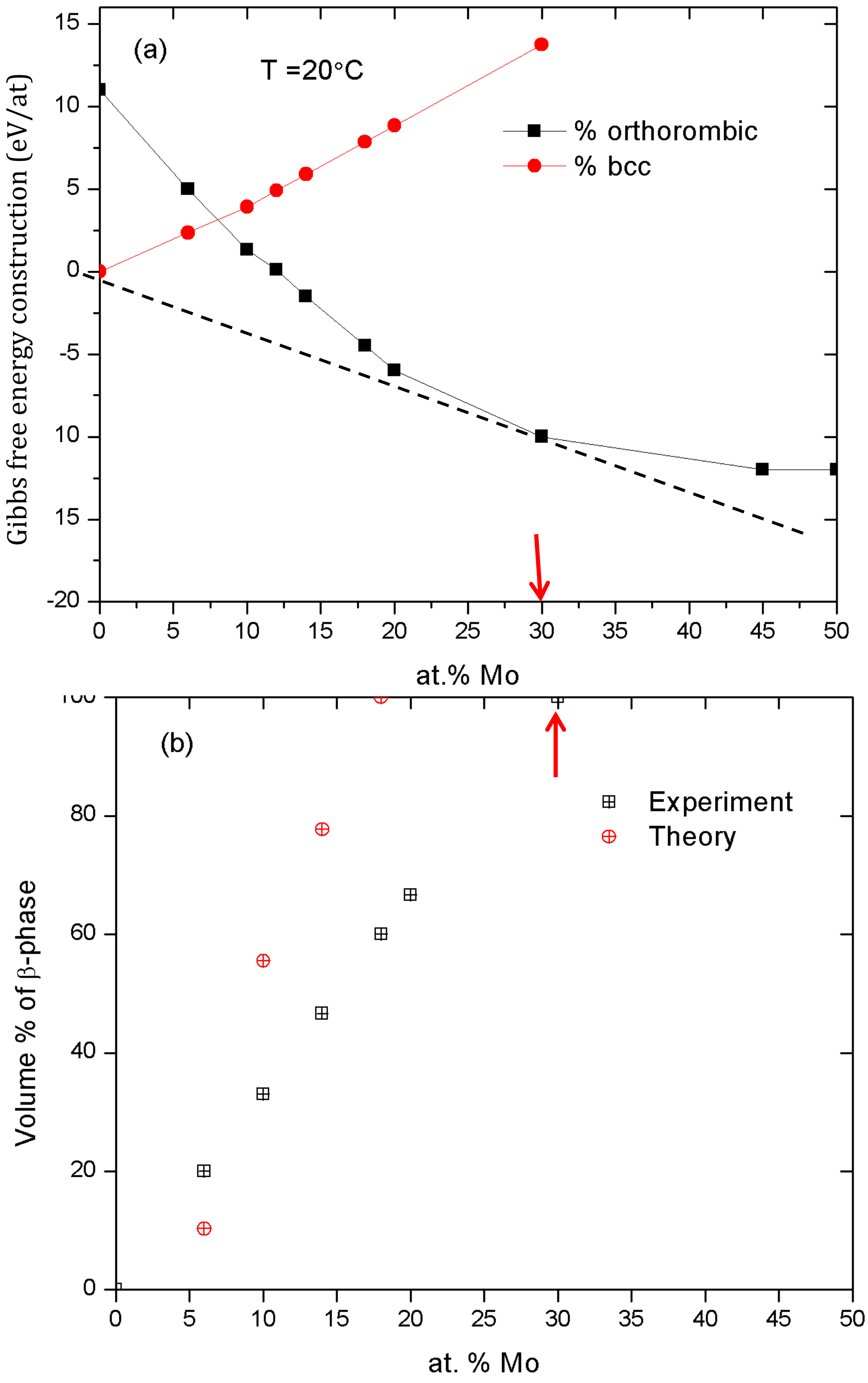

Figure 4.6(a) Gibbs construction and (b) volume fraction of the β phase of Ti-Mo alloy are shown. The volume % of β phase as determined by DFT calculation method is shown by (black) crossed block, while the red crossed circles are experimental determined volume %. The red arrow marked the threshold concentration for single β phase of the alloys. The error bars fall with the symbol size.

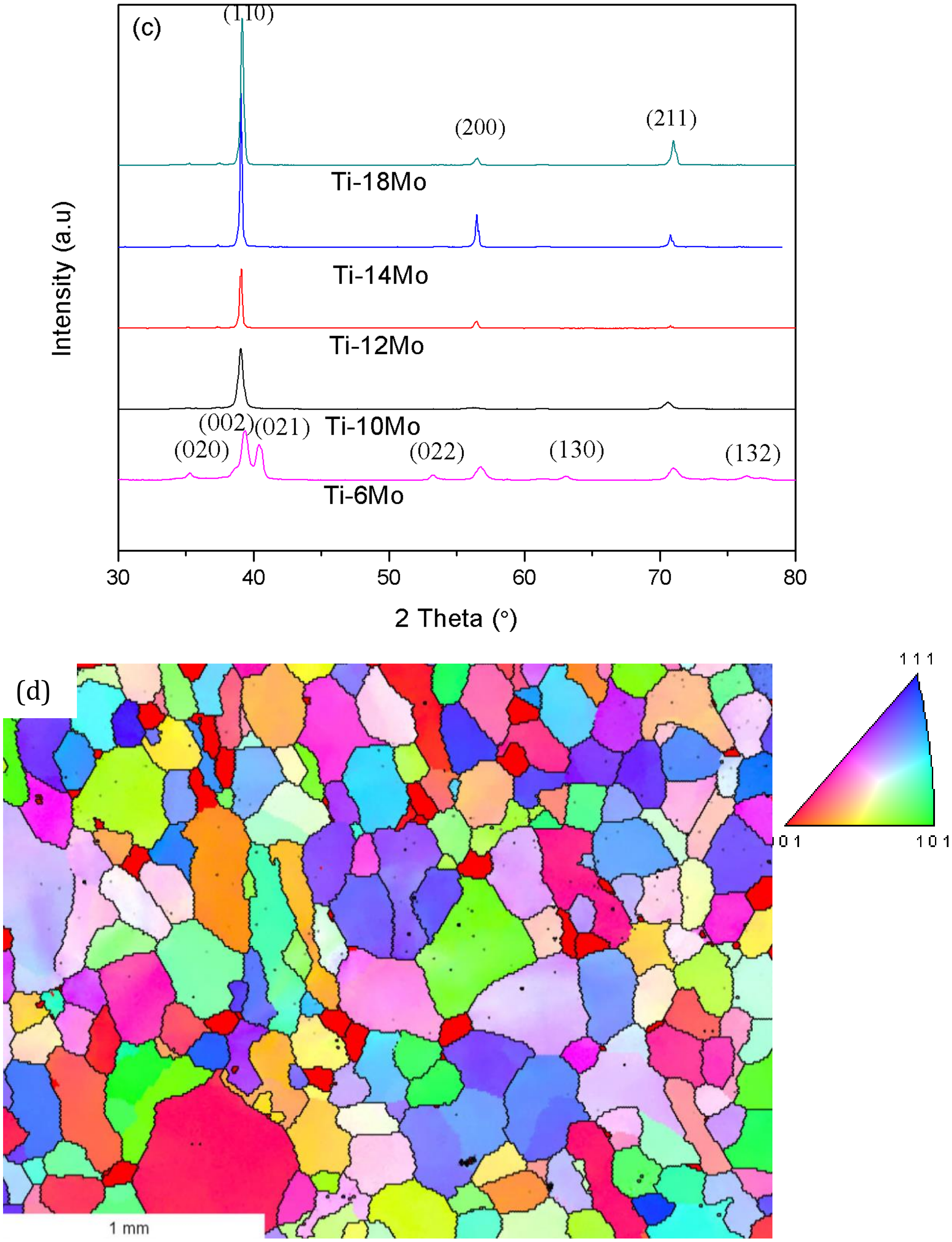

Ti-18Mo

Figure 4.6 (c) For comparison, the indexed diffraction spectra from XRD scanned from 30 to 80 degrees in diffraction angle, revealing reflections due to the phases for the of Ti-χMo alloy, (where χ= 6,10,12,15, 18 at. %) reveals the phase structures; (**d**) EBSD image of the experimental observed microstructure of Ti-30Mo. The EBSD image reveals an isotropic grain shape and a random texture. Colour code; miller index in standard triangle of lattice directions pointing in normal and casting direction.

Table 4.3: Experimentally observed volume fraction of the phases based on XRD measurement with Cu. Kα_1 radiation.

Phase content by XRD method.	6Mo	10Mo	14Mo	18Mo	Ti-23Mo	TI-30Mo
Vol. %,α″phase	80	67	46.6	40	33.4	0
Vol. %, β-phase	20	33	53.4	60	66.6	100

4.4.3 Elastic modulus and phase stability

Having determined the thermodynamic stability behaviour, let us now focus on predicting and comparing the elastic properties determined from the first principle total energy calculation and experiment. This is not trivial, however, since the exact distribution of Ti and Mo atoms over the lattice position of two different atomic symmetries are not known. The elastic constants — i.e., the C_{ijs}— were modelled with these two different atomic symmetries and arrangements; namely, the orthorhombic and BCC with the same composition were modelled based on Eqns. 4.14, 4.31, 4.32, 4.33 and 4.34. These theoretical predicted properties are summarised in Table 4.4 and compared with both present and past experiment results in the literature. In order to analyse these data, we first focus on the relative stability between the two phases. The $C^{'}$ and A are also listed in Table 4.4. $C^{'} = (C_{11} - C_{12})/2$, is a tetragonal shear parameter related to the stability of the BCC structure [44], and the anisotropic factor $A = \frac{C_{44}}{C^{'}}$ (A=1 for isotropy). As the HCP - BCC boundaries are approached, $C^{'}$ decreases, this often correlates with deformation by twinning, and A approaches zero at the incidence of β stability.

As shown Table 4.4, the elastic constant C_{44} decreases steadily with increasing x, apart from the alloy x= 6% — C_{11} (C_{12}) increases (decreases) respectively with x, which results in a softening of the tetragonal elastic constant $C^{'}$. This indicates a marginal elastic stability towards a uniform tetragonal distortion [47, 48]. The change at x= 6% is not so clear. However, a possible explanation could be one of two reasons: one is a close symmetry change from $\alpha'' \rightarrow \beta$ and the other is the high volume fraction of α'' phase at this composition boundary in accordance with previous microstructural observations.

Table 4.4: Elastic constants of the Ti-xMo (x=3, 6, 10, 14, 18,23at. %) alloys in unit of GPa.

materials	C_{11}	C_{12}	C_{13}	C_{33}	C_{44}	$C_{12} - C_{44}$	A
βTi(theory)	167.6	87.6	73.7	190.8	34.3	53.6	0.85
βTi(theory)[1]	87.8	112.2			39.8	−24.4	
Ti (Exper.)[46]	162.4	92.1	70.0	179.8	47.9	44.2	1.36
Mo(theory)	133.1	107.9	131.2		57.3	50.6	4.5
Mo (Exper.)[46]	163.0	118.3			75.9	42.4	3.39
Nb theory[49]	227	129			22	107	0.45
Nb (Exper.)[53]	246	113			28	85	0.42
Ti-3Mo	159.3	115.0	62.1	58.2	193.2	-78.2	8.72
Ti-6Mo	111.3	69.07	42.1	53.2	103.2	-34.1	4.89
Ti-10Mo	167.0	19.6	27.5	12.4	13.46	6.14	0.183
Ti-14Mo	179.2	17.9	23.5	12.0	13.2	4.7	0.164
Ti-18Mo(Exp.)[23]	168	42.1			31.9	10.2	0.49
Ti-18Mo [..]	192.6	16.3	18.30	9.10	12.7	3.6	0.144
Ti-23Mo	197.5	16.0	17.5	6.2	10.1	5.9	0.13

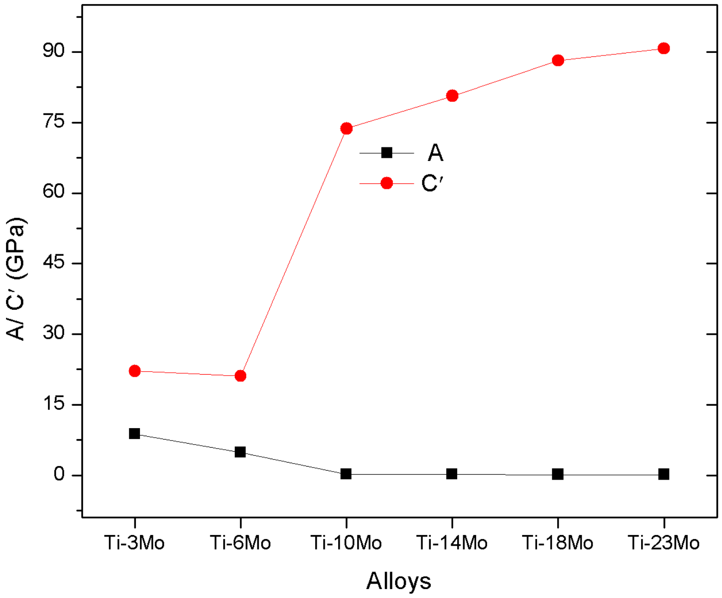

Figure 4.7: Theoretical shear modulus C' of the multiphase Ti-Mo alloys and the elastic anisotropic factor with respect to the concentration of x (lower abscissa).

The anisotropy of a crystal is a measure of the bonding anisotropy between atoms. In order to get an idea of the connection between the elastic constants and the relative stability of the α'' and β phases in Ti-Mo alloy system, we plot the elastic anisotropic factor A as a function of x content in Figure 4.7. It can be seen that A almost decreases with increasing x. The factor A is higher for the lean x compositions, related to strong anisotropic chemical bonding and marginal mechanical stability of β phase at close proximity of α phase transformation; conversely a low A corresponds to greater stability of the β phase, in agreement with the correlation found for other Ti-alloys such as Ti-Nb; Ti-Ni based alloys [44, 47, 48], suggesting that A approaches zero as the HCP -BCC boundaries are approached. In line with this, a large C' and lower A correspond to a lower transformation temperature (T_M), in agreement with the correlation found for alloy with shape memory possibilities such as

Ti-Nb and NiTi based alloys [44, 49, 50].

Finally, in order to verify the theoretical predictions, we conduct a check on our calculated and measured bulk polycrystal elastic properties, namely the homogenized multiphase composites Young's modulus $(\tilde{Y})^*$, Poisson's ratio$(\tilde{\eta})^*$, Shear modulus (μ) and Bulk modulus$(\tilde{B})^*$. The results are listed in Table 4.5.

Table 4.5: The calculated and measured bulk polycrystal elastic properties in units of GPA

materials	B_{the}	μ_{the}	$\mu_{exp.}$	$\tilde{Y}_{the}$	$\tilde{Y}_{exp.}$	η_{the}	$\eta_{exp.}$
Ti[18,20,46]	111.3	39.4	44	105.6	114.6	0.5	0.33
Mo[18,46]	120.3	22.5		63.3	301	0.41	0.37
Ti-3Mo	60.73	39.2	30.7	90.2	78	0.43	0.38
Ti-6Mo	49.0	42.18	33	80.6	64	0.59	0.40
Ti-10Mo	34.83	20.46	40	86.5	80	-0.7	0.41
Ti-14Mo	28.2	16.12	51.7	98.1	82	0.75	0.42
Ti-15Mo[50]					79		
Ti-17Mo[51]					73		
Ti-18Mo	13.7	10.0	38.7	109.9	86	0.78	0.42
Ti-18Mo[51]					83		
Ti-23Mo	9.1	6	21	111.9	90	0.80	0.41

The results as presented in Table 4.5 show that the bulk modulus (B) and shear modulus (μ) decreased linearly with alloying element, the Poisson's ratio (η) increased linearly, but the Young's modulus ($\tilde{Y}$) was not dramatic in its change. This means: Mo softens the matrix and enhances the shear deformability of the β phase; the Poisson's ratio has similar but weak effect; and the negative sign at 10% is similar to the results obtained elsewhere [18], which can be attributed to β phase instability at the composition [18, 20]. To confirm the importance of this assumption, we plotted the compositional dependence of the theoretical homogenised polycrystalline (a) bulk modulus ($B_{\alpha''\beta}$), (b) shear modulus and ($\mu_{\alpha''\beta}$) and (c) Young's modulus ($\widetilde{Y}_{\alpha''\beta.}$) respectively as a function of the β volumetric phase content of the alloys in Figure 4.8. The resulting dependence of the homogenised multiphase properties has been found, both the bulk modulus and shear modulus show a positive deviation from the volumetric phase fraction. This is not unexpected, since bulk properties are expected to increase with increasing concentration. In contrast, non-linear composition dependence is apparent in the Young's modulus trends for the Ti-Mo alloy system. The result highlights the overall importance of using homogenised schemes in agreement with those reported [20]. Based on this trend in Young's modulus, however, the Young's modulus of Ti-Mo alloy may be considered to exhibit large anisotropy. This is because the anisotropy of the mechanical properties of β-type titanium alloy has been reported to be significantly larger than those of other metallic materials such as carbon steel [51]. Other findings [52, 53] indicate a variation in Young's modulus of Ti-Mo-Cr and Ti-Mo-Ta, Ti–(15-17) Mo–ST alloys due to homogenisation treatments. Tane *et al.* [54] revealed variation in modulus due to orientation in Ti-Nb-Ta-Zr single crystal.

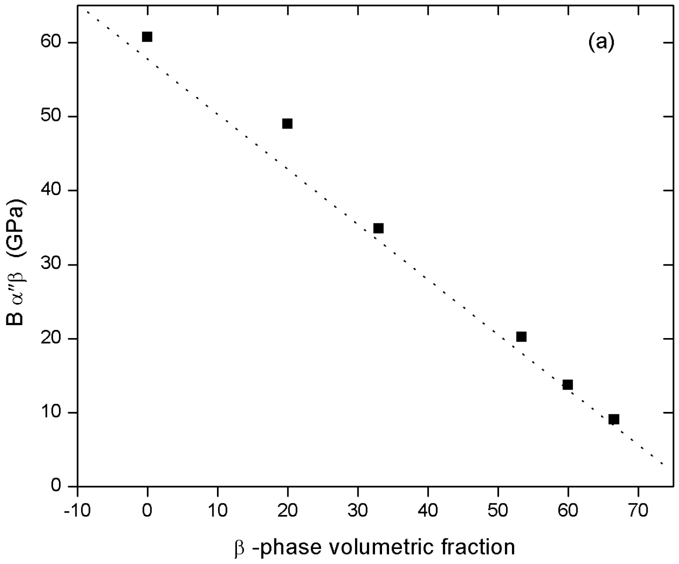
(a)
B α″β (GPa)
0
10
20
30
40
50
60
-10
0
10
20
30
40
50
60
70
β -phase volumetric fraction

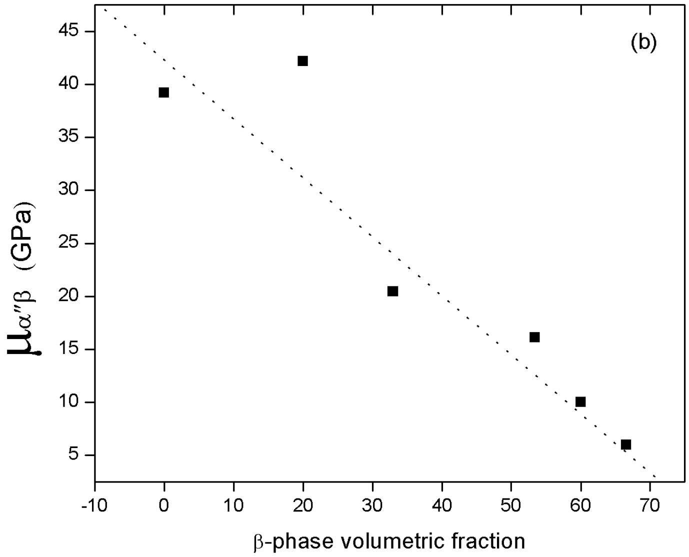
(b)
μα″β (GPa)
5
10
15
20
25
30
35
40
45
-10
0
10
20
30
40
50
60
70
β-phase volumetric fraction

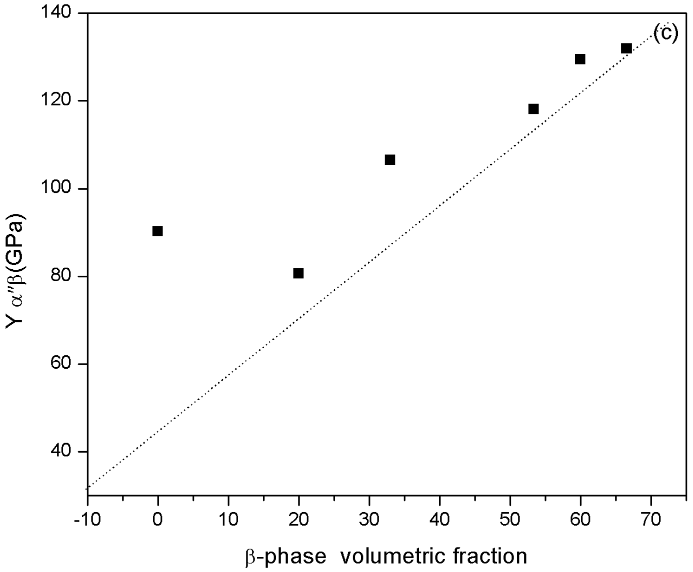

Figure 4.8: Theoretical predicted dependence of (a) Bulk modulus (B); (b) shear modulus (μ) and Young's modulus of the Ti-Mo component as a function of the β phase volumetric content. The lines are only to guide the eye.

In order to verify the influence of material anisotropy on the theoretical predictions of Young's modulus, the cast and homogenised microstructure of β-type Ti alloys has been investigated in the Ti-18Mo alloy using EBSD observation. The effect of initial textures on anisotropy of the cast and homogenised Young's modulus for the Ti-18Mo alloy is discussed below using the pole figures and inverse pole figures of cast, and as homogenised at 1173 K in Figures 4.9, (homogenised ODF shown in 4.6).

Figure 4.9 shows the pole and inverse pole figures corresponding to the three directions in the Ti-18Mo alloy. The pole and inverse pole figures of the as cast materials in Figures 4.9 (a) and (c) indicate that a well-developed {001}{110} texture is formed due to casting; whereas, due to homogenisation treatment in Figures 4.9 (b) and (d), the random texture is formed with no significant strong peak, indicating that homogenisation of the alloy has led to a weak texture.

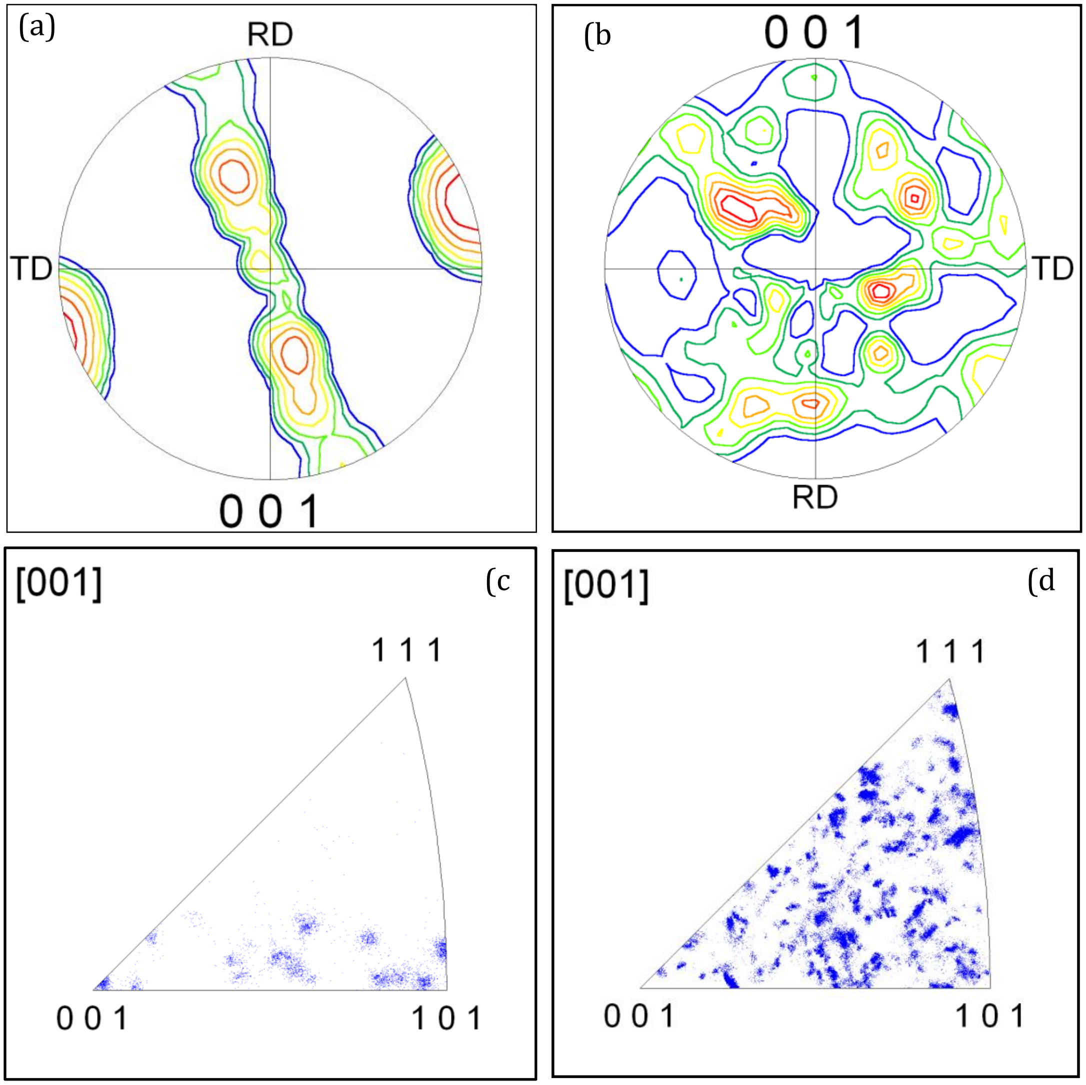

Figure 4.9: [001] pole figures of the (a) as cast Ti-18Mo alloy; (b) as homogenised Ti-18Mo alloy and inverse pole figures along different directions in the rolling plane for the (c) cast Ti-18Mo and (d) homogenised Ti-18Mo alloy.

The importance of using T-Matrix to account for the dual phase nature of Ti-Mo and orientation dependence of Young's modulus in β-type Ti alloys is illustrated in Figure 4.10. Here, the theoretical determined single crystal and multiphase polycrystalline Young's modulus is compared with the homogenised ultrasonic determined Young's modulus of the alloys. The single crystal Young's modulus increases monotonously with increasing Mo content. Such a trend may have completely ignored the influence of different phases in the matrix, contributing to the Young's modulus and mechanical behaviour of the alloys. Though the T-Matrix approach (in the black rectangle) did not completely resolve this, the overall trend is however qualitatively better and closer to the values of Young's modulus obtained from homogenised experimental materials. This is also in line with measurements taken by other researchers (as shown in Figure 4.10). The Young's modulus increment was quite slow and close to what had been observed experimentally, emphasising the need for adoption of this technique in predicting the modulus of Ti alloys. Although the DFT theoretical predictions overestimated the overall elastic constants, in general the theoretical predictions for the Ti-Mo alloys have shown similar trends within ≈1-10GPa of the experimental values. Other small discrepancies in the value of Young's modulus could reflect differences in temperature, minor experimental errors or the approximations inherent to DFT-GGA [18, 30]. The excellent agreement for both results indicates, however, that low Young's modulus could possibly be optimised via the least stable β phenomenon that exhibited the lowest Young's modulus. The coupling with homogenised multiphase elastic constant might lead to something outlandish with respect to reducing the Young's modulus of metallic biomaterials.

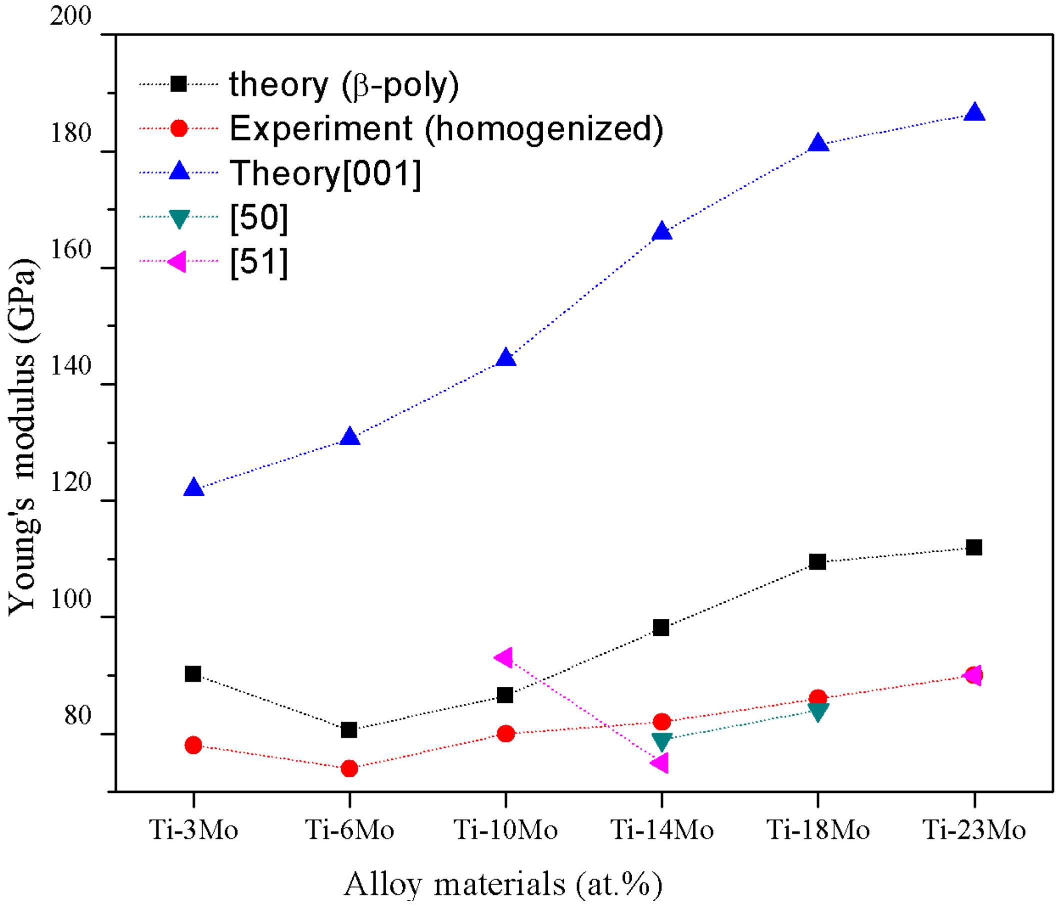

Figure 4.10: Predicted and experimentally obtained Young's moduli of the Ti-Mo alloys and data from the literature are given. The lines are only for eye guides. The error bars fall within the symbol size.

4.4.4 Electronic properties

In order to understand the intrinsic mechanism of how alloying elements influence phase stability and transformation, we can compare the total electronic density of states (DOS) of α'' and β crystal structures with x=3, 6, 8, 10 and12 at.% in Figure 4.8 and 4.9 respectively. The shape of the density of states can be understood by re-examining Figure 4.5, as it is at a similar region of interest to where the formation energies lines are closest that we are focused.

The pure Mo usually exhibits broad valence features that result from a strong hybridisation of 4d orbitals. Even more changes appear in the d- bands, as the DOS plots in Figure 4.10 (a) and (b) and (c) illustrate. It is clear that the extent of the covalent bonds is mainly due to the hybridisation between the d-electronic states of Ti and Mo atoms. As shown in Figure 4.11(a), similar type of pseudogap exists on the DOS of α'' phase at $\approx$ 0.05eV below the Fermi level, indicating the covalent bonding region character between the Ti and Mo atoms.

In this fashion, the obtained results indicate that the structural stability change in the Ti-Mo system is connected with the $N(E_F)$ enhance due to Mo d-band, as was suggested earlier, but with also the statistical weight of Ti d-states at E_F. The exciting part comes from the difference that alloying concentration makes in the DOS electronic energies slopes of the alloys. This is because it is not the length or width of the ridges in DOS which are important, rather it is the magnitude of the peaks in these ridges. For the alloys consisting of 3%, 6%, 10% and 12%, the DOS electronic energies are 20eV, 6eV, 20eV and 30eV respectively. The reason is clear: the states below the pseudogap represent the bonding state, whereas those above the pseudogap represent the antibonding state.

Some of the antibonding states in α'' phase are occupied by electrons. The occupation of antibonding states generally weakens the covalent bond and lessens phase stability. β phase instability is therefore more pronounced and Ms is higher, the purer are the antibonding Ti d-states at Fermi level.

Let us now discuss the core in shift in the d-state, by first turning to Figure 4.6. The formation energy contributes maximally to bonding or antibonding. As this alloy with small x concentration of Mo exhibits the highest negative formation energy, implicitly, α'' is more stable at this composition (6%). The significant drop in DOS bonding energy at 6% indicates greater stability of α'' phase due to strong Ti-Ti covalent bonds. As the α'' phase transforms to β (≈ ≥ 10%), the pseudogap becomes narrower and moves up in energy, showing the covalent bond has been weakened. In considering this energy function, we make the assumption that it is interplay between electronic band structure and crystallographic bonds which are related to one another by symmetry that play a central role in the energetics. A pseudogap is believed to be formed when the Fermi sphere with a diameter of 2KF makes simultaneous contact with a number of equivalent Brilliouin zone planes associated with reciprocal lattice vector Khkl, E_{111}, assuming a BCC crystal lattice, on Γ lattice point of the band structure.

In the β phase (see Figure 4.11(b)), the Fermi level is located right in the valley of the pseudogap — i.e. the bonding states are fully occupied and the antibonding states are empty — thus indicating that the covalent bond in the β phase is stronger with more Mo concentration than in the α″ phase. It has been shown above that around EF, d-states are dominant. By taking this into account, together with a general rule of lattice parameter behaviour (Figure 4.4), one can suppose that Ti-Ti instability is exclusively determined by Ti-Mo interaction that changes with lattice parameter variations (Figure 4.3). In other words, the competition of α″, β phases in Ti and its β alloy compounds are due to a change of interatomic Ti-Ti distance that defines the Ti d-filling character.

A correlation between the positions of the density maximum of the states in the valence zones was observed by Pettifor *et al.* [14, 15] when examining the binary of some transition metals (Cu). This study correctly determined differences in energy between the BCC, FCC and HCP systems, thus indicating that occupied density of state is related to the Fermi energy level according to Equations 4.37 and 4.38. Hence, DOS and band filling can be used to find the relative stability of crystal structures. From the plot of integrated DOS in Figure 4.10, lowering of the Fermi energy due to rising Mo content in 6at.%, 8at.% and 10 at.% is evident and can probably be the reason why β is more stable in the high Mo regions of the phase diagram.

$$\frac{\partial E_{bs}}{\partial n} = \varepsilon_f \qquad (4.38)$$

$$\frac{\partial^2 E_{bs}}{\partial n^2} = \frac{1}{g(\varepsilon_f)} \tag{4.39}$$

Additionally, in the β phase, it can be seen that the majority of the antibonding DOS states are splitting, probably due to α″ transformation to β phase with rising Mo content. Apparently, this subbanding behaviour has a genetic connection with Mo d-states and there may be extra electronic interactions between the Ti and Mo atoms in the β phase. This phenomenon can also contribute to the improved stability of the β phase relative to the α″ phase. This trend of the DOS is in agreement with the decreasing stability of α″ phase and increasing β with increasing Mo element.

The observed DOS behaviour in α″ and β indicates that the bond change in the Ti-Mo system with concentration is stipulated, first of all, by Ti and Mo d-states. The change of Ti-Ti interaction, which is caused by enriching the E_F, dominates in spite of all other factors.

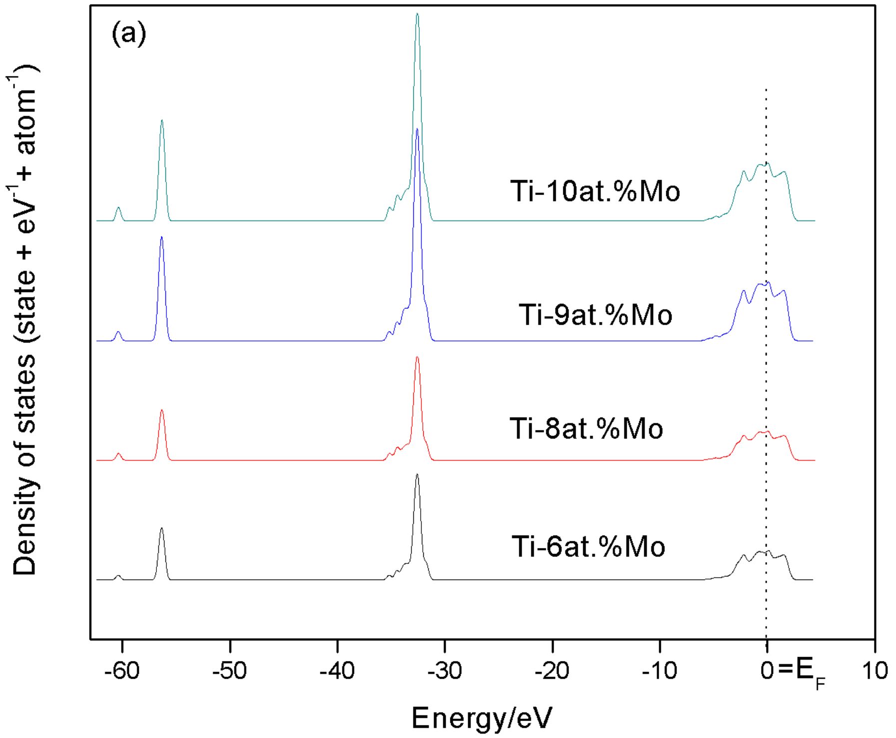
(a)
Density of states (state + eV^{-1}+ atom^{-1})
Ti-10at.%Mo
Ti-9at.%Mo
Ti-8at.%Mo
Ti-6at.%Mo
-60
-50
-40
-30
-20
-10
0=E$_F$
10
Energy/eV

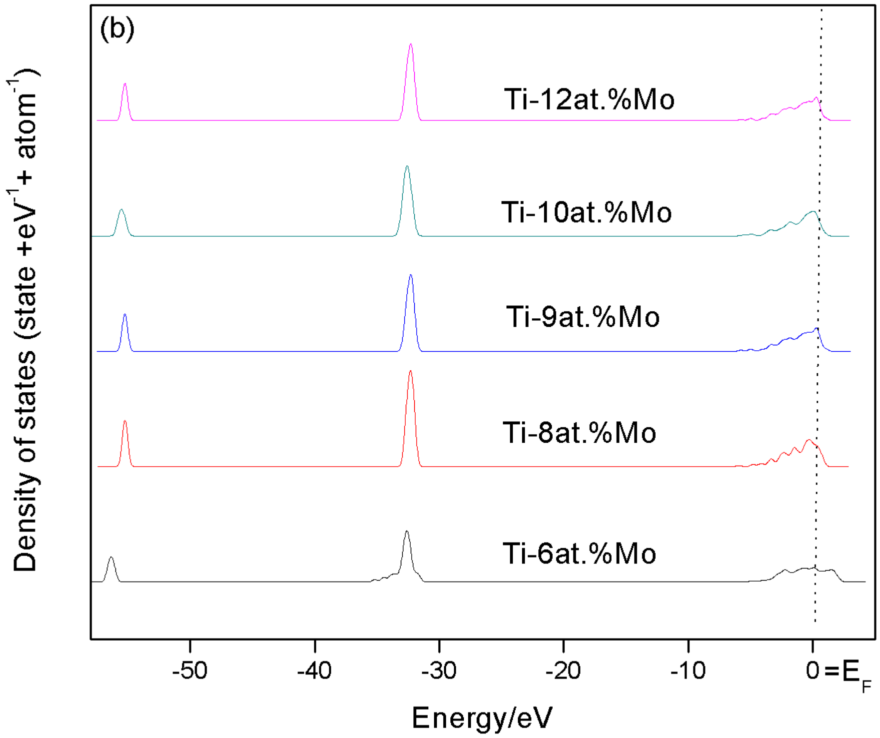
(b)
Density of states (state +eV^{-1}+ atom^{-1})
Ti-12at.%Mo
Ti-10at.%Mo
Ti-9at.%Mo
Ti-8at.%Mo
Ti-6at.%Mo
-50
-40
-30
-20
-10
0=E$_F$
Energy/eV

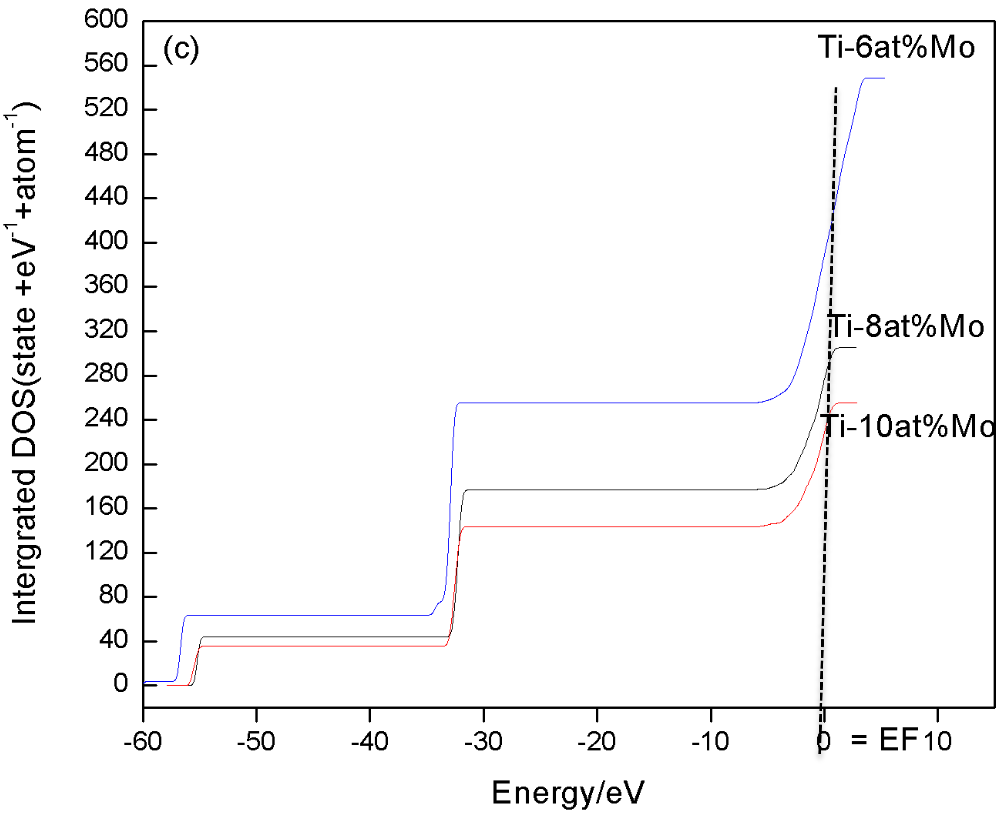

Figure 4.11: Total density of states for the Ti-Mo system consisting of (a) orthorhombic α″ crystal structure; (b) bcc β crystal structure and (c) Integrated total density of states of βTi-Mo alloys showing the effect of increasing Mo alloying in the Fermi energy of the Ti-Mo system consisting of 6at.%Mo;8at.%Mo and 10at.% Mo. The vertical dotted lines indicate the Fermi levels.

4.5 Summary and conclusions

A combinatorial approach was used to predict and verify the microstructural evolution and its relationship to the properties in multiphase Ti–Mo alloy. The approach combines lattice/bond interactions, thermodynamic analyses of multiphase stability to predict elastic constant and electronic properties. The lattice interactions and thermodynamic analyses were used to estimate composition, volume fraction and polycrystal elastic constants. The good agreement of the theoretical calculation with experimental verification data for thermodynamic stability, composition and elastic constant justify the use of the approach in the present work for evaluating property.

Both the bond interaction and thermodynamic analyses predicted the α″ phase and β-phase at 6at.% Mo: 94at.%Ti and at 9at.%.Mo:90at.%Ti respectively. Although our theoretical thermodynamic analysis overestimates the volume fractions of the phases compared to those experimentally found, the predicted compositional trend is qualitatively correct.

Although the predicted modulus values are generally higher than experimentally observed, the trends are well in agreement. The resulting prediction shows a positive deviation of the bulk and shear modulus with the Mo concentration and β volumetric fraction. Young's modulus, however, did not show such a trend. The lowest modulus was obtained in the least stable β alloy (6at. %Mo).

Based on the agreement in the theoretical and experimentally observed data, we can conclude that a low Young's modulus and stiffness can be achieved by having a good matrix of the soft α″ phase, at the least β stable microstructure alloy, to about 42GPa, which is predicted in a Ti-Mo alloy containing 6at.%Mo .

Although the predicted modulus values are generally higher than experimentally observed, the trends are well in agreement. The resulting prediction shows a positive deviation of the bulk and shear modulus with the Mo concentration and β volumetric fraction. Young's modulus, however, did not show such a trend. The lowest modulus was obtained in the least stable β alloy (6at.%Mo). Based on the agreement in the theoretical and experimentally observed data, we can conclude that a low Young's modulus and stiffness can be achieved by having a good matrix of the soft α″ phase, at the least β stable microstructure alloy, to about 42GPa, which is predicted in a Ti-Mo alloy containing 6at.%Mo .

In order to understand the intrinsic mechanisms by which alloying elements influence thermodynamic phase stability, we can compare the total electronic density of states (DOS) of α″ and β crystal structures. The results indicate that the structural stability change in the Ti-Mo system is connected with the lowering of $N(E_F)$. This is due to hybridisation of the d- electronic states of the Mo atom, providing for the increasing covalent bonds between the two atoms.

4.6 References

[1] Liu Y. C., and Margolin H.; "*Martensite Habit Plane in Quenched Ti-Mn Alloys,*" Trans. AIME 197 (1953), 667.

[2]. Liu Y. C.; "*Martensitic Transformation in Binary Titanium Alloys*," Trans. AIME 206 (1956), 1036.

[3] Williams A. J., Cahn, R. W., and Barrett C. S.; *"Crystallography of Beta-Alpha Transformation in Titanium,"* Acta Met. 2 (1954), 117.

[4] Newkirk J. B., and Geisler A. H.; "*Crystallographic Aspects of the Beta to Alpha Transformation in Titanium*," Acta Met. 1 (1953), 370.

[5] Blackburn M. J.; "Phase Transformations in the Alloy Ti -8A1-1MO-1V," Trans. ASM 59, (1966), 876.

[6] Williams J. C., and Blackburn M. J.; "*A Comparison of Phase Transformations in Three Commercial Titanium Alloys,*" Trans. ASM 60 (1967), 373.

[7] Armitage W. K.; "*Metallography of Titanium Martensites*," ISI Spec. Rept. 93 (1965), 76.

[8] Hammond C., and Kelly P. M.; "*Crystallography of Titanium Alloy Martensites*," Acta Met. 17 (1969), 869.

[9] Bagariatskii lu. A., Nosova G. I., and Tagunova T. V.; "Factors in the Formation of Metastable Phases in Titanium-Base Alloys," Soviet Phys.-Doklady, 3 (1959), 1014.

[10] Brown A. R. G., Clark P., Easterbrook J., and Jepson K. S.; "*Note on the Martensitic Transformation in the Ti-Nb System*", Nature 201 (1964), 914.

[11] Deegan R. A.; J: Phys. C 1 (1968) 763.

[12] Dalton N. W., Deegan R. A.; J. Phys. C 2 (1969) 2369.

[13] Friedel J., in: J. M. Ziman (Ed.); The Physics of Metals, Cambridge University Press, Cambridge, 1969, p. 340.

[14] Pettifor D. G.; J. Phys. C 3 (1970) 367.

[15] Duthie J. C., Pettifor D. G.; Phys. Rev. Lett. 38 (1977), 564.

[16] Pettifor D. G.; Calphad 1 (1977) 305.

[17] Ghosh G., Delsante S., Borzone G., Asta G., and Ferro R.; "*Phase stability and cohesive properties of Ti–Zn intermetallics: First-principles calculations and experimental results*", Acta Mater. 54 (2006), 4977–4997.

[18] Dai J. H., Wu X., Song Y. and Yang R,; *"Electronic structure mechanism of martensitic phase transformation in binary titanium alloys*", J. App. Phys.112 (2012), 123718-24.

[19] Song Y. Xu, Yang D. S., Li R., Wu D., W.T. Guo Z.X; "*Theoretical study of the effects of alloying elements on the strength and modulus of β-type bio-titanium alloys"*, Mater. Sci. & Eng. A, 260 (1999), 269-274.

[20] Raabe D., Sander B., Fri´ak M., Ma D., Neugebauer, J.; "*Theory-guided bottom-up Design of Beta-titanium alloys as bioMaterials based on first principles calculations: Theory and experiments*", Acta Materialia 55, (2007), 4475–4487.

[21] Ho W. F., Ju C. P., and Chern Li J. H.; *"Structure and properties of cast binary Ti-Mo alloys*", Biomater. 20 (1999) 2115-2122.

[22] Davis R., Flower H. M., and West D. R. F.; "*Martensitic transformations in Ti-Mo alloys*", J. Mater. Sci. 14 (1979), 712-722.

[23] Hao Y., Li S., Sun B., Sui M., and Yang R.; "*Ductile Titanium Alloy with Low Poisson's Ratio*", Physical Rev. Letts. 98 (2008), 1-4.

[24] Sluiter M. H. F.; "*Some observed bcc, fcc, and hcp superstructures,*" Phase Transitions 80 (2007), 299–309.

[25] Collings E. W.; *"The Physical Metallurgy of Titanium Alloys*", ASM Handbook, 3 (1991), 14.

[26] Boyer, R. R., Rosenberg H. W.; "*Beta Titanium Alloys in the 1980s",* AIME, New York, 1984; 209.

[27] Xing H., Sun J., Yao Q., Guo W., and Chen R.; "*Origin of substantial plastic deformation in Gum Metals*", Applied Phys. Letts. 92 (2008), 151905-9.

[28] Zhang L. C., Zhou T., Alpay S. P., Aindow M., and Wu M. H.; "*Origin of pseudoelastic behaviour in Ti–Mo-based alloys*", Applied Phys. Letts.87 (2005), 241909.

[29] Zhang L. C., Zhuo T., Aindow M., Alpay S. P., and Blackburn M. J.; "*Nucleation of stress induced martensites in a Ti/Mo –based alloy*", J. Mater. Sci. 40 (2005), 2833-2836.

[30] Segall M. D., Philip J. D. L., Probert M. J., Pickard C. J., Hasnip P. J., Clark S. J. and Payne M. C.; *"First-principles simulation: ideas, illustrations and the CASTEP code*", J. Phys. Condens. Mater 14 (2002), 2717–2744.

[31] Kohn W., and Sham L.; "*Self-consistent equation's including exchange and correlations affects*", Phys. Rev. A 140 (1965), 1133.

[32] Perdew J. P., Burke K., and Ernzerhof M.; "*Generalized Gradient Approximation Made Simple*", Phys. Rev. Letts. 77, (1996), 3865.

[33] Zeller R., Dederichs P. H.; Phys. Stat. Solid. B 55, (1973), 831.

[34] Middya T. R., Basu, A. N. J.; Appl. Phys. 59(1986), 2368.

[35] Middya T. R., Paul M., and Basu A. N. J.; Appl. Phys. 59, (1986), 2376.

[36] Davidson L. D.; "*Transition metal alloys: elastic properties and Peierls-Nabarro stresses*", Mater. Sci. & Eng. A293, (2000), 281-291.

[37] Mofiat D. L., and Larbalestier D. C.; *"The Competition between Martensite and Omega in Quenched Ti-Nb Alloys"*, Met. Trans. 19A, (1988), 1677-1686.

[38] Cotton A., Daniels L. M., Hillard E. A., and Murillo A. Carlos; "*The lengths of molybdenum Quadruple bonds: correlation, Explanations and corrections*", Inorganic Chemistry 41(2002) 2466-2470.

[39] Grad G. B., Benites G. M., Aurelio G., and Fernandez Guillermet; "*Bond-length analysis of the omega structure in Ti, Zr, Hf and their alloys: experimental data, new correlations and implications for chemical bonding models*", Mater. Sci & Eng. A 273–275 (1999) 175–180.

[40] Aurelio G., and Fernandez Guillermet A.; *"interatomic distances of the hexagonal omega structure in Ti-V alloys: Neutron diffraction study and analysis of bonding related regularities"*, Scripta Mater .43 (2000) 663-669.

[41] Dupouy J. M., and Averbak B. L.; "*Atomic arrangements in titanium-molybdenum solid solutions*" Acta Metal. 9, (1961), 755-763.

[42] Hake R. R., Leslie D. H., and Berlingcourt T. G.; "*Electrical resistivity, Hall Effect and superconductivity of some bcc Ti-Mo alloys*", J. Phys. Chem. Solids 20 (1961) 177-186.

[43] Kaufman L.; Act Met. 7. (1959), 575.

[44] Hickman B. S. J.; Inst. Metals 96, (1968), 330.

[45] Fisher E. S., and Dever D.; "*Relation of the c′ elastic modulus to stability of b.c.c. transition metals*", Acta Met. 18 (1970), 265-269.

[46] *Metals, Thermal and Mechanical data,Vol 16 of International tables of selected constants*, edited by S. Allard (Pergamon Press, New York,1969).

[47] Bungaro C., Rabe K. M., and Dal Corso A.; Phy.Rev.8, (2003) 68.

[48] Wuttig M., Lui L. H., Tsuchiya K., and James R. D.; J. Appl. Phys.87 (2000) 4707.

[49] Ren X., and Otsuka K.; Mater. Sci. Forum 327-328 (2000) 429.

[50] Ren X., Otsuka K., and Suzuki T.; J. Alloys and Compds. 355(2003)196

[51] Niinomi M.; "Low Modulus Titanium Alloys for Inhibiting Bone Atrophy", Biomater. Sci. & Eng.15 (2011)249-268.

[52] Zhoua Y-Long, Luob D. M.; "*Microstructures and mechanical properties of Ti–Mo alloys cold-rolled and heat treated*", Materials Characterization 62 (2011) 931-937.

[53] Zhao X., Niinomi M., Nakai M., and Hieda J.; "*Beta type Ti–Mo alloys with changeable Young's modulus for spinal fixation applications",* Acta Biomater. 8 (2012) 1990–1997.

[54] Tane M., Akita S., Nakano T., and Hagihara K.; Acta Mater. 58 (2010) 6970.

Chapter 5

Systematic Characterisation of Orthorhombic Phase in Binary Ti-Mo Alloys

5.1 Summary

A detailed investigation has been made of the formation of orthorhombic martensitic phase in the Ti-Mo alloy system. The reason for the orthorombicity has been attributed to atomic movement along the y coordinate plane without breaking the group symmetry, assuming the size factor influence is negligible. The orthorombicity tends to disappear with increase in molybdenum content.

5.2 Introduction

It has been reported that the phase transformation of β-Type Ti alloys is strongly influenced by the content of different alloying elements [1-2]. This pertains to their formation in both equilibrium and non-equilibrium phases. Most of the important properties of these alloys seem to be strongly dependent upon the lattice instability of β phase and the amount of thermal treatment. The β phase is stabilised by the alloying elements known as β stabilisers. For example: transition metals such as Mo, Nb, Ta, W, V, etc. are known as β stabilising elements of titanium alloys. Among these, the binary Ti-Mo alloy system shows almost all the types of phase transformations that are reported in titanium alloys [1, 2]. Apart from the equilibrium phases β and α, the Ti-Mo system exhibits non-equilibrium phases after quenching, such as hexagonal martensite (α'), orthorhombic martensite (α'') and ω phases. The importance of these non-equilibrium phases is highlighted by a huge interest in them in recent literature. For example, a detailed study of reverse transformation α'' to β phase has been reported in literature [3-7]. In the past, this system has also been examined in the study of biocompatibility [8-10]. This involves an evaluation of the functional characteristics of the alloys such as Young's modulus and shape memory effect.

The hexagonal martensite (α') and orthorhombic martensite (α'') types of martensitic structures have been observed in titanium alloys, depending on the content of β alloying elements and cooling rates applied [1,2, 8-20]. Higher β stabilising content results in the formation of α'' martensite in preference to α'. The critical composition limits of the β alloying elements in binary Ti-X (Mo, Nb, Ta, W, etc.) alloys for the formation of α'' phase have been reported in the literature, but agreements concerning Ti-Mo alloys is not present in the literature.

The solute influence on the kinetic of β-α'' transformation has been studied by Jepson *et al.* [20] using a series of Ti-Nb alloys. They showed that martensitic transformation temperature (Ms) depends on the critical cooling rate (r_c), which decreases with an increase in Nb concentration. In effect, this decreases the Ms and makes the β-α'' transformation more sluggish. The critical cooling rate, r_c for unalloyed Ti, is 10^2°C/s and reduces to 0.3 °C/s after the addition of 10 at.% Nb [20].

It was Jepson *et al.* [2] that were first to report on the structure of α″ martensite being orthorhombic with Cmcm (mmm point group symmetry) space group [11]. The unit cell has one type of Wyckoff position, which is 4(c) — (0, y, 1/4), (0, y, 3/4), 91/2, y+1/2, 1/4), and (1/2, y+1/2, 3/4) — with site symmetry m2m. The details of the crystallographic structure of α″ phases, such as lattice number of atoms per unit cell, space group, equivalent position of atoms, and their respective symmetries are given in Table 5.1. Noting that α″ is a disordered phase, all the 4(c) positions in Table 5.1 are occupied by all the alloying elements. From this data, β-α″ transformation can be viewed in terms of sub group/supergroup symmetry relations among the high symmetry BCC (1m-3m) to lower symmetry orthorhombic (Cmcm) subgroups as proposed by Bendersky *et al.* [10]. The sub groups are connected to each other with arrows pointing in the direction of decreasing symmetry. This can be shown as

$(1m - \bar{3}m)(\beta)$ →14/mmm→ $Fmmm \rightarrow Cmcm$(α″)

It has been explained that the direct formation of the lowest symmetry phase is made possible by reconstructive transformation.

It is well known that alloy properties are governed by phase content and they depend additively on the ratio and properties of the constituent phases. Considering that α″ phase has been observed in several commercially important α+β and β Ti-Mo alloys (for technological reasons such as potential use as a biomaterial), and the goal of this work, it is important that we carry out the comprehensive investigation of α″ phase in Ti-Mo alloy systems that is lacking. The effect of Mo element on phase stability and the deformation mechanical behaviours of Ti-Mo alloys were studied at cast condition.

Table 5.1: EDX chemical composition (at. %) of the multi component specimens, (Md is in eV) and α'' phase parameters.

Alloys	Mo	O	N	Ti	e/a	S.occ.	Y(Å)	Lat. (a)(Å)
Ti-3Mo	3.2	0.05	0.023	bal.	4.07	0.086	0.1821	2.994
Ti-5Mo	5.15	0.06	0.013	bal.	4.08	0.132	0.188	3.007
Ti-6Mo	6.3	0.07	0.013	bal.	4.09	0.156	0.194	3.021
Ti-7Mo	7.12	0.09	0.017	bal.	4.12	0.17	0.195	3.061
Ti-8Mo	8.21	0.05	0.017	bal.	4.14	0.174	0.219	3,213
Ti-9Mo	9.3	0.05	0.11	bal.	4.18	0.181	0.221	3.212
Ti-10Mo	10.30	0.05	0.017	bal.	4.2	0.19	0.224	3.211
Ti-12Mo	12.2	0.05	0.005	bal.	4.24	0.211	0.228	3.209
Ti-15Mo	15.16	0.06	0.017	bal.	4.28	0.22	0.271	3.202
Ti-20Mo	20.12	0.09	0.022	bal.	4.38	0.241	0.281	3.1788

5.3 Experimental Procedures

5.3.1 Design and fabrication processes

The alloys were prepared by arc melting appropriate amounts of high purity Ti and Mo rods (99.98%) with a non-consumable tungsten electrode under a high purity argon atmosphere. The chemical compositions, as well as details of the atomic parameters and the e/a numbers [1-2] of all the alloys are presented in Table 5.1.

To ensure optimal chemical and structural homogeneity, each button was remelted and turned over six times. The final ingot was cast into a cylindrical sample of ≈ 90 mm in length and 8mm in width. This led to rapid solidification and suppression of dendritic formation. The copper mould had a temperature of about 20^0C, which led to rapid solidification and suppression of segregation. All the cast samples were subjected to homogenisation in quartz tubing at 1200 °C in an argon atmosphere for five hours in to remove microsegregation. These samples were quenched in water, which led to rapid solidification to suppress dendrite formation, while mild solution heat treatment was carried out at 1100°C for five hours to remove microsegregation.

In agreement with earlier works by Blackburn *et al.* and Saito *et al*. [1-4], the composition range for the alloys studied was designed within the range where α, β+ α″ or only β exist in the Ti-Mo system. The chemical composition of the specimens with differing Mo concentrations are given in Table 5.1. (In this work, all the compositions are given in at.% units unless otherwise noted.) Mo is known as a one of the best β stabilising elements. According to the coefficient of β stabilisation, the stability of β is defined in eqn. 5.1 as:

$$K_\beta = \sum_i \frac{c_i}{\beta_{c_i}} \tag{5.1}$$

Where, βc_i is the concentration of the β stabilising element in the alloy and $\beta_{c_i}$is its critical concentration. The Titanium alloy whose K_β is in the region of 1-1.5 (i.e. 1 <K_β <1.5) was defined as metastable β alloy. For Ti-5Mo alloy, the K_β is 1.1, which classifies the alloy as the metastable β category. Previous experimental investigations have shown that α'' and β phases coexist within 5 -10 at.% Mo threshold [4]. In effect: we chose Ti-5 at.% Mo alloy to evidence the effect of $\beta+\alpha''$ coexistence in deformation behaviour and to evaluate the influence of biocompatible elements such as Mo, Nb, Ta, Zr, Hf and Sn on Ti phase stability and Young's modulus lattice. This is discussed in the next part of this study, Chapter 6.

5.3.2 Microstructural observation

The samples for light and secondary electron microscopy were prepared by mechanical polishing using 10% H_2SO_2 in 0.25 μm colloidal silica, and then etching in a solution of 8 vol. % HF and 15 vol. % HNO_3.

In order to identify the constituent phases of the binary Ti-Mo alloy microstructures, wide angle XRD was done on Siemens D5000, using Cu Kα radiation and graphite monochromator operated at 40 kV and 250 mA.

Optical microscopy was carried out on a Leica DFC320 image analyser (Model: Q550IW) interfaced with Leica Q-win V3 Image analysis software, while scanning electron microscopy (SEM) images were obtained using Inspect F-FEG SEM operating at 20 KV. Optical micrographs of the polished samples were taken using a digital camera attached to the microscope and interfaced with a computer. Samples were prepared by following standard metallographic techniques. The polished samples were etched with Kroll's reagent (10 vol. % HF and 5 vol. % HNO_3 in water). For the quantitative phase, analysis was performed with an X'Pert Highscore software package.

Orientation maps of T1-5Mo specimen were acquired using the technique described in section 3.4 of Chapter 3. These specimens were assumed to have random orientations.

5.3.3 X-Ray measurements and analysis

Phase constitution was investigated using XRD diffuse scattering measurements at room temperature with monochromatic CuK and radiation diffracted from a bent silicon crystal cut to the (111) orientation. The detecting assembly consisted of a proportional counter and a pulse height analyser arranged to eliminate the one-third wavelength of the white radiation (the one half component was eliminated by the silicon crystal), the cosmic background and the fluorescence radiation from titanium. Readings were recorded continuously on a horizontal spectrometer with the counter rotating at 0.25^0 in 2Θ/min, and measurements were made from 10 to 100^0 in 2Θ. Flat samples were used and the geometry of the system satisfied the usual focussing condition.

The microstructure was cross examined using electron backscatter diffraction (EBSD) after grinding on 400, 600, 1200 and 2400 paper with subsequent use of 6 μm(35min), 3μm (20min), and 1μm(15min) polishing.

5.3.4 Evaluation Mechanical properties

The mechanical properties of the prepared alloys were evaluated by performing a hardness test and Young’s modulus measurements. The static indentation test was performed using a 10N load for one minute on a Vickers's pyramid shaped indenter on the surface of the metallic specimens after mirror surface polishing. The relationship of the load to the area of indentation is a measure of hardness.

The Young's modulus measurements were calculated to investigate the change in Young's modulus with x content of Mo, which are essential elements in the alloy.

The Young's modulus of the samples was measured by ultrasonic method on an ultrasonic velocity gauge, Olympus 62, UK. A normal incident probe (model M110, 5MHz) and a shear probe (model V221, 5MHz) were used for the measurement of normal and shear velocities of the wave, respectively. The density of the samples was measured on an automatic density meter; for at least five times.

The relationships between ultrasonic velocity and the elastic properties of materials are given below [24-29].

Young's modulus (E) is expressed as:

$$E = \frac{\rho V_S^2(3V_L^2-4V_S^2)}{V_L^2-V_S^2} \qquad (5.2)$$

Shear modulus (G) is the ratio of shearing stress τ to shearing strain γ within the proportional limit of a material and is expressed as:

$$G = \rho V_S^2 \qquad (5.3)$$

Poisson's ratio υ is the ratio of transverse contraction strain to longitudinal extension strain in the direction of stretching force, and is expressed as:

$$\upsilon = \frac{\left(\frac{1}{2}\right)(V_L^2 - 2V_S^2)}{V_L^2 - V_S^2} \qquad (5.4)$$

In the above set of equations, *V*L and *V*S are the ultrasonic longitudinal and shear wave velocities, respectively, and ρ is the density of the material.

5.4 Results and discussion

5.4.1 Chemical analysis

The x-ray energy dispersive spectoscopy (EDX) were performed in many different areas (Bulk and surface) and results show that the actual chemical composition of the alloys is close to their nominal values (Table 4.1) and agrees with ASTM F-67. The chemical composition of the alloys was homogeneous and no expressive differences between surface and bulk were found.

5.4.2 Metallographic analyses

The martensitic structure in the as quenched Ti-(2-4) Mo alloys are predominantly of the type of massive colonies of parallel plates separated by small angle boundaries. Since this area is not our main area of interest, we have shown Ti-4% Mo is a representative of α′ microstructure in Figure 5.1(a). The structure is made of a greater proportion of relatively large plate-like crystals, with some massive colonies as well as dislocations and stacking faults were also observed in the alloy; while in the alloy with higher molybdenum content — for example in Figure 5.1(b) (Ti-6%) — colonies of acicular martensitic structure of α″ phase were observed. When Mo content was 7% at.% (Figure 5.1c), the greater part of the sample was dominated by the α″ phase. Above this composition, increased precipitation of Mo and internal twinning of the plate type was occasionally observed, as shown in Figure 5.1 (d-f). A significant amount of equiaxed, retained β phase became the only dominant phase.

It is observable that the microstructure changed or refined progressively with increasing molybdenum content. This is evident in Ti-10% alloy in Figure 5.1e. The microstructures of the series of Ti-Mo alloys (as shown in Figure 5.1) were consistent with the XRD results. The absence of martensitic structures in the specimens having Mo ~>6at% shows that perhaps Mo is a better β stabiliser even at lower e/a, Md and Bo parameters than Nb, which is reported to gain β stabilisation at high e/a (~4.25).

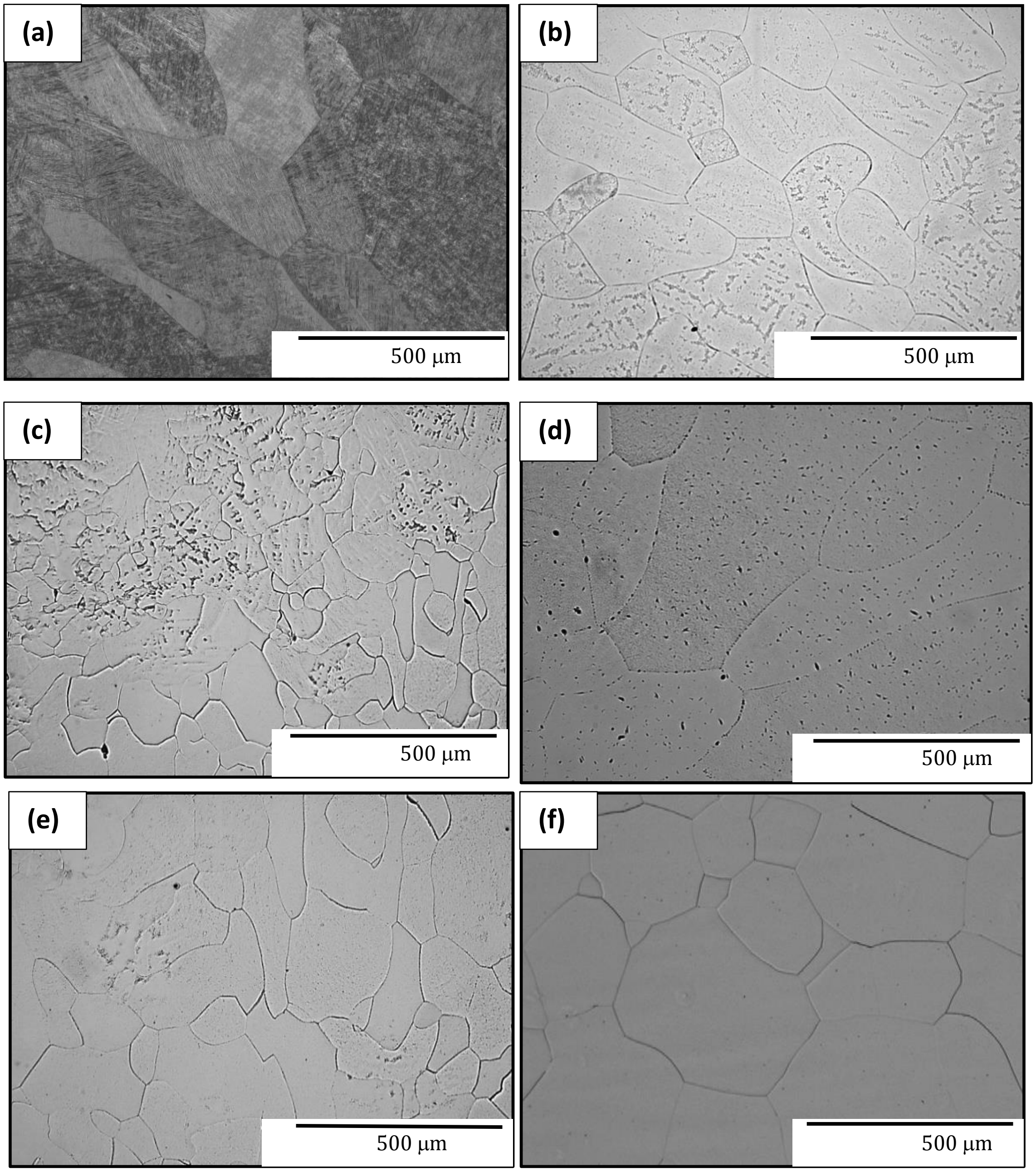

Figure 5.1: optical micrograph of (a) Ti-4Mo alloy; (b) Ti-6Mo alloy; (c) Ti-7Mo; (d) Ti-8Mo alloy; (e) Ti-12Mo alloy and (f) Ti-15Mo alloy revealing the internal structure the specimens. The observed plane is normal to the casting direction (CD) and the horizontal direction is parallel to the rolling direction (RD).

5.4.3 **XRD analyses**

In order to investigate the phase constitutions in the binary Ti-Mo system, XRD analyses was carried out at room temperature. Figures 5.2(a), (b) and (c) show the XRD profiles in groups of Ti-(2-4)Mo, Ti-(6-9)Mo and Ti-(10,12,20,25)Mo alloys respectively, scanned from 30 to 80 degrees in diffraction angle (2θ).

The results obtained in this study show that the crystal structure of the binary Ti-Mo alloys is sensitive to the molybdenum concentration (Figure 5.2). By comparing the results obtained for different alloys (Fig. 5.2), it can be seen that the martensitic structure gives rise to a mixture of the hexagonal α and that α′ phases was observed for the Ti-(2-4) Mo. In addition, a mixture of α′ and ω were observed almost exclusively when the concentration of Mo was added to the Ti reaching 4%. The strain in the lattice resulting from the martensitic transformation (see Figure 5.2) caused a slight broadening of the high angle lines, but no lines due to the β phase were observed.

The diffraction patterns — as shown in Figure 5.2 for the TI-(6-9) Mo alloys — were notably different. The splitting of 110 β diffraction peak into {00n} lines was observed in the Ti-(5-6) alloys. These were consistent with the (002) and (020) peaks of α″ martensite by Ho *et al.* [17], due to a change in crystal symmetry from hexagonal to orthorhombic at composition greater than 4%. The splitting of the diffraction lines was greater in the 6% alloy due to an increased orthorhombic distortion, and no lines due to β phase could be detected in the 5%.

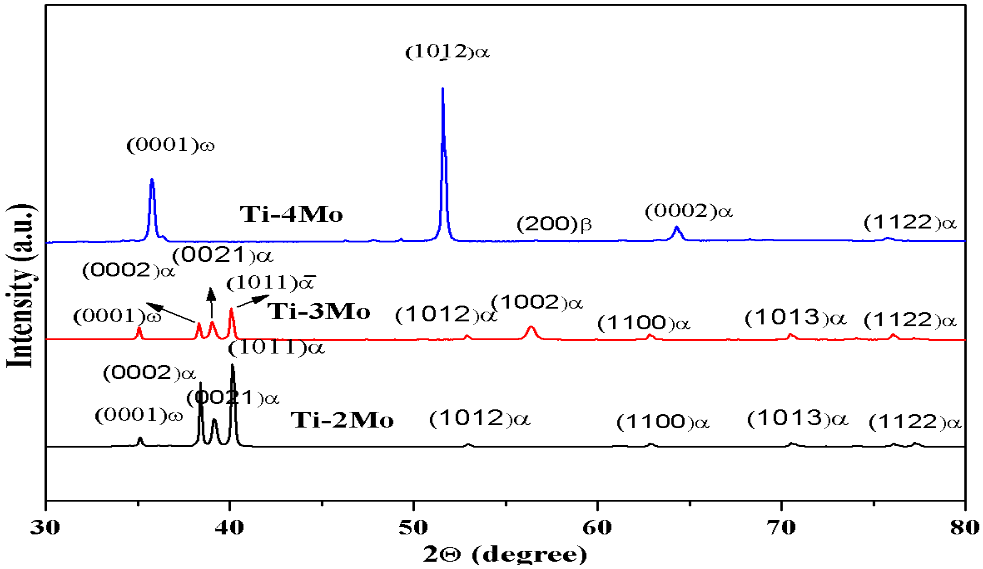

Figure 5.2.: XRD profiles of Ti-(2-4) Mo alloys, scanned from 30 to 80 degrees in diffraction angle (2θ), revealing reflections due to the phases in the Ti-Mo specimens.

A significant retention of β phase is observed for the alloys containing 7%; while, for the higher Mo concentrations shown in Figure 5.4, retention of single β phase is very apparent in the X-ray diffraction spectra. A high intensity of the first two reflections of β phase that occurs at angles of ~38.5 (110β) and ~55.5 (200β) are evident in their profiles. This retention is reminiscent of Ti alloys with higher Mo concentrations in accordance with results presented earlier by Davis *et al.* [15], who reported that in Ti-Mo systems martensitic structures change from hexagonal α′ to orthorhombic α″ at Mo rates of 6%. The diffraction peaks of the α″ or ω phase have not been detected, although the intensity of ω phase is not always high enough to provide evidence of the presence of ω phase when the ω phase has quite a small size or volume fraction. It is known that, under the Ti-Mo binary system, Mo lowers the β transus and promotes the formation of the β phase, while also suppressing ω and α″ in high concentrations alloys. This finding is in agreement with past studies in which Mo was found to stabilise the β phase for Mo concentrations exceeding 5 at.% [1-2]. This suggests that we may control the phase stability and enhance solid solution strengthening by increasing molybdenum content in Ti.

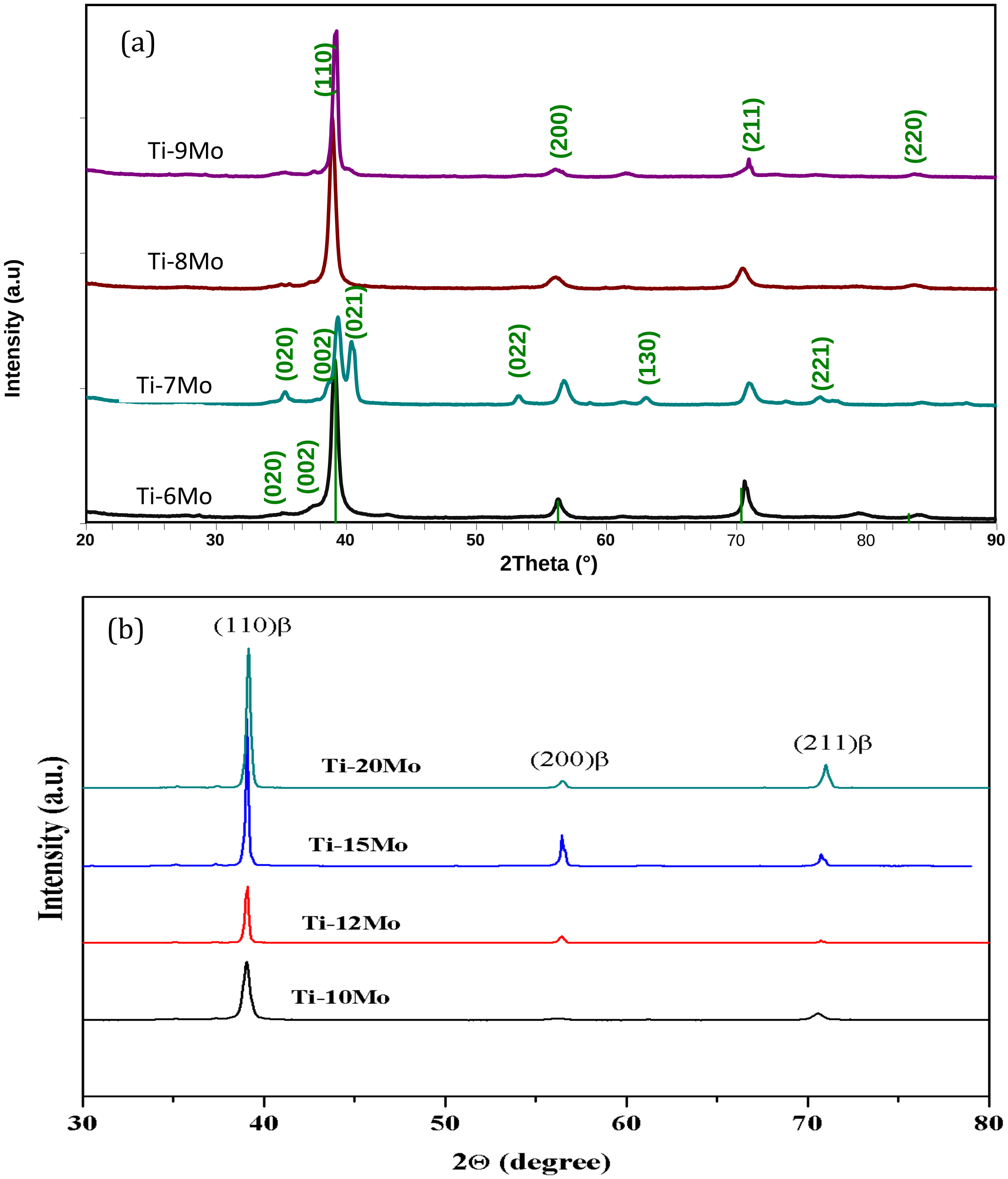

Figure 5.3: XRD profiles of (a) Ti-(6-9) Mo alloys and (b) Ti-(10, 12, 15, 20) Mo alloys, scanned from 30 to 80 degrees in diffraction angle (2θ), revealing reflections due to the phases in the Ti-Mo specimens.

It is well known that the identification of α" by XRD is precise usually only to a value of 1–3 vol. %. In addition, the presence of crystallographic textures will usually further reduce the precision of the X-ray analysis for small amounts of a second phase. Cu Kα_1 radiation may create minor false intensity contributions such as those caused by fluorescence. The use of electron microscopy can also be problematic, as other crystal forms of the martensite phase have mistakenly been observed. For example: a face-centred cubic or tetragonal martensite has been detected in some Ti alloys [21]. To evidence the stability, we combined electron microscopy with the EBSD map shown in Figures 5.4 and 5.5 to determine the volume fraction of the least stable β alloy (i.e. Ti-5 at.%Mo), which proved helpful in evaluating the effect of elemental addition on the alloy. An advantage of this approach by EBSD is that it can be easily obtained automatically from variations in the grain and subgrain sizes of the alloys.

The SEM micrographs of various degrees of magnification and EBSD map of Ti-5 at.%Mo alloy are presented in Figure 5.5, illustrating a typical finer acicular martensitic structure also indicative the α′′ phase. This observation is in agreement with that offered by the Ti-Mo-Al alloys, in which the martensitic microstructures become finer with increases in Mo content. The EBSD images presented in Figure 5.5(a) give experimentally observed microstructures for Ti-5at.% Mo binary alloys. One can observe from Figure 5.5(b) that grain sizes in the range 0- 100μm, are actually the martensitic structures that have been quantified as sub grain structures in the map. Based on this technique, we have calculated the volume fraction of orthorhombic martensite in Ti-5Mo to be ~37% of the matrix.

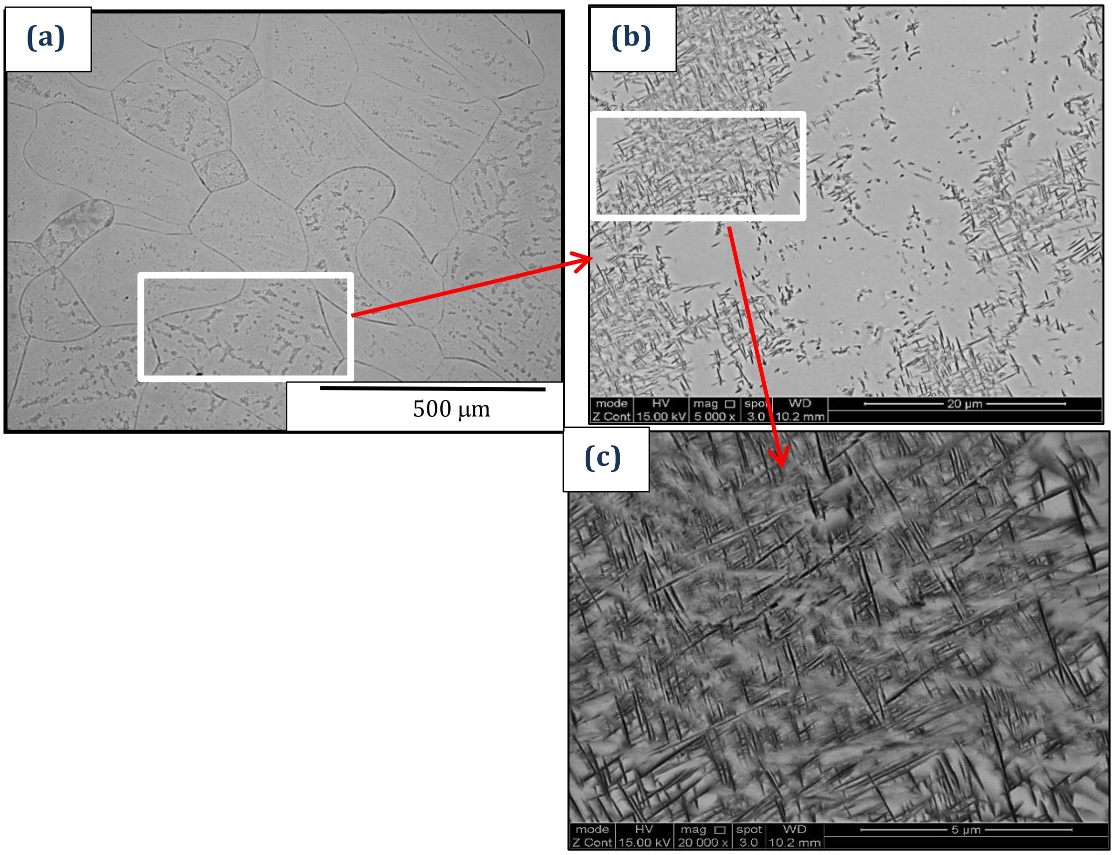

Figure 5.4: Acicular martensitic areas from (a) Light optical micrograph of Ti-6Mo; (b) high magnification SEM image of the area marked in (a) and (c) higher magnification of (b) revealing orthorhombic α′′ martensitic phase in the specimens.

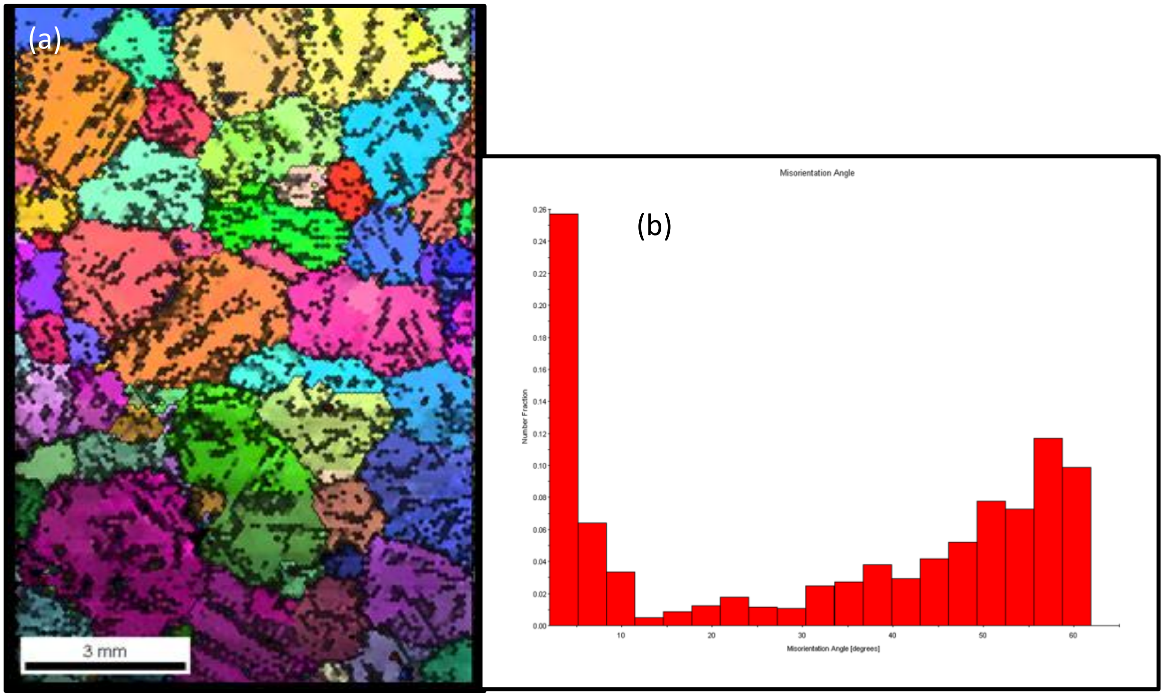

Figure 5.5: (a) EBSD map of Ti-6Mo alloy indicating revealing the α'' martensitic structure ; and (b) quantified volume fraction for the grain and sub grain structures of the map In (a).

5.4.4 Analyses of structural transformation in Ti-Mo

The XRD profiles obtained from the experimental alloys have been subjected to the Rietveld refinement technique using XPERT PLUS software [22]. The data for the initial models for the Rietveld refinement (such as space group, Wyckoff positions) corresponding site occupancy and alloy composition have been taken from Tables 5.1.

A schematic of the crystal structures of the β and α'' phases and their lattice correspondence are shown in Figures 5.6(a) and 5.6(b) [23]. The [001] projection and atomic projection according to the international Table for crystallography for α''phase is given in Figure 5.6(c). A critical observation of the 4 (c) positions of the α′′ phase (Table 5.1 and Figure 5.6) reveal that all the atoms in ¼ and ¾ layers are related to the diagonal and axial glide movements. This means that an atom that lies on either ¼ or ¾ layers can move along the mirror plane parallel to the Y-axis (parallel to the B-axis) and the range of this movement is limited by the position of the projected glide planes.

The present alloys consist of Ti and Mo atoms which are of unequal atomic sizes. The atoms can therefore move along the Y-axis in the range 0-b/2, before atomic size concerns. As a consequence, assuming d is the diameter of the atoms, the actual limit of atomic movement of one of the Wyckoff positions without breaking Cmcm space group symmetry is between d/2 and (b/2-d/2), implicitly leading to a contracting of the “a” axis. Here, “b” is one of the lattice constants of the α′′ phase parallel to Y-axis.

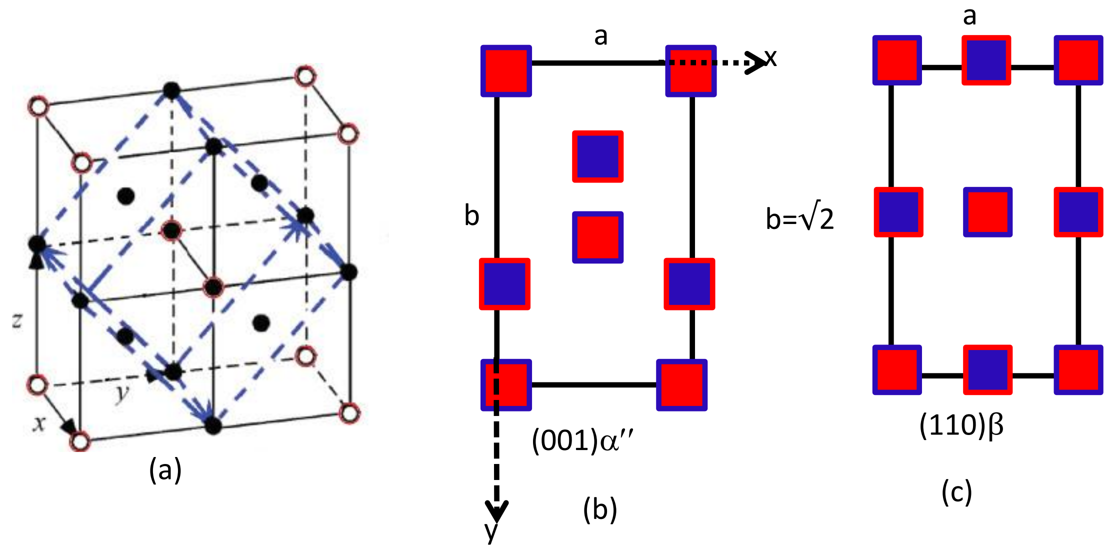

Figure 5.6: Schematic representation of the lattice correspondence between β and α′′ phases. (a) A combination of four BCC unit cell. The atoms that are involved in the formation of the α′′ phase are shown in filled circles while the corner atoms are open circles [2]; (b) the (001) projection of the α′′ phase with atoms presented by blue dotted circle on red border line corresponding to ¼ layer while the atoms filled with red on blue border line correspond to ¾ layer; and (c) the (110) projection of β phase, blue filled represented atoms on the layer below or above the layer corresponding to the atomic coordinate for α′′.

The refinement has been done for the α′′ phase by fixing the space group (Cmcm) and the corresponding Wyckoff positions. The occupancies of the Ti and Mo atoms on 4(c) sites are fixed according to the analysed alloy compositions (Table 5.1). The refinement data has a goodness of fit (GOF) and their corresponding lattice parameters can be seen in Table 5.1.

The refined values of y coordinates for the alloys studied are given in Figure 5.7 (see Table 5.2). From the table, it is evident that the values of the coordinate are within the limit described above, and that they increase with an increase in Mo concentrations. The variations in the Y coordinates seen in the results justify the atomic movement and shift in the alloy with increasing Mo concentrations. As explained previously, as a consequence of the variations in y coordinates and interatomic potentials, the bond length in the respective neighbour atoms can be expected to change with an increase in Mo content.

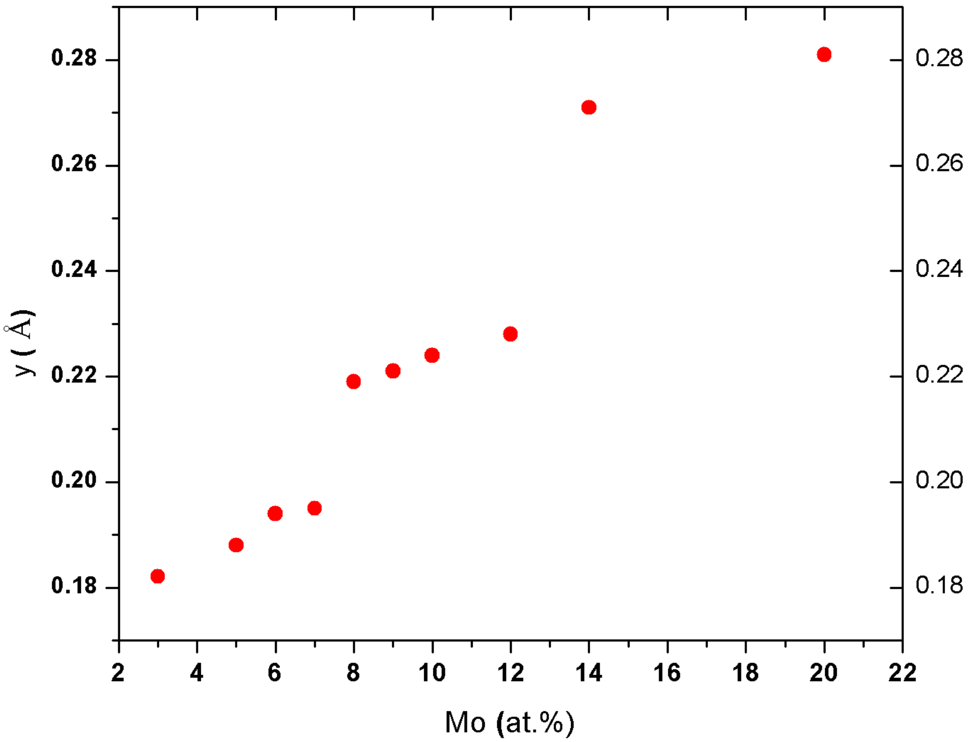

Figure 5.7: the variation of y coordinates as a function of Mo concentration.

The usual position of y corresponding to hexagonal symmetry is 0.1666 [24]. The corresponding positions obtained in the experimental alloys consisting of an orthorhombic α'' and body-centered β crystal phases are higher than 0.1666 and increase with an increase in Mo concentration. It can be inferred from this result that orthorhombic α'' martensite exists in Ti-Mo alloys beyond the critical composition of the β alloying of elements [1-2]. In the case where the Mo is lower (Ti-2Mo, Ti-3Mo and Ti4Mo), the fact that orthorhombic α'' is not observed is evidence of the existence of hexagonal α in the specimen. Additionally, due to a higher concentration of Mo (β stabilising), the atoms are not able to reach the hexagonal positions during martensitic transformations, thereby breaking hexagonal symmetry and forming orthorhombic α′′ crystal structures. It is to be noted that this space group (Cmcm) is an intermediate subgroup of the β ($1m\overline{3}m$) as well as the α′ ($P6_3/mmc$) phases. The increase in the y values with increases in Mo concentration also suggests that the atomic shift in the more stabilised β phase is expected to become difficult during β→α′′ transformation. As a result, alloys with higher concentrations of β stabilisers (Mo) exhibit the highest value of Y.

The lattice parameters of the experimental alloys obtained by Rietveld refinement technique are given in Table 5.2. This data evidently reveals that the "a" parameter expands with an increase in Mo content, while the "b" and "c" parameters contract with an increase in Mo concentration. The results are in agreement with those gathered by Kim *et al.* [23]. The orthorhombicity $\left(\mathrm{b/a}\sqrt{3}\,\right)$ of the present study has been plotted against Mo concentration and presented in Figure 5.8, which decreases with Mo concentration. This trend is in line with the observation of Bywaters *et al.* [19] on orthorhombicity with an increase in Mo equivalent in Ti-Ta binary alloys.

Brown *et al*. [11] observed that, since the crystal structure of the martensitic phase has shown an eightfold coordination around each (Ti, Nb) atom with four additional neighbours at a slight greater distance, the reason for the formation of the α′′ in preference to α′ in Ti-Nb binary alloy beyond a critical concentration of Nb may be a reflection of a tendency for Nb to retain the eightfold coordination obtained in BCC titanium. On the other hand, looking at the results of the present study, we think that the difference in atomic size of both Ti and Mo atoms will likely account for the distortion leading to the orthorhombic symmetry, unlike in Ti and Nb where their atomic radii are nearly the same.

Similarly, the calculated result of principal strains for pure Ti and Ti-Mo alloys having both α′ and α″ martensitic phase, as demonstrated by Davis *et al.* [18], show that the ε_3 is small in all the martensitic structures. The values of all the principle strains are reduced in the orthorhombic α″ martensitic phase, as compared to those of the hexagonal (α′) phase. It has been explained that orthorhombic α″ martensitic structure is an intermediate phase between the BCC and hexagonal structures. As a result, β →α″ transformation is associated with a smaller strain than that of β→α′.

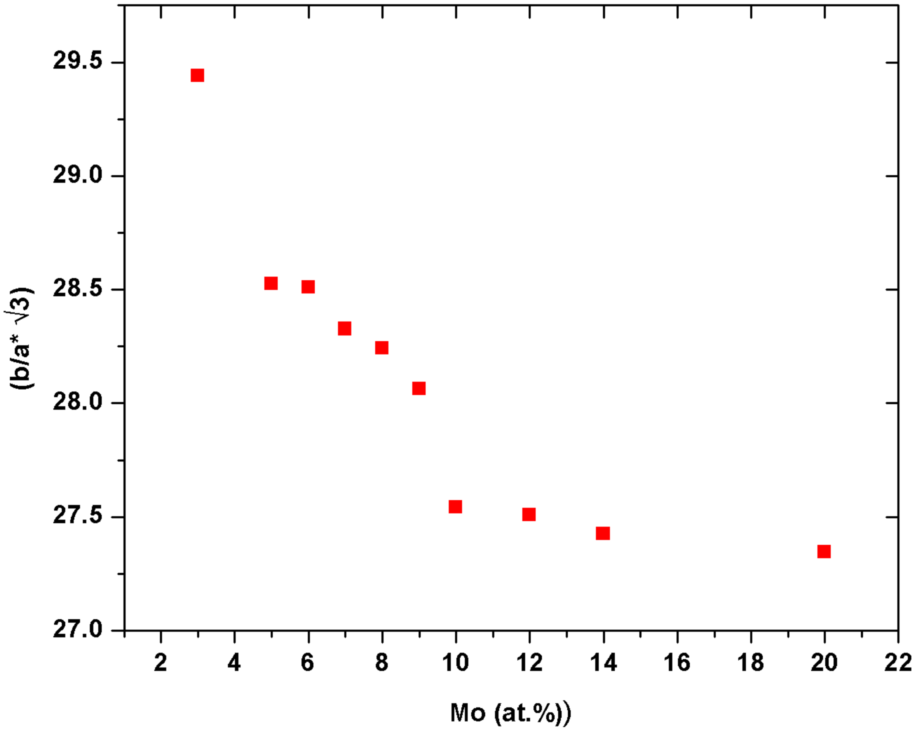

Figure 5.8: Variation of orthorhombicity with Mo concentration.

5.4.5 Evaluation of stress induced martensite

Stress-induced transformation was studied in two alloys: one representing low Mo (metastable) alloy (Ti-10at%Mo), while the other is fully transformed β (Ti-20%Mo) alloy. We performed cold rolling in order to study the stress required for stress-induced martensite to occur in the two alloys. Applied stresses ~ 210 MPa was enough to study the inducement of β→α″ martensite transformation in both alloys. The initial micrographs and XRD profiles of the two Ti-Mo alloys before cold rolling consisted of single β phases. The investigation has shown that application of stress to metastable alloys induces transformation to martensite, which is an orthorhombic structure. Figure 5.9(a) has shown that it is thermodynamically possible for stress induced martensite to form in metastable β alloys upon deformation, because while their Ms temperatures ranges lie well below room temperature, the Md, (i.e., upper temperature limit above which transformation cannot occur under stress) lies around room temperature. This is because the specific volume of α″ and β are identical and β →α″ transformation involves smaller principal strains (< 3%) than those required to produce the HCP structure, an applied stress can simply stabilize those martensitie variants which best accommodate the applied stress. Following this, orthorhombic structure can easily be visualized as an incomplete progression of the β →α reaction, an intermediate structure between β and α, as evidence in the complementary XRD spectra dominated by α″ instead of β in Figure 5.8(c).

In contrast, high density of randomly arranged dislocations, rather than the stacking faults and twins are observed in Figure 5.9(b) after deformation. This is not unexpected since metastable β alloys that have lower solute content are prone to such transformations. Since the Ms is above room temperature, it is possible for martensite to form by by shearing the metastable β alloy, because the Ms, depends upon the net driving force, it can be raised or lowered by the application of external stress.

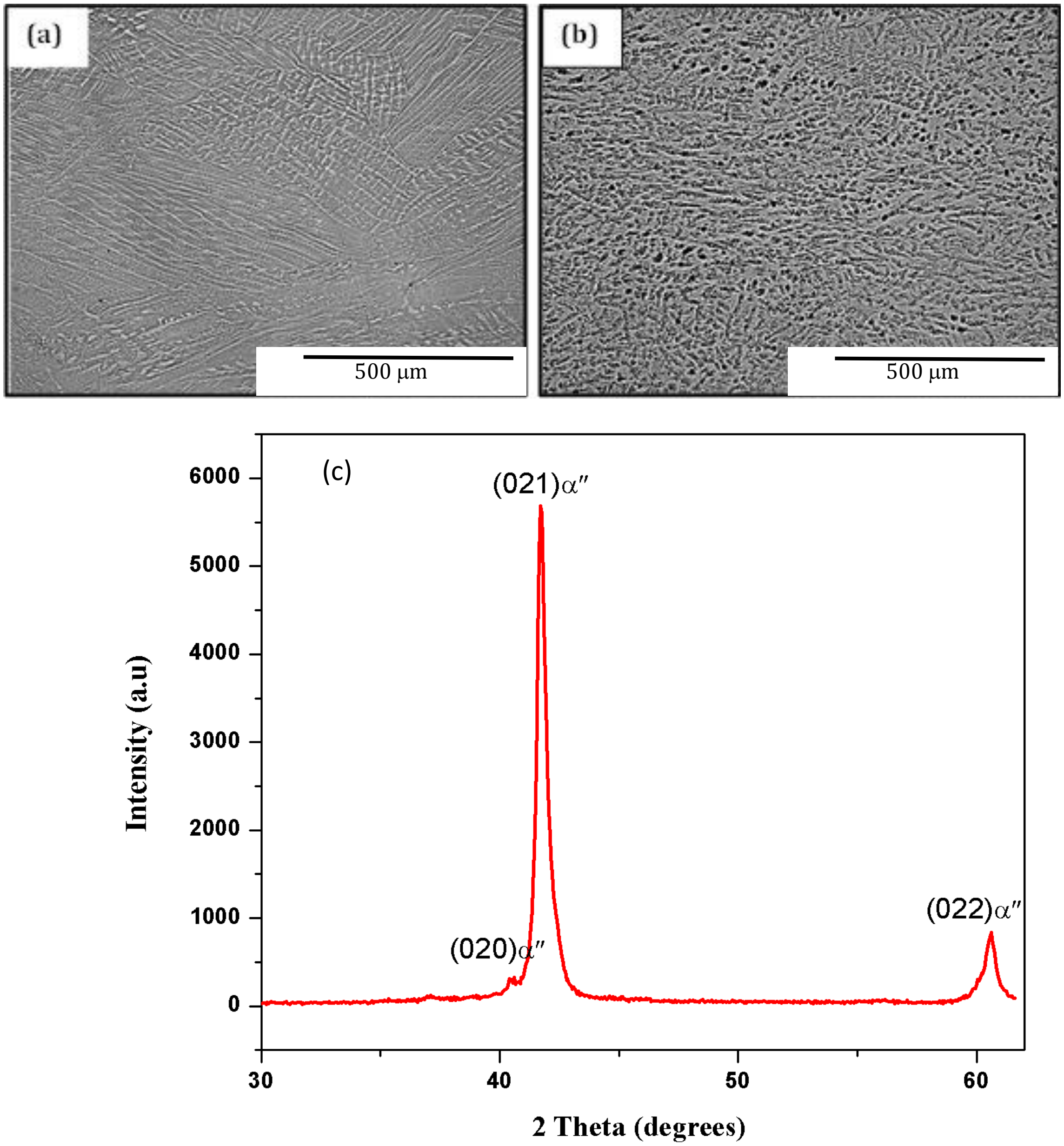

Figure 5.9: Microstructure of as deformed condition (a) light micrograph of Ti-20%Mo and; (b) Ti-10%Mo, revealing the difference in internal structure as a result of phase difference for the specimens, (c) the XRD profile obtained after cold deformation of (a).

5.4.6 Mechanical properties

Figure 5.10 compares the measurements of hardness of a series of the binary Ti-Mo alloys and Ti-6Al-4V. This is because Ti-6-4 has been, for some time, an alloy of choice for bio metallic implant application. The trend depicted in the Figure shows that alloys that exhibit α″ orthorhombic martensitic phase (Ti-6Mo and Ti-7Mo) possess significantly lower hardness values (≈301-305 HV), and that the β phase alloys had the highest value — particularly the alloy at the onset of β phase stability. Generally, it is well known that unalloyed Ti is less hard than most of the alloys, including those of Ti-Mo. This can be attributed to two factors: the first is the higher solid solution effect, precipitation hardening exhibited by β phase due to increasing Mo concentration. The other can be linked to the grain size and phases exhibited by the samples.

The low hardness observed in the alloy containing α″ orthorhombic is not unexpected as this is mixture of the hexagonal and orthorhombic martensite, with smaller strain manifested in the form of twinnings required for its transformation from dislocated hexagonal phase into β.

It is notable that the more stable β alloys of Ti-15Mo and Ti-20Mo had 324.13HV and 326.98 HV respectively, which compares very well with the hardness 325.87 HV of solution-treated TI-6-4 alloys that have been accepted by bio-implant research community as a material of choice. It is clear why the hardness of Ti-5Mo was that high: since casting defects such as microsegregation and voids were not obvious in the microstructure under SEM and light microscope, the high hardness observed for the metastable β is attributable to the sensitivity of the solid solution effect.

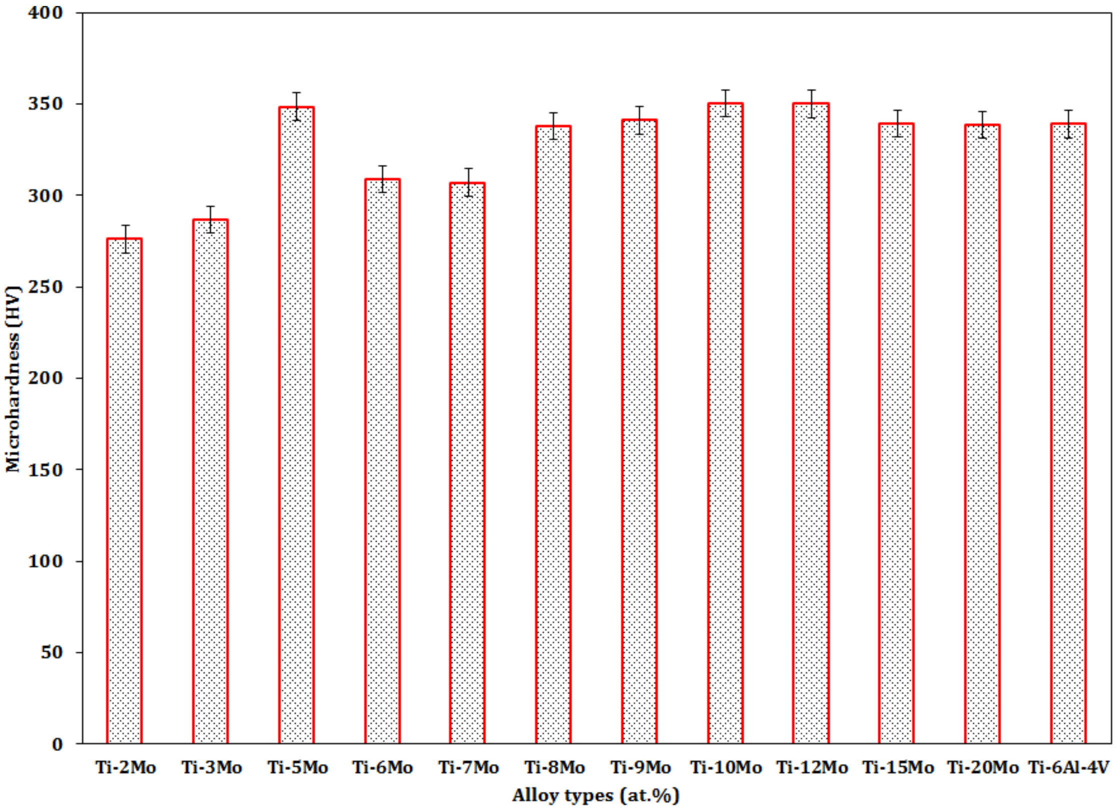

Figure 5.10: Microhardness of Ti-Mo binary alloys compared to Ti-6Al-4V alloy

Figure 5.11 shows the Young's moduli of the Ti-(3-20) Mo alloys subjected to solution treatment. All the alloys exhibit low Young's modulus, which is much lower than those of SLS 316L, CP Ti and Ti-6-4 [27]. Similar to the microhardness, the trend in Young's moduli of the alloys indicates sensitivity to the phase or crystal structure; thus, the Young's modulus first decreases and Ti-6Mo and Ti-7Mo show the lowest Young's moduli of the design alloys.

It can be recalled that the XRD and EBSD/SEM in Figures 5.3(a) and 5.5 indicated that these two alloys had α″ orthorhombic martensite phase. Thus, with a further increase, the α″ in the alloy disappears; giving way for a transition to BCC crystal structure, and the solid solution strengthening becomes the dominant factor accounting for the changes in the Young's modulus. The modulus increases as the BCC β lattice contracts at the increase in the Mo content. In line with past observations by Davis *et al.* [27] and Duerig *et al.* [28], the present results indicate that the metastable orthorhombic α″ structure in Ti-Mo alloys have the lowest Young's modulus among the α′,α″ and β phases. This could be the primary reason for the low Young's modulus around the required Mo concentration of 6 and 7%.

It is worth noting that the Young's modulus of the Ti-Mo was even lower than that of the Ti-6-4 alloy. This advantage of α″ orthorhombic structure could be exploited to further reduce the Young's modulus of future metallic biomaterials.

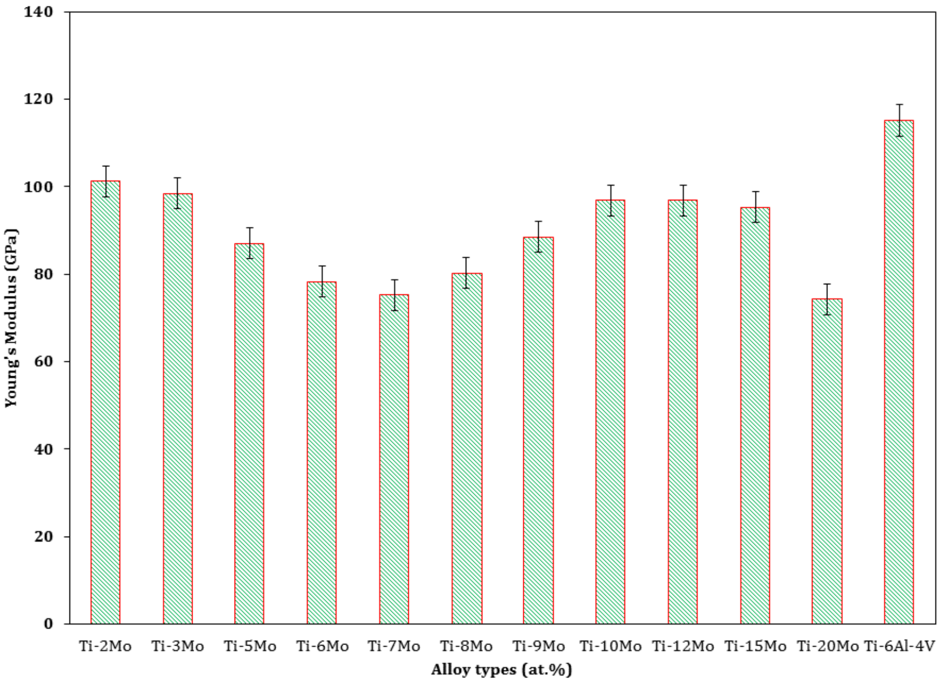

Figure 5.11: Young's moduli of the Ti-Mo binary alloys studied compared to Ti-6Al-4V alloy.

5.5 Summary

The structural properties relating to the α′′ orthorhombic phase transformation in the Ti-Mo alloy system have been studied using an optical microscope, SEM, EBSD and Rietveld refinement of XRD profiles.

1. The α′ phase exhibited massive type of colonies of parallel plates separated by small angle boundaries, while Ti-(6-7) at.% Mo alloys are observed to contain a fine acicular martensitic structure of orthorhombic α′′ phase. A further increase in Mo content resulted in a α″ transition to single β phase formation in the samples.

2. Three main reasons have been ascribed to the formation of the orthorhombic phase: (a) in view of an eightfold coordination around each (Ti, Mo) atom with four additional neighbours at a slight greater distance, the reason for the formation of the α′′ in preference to α′ in Ti-Mo binary alloy beyond a critical concentration of Mo could be a reflection of a tendency for Mo to retain the eightfold coordination obtained in BCC titanium; (b) atomic size difference can also lead to a distortion of the crystal structure; and (c) assuming the major influence of atom size is ignored, the movement/shift of the atoms along Y-atomic coordinates without breaking the group symmetry is another possible explanation. Additionally, the orthorhombicity in this alloy decreases with an increase in Mo content.

3. Possible formation of stress-induced transformation was investigated in Ti-10Mo and Ti-20Mo two alloys. The investigation has shown that application of stress of about 120Mpa to this metastable alloy (Ti-10Mo)

induced transformation in martensite that is orthorhombic in structure, but not in Ti-20Mo alloy.

4. The alloys Ti-6-7at.% containing the α'' phase had the lowest hardness of all, while the less stabilised β is observed to exhibit the highest hardness. We suggest that solid solution strengthening might be responsible.

5. The trend observed in the Young's moduli of the samples followed a similar direction to that of the hardness, suggesting that α'' might be responsible for the low hardness and Young's modulus because both are structurally related properties. It is worth noting, however, that the Young's modulus of the Ti-Mo was even lower than the Ti-6-4 alloy. Such an advantage of α'' orthorhombic structure could be exploited to further reduce the Young's modulus of future metallic biomaterials.

5.6 References

[1] Collings E. W.; Physical metallurgy of Titanium alloys (American Society of Metals, Materials Park, Columbus, OH, 1984).

[2] Boyer R., Welsh G., and Colling E. W.; Materials Properties Handbook; Titanium alloys (ASM International, Materials Park, OH, 1994).

[3] Saito T. *et al.*; Science 300, (2003), 464; Kuramoto S et al., Mater. Sci. & Eng. A 442, (2006), 454; Gutkin M., Ishizaki T., Kuramoto S., and Ovid'ko I. A.; Acta Mater. 54; 2489 (2006), 2489. W. F. Ho, *et al.*, Biomaterial 20 (1999) 2115-2122.

[4] Blackburn M. J., and Williams J. C.; "*Phase Transformation in Ti-Mo and Ti-V Alloys*", Trans. TMS-AIME, 242 ;(1968), 2461-2469. T. Grossdidier *et al.*, Mater. Sci. Eng. A291 (2000) 218-223.

[5] Hosoda H., Hosoda N., and Miyazaki S. *et. al.;* Trans. MRS-J 26 (2001) 243-246.

[6] Kim H. Y. *et al.*; *"Mechanical Properties and Shape Memory Behavior of Ti-Mo-Ga Alloy*s", Mater.Trans.45 (2004) 1090-1095.

[7] Almeida A., Gupta D., Loable C., Vilar R.; *"Laser-assisted synthesis of Ti–Mo alloys for biomedical applications",* Mater. Sci. Eng. C 32 (2012) 1190–1195.

[8] Al-Zain a Y., Kim H. Y., Hosoda b H., Namc T. H., Miyazaki S.; *"Shape memory properties of Ti–Nb–Mo biomedical alloys***",** Acta Mater. 58 (2010) 4212–4223.

[9] Sutou Y., Yamauchi K., Takagi T., Maeshima T., Nishida M.; Mater. Sci. Eng. A438 (2006) 1097-1100.

[10] Bagariatskii A., Nosova G. I., and Tagunova T. V.; Sov. Phys. Doki.3, (1953) 1014.

[11] Brown A. R. G., Clark D., Eastabrook J., and Jepson; "*Note on the Martensitic Transformation in the Ti-Nb System*", Nature 201 (1964), 914.

[12] Young M., Levine E., and Margolin H.; Metall.Trans.5 (1974), 1891.

[13] Abdel-Hady M., Honishita K., and Morinaga M.; Scr. Mater 55(5) (2006) 477-480.

[14] Tang X., Ahmed T., and Rack H. J.; J. Mater. Sci. 35(2001) 1805-1811

[15] Davis R., Flower H. M., West D. R. F.; J. Mater. Sci. 14 (1979) 22–28.

[16] Bania P. J.; In: D. Eylon, R. Boyer, D. Koss (Eds.), Beta Titanium Alloys in the 1990's, TMS, Warrendale, PA, 1993.

[17] Hao Y. L., Li S. J., Sun S .Y., Zheng C. Y., and Yang R.; Acta Biomat. 3(2), (2007) 277.

[18] Niinomi M.; Mater Sci. Eng. A, 243, (1998) 231 – 6.

[19] Bywater K. A., and Christian J. W.; Philos.Mag.25, (1972) 1249.

[20] Jepson K. S., Brown A. R. G., and Gray J. A.; Proceedings of the First International conference on Titanium edited by R.I Jaffee and W. E. Promisel (Pergamon, London, 1970), 677.

[21] Williams J. C., Plichta M. R, and Aaronson H. I: On the Existence of the β-α transformation in the alloy systems containing Ti-Ag, Ti-Au, and Ti-Si", Met. Trans. A, 8A; (1977), 1885-1892.

[22] http://panalytical-x-pert-highscore.software.informer.com

[23] Kim H. Y. *et al.*; "*Martensitic transformation, shape memory effect and superelasticity of Ti-Nb binary alloys",* Acta Mater., 54(9)(2006), 2419-2429; (b) Nakai K Ohmori Y, Ogo T and Kaobayashi S: "*Effects of ω-phase precipitation on α′ and α′′ transformations in a metastable β titanium alloy"*, Met. Sc. & Eng. A 312 ; (2001), 182-188.

[24] Hatt B. A. and Rivlin V. G.; J. Phys. D 1. (1968), 1145.

[25] Hanada S., and Izumi O.; Meta.Trans. A 18A (1987), 265-271.

[26] Hwang J. H., Kuramoto S., Furuta T., Nishimo K., and Saito T.; J. Mater. Perf.14 (2005) 747-754.

[27] Hanada S., Ozeki M., and Izumi O.; Metall. Trans. A 16 A (1985) 789-795.

[28] Pillar R. M.; "*Modern metal processing for improved load bearing surgical implants*", Biomat. 12(1991) 95-100.

[29] Davis R., Flower H. M., West D. R. F.; *"Martensitic transformations in Ti-Mo alloys"*, J. Mater. Sci. 14(1979) 712-722.

[30] Duerig T. W., Richter A. J., Fisher P.; "*Formation and reversion of stress induced martensite in Ti-10V-2Fe-3Al"*, Act Metall. 30 (1982) 2161-2172.

Chapter 6

A Search for Bone Matching Modulus Additives to Ti-Mo for Biomedical Applications

6.1 Abstract

In this chapter, we consider theoretical and experimental relationships between important structural variables, such as composition, lattice constants, and thermodynamic stability with a major focus on α'' to β phase transformation in binary Ti-Mo alloys. We look specifically at the effect of combining biocompatible elements, such as Ta, Nb, Sn, Zr, Hf on phase stability, elastic properties and other mechanical properties in a multicomponent Ti-Mo system as potential biomedical materials. The aim of this analysis is to show the dependence of microalloying on phase stability and mechanical behaviours elastic moduli as an important property of biomedical material. Following this, a review of the analysis methods used in this thesis will be given as a guide to improving future results.

6.2 Introduction

Ti based alloys have been established as a competitive class of industrial materials owing to their unique combination of good properties such as:

1. Excellent corrosion resistance — corrosion resistance is by far the most important property of a Ti alloy. Ti alloys are usually well resistant to low and high-temperatures oxidation and localised corrosion, e.g. pitting and crevice corrosions, and stress-corrosion cracking in seawater. Previous reports suggest that Ti-Mo grades containing 5-15% Mo (mass %) are more resistant to SCC in chlorides and caustic alkali media than austenitic steel grades. [1]
2. Most Ti based isomorphs such as Ti-Mo , Ti-Nb and Ti-Ta alloys tend to be relatively cheaper than the Ti-Ni and austenitic stainless steel grades that dominate the biomaterials implant world market. The price of Nickel raw materials represent as much as 40–45% of the price of the austenitic stainless steels, such as Type 304. The price of nickel is increasing rapidly due to high demand outstripping its supply, therefore the Ti-Ni and austenitic stainless steel — the largest consumer of nickel — has maintained a high-price.
3. Health concerns and issues — studies suggest that Vanadium and nickel (a major component of Ti 6-4 as well Ni in Ti-Ni and austenitic grades) can cause physical health problems such as dermatological allergies while used in contact with human body [2-5]. This phenomenon explains why biocompatibility and low Young's modulus must be carefully considered in the design of Ti alloys for biomedical applications.

4. In order to guarantee and prevent the implant from premature failure resulting from ‘stress shielding’, a significant drop in the elastic modulus is targeted by biomaterial scientists.

Owing to context, soluble additives that tend to improve both strength and low Young’s modulus of Ti alloys are particularly desired. These two important qualities are major concerns that potentially limit their use for biomedical applications in particular. At least one such soluble additive is known to exist: Molybdenum. Molybdenum has been judged to be non-toxic, non-allergic and has been selected as a safe alloying element for developing low elastic modulus Ti alloys with high strength for bone implant applications [6-20]. It is the most effective β-phase stabiliser preferable for the Ti biomaterials. Three problems arise however: (1) lack of low temperature ductility, indicating brittle behaviour may be inherent in Mo; (2) potent for improving high strength, but the element Mo belongs to refractory elements with very high melting points of ≈ 2896K [21]; and (3) they have heavy densities of 10.28g/cm3 [21]. This implies an increase in their alloying contents tends to increase both the melting points and densities of obtained Ti alloys, which is very undesirable for biomedical applications. These considerations make Mo unsuitable for this application. Nevertheless the existence of at least one or two ductilizing solute elements such as Nb, Ta, Zr, Hf, and Sn, which have been judged to be non-toxic, non-allergic and safe to improve the inherent ductility and density of Ti-Mo alloy system, are particularly desired, as the effectiveness of low Young’s modulus strategy might not explicitly be dependent on microstructure stability. This therefore raises the possibility of developing low elastic modulus Ti alloys with high strength for bone implant applications [6-20].

In addition, in the case of β stability, past studies have shown that concentration of alloying elements, such as Mo, Nb, and Ta to be retained in β after quenching from β phase field are 5, 15, and 20 atomic % (hereafter, atomic will be omitted), respectively for binary Ti – Mo [22], Ti – Nb [23], and Ti – Ta alloys [24]. According to the above viewpoint, it can be expected that Mo is the most effective β stabiliser and the β type Ti – Mo alloys are more suitable than the other β Ti alloys for biomedical applications. Nonetheless, most previous studies have focused on Ti-Nb alloys. Thus far, various ternary and quaternary β-phase Ti alloys composed of non-toxic elements have been developed; e.g. Ti–Nb–Ta–Zr [25], Ti–Nb–Zr–Sn [26], Ti–Nb–Sn [27], etc. The Young's modulus of these alloys is about 60–80 GPa, which is still higher than that of natural human bone — 20–40 GPa. Up to now, Ti – 15Mo alloy [28], Ti – 7.5Mo alloy [29], Ti-10Mo and Ti-20Mo [30] have been developed for biomedical applications in binary Ti – Mo alloys. Such effort notwithstanding, a review of the literature indicates that multicomponent β Ti-Mo alloys have received considerably less attention [19, 29, 30], even as the Ti-Mo system has proved to be a good substitute for developing absolutely safe Ni-free biomedical Ti alloys due to their being non-toxic elements that do not cause any adverse effects on the human body. Nevertheless, the Young's moduli of the Ti-Mo alloy systems reported so far are not low enough [28-31], and there has been little research effort into the Young's moduli of metal stable β-phase Ti-Mo alloys. Moreover, a central theoretical framework of low modulus determining factors in alloys remains elusive and our understanding is not nearly as sharp in the area. A much better understanding could be obtained by taking into account the effect of the elements on electron band structure using ab initio calculations.

It is well known that Ti and other 3d transition metal (such as Zr and Hf) have special d band structure, and localisation of the d electrons accounts for the unique electronic properties of the materials. In addition, microalloying addition of non-toxic elements such as Nb, Ta, Zr, Hf, and Sn on Ti-Mo can implicitly alter the stability of the electronic structure, which could lead to something outlandish. This is a reason why the comparative study on Nb, Ta, Zr, Hf, and Sn on Ti-Mo is treated in the present study in a consistent way. We begin with the ab initio calculations (details provided in the section on calculation method) and/or experimental validation to design low Young's modulus Ti alloys and propose a relation which could provide a theoretical guide to the design of low Young's modulus biomedical Ti alloys.

6.3 Theoretical and experimental verification process

6.3.1 Computational method

The study is based on the electronic density-functional theory (DFT) calculation implemented using the commercial version of Cambridge Serial

Total Energy Package (CASTEP code) [32]. The exchange and correlation are treated using the generalised-gradient approximation (GGA) of Perdew, Burke and Ernzerhof (PBE) formalism, based on the ultrasoft pseudopotentials proposed by Vanderbilt [32] and provided by the package due to its computational efficiency. The motivation for our choice is that the (PBE) methods are efficient, due to its accuracy in describing the bulk properties of many materials, and flexible enough to describe the random distribution of the impurity atoms on Ti lattice [33,34]. The PBE functional is designed to reproduce closely the PW91 results, but the PBE formulation is more robust. To guarantee a high level of convergence, cut-off energy of 500 eV and the Methfessel and Paxton [35] Gaussian smearing method with 0.1 eV smearing of the electron levels. Further details of the calculation have been given previously in Chapter 3.

The plane wave cut of energy was chosen to be 500 eV because this cut off energy was found to achieve the convergence of the formation energies with 0.01eV, as compared to the result of cut off energies up to 850eV and less than 400eV. The fundamental quantity expressing the thermodynamic stability of an alloy is the alloy formation energy. The formation energy (per atom) of the multicomponent Ti-Mo in configuration is calculated. The formation energies were calculated to investigate the alloying effect of Nb, Ta, Zr, Hf and Sn on the β-phase stability and mechanical behaviour of Ti-Mo alloys. Our computational method consisted of evaluating the formation energy for different single phase BCC alloys of form Ti $\frac{\mathrm{E}_{\mathrm{tot}}^{\mathrm{bulk}}((Ti_xMo_6+U+G))}{\sum_i N}$ supercells. Here

$U + G$ represents one or two combined atoms of M (M= Nb, Ta, Zr, Hf, and Sn), 5at.% of molybdenum and a balance of titanium atoms were constructed using the optimised lattice parameters. This stoichiometry was chosen for five reasons: (1) In the previous chapter work on binary Ti–Mo-based alloys we have seen that some important elastic response such as Young's modulus is a sensitive function of composition, requiring Mo contents lower than a critical level of about 6at.%, thus requiring composition of around the least stable β phase in the Ti-Mo alloy system. (2) Further, it has been shown previously that the composition of the least stable β phase alloy, βc, correlates in some ways with the emergence of many unique properties, such as non-linear superelasticity and very low work hardening rate [34]. (3) The chosen stoichiometry facilitates the construction of a supercell of a tractable size for computation. (4) Holding the stoichiometry constant provides an atom-for-atom comparison of the relative potency of different substitutional solutes to enhance β stability; and finally, (5) holding the symmetry and size of the supercell constant promotes maximum cancellation of numerical errors. This composition chart is shown in Figure 6.1.

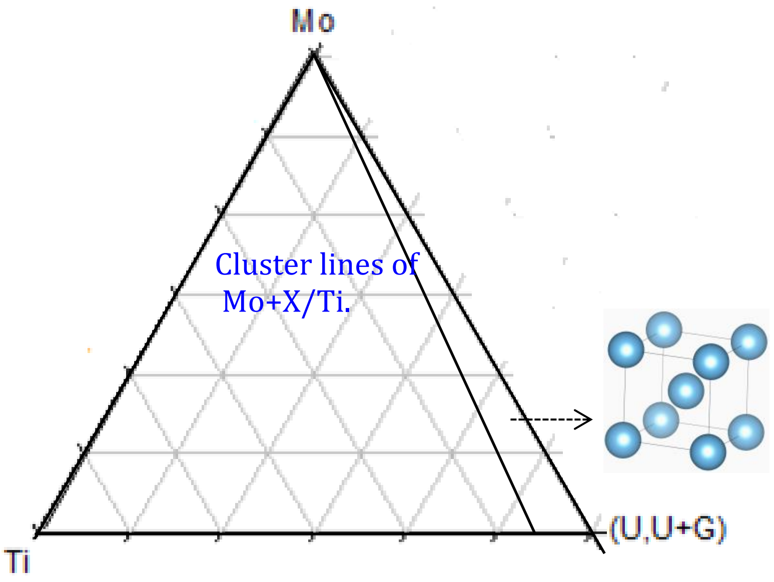

Figure 6.1: Composition chart of Ti-Mo-U-G multicomponent ternary phase diagram and cluster line of Mo+U+G/Ti.

The position of the first nearest neighbours Ti atoms from M atoms were varied to achieve equilibrium and relaxed to minimise the total energy. The formation energies were then calculated from the total energies of the supercells and the isolated atoms. For example: the formation energy of a Ti-Mo-Sn alloy, E_{FM} is defined in eqn. 6.1 as:

$$E_{Fm} = E_{Fm}(Mo) + E_{Fm}(Sn) + \sum_i N\, E_{Fm}(Ti) - \frac{E_{super}(TiMoSn)}{\sum_i N} \qquad (6.1)$$

E_{Fm} are the formation energies of isolated atoms, while E_{super} is the formation energy of the supercell. The formation energies are normalised by the number of atoms in the supercell. The computational unit cell for the current calculations is shown in Figures 6.2 and 6.3.

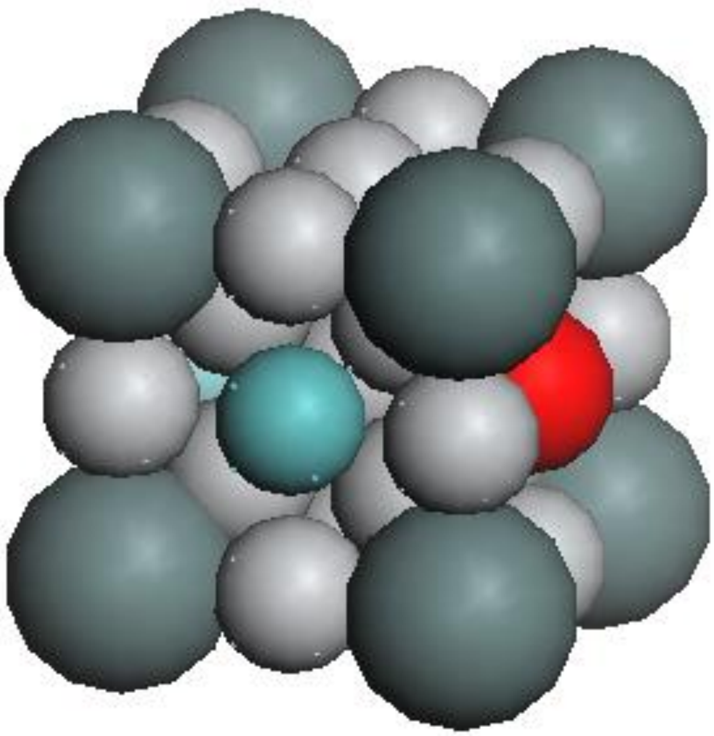

Figure 6.2: Unit cell of   formation energy and elastic matrix calculations. U and G atoms are shown in red and dark green, the grey and deep green for Ti and Mo.

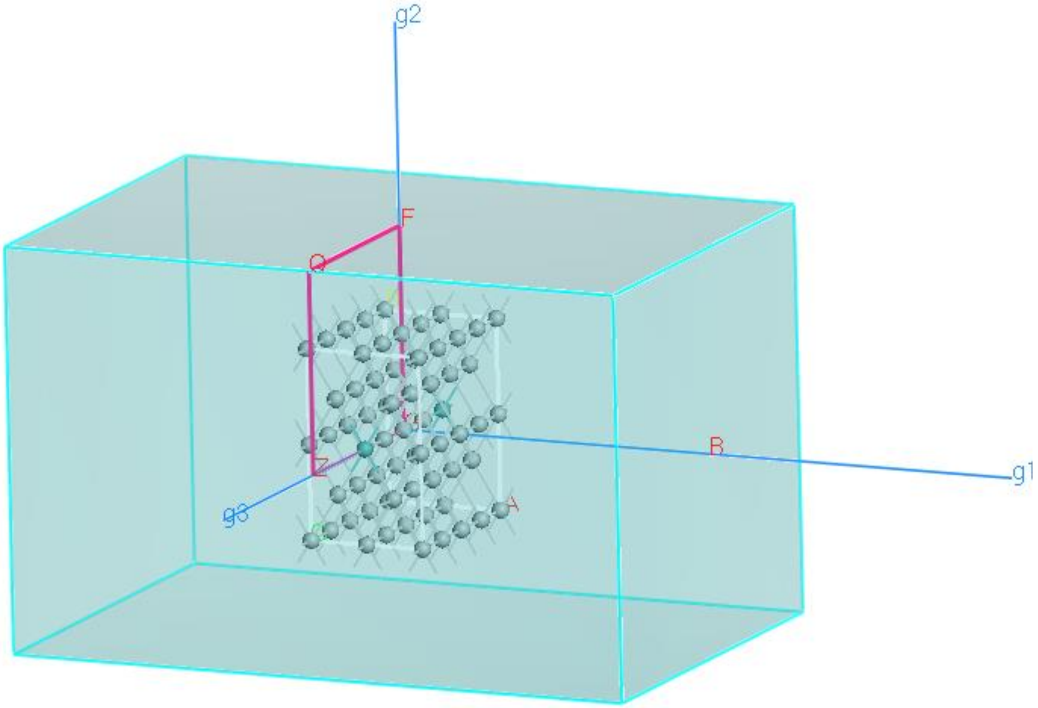

Figure 6.3: Layer slab super cell for (110) surface energy and elastic matrix calculations.

To predict the effect of the additional elements on the elastic constant of the Ti-Mo alloy, the single crystal elastic constant of the alloys were calculated. Generally, the single-crystal elastic constants can be obtained by *ab initio* electronic-structure methods by calculating the total energy as a function of appropriate lattice deformations. Depending on the crystal system and the type of imposed lattice deformation, the curvature of the total energy versus strain curves defines either a particular elastic constant or a combination of elastic constants.

The internal energy (E (V, {e_i})) of a crystal under an infinitesimal strain e_i, referenced to the energy of the equilibrium geometry can be used to obtain some or all of the elastic constants upon full optimisation at ground state energy from CASTEP as defined by [20] through eqn. 4.1:

$$E(V,\{e_1\}) = E(V_0\,,0) + \frac{V_0}{2}\sum_{ij} C_{ij}e_ie_j + \qquad (6.2)$$

Here, V_0 is the volume of the unstrained crystal with E (V_0,0) being the corresponding energy; Cijs are the single crystal elastic constants; and the members of strain tensor e{e_i, e_j, . . .} are given in Voigt notation. For a phase with cubic lattice symmetry, there are three single crystal elastic constants: C_{11}, C_{12}, and C_{44}. Material with orthorhombic symmetry possesses nine independent elastic constant Cijs and nine elastic compliance S_{ij}, which are components of a fourth-rank tensor (C_{11}, C_{12}, C_{13}, C_{22}, C_{23}, C_{33}, C_{44}, C_{55} and C_{66},) and (S_{11}, S_{12}, S_{13}, S_{22}, S_{23}, S_{33}, S_{44}, S_{55} and S_{66}). If we invoke the Voigt contraction convention, these can be arranged in a symmetrical six-by-six matrix. The product of the two matrices gives the six-by-six identity matrix to extract the single crystal elastic moduli.

$$C_{ik}S_{ik=}\,\delta_{ij} \qquad (6.3)$$

Here δ_{ij} denotes the Kronecker delta.

For an elastically anisotropic cubic phase — as is the case with our Ti-Mo materials — the total homogenised polycrystalline shear and Bulk Bo can be estimated from the single crystal elastic via methods due to Voigt [21], Reuss [22] and Hill [23]. Voigt based his assumption on uniform local strain, the isotropic shear modulus defined as:

$$\mu_V = \frac{C_{11}-C_{12}+3C_{44}}{5} \qquad (6.4)$$

The assumption made by Reuss has been based on uniform local stress, and the isotropic shear modulus expressed as:

$$\mu_V = \frac{5}{4(s_{11}-S_{12})+3S_{44}}. \qquad (6.5)$$

Here, S_{ij}s is referred as the elastic compliances; however, Hill [23] found that neither of the two relations is believed to be exact as the Voigt equation provides an upper limit for (G) and Reuss's equation gives the lower limit of (G). Hill suggested averaging by either the arithmetic or geometric mean of these two limits, i.e.

$$G_{Hill} = \frac{G_V+G_R}{2} \quad \text{or} \quad \sqrt{G_V G_R}$$

(6.6)

Once G and B have been determined, the Young's Modulus (Y) and the Poisson's for homogenised anisotropic polycrystalline aggregate can be determined using standard elasticity relationships: where the polycrystalline

Young's modulus and Poisson's ratio can be calculated via eqns. 4.5 and 4.6 respectively.

$$Y = \frac{9B_O G_H}{3B_0 + G_H}$$

(6.7)

$$v = \frac{3B_0 - 2G_{Hill}}{3(2B_0 + G_{Hill})} \qquad (6.8)$$

6.3.2 Experimental verification process

6.3.2.1 Material preparation

Based upon our previous work in Chapter 5, a series of eight multicomponent experimental Ti–Mo-based alloys were synthesised by vacuum-arc melting. The alloys were fabricated by an arc-melting method using an appropriate amount of pure Ti, Nb, Mo, Ta, Zr, Hf and Sn (99.8 %) as raw materials.

To ensure homogeneity, the ingots were inverted and remelted at least six times before casting into cylindrical rods; though the copper mold had a temperature of about 20° C, which led to rapid solidification to suppress dendrite formation. The ingots were further homogenised in a vacuum at 1273K for 21.6ks in order to eliminate the as-cast microscopic segregation. Following this, the specimens were acid etched to oxide skin.

6.3.2.2 X-Ray measurements and analyses

Phase constitution was investigated using XRD diffuse scattering measurements at room temperature with monochromatic Cu-$K\alpha_1$, radiation diffracted from a bent silicon crystal cut to the (111) orientation. The detecting assembly consisted of a proportional counter and a pulse height analyser arranged to eliminate the one-third wavelength of the white radiation (the one half components was eliminated by the silicon crystal), the cosmic background and the fluorescence radiation from titanium. Readings were recorded continuously on a horizontal spectrometer with the counter rotating at 0.25° in 2Θ/min and measurements were made from 10 to 100° in 2Θ. Flat samples were used and the geometry of the system satisfied the usual focussing condition.

Table 6.1: Chemical composition and β stability indicator of the studied alloys, the elements, alloys and β indicators highlighted (Md is in eV).

Composition (atomic %)								**β stability indicators**		
materials	**Mo**	**Ta**	**Zr**	**Hf**	**Nb**	**Sn**	**Ti**	**e/a**	**Md**	**Bo**
Ti-Mo-Sn	5.021					2.01	bal.	4.12	2.375	2.798
Ti-Mo-Zr	5.21		2.55				bal.	4.12	2.413	2.834
Ti-Mo-Ta	5.01	1.31					bal.	4.13	2.394	2.836
Ti-Mo-Nb	5.013				2.52		bal.	4.15	2.389	2.835
Ti-Mo-Ta-Sn	5.02	1.28				1.96	bal.	4.13	2.397	2.812
Ti-Mo-Nb-Zr	5.012		2.49		2.45		bal.	4.14	2.412	2.848
Ti-Mo-Ta-Zr	5.031	1.32	2.52				bal.	4.13	2.417	2.849
Ti-Mo-Ta-Nb	5.02	1.27			2.48		bal.	4.16	2.393	2.850

6.3.2.3 Microstructural observation

The samples were first prepared by following standard metallographic technique. The polished samples were etched with Kroll's reagent (10 vol. % HF and 5 vol. % HNO3 in water). Scanning electron microscopy (SEM) images were obtained using Inspect F FEG SEM operating at 20 KV. Samples were prepared by following standard metallographic technique. The polished samples were etched with Kroll's reagent (10 vol. % HF and 5 vol. % HNO3 in water).

6.3.2.4 Measurement of modulus of elasticity

In the previous chapter's work on binary Ti–Mo-based alloys, we have seen that some important elastic response — such as Young's modulus — is a sensitive function of composition, requiring Mo contents lower than a critical level of about 6at.%. Young's modulus of elasticity is defined as the ratio of stress (force per unit area) to corresponding strain (deformation in the elastic region of deformation of a material loaded under tension or compression). This basic material's property is of interest in many manufacturing and research applications and is related to the atomic bonding of the materials.

The case of biomaterials for load-bearing applications is even more pertinent. The elastic modulus is an important parameter because of the stiffness mismatch between implant and surrounding bone leads to "stress shielding" of the bone. Higher stiffness or Young's modulus of implant will result in a greater bone loss, bone fracture and loss of bone interface. Additionally, loss of bone due to stress shielding makes revision surgeries more difficult. A finite element analysis has suggested that a low elastic modulus hip prosthesis can stimulate better bone growth by distributing the stress to the adjacent bone tissue [46-49]. The elastic modulus of the materials can be determined by different methods, such as ultrasonic and nano-indentation techniques. The Young's moduli of these multicomponent alloys were evaluated by ultrasonic measurement with Olympus 620 detector.

In ultrasonic technique, the velocity of the ultrasonic waves in a solid medium is directly related to the elastic properties and density of the material, as the elasticity of the material delays the transmission of the wave and introduces a time delay, i.e. a phase lag [41]. When the frequency of the wave is higher than the audible range, it causes an elastic wave or ultrasound. Two types of vibration–induced deformation resulting in compression or shear are generally possible in an infinite medium. These are associated with two modes of elastic wave propagation: *longitudinal wave,* where particles are displaced along the direction of elastic wave, and *transverse* or *shear wave*, where particles are displaced perpendicular to the direction of propagation. The velocity of propagation of elastic waves in a body is characteristics of the materials [8].

The Young's moduli are measured by the generating of ultrasonic waves in the materials by a transmitter (Olympus 620) instrument oscillating at the desired waveform and frequency, with collection by a detector. Ultrasonic velocity changes are determined by the time of flight measurements using a pulse-echo method. A normal incident probe, model M110, 5MHz and a shear probe, model V221, 5MHz were used for the measurement of normal and shear velocities of the wave, respectively. The relationships between ultrasonic velocity and the elastic properties of materials are given below [42–44].

Young's modulus (E) is expressed as:

$$\mu_V = \frac{5}{4(S_{11}-S_{12})+3S_{44}}. \tag{6.5}$$

Shear modulus (G) is the ratio of shearing stress τ to shearing strain γ within the proportional limit of a material and is expressed as:

$$G_{Hill} = \frac{G_V+G_R}{2} \quad \text{or} \quad \sqrt{G_V G_R} \tag{6.6}$$

Poisson's ratio υ is the ratio of transverse contraction strain to longitudinal extension strain in the direction of stretching force and is expressed as:

$$v = \frac{3B_0-2G_{Hill}}{3(2B_0+G_{Hill})} \tag{6.8}$$

In the above set of equations, V_L and V_S are the ultrasonic longitudinal and shear wave velocities respectively, and ρ is the density of the material.

6.4 Results and discussions

6.4.1 Thermodynamic phase stability: theory

In order to study the influence of alloying elements on the phase stability, the formation energies for pure body centered cubic ternary and multicomponent Ti-5Mo +U (U=Nb, Zr, Ta, Sn, Ta+Sn, Nb+Sn and Sn+Zr) supercells at T= 0K were performed using the first principle calculations based on equation 6.1. The concentration dependence of formation energies is summarised in Figure 6.4. It is well known that, for an alloy to be thermodynamically stable, its formation energy (E_{Fm}) must be negative (exothermic) [44, 45, 46]. This indicates that the alloying elements and combinations considered here are good β stabilisers, as they set off strong negative offset in the (E_{Fm}) of β-Ti-Mo alloy system. Alloying of the elements will therefore induce a significant exothermic action on the initial composition of the least stable β phase alloy — apart from alloy bearing Ta+Sn, whose negative E_F is less notable. This reflects strong chemical bonding interactions between these atoms and the titanium–molybdenum system in the β phase, which represents index β-phase stability in the alloy. This implies that the ternary addition of Nb, Zr or their synergic microalloying additions are energetically favourable to stabilising the β-phase with low composition (<5 at. %) in Ti-Mo alloy.

Based on this ab initio electronic energy calculation, the formation energy was used to determine the index of stability and strength of the bonding interactions of the ternary elements in Ti-5Mo system for the stability of β-phase as Nb > Zr > Ta > Sn for an increased stability of 18.2%, 16.2%, 9.4% and 9.1% respectively. Nb, Zr, Ta and Sn microadditions could therefore be alloyed to suppress the presence of ω, α' and α'' phases, and a single β-phase stabilised at low Mo concentration in Ti-Mo alloy system.

Although both Ta and Nb belong to the Im-3m (Space group number: 229), the high stability index of Nb is not unexpected as it is the nearest neighbour element to the right of Mo in the periodic table with the closest atomic size difference. The power of an atom when in a molecule to attract electron density to itself was noted by Linus Pauling to be the element's electronegativity. Based on this scale, Nb has 1.6 — larger than the 1.5 for Ta. In contrast to Nb and Ta, Zr and Sn are well-known neutral elements (i.e. completely soluble in both α and β phase in the Ti-Zr or Ti-Sn binary diagram respectively) [34]; therefore, the β stabilising effect of Zr and Sn is associated with phase stability of the alloy, arising from the alloying elements other than them. The decrease of 9.9% formation energy of Ti-Mo-Nb by the addition of Zr is related simply to the rise in exothermic energy (i.e., negative formation energy)/Ti ratio in the alloy caused by the addition of neutral elements, viz: Zr and Sn.

Another observable feature is that, whereas Zr belongs to P63/mmc (Space group number: 194) and has a similar HCP (hexagonal close-packed) structure to Ti, it is next to Nb with just 2% difference in the β stabilising effect, which is attributable to the electronegative power of 2.16 for Mo — higher than the 1.54 of Ti — to attract electron density to itself. The influence of the site occupation of alloying elements on the stability of β-phase was weak and of no effect. The present results are consistent with other calculations [44, 45, 46]. Some of this trend was confirmed as experimental, as explained below.

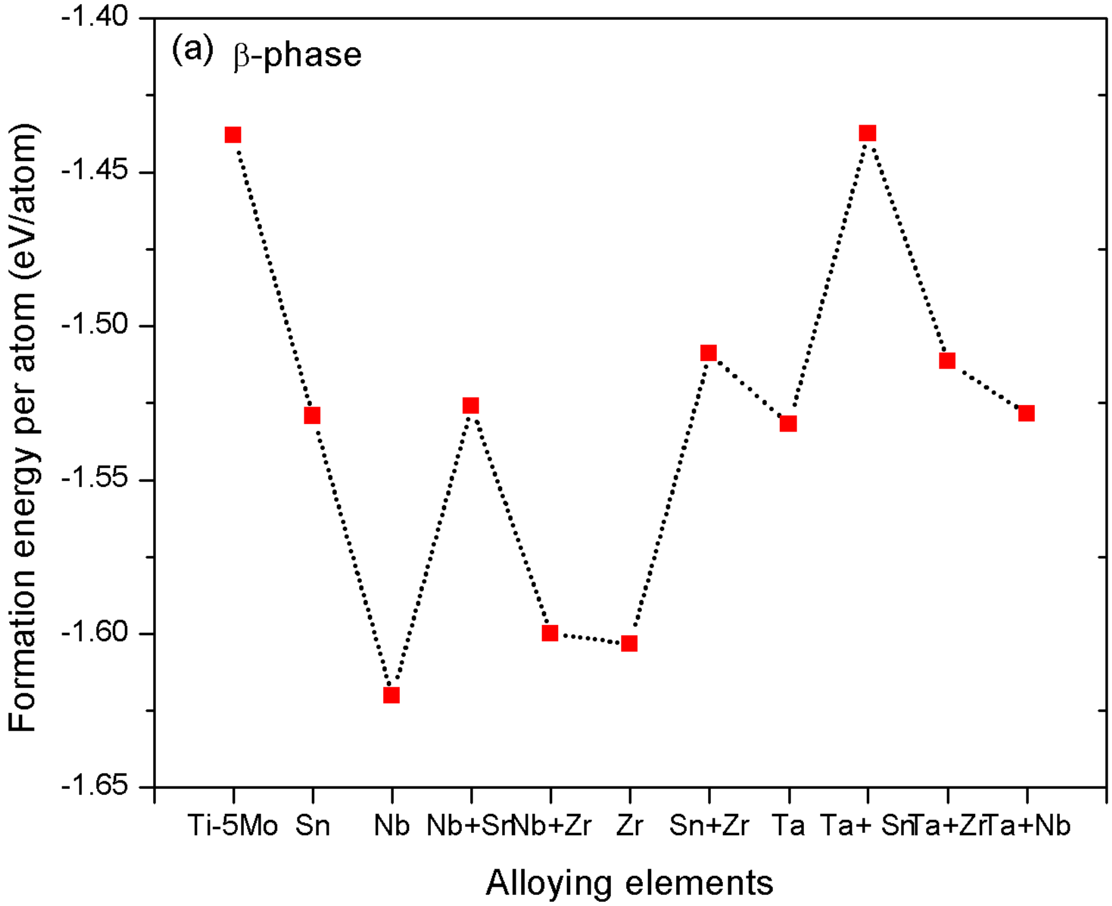

Figure 6.4: Formation energy (dependency on the microalloying elements for pure body centered cubic multicomponent Ti-5Mo +U (U=Nb, Zr, Ta, Sn, Ta+Sn, Nb+Sn and Sn+Zr) alloying.

6.4.2 Comparison with experimental data: Microstructure investigation

Previously (in Chapter 5), we determined β/ (β+α″) phase boundary for the composition of the least stable β phase in the Ti-Mo alloy system at Ti-5at.% Mo (i.e. 10wt.%). Here, the least stable β-phase alloy is defined as the alloy containing the least amount of the β-stabilising elements to get a β single phase [2]. The composition of the least stable β-phase alloy, βc, also correlates in some ways with the emergence of many unique properties, such as non-linear superelasticity and very low work hardening, as discussed in [34]. This is in agreement with previous works by Blackburn *et al.*, and by Saito *et al.* [35]. In effect, we chose Ti-5 at.% Mo (Figure 6.2) as a composition to evidence the effect of the alloying elements — namely, Mo, Nb, Ta, Zr, Hf and Sn — on β-phase stability, microstructure evolution and Young's modulus of β Ti-Mo base alloys as potential biocompatible materials.

Further, ten Ti-Mo based multicomponent alloy specimens were designed in the region across β/β+α″ phase boundary [46]. The chemical compositions, alloy designations, and β stability indicators of the multicomponent Ti – Mo alloys are listed in Table 6.1. (In the present work, all the compositions are given in at.% units unless otherwise noted.) The table reveals that the chemical compositions of the multicomponent alloys are closely related to their nominal compositions. Thus, the Ti – Mo alloys were synthesised successfully. The phases existing in the specimen were identified by conventional X-ray diffraction (XRD) using Ni filtered Cukα radiation.

6.4.2.1 Effects of ternary additions on Ti-Mo alloy: Phase identification

Figure 6.5 shows the XRD profile of the ternary Ti-5Mo-X(X=Nb, Ta, Zr, Hf and Sn) alloys quenched from 1223K. All the patterns of the alloys in Figure 6.5 appear to reveal that each specimen is a single phase β. Thus, it was apparent that Nb, Zr, Sn, Ta microadditions could suppress the presence of ω, α and α″ phases, and maintain a single β-phase at low concentration in the Ti-

5Mo alloy system. The present result is consistent with both the theoretical and other previous experimental reports [12, 13, 19, 22, 23, 30], indicating that the results are closely related. We can conclude that the plot represents the real effect of these elements in metastable β-phase boundary of the Ti-Mo alloy system, due probably to the large perturbation and ground state minimisation used in the calculation.

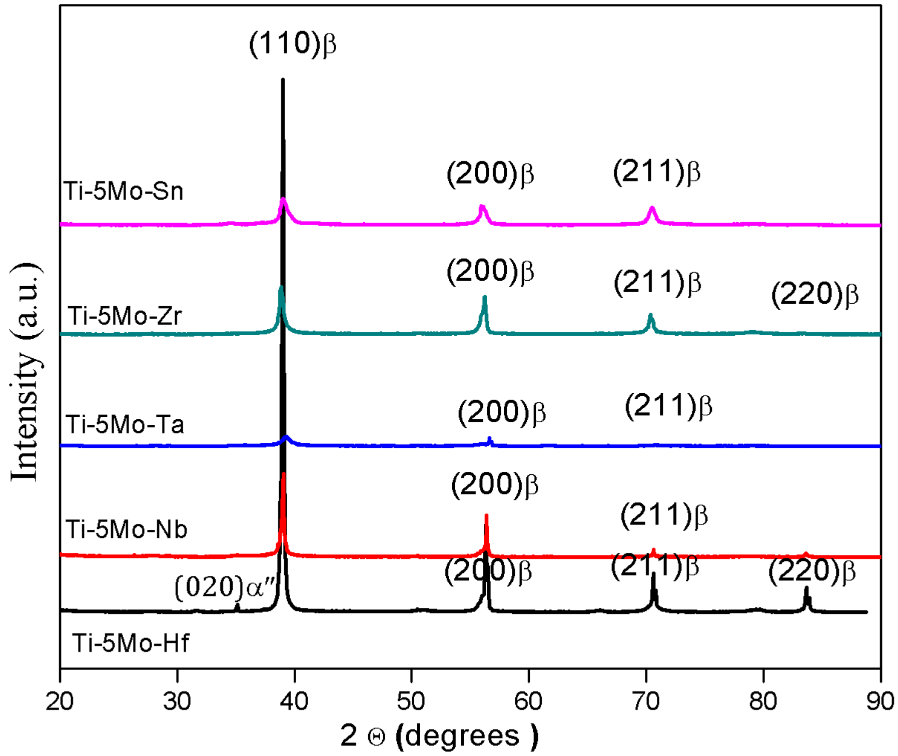

Figure 6.5: XRD patterns of the ternary specimens.

Furthermore, the broadening of the (110) peaks of the β phase can be seen in Ti-5Mo-Nb alloy. This can be an indication of grain refinement. Previous studies on Ti–10Mo–10Nb reveal significant grain refinement can be achieved by adding Nb element to Ti-Mo [19,37, 47]. Significant strengthening with grain refinement can therefore be expected, in accord with the well-known Hall–Patch relationship. On the other hand, the formation of the fine structure also depends on the cooling rate applied during solidification. Arc melting on a water-cooled copper hearth results in an eutectic microstructure with grain size in the range of 200-300mm range. Copper mould casting, however, reduces the size down to the scale of 30-70um, because a higher cooling rate is achieved by this method. A smaller grain size corresponds to higher yield strength. Some of the microstructural trend was confirmed experimental, as explained below.

The trend of (110) peaks in Figure 6.5 suggests a similar trend with the aforementioned ab initio β stability index and, apparently, the additions effectively supressed the appearance of ω, α or α′′ phases in Ti-Mo based alloys. Similar effect on Ms, temperature was reported in Ti-30Ta-Zr [48], Ti-15Mo-Fe [49], Ti-Cr-Zr [50], Ti-Nb-Ta [50], Ti-Nb-Zr [51]. In contrast, it was reported that the Zr, Ta, Nb addition to Ti-Ni alloys raised the Ms temperature [52].

6.4.2.2 Effects of ternary additions on Ti-Mo alloy: Microstructural characteristic

The SEM micrographs of the ternary alloys are shown in Figure 6.6. It can be observed that these alloys exhibit a pronounced microstructural sensitivity with the alloying elements. Invariably, a significant change in property can be expected, as microstructure strongly affects almost all properties of materials [53].

Figure 6.6(a) shows the microstructure obtained after quenching Ti-5Mo-xSn, consisting of equiaxed refined grains with average diameter ranging from ~0.1 to 10 μm in size without any precipitates. It is shown in Figure 6.6(a-d). However, many bands of obvious fibrous twinning stripes are a feature readily observable in the entire samples in Figure 6.6. This structure will be explained later with higher resolution micrographs of the twining structures.

The structure observed in Ti-5Mo-xNb is shown in Figure 6.6(b). The bright batches in the micrograph show reflections of the β phase of the alloy. While the dark patches may represent niobium-rich β, it is possible that these are merely artifacts produced during electropolishing. Samples prepared from a relatively hydrofluoric-sulfuric–lactic acid electrolyte also exhibited a similar structure. Micrographs of the alloy, however, demonstrated that a single phase could be observed; thus the results of the microstructural characterisation are identical to those of Gordin *et al.* [54] and confirm the expected effect of Ti replacement by Nb.

Figure 6.6(c) shows the microstructure of Ti-5Mo-XTa. What we can observe in this microstructure is in good agreement with the XRD profile of the specimen, the obvious fine needle-like structures can be ascribed to the α'' around the grain boundaries. In contrast to the banded structure of binary Ti-Mo abundant in the literature [28, 29, 30], evidence of significant grain refinement is observable in the microstructures, with average diameter ranging from ~50 to 200 μm in size. Conversely, the microstructure obtained for Ti-5Mo-xZr in Figure 6.6(d) has a resemblance of amorphousness. Further investigation is required however, as Zr is an element of choice to stimulating amorphous properties in metallic glass alloys. It was very difficult discerning the actual grain size due to the blurry structural features of clustered lentoid twin boundaries.

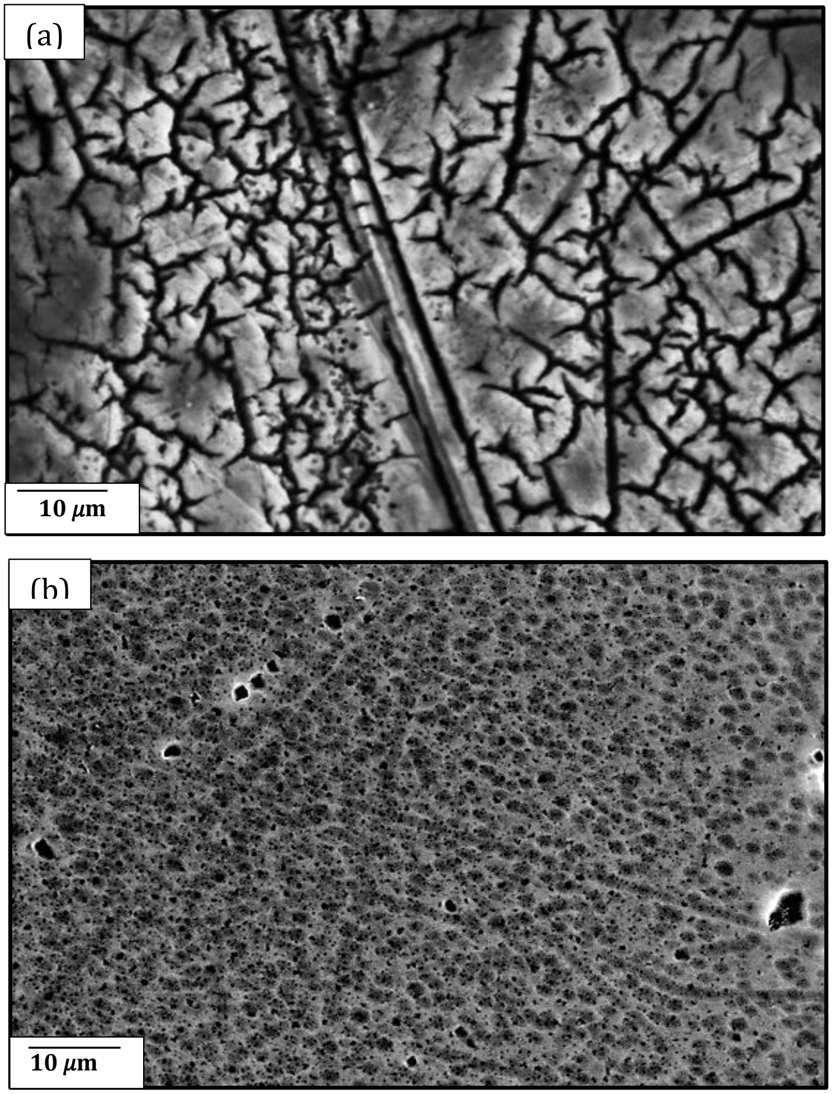

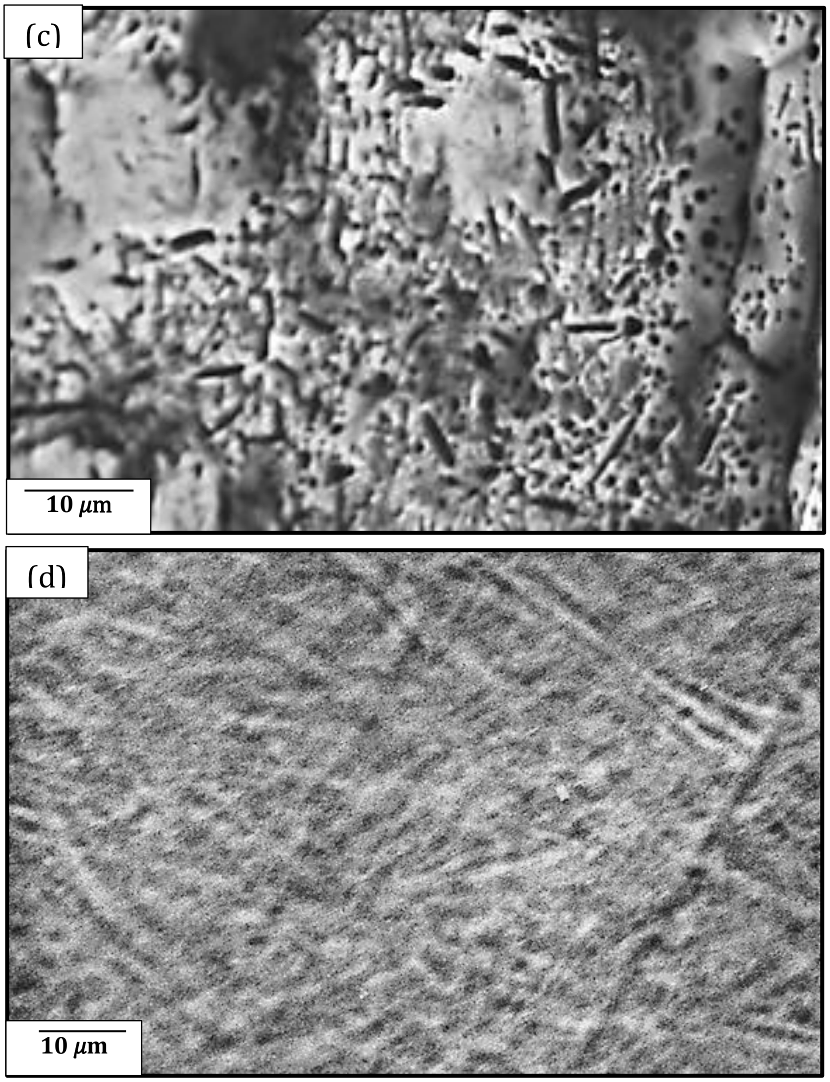

Figure 6.6: SEM microstructure in as quenched condition for (a) Ti-5M0-xSn; (b) of Ti-5M0-xNb; (**c**) Ti-5M0-xTa; and (**d**) Ti-5M0-xZr, revealing the internal structures of the studied ternary alloys.

The role of twinning can be affected dramatically by temperature, strain rate, texture and chemical composition [54, 55]. It is also generally understood that {112}⟨111⟩ or {332}⟨113⟩ twinning is the most important deformation mechanism in body centered cubic (BCC) metallic alloys [56, 57]. Recently, a multifunctional β-titanium alloy with nominal composition of Ti-24.5Nb-

0.7Ta-2Zr-1.4O (at.%) exhibited multiple deformation mechanisms by modifying the chemical composition of Gum-Metal. Despite this, the manner in which alloying elements affect twin formation and growth has not yet been fully elucidated; hence further comments can be made. Lagerlof [58] suggested a mechanism that seems reasonable to interpret the formation of twins and proposed a new model, explained elsewhere [60]. Due to lack of direct observation of the aforementioned twinning process however, substantial experimental evidence is still needed to prove this mechanism. We have used stereological angle techniques on high magnified SEM to estimate and describe twin activity and these show subtle differences in their dependence on alloying elemental additions in Ti-Mo alloys. The SEM micrographs and chemical composition revealing the twinning differences due to variations in ternary element additions in Ti-5Mo alloy are presented in Figure 6.7 and Table 6.1 respectively.

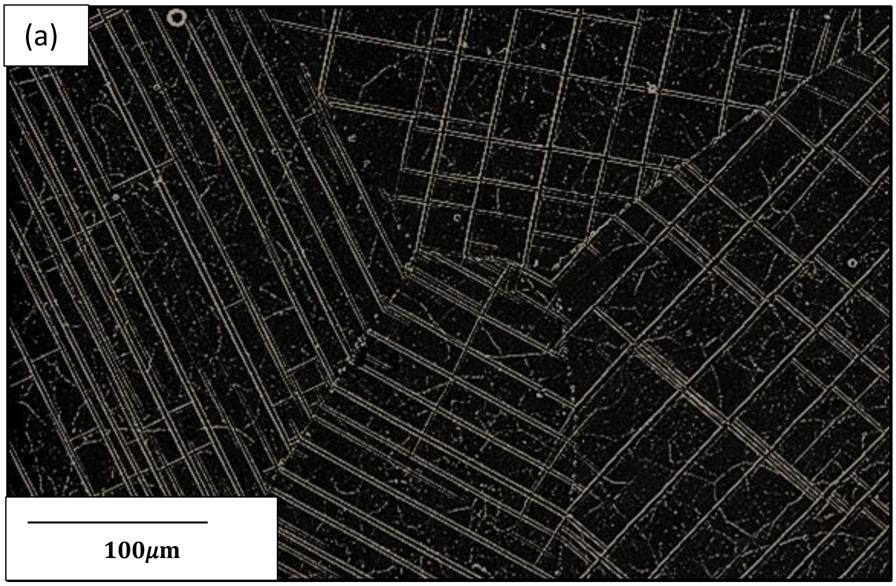

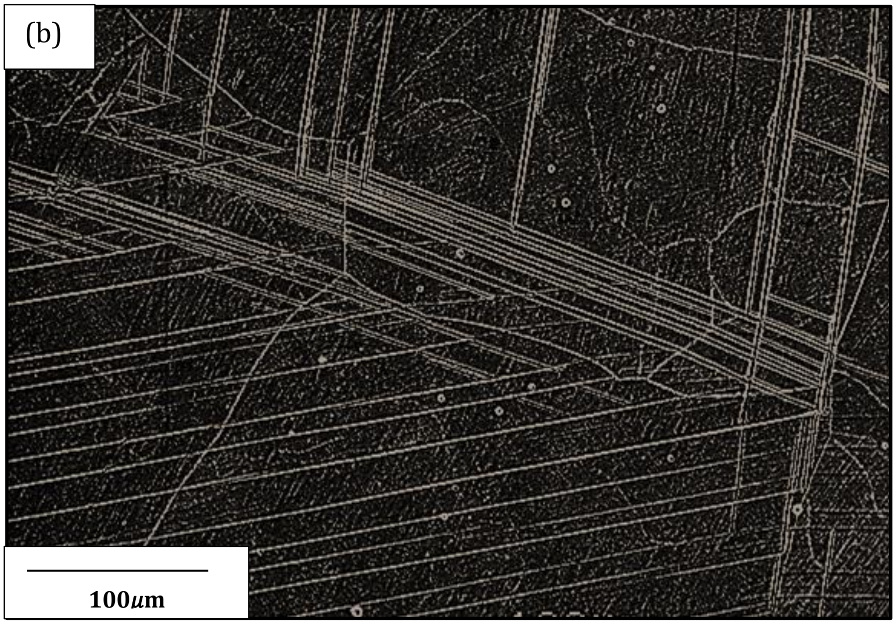
(b)
100μm

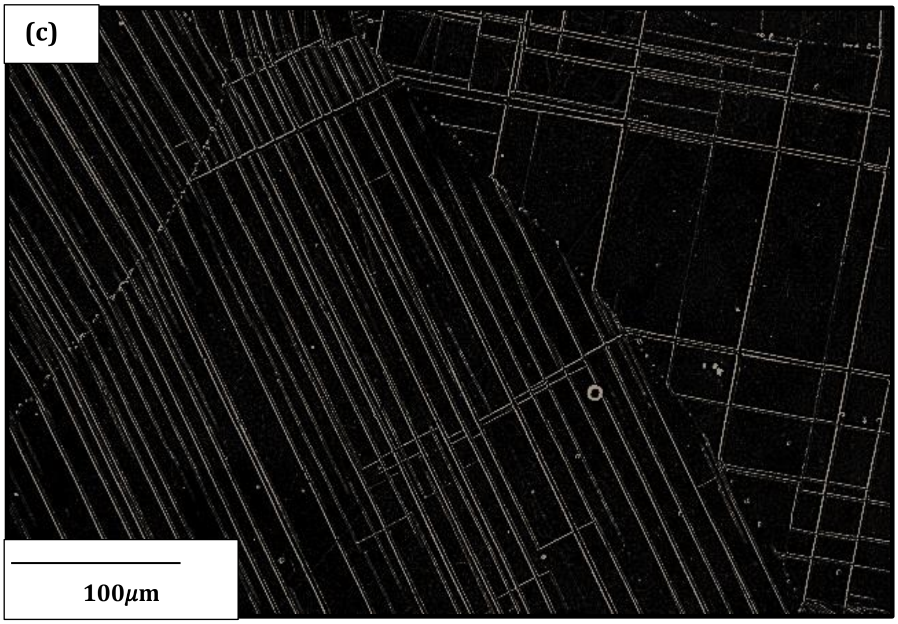
(c)
100μm

Figure 6.7: SEM microstructure in as quenched condition for (a) Ti-5Mo-xTa; (b) of Ti-5Mo-xZr; (**c**) Ti-5Mo-xSn; and (**d**) Ti-5M0-xNb, revealing the twinning structural differences of the ternary alloys.

Accordingly, straight twinnings are evident in the alloys in line with the suggestion that non-straight mechanical twins can hardly be observed in BCC metals [60]. Previously [60] we have seen that the included angle in BCC crystal between [122] and [100] direction is 70.53° around the [011] axis, which is just the crystallographic misorientation of {112}⟨111⟩ twins with the matrix [61, 62]. This is equivalent to the adjacent variants of a zigzag-shaped latte of ~38-40° determined from the current view of 6.7(a)-(c). This suggests that the zigzag-shaped lathes in Figure 6.7 (a), (b) and (c) are the {112}⟨111⟩β twins with a thickness ranging between ~0.1 and 1um. This indicates that the model for zigzag–shaped [112]⟨111⟩ twinning is in accord with our observation.

Conversely, from the scaffolding morphology of Ti-5Mo-XNb twinnings in Figure, 6.7(d), the observation of zigzag-shaped {112}⟨111⟩ twins was not obvious. The measurements of the included angles between two adjacent twin variants were between ~60 and 65°. Theoretical modelling has shown, however, that the included angle between two adjacent twin variants of zigzag-shaped {112}⟨111⟩ twins from the view of $[111]_{\mathrm{matrix}}$// $[111]_{\mathrm{twin}}$ is 60° [60]. Having said this, the exert formation mechanism is not very clear. A theoretical calculation of stacking fault energy of Ti-Nb β alloy using first principle [62] suggested stacking energy change with increase in *e/a,* viz alloying content should be one of the main factors controlling the {112}⟨111⟩ twins and influencing the morphology of {112}⟨111⟩ twins [60, 62]. In an alloy with low stacking fault, it is difficult to restrict the extended dislocation [63]. The extended dislocation can only glide on one crystal plane, which is implicitly why formed {112}⟨111⟩ twins are straight — while in alloys with high stacking fault energy, the perfect dislocation cannot dissociate at all, and twinning is finally suppressed.

6.4.2.3 Effects of multicomponent additions on Ti-Mo alloy: Phase identification

Next, the changes in the constitution of alloy phases due to the synergic addition of two elements to Ti-5Mo are presented. Figure 6.8 shows the XRD profiles of the specimens. Aside from the alloy consisting of Ta+Sn, a significant retention of single β-phase in the alloys in agreement with the theory calculation and other past results [37-42] are evident. Previously [62], we observed that β phase retention is reminiscent of Ti alloys with higher β stabilising concentrations in Ti-Mo systems, therefore the β phase stability can be ascribed to the increasing influence of β element concentrations in line with the theoretical result.

The two major martensitic peaks at 39.0° and 39.9° correspond exactly to those expected for 002 and 111 in the α″ phase, where a=0.301 nm, b=0.491 nm, and c=0.463 nm can be seen in the multicomponent alloy consisting of Ta +Zr. This indicates that the synergy of Ta with Zr was not able to suppress the appearance of the martensitic α′′ phase. Such an effect was reported for low Zr containing β Ti type alloys, Ti-Cr-Zr [40], Ti-Nb-Sn-Zr [19]. We recall that Zr and Sn are known neutral elements, so the β stabilising effect can be associated with the phase stability of the alloy arising from alloying elements other than them. In other words: when used as ternary Ti-Mo addition, the β stabilising effect of Mo seems to have dominated, but since Ta is a mild β stabiliser and there is wide equilibrium α+β phase field and Zr and Hf has a complete solubility in both α- and β- phases in the Ti-Zr and Ti-Hf binary diagram respectively [43], there is greater affinity for stabilising α″-phase when alloyed with Ta element that is more or less obvious.

It is however important to mention here that no trace of ω was detected in the ternary and quaternary alloys, implying that the effectiveness of the elements in supressing the ω- phase is detrimental to the strength of the alloys. We can therefore conclude that the theoretical plot represents the real effect of the elements in metastable β-phase boundary of the Ti-Mo alloy system.

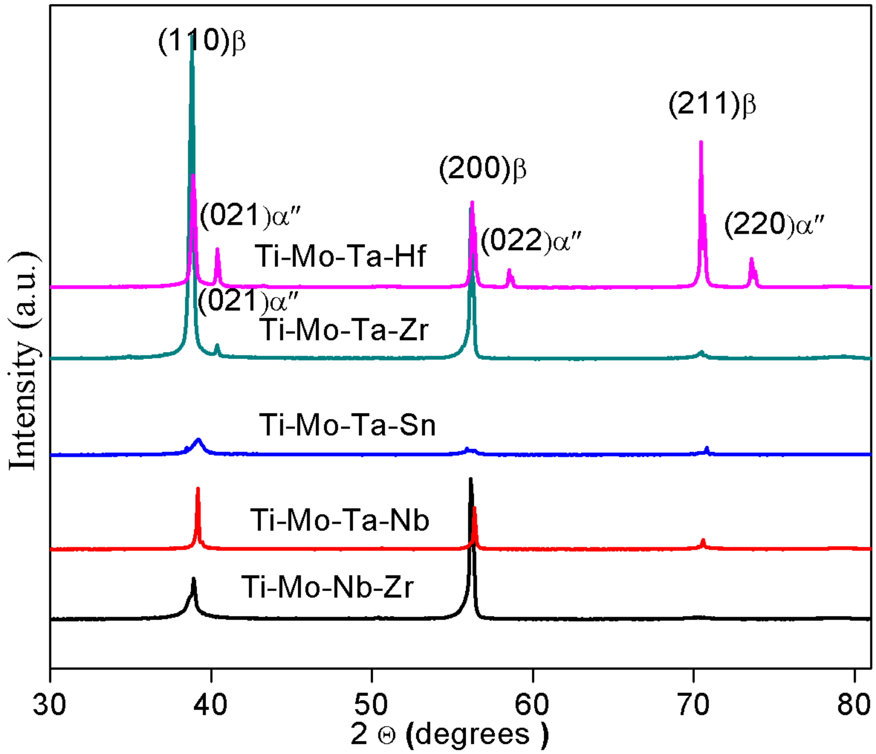

Figure 6.8: XRD patterns of the multicomponent Ti-Mo alloys.

6.4.3 Correlation of elastic moduli with properties for possible biomedical applications

6.4.3.1 Elastic constants of multicomponent Ti-Mo alloy: Theory

The elastic constants and the moduli of the multicomponent Ti alloys were evaluated by first principles total energy calculations according to eqns. 6.3, 6.4, 6.5, 6.7 and 6.8. The six important independent elastic constants — C_{11} , C_{12}, C_{33}, C_{13}, C_{44}, and C_{66} — for an alloy consisting of body-centred cubic and probable orthorhombic structures are evaluated. The evaluated values of the elastic constants are presented in Table 6.2. In order to analyse these data, we first focus on the relative stability between the two phases. The tetragonal shear constant, $C^{\prime}$ and anisotropy factor, A, are also listed in Table 4.4. $C^{\prime} = (C_{11} - C_{12})/2$ is a shear parameter which corresponds to specific phonon vibration mode in atomic structure and can be related to the stability of the BCC structure [44] and the anisotropy factor $A = \frac{C_{44}}{C^{\prime}}$ (A=1 for isotropy). As the HCP-to-BCC boundaries are approached, $C^{\prime}$ increases, which often correlates with deformation by twinning, and A approaches zero at the β phase boundaries. It is seen that A tends towards zero with the addition of the β stabilising elements, which corresponds to the exothermic formation energy obtained earlier. Accordingly, high $C^{\prime}$ corresponds to higher β stability as reported earlier in the literature [64, 65, 66, 67]. A correlation was also found between measured transition temperature (T_M) and high $C^{\prime}$ for Ti alloys undergoing shape memory behaviours such as TiNi based alloys [68]. This result is in agreement with the theoretical calculation of formation energy (Figure 6.4) at T=0K and the actual phase stability (Figures 6.6, 6.7 and 6.8) of the multicomponent alloying in the Ti-Mo system. The polycrystalline elastic properties such as bulk (B) and shear moduli (G) were evaluated from the methods due to Hill [23]. Hill found that neither Voigt [21] nor Reuss [22] relations are believed to be exact, since the Voigt equation provides an upper limit for (G) and Reuss's equation gives the lower limit of (G). Hill suggested averaging by either the arithmetic or geometric mean of these two limits. The calculated elastic moduli are shown in Table 6.3. In our previous work in Chapter 5 and earlier [44], it was noted that most Ti alloys are textured in

$\langle 001 \rangle$ direction in as cast condition. The results by [69, 19] found a variation in Young's modulus of Ti-Mo-Cr and Ti-Mo-Ta, Ti–(15-17) Mo–ST alloys due to homogenisation treatments. In the present study, we evaluated the theoretical Young's moduli (E) of the multicomponent elastic materials expressed in the $\langle 001 \rangle$ direction, E_{001} by eqn. 6.9:

$$E_{001} = \frac{(C_{11}+2C_{12})(C_{11}-C_{12})}{C_{11}+C_{12}} \qquad (6.9).$$

E_{001} denotes the young's modulus between the $\langle 011 \rangle$ and $\langle 010 \rangle$ planes, which is the texture direction in Ti-Mo system. Further studies are on-going in the group to establish the exact textures and formation processes. Previously, theoretical calculations by first principles indicated that most Ti metal alloys have a special elastic anomaly with elastically softened directions.

In order to verify the theoretical predictions, the calculated and actual experimental results determined that Young's and shear moduli results of the quenched multicomponent alloys are present for comparison in Table 6.3 and Figure 6.9. Some important comparisons of the theoretical and experimental elastic properties trend were confirmed, as explained below.

Table 6.2: Theoretical predicted elastic constants and phase stability indicators *tetragonal shear modulus* ′ and *anisotropy factor* A for multicomponent Ti-Mo alloys are given. (For composition details, see Table 6.1.)

Materials	C_{11}	C_{12}	C_{13}	C_{33}	C_{44}	C_{66}	C'	A
Ti-Mo-Sn	162.23	107.26	99	65.64	39.4	28.53	27.49	1.43
Ti-Mo-Zr	155.06	97.17	98.51	95.46	36.43	32.56	28.95	1.26
Ti-Mo-Ta	153.56	104.71	99.37	106.3	36.54	-38.5	24.43	1.49

Ti-Mo-Nb	174.89	116.35	95.9	111.6	34.39	33.83	29.27	1.17
Ti-Mo-Ta-Sn	160.85	104.4	91.84	125.45	37.57	27.75	28.43	1.32
Ti-Mo-Nb-Zr	163.99	108.28	89.25	98.1	34.7	31.52	55.71	0.63
Ti-Mo-Ta-Zr	152.3	122.45	90.99	125.45	35.67	-30.3	14.93	2.39
Ti-Mo-Zr-Sn	161.63	120.64	91.41	90.03	35.52	24.78	20.50	1.73
Ti-Mo-Nb-Sn	172.55	121.23	90.1	100.1	36.5	25.47	25.66	1.42
Ti-Mo-Ta-Nb	173.62	141.24	96.14	148.9	28.44	32.75	16.19	1.76

6.4.3.2 Elastic properties of multicomponent Ti-Mo alloy: Comparison of theory and experiment

The measured dynamic elastic properties (moduli) of the quenched multicomponent Ti-Mo alloys being studied and the theoretical determined values are shown in Table 6.3 and Figure 6.9 as functions of the alloying element. The elastic properties reported in the present works are the Young's modulus, and shear and bulk modulus represented by E, G, and B respectively. These properties are linked directly to the tensile, shear and hydrostatic loading respectively. As they are exclusively controlled by the interatomic bond interactions, they can be considered the fundamental properties of any material. Their correlation has shown specific trends with a range of properties including hardness, yield strength and toughness [64, 70], and where there are discrepancies these could be caused by the intrinsic effect of different alloying elements on modulus. Very recently, a simple relationship between the electronic structure (DOS) and mechanical (Young's modulus and hardness) and thermal properties of glassy Zr-TL alloys was reported [71].

Accordingly, the correlation of E, G, and B as a function of the multicomponent elemental additions in Table 6.3 and Figure 6.9 suggests a link between the properties and some alloying content. This relationship was confirmed, as explained below.

The theoretical and measured E of multicomponent Ti-Mo alloys studied is shown in Figure 6.9(a). It can be noted that the Ti – 5Mo-Zr alloy has the lowest elastic modulus of 45.26 GPa and the Ti-Mo-Ta-Sn alloy has the highest modulus of 112 GPa. It is well known that the elastic modulus, one of the intrinsic properties of materials, is determined by the bonding force among atoms [73, 74]. This bonding force is related to both the crystal structure and also the distances between atoms, which can be affected by alloying addition, heat treatment, and plastic deformation [6-7, 11, 14-17, 18, 74]. Thus, the observed Young’s modulus differences may be primarily ascribed to the sensitivity of these alloying elements. This inevitably leads to the variation of the lattice parameters and unit-cell volume of its crystal structure. Accordingly, the resulting variations in distances between the atoms alter the modulus of the alloys.

Previous experiments have shown that the high modulus titanium implants transfer insufficient load to adjacent remodeling bone and result in bone resorption and eventual loosening of the prosthetic devices [75]. The Young’s modulus of popular biomaterials, such as stainless steel and Co-based alloys, is 206 and 240 GPa respectively, which is significantly higher than that of bone tissue (~10–40 GPa). The elastic modulus of cp-Ti, near β and β Ti alloys also varies between 121 and 57 GPa, which is higher than 42.19 and 45 .26 GPa obtained from theory and experiment on our newly designed Ti-5Mo-Zr alloy, which is much closer to natural bone that will minimise the bone resorption arising from the stress shielding effect and consequently increase the long-term stability of the implants. The values from theoretical and measured results confirm a good agreement of the Young's modulus with ± 5% and increase in the sequence Zr < Ta+Zr < Zr+Sn < Nb+Sn < Ta < Sn < Nb < Ta < Ta+Nb < Ta+Sn < Nb+Zr < Ta+Sn. This sequence is slightly different from the sequence of β phase stability in Figure 6.4.

There are different reports on Young's moduli of the various phases in Ti alloys. It was reported that the α-phase exhibits a much higher elastic modulus as compared with the β-phase and the elastic modulus of the phases of titanium alloys increase in the sequence β <α″ <α <ω [9, 26]. Ho *et al.* [11] found, however, that the martensite α″ phase with 7.5% Mo has the lowest modulus among α″ and β phases in the Ti–Mo system, whereas Hao *et al.* [26] reported that the α″ andβ phases have nearly the same Young's modulus in the Ti–29Nb–l3Ta–4.6Zr alloy. Moreover, Kim *et al.* [76] reported that the metastable β phase has lower elastic modulus than stable β phase. Kim's and Hao's reports are consistent with the present study and in good agreement with other theoretical [44, 45, 46] and experimental [11, 13, 14, 19] results. First, we recall that the XRD profile of Ta+Zr, which possesses the second lowest Young's modulus and contains the two major martensitic peaks at 39.0° and 39.9°, corresponds exactly to those expected for (002) and (111) in the α″ phase with a=0.301 nm, b=0.491 nm, and c=0.463 nm, thus indicating that the synergy of Ta with Zr was not able to suppress the appearance of the martensitic α′′ phase. Such an effect was reported earlier for low Zr containing metastable β Ti type alloys, Ti-Cr-Zr [40], Ti-Nb-Sn-Zr [19]; thus the result is due to the intrinsic effect of alloying elements [12].

In Chapter 4 we observed from EBSD analysis that most binary Ti-Mo alloys are textured in ⟨001⟩ direction in as cast condition. Additionally, the reports by [69, 19] found a large variation in Young's modulus of Ti-Mo-Cr and Ti-Mo-Ta, Ti–(15-17) Mo alloys respectively, due to homogenisation treatments. Consequently, the Young's modulus (E) of the multicomponent alloys was expressed in the ⟨001⟩ direction, E_{001} by eqn. 6.9. The excellent relationship obtained between theory and experimental data is notable. Although the exert basis for the coincidence requires more studies, there are ample reasons to infer that other factors are involved; and if it were a coincidence, what could possibly explain the effect of the observed ⟨001⟩ texture in as cast Ti–Mo alloy systems.

It is evident that the shear modulus G trend in Figure 6.9(c) could not reflect similar agreement as in E. It is not surprising since each manifests different characteristics of materials: E is a measure of resistance to a change in atomic separation distance within the plane of the bond, and so can be determined from the linear portion of the interatomic potential. G quantifies the resistance to shear loading. Elastic moduli are therefore controlled by interatomic interactions and so may be considered a fundamental property, whereas G is proportional to the activation energy for a shear event in materials. Based on this premise, it is suggested [77] that experimentally measured moduli (by resonant ultrasound spectroscopy and ultrasonic time-of-flight measurements) may not be controlling macroscopic deformation since they are an average across the whole sample. B (Figure 6.9(b)), since it corresponds to a volumetric dilatation, is dependent on the electronic properties of a solid, i.e. the compressibility of the electron gas.

To verify the influence of texture on the predicted Young's modulus, DFT-GGA calculation was performed for Ti-5Mo-xZr alloy (i.e. the lowest Young's modulus alloy) and found 64.12 GPa and 20.23 for E_{100} and E_{111} respectively. This is presumably why most Ti alloys was predicted to be elastically anisotropic [41]. As Table 6.2 and Figure 6.9(a) reveal, however, this material is actually quite isotropic. In general the theoretical predictions for the Young's modulus are within a difference of 5% with experimental values. The small discrepancy could reflect differences in temperature, minor experimental error or approximations inherent to DFT-GGA.

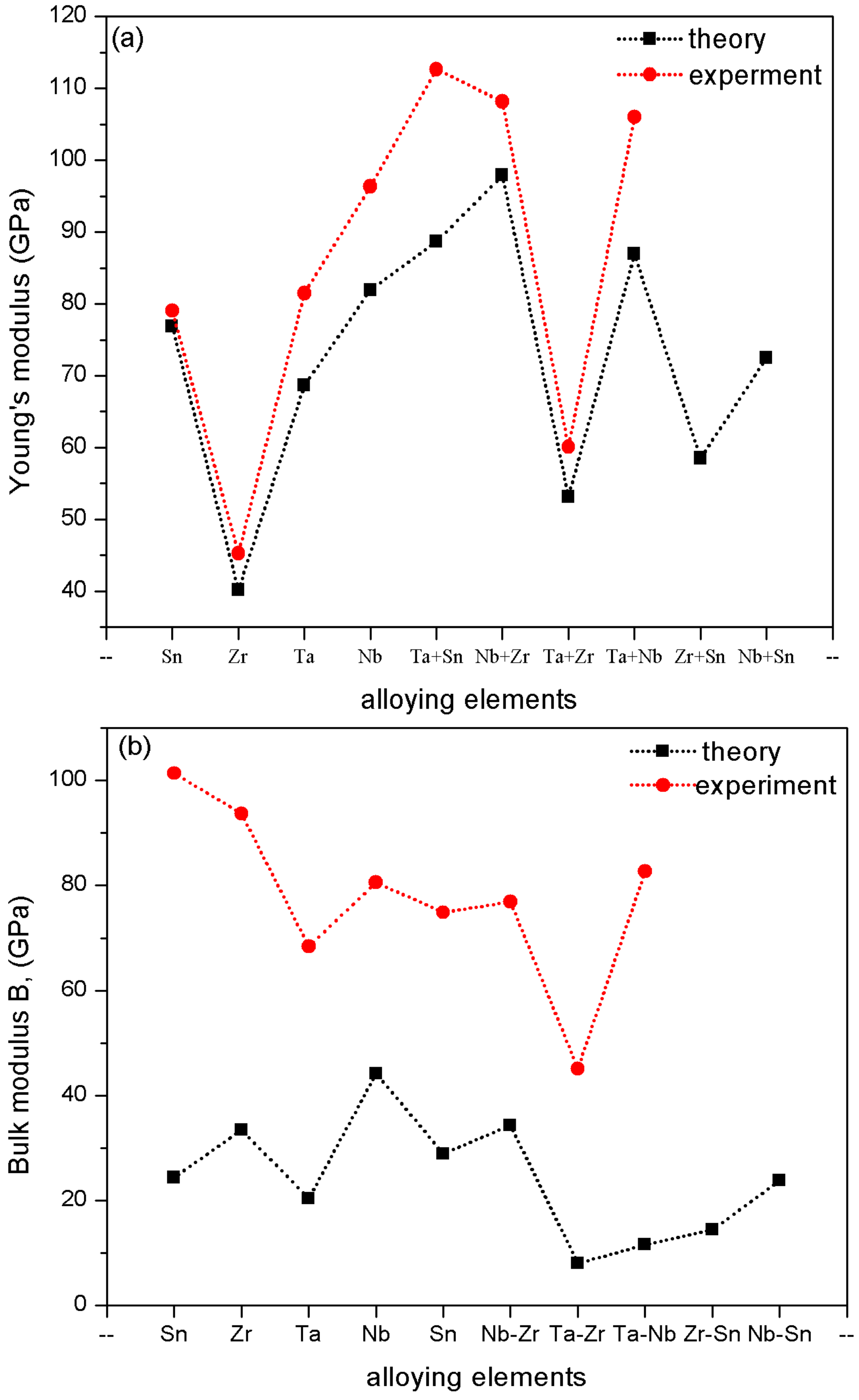
(a)
theory
experment
Young's modulus (GPa)
120
110
100
90
80
70
60
50
40
--
Sn
Zr
Ta
Nb
Ta+Sn
Nb+Zr
Ta+Zr
Ta+Nb
Zr+Sn
Nb+Sn
--
alloying elements
(b)
theory
experiment
Bulk modulus B, (GPa)
100
80
60
40
20
0
--
Sn
Zr
Ta
Nb
Sn
Nb-Zr
Ta-Zr
Ta-Nb
Zr-Sn
Nb-Sn
--
alloying elements

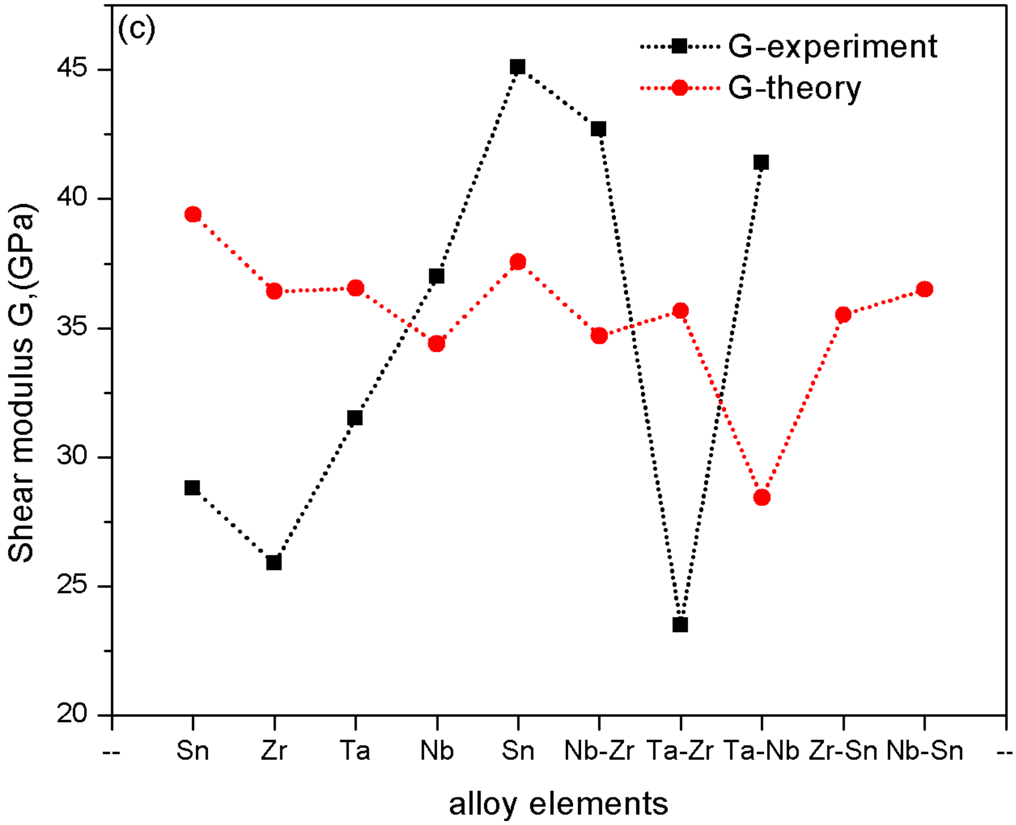

Figure 6.9: Plots revealing the effect of alloying elements on the Young's (E), Bulk (B)and Shear moduli, (G) of the multicomponent Ti-Mo alloys.

Table 6.3: Comparison of theoretical predicted and measured elastic parameters are given, along with literature data for other BCC 1Ti alloys of the multicomponent Ti-Mo alloys in units of GPA. (For composition details, see Table 6.1.)

Materials	E_{TH}	E_{EXP}	B_{TH}	B_{EXP}	ν_{TH}	ν_{EXP}	G_{TH}	G_{EXP}
Ti-Mo-Sn [present study]	76.85	79.05	24.41	101.4	-0.25	0.37	39.4	28.8
TMZF (Ti–12Mo–6Zr–2Fe) [41]		79.5						
Ti–12Mo–5Zr [78](sol)		64.5						
Ti–12Mo–5Zr [78](Hom)		90						
Ti-Mo-Zr [present study]	42.19	45.26	33.47	93.7	0.21	0.41	36.4	25.9
Ti-Mo-Ta [present study]	68.66	81.51	20.41	68.4	-0.61	0.37	36.5	31.5
Ti–6.6Mo–1.47Ta [54]		74						
Ti-Mo-Nb [present study]	81.93	96.37	44.21	80.6	0.61	0.30	34.4	37.0
Ti–6.6Mo–1.47Nb [13,54]		105						
Ti-Mo-Ta-Sn [present study]	88.67	112.66	28.94	74.9	0.46	0.25	37.6	45.1
Ti-Mo-Nb-Zr [present study]	97.87	108.14	34.33	76.9	0.22	0.27	34.7	42.7
Ti-Mo-Ta-Zr [present study]	53.15	60.10	8.04	45.1	-0.39	0.33	35.7	23.5
Ti-Mo-Ta-Nb [present study]	86.91	106	11.58	82.7	-0.67	0.29	28.4	41.4
Ti-Mo-Zr-Sn [present study]	58.51		14.42		-0.37		35.5	
Ti-Mo-Nb-Sn [present study]	72.50		23.84		-0.60		36.5	
c.p. Ti (grade 2)[79]		105						
ASTM F75 (Co–Cr–Mo)[15]		220						
V316 (stainless steel)[15]		379						
Ti–6Al–4V (grade 5) [79]		114						

6.5 Summary and concluding remark

The major findings of Chapter 6 are summarised as follows.

Based on the DFT-GGA electronic calculation implemented on CASTEP code for stable solid solutions, a number of metastable body-centred cubic ternary and multicomponent alloys were experimentally and theoretically designed to correspond to the composition formula of Ti-5Mo +U (U=Nb, Zr, Ta, Sn, Ta+Sn, Nb+Sn and Sn+Zr) supercells at T=0K. Using the first principle calculations, their β phase thermodynamic stability, microstructure and mechanical properties — especially low Young's modulus — were obtained, which compared well with experimental validation of properties. The main findings of this chapter are as follows:

The trend of the electronic formation energy attests to significant sensitivity of the system to micro-elemental addition. The calculated parameters qualitatively track the known elemental behaviour in Ti-Mo binary system, which indicates that DFT-GGA is favourable to the computational screening of relative phase stability of alloys.

On an atom-for-atom basis, the β phase stability trend shows an increasing potency in the sequence Nb > Zr > Ta > Sn with ternary micro-additions and Nb+Zr > Ta+Nb > Ta+Sn > Ta+Zr > Ta+Hf for the complex alloys respectively. In agreement with theoretical results, both the experimental analyses show single β phase, indicating the micro additions are enough to suppress the presence of ω and α″ in the ternary and other complex alloys.

The calculated and measured Young's modulus of the investigated alloy varies between 45.19 and 118GPa. Our newly designed Ti-Mo-Zr alloy exhibited the lowest Young's modulus of 45 GPa (42.19GPa from theory), which is significantly lower than elastic modulus of conventional metallic implant materials (cp-Ti, near β and β Ti alloys) — which varies between 121 and 57 GPa — and much closer to natural bone, which will minimise the bone resorption arising from the stress shielding effect and consequently increase the long-term stability of the implants.

Both theory and experiment confirm a good agreement of the Young's modulus within ± 5% and increase in the sequence Zr < Ta+Zr < Zr+Sn < Nb+Sn < Ta < Sn < Nb < Ta < Ta+Nb < Ta+Sn < Nb+Zr < Ta+Sn in Ti-Mo system. This sequence is slightly different to the sequence of β phase stability, implying that the effectiveness of low Young's modulus strategy might not be explicitly dependent on β phase microstructure stability. Thus, the strategy can be a good step towards developing future metallic biomaterial with bone matching Young's modulus for orthopaedic implant applications.

Finally, this work suggests a link between cast material texture and the directionality of calculated Young's modulus of the alloys. Although more study is obviously needed to establish this, the calculated Young's modulus in the direction E_{001} showed a good agreement with cast Young's modulus values.

6.6 References

[1] KESSLER: "*Titanium-the Space-age Metal*", ASTM Standardization News (1984) 26-27. (1b) H.D Nishimura T: J. Power Energy Syst. 2 (2008), 530–537. [1c] Weiss I and Semiatin S.L: Mater. Sci. Eng. A243 (1998) 46–65.

[2] Aziz-Kerrzo M., Conroy K. G., Fenelon A. M., Farrell S. T.; Breslin CB: Biomaterials 22(2001), 531.

[3] Yu S. Y., Scully J. R.; Corrosion 53 (1996), 965.

[4] Godley R., Starosvetsky D., Gotman I.; J. Mater Sci –Mater Med. 17 (2006), 63.

[5] Li S. J., Yang R., Li S., Hao Y. L., Cui Y. Y., Niinomi M.; Wear 257(2004), 869.

[6] Niinomi M.; *"Recent metallic materials for biomedical applications*", Metall. Mater Trans. A 33 (2002), 477–86.

[7] Niinomi M.; "*Mechanical properties of biomedical titanium alloys*", Mater Sci. Eng. A 243 (1998), 231–6.

[8] Long M., Rack H. J.; "*Titanium alloys in total joint replacement—a materials science perspective*", Biomaterials 19 (1998), 1621–39.

[9] Hon Y. H., Wang J. Y., Pan Y. N.; *"Composition/phase structure and properties of titanium–niobium alloys*". Mater Trans 44 (2003), 2384–90.

[10] Matsumoto H., Watanabe S., Hanada S.; "*Microstructures and mechanical properties of metastable β TiNbSn alloys cold rolled and heat treated*", J. Alloy Compd. 439 ;(2007), 146–55.

[11] Ho W. F., Ju C. P., Chern Lin J. H.; "*Structure and properties of cast binary Ti – Mo alloys*", Biomaterials 20 ;(1999), 2115 – 22.

[12] Delvat E., Gordin D. M., Gloriant T., Duval J. L., Nagel M. D.; "*Microstructure, mechanical properties and cytocompatibility of stable beta Ti – Mo – Ta sintered alloys*", J. Mech Behav Biomed Mater 1;(2008),345 – 51.

[13] Gordin D. M., Gloriant T., Texier G., Thibon I., Ansel D., Duval J. L.; "*Development of a β-type Ti – 12Mo – 5Ta alloy for biomedical applications cytocompatibility and metallurgical aspects*", J. Mater Sci. Mater M 15; (2004),885 – 91.

[14] Zhou Y. L., Niinomi M., Akahori T.; *"Effects of Ta content on Young's modulus and tensile properties of binary Ti–Ta alloys for biomedical applications*". Mater- Sci. Eng. A 371, (2004), 283–90.

[15] Zhou Y. L., Niinomi M., Akahori T.; "*Decomposition of martensite α″ during aging treatments and resulting mechanical properties of Ti–Ta alloys*", Mater-Sci. Eng. A 384; (2004), 92–101.

[16] Zhou Y. L., Niinomi M.; "*Microstructures and mechanical properties of Ti-50 mass% Ta alloy for biomedical applications*", J. Alloys Compd. 466; (2008), 535–42.

[17] Zhou Y. L., Niinomi M.; "*Ti–25Ta alloy with the best mechanical compatibility in Ti–Ta alloys for biomedical applications*", Mater-Sci Eng. C 29 (2009), 1061–5.

[18] Ferrandini P. L., Cardoso F. F., Souza S. A., Afonso C. R., and Caram R.; "*Aging response of the Ti–35Nb–7Zr–5Ta and Ti–35Nb–7Ta alloys*". J Alloys Compd. 433(2007), 207–10.

[19] Hanada S., Matsumoto H., Watanabe S.; "*Mechanical compatibility of titanium implants in hard tissues*", International Congress Series; (2005), 239–47.

[20] Silva H. M., Schneider S. G., Neto C. M.; "*Study of nontoxic aluminium and vanadium-free titanium alloys for biomedical applications*", Mater Sci. Eng. C 24;(2004), 679–82.

[21] The University of Sheffield and Web Elements Ltd., UK, website.
http://www.webelements.com/niobium/physics.html
http://www.webelements.com/tantalum/physics.html
http://www.webelements.com/molybdenum/physics.html.

[22] He G., Eckert J., Dai Q. L., Sui M. L., Löser W., Hagiwara M. *et al.*; "*Nanostructured Ti-based multi-component alloys with potential for biomedical applications*". Biomaterials 24; (2003), 5115 ‐ 20.

[23] Bagariatskii I. A., Nosova G. I., Tagunova T. V.; "*Factors in the formation of metastable phases in titanium-base alloys*". Sov Phys Dokl. 3; (1959), 1014 ‐ 8 [transl. of Dokl. Akad. Nauk. SSSR, Vol.122; (1958), 593 ‐ 596.

[24] Fedotov S. G., Chelidez T. V., Kovneristyy Y. K., Sanadze V. V.; "*Phase transformation during heating of metastable alloys of the Ti–Ta system*", Phys. Met. Metall. 62; 2 (1986), 109–13.

[25] Niinomi M.; "*Multifunctional low-rigidity β-type Ti-Nb-Ta-Zr system alloys as biomaterials*", Biomaterials 24; (2003), 2675-84.

[26] Hao Y. L., Li S. J., Sun S. Y., Zheng C. Y., Yang R.; "*Elastic deformation behaviour of Ti–24Nb–4Zr–7.9Sn for biomedical applications*", Acta Biomater 3(2007), 277-286.

[27] Matsumoto H., Watanabe S., Hanada S.; "*Beta TiNbSn Alloys with Low Young's Modulus and High Strength*", Mater Trans. 46 ;(2005), 1070-84.

[28] Wang K.; "*The use of titanium for medical applications in the USA",* Mater-Sci. Eng. A, 213 (1996), 134–7.

[29] Ho W. F.*; "A comparison of tensile properties and corrosion behaviour of cast Ti–7.5Mo with c.p. Ti, Ti–15Mo and Ti–6Al–4V alloys*", J Alloy Compd. 464; (2008), 580–3.

[30] Ying-Long Z. and Dong-Mei L.; *"Microstructures and mechanical properties of Ti–Mo alloys cold-rolled and heat treated*",Mater-Charact. 62; (2011), 931-937.

[31] "Least square Unit cell refinement" Program after Appleman and Evans (1973), implementation by R.G.

[32] Segall M. D., Philip J. D. L., Probert M. J., Pickard C. J., Hasnip P. J., Clark S. J. and Payne M. C.; *"First-principles simulation: ideas, illustrations and the CASTEP code*", J. Phys. Condens. Mater 14 (2002), 2717–2744.

[33] W. Kohn and Sham L.: "*Self-consistent equation's including exchange and correlations affects*", Phys. Rev. A 140 (1965), 1133.

[34] Perdew J. P., Burke K. and Ernzerhof M.; "*Generalized Gradient Approximation Made Simple*", Phys. Rev. Letts. 77, (1996), 3865.

[35] Duthie J. C., Pettifor D. G.; Phys. Rev. Lett. 38 (1977), 564.

[36] Mandi S., Ruschenbach B.; Surf.Coat. Technol. 156 (2002) 276-283.

[37] Gasser B., in: D.M Brunette, P. Tengvall, M. Texfor, P. Thompson (Eds.). Titanium in Medicine, Springer, New York (2001) 673-701.

[38] Okazaki Y., Ito Y, Tateishi T: MATER. Trans. JIM 37(1996) 843-849.

[39] Pharr, G. M., Oliver, W. C.; *"Measurement of thin film mechanical properties using nanoindentation"*, MRS Bulletin 17, (1992), 28–33.

[40] Volinsky A. A., Gerberich W. W.; Microelectron. Eng.69 (2003) 519-527.

[41] Majumdar P., Singh S. B. and Chakraborty M.; "*Elastic modulus of biomedical titanium alloys by nano-indentation and ultrasonic technique-A comparative study*", Mater. Sci. Eng. A 489(2008) 419-425.

[42] Augereau F., Laux D., Allais L., Mottt M. and Caes C.; Ultrasonics 46(2007), 34- 41.

[43] Dogbmane M., Hadjoub F., Dogbmane A. and Hadjoub Z.; Mater. Lett. 61(2007) 813-816.

[44] Raabe D., Sander B., Fri´ak M., Ma D., Neugebauer J.; "*Theory-guided bottom-up Design of Beta-titanium alloys as bioMaterials based on first principles calculations: Theory and experiments*", Acta Materialia 55, (2007), 4475–4487.

[45] Dai J. H., Wu X., Song Y. and Yang R.*; "Electronic structure mechanism of martensitic phase transformation in binary titanium alloys*", J. App. Phys.112 (2012), 123718-24

[46] Abdel-Hady M., Hinoshita K., Morinaga M.; "*General approach to phase stabililty and elastic properties of b-type Ti-alloys using electronic parameters"*, Scripta Mater. 55, (2010)477-480.

[47] Tadaki T., Tokoro M. and Shimizu K.; Mater. Trans. JIM. 16; (1975) 285.

[48] Louzguina-Luzgina L. V., Dmitri V. L. and Inoue A.; "*Influences of additional alloying elements (V, Ni, Cu, Sn, B) on structure and mechanical properties of high-strength hypereutectic Ti–Fe–Co bulk alloys*", Intermetallics 14 (2006) 255–259.

[49] Xu l. J., Chen Y. Y., Liu X. G. and Kong F. T.; "*The microstructure and properties of Ti–Mo–Nb alloys for biomedical application*," J. Alloys and Compd. 453 (2008) 320–324.

[50] Ikeda. M. *et al*.; J. Alloy. Mater. Trans.45, (2004), 1106.

[51] Mina X. H., Emura S., Sekido S., Nishimura T., Tsuchiya K. and Tsuzaki K.; "*Effects of Fe addition on tensile deformation mode and crevice corrosion resistance in Ti–15Mo alloy";* Mater. Sci. & Eng. A 527 (2010) 2693–2701.

[52] Tang X., Ahmed T., and Rack H. J.; J. Mater.Sci.35 (2000) 1805.

[53] Otsuka, K. and Ren X.: Intermetallics 7(1999), 511.

[54] Gordin D. M., Gloriant T., Nemtoi Gh, Chelariu R., Aelenei N., Guillou A. and Ansel D.; Mater. Lett. 59 (2005) 2959–2964.

[55] Meyers M. A., Vohringer O. and Lubranda V. A.; Acta Mater 49, (2001) 4025.

[56] Ikeda M., Komatsu S., Sigmoto T. and Kamei K. J.: Jpn. Inst.Met.53, (1989) 664.

[57] Blackburn M. J. and Feeney J. A.; J. Inst. Met. 99 (1971) 132.

[58] Lagerlof K. P. D.; Act Metall. 41 (1993) 2143.

[59] Yang Y., Li G. P., Cheng G. M., Li Y. L., Li Y. F., Yang K., and Ge P.; Acta Mater. 58, (2010) 2778.

[60] Yang Y., Li G. P., Wang H., Wu. S. Q., Zhang L. C., Li Y. l. and Yang K.; *"Formation of zigzag shaped {112}⟨111⟩ β mechanical twins in Ti-24.5Nb-0.7Ta-2Zr-1.4O alloy"*, Scr. Mater. 66 (2012) 211-214.

[61] Hsiung L. M. and Lassila D. H.; Scripta Mater.38 (1998) 1371.

[62] Yu N. Y., Yang P., Qiang W. J. and Chen L.; Foundation Materials Science and Technology press, 1990.

[63] Davis R., Flower H. M. and West D. R. F.; *"Martensitic transformations in Ti-Mo alloys"*, J. Mater. Sci. 14 (1979) 22–28.

[64] Fisher E. S. and Dever D.; *"Relation of the c′ elastic modulus to stability of b.c.c. transition metals"*, Acta Met. 18(1970), 265-269.

[65] Saito T., Furuta T., Hwang J., Kuramoto S., Nishino K., Suzuki N., Chen R., Yamada A., Ito K., Seno Y., Nonaka T., Ikehata K., Nagasako N., Iwamoto C., Ikuhara Y., and T. Sakuma; Science **300**, (2003), 464.

[66] Ikehata H., Nagasako N., Furuta T., Fukumoto A., Miwa K., and T. Saito; Phys. Rev. B 70, (2004), 174113.

[67] Li T., Morris J. W., Jr., Nagasako N., Kuramoto S., and Chrzan D. C.; Phys. Rev. Lett. 98, (2007) 105503.

[68] Hu Q. M., Yang R., Lu J. M., Wang L., Johansson B. and Vitos L.; Physic.Rev.B 76, (2007), 224201.

[69] Xingfeng Zhao, Niinomi M., Nakai M., Hieda J.; "*Beta type Ti–Mo alloys with changeable Young's modulus for spinal fixation applications*", Acta Biomater. 8 (2012) 1990-1997.

[70] Gu X. J., Mcdermott A. G., Poon S. I. and Shiflet G. J.; Appl. Phys. Let.88, (2006) 211905.

[71] Lewandowski J. J., Wang W. H., and Greer A. L.; Phil.Mag.Lett.85 (2005) 77-87.

[72] Ristić R., Stubičar M., and Babić E.; *Philos. Mag.* **87** (2007) 5629–5637 and reference therein.

[73] Ikeda M., Komatsu S. Y., Sowa. I., and Niinomi M.; Met. Mater. Trans. A 33 (2002) 487–493.

[74] Geetha M., Mudalki M. U., Gogia A. K., Asokamani R., and Raj B.; Corros. Sci. 46, (2004) 877–892.

[75] Hao Y. L., Niinomi M., Kuroda D., Fukunaga F., Zhou Y. L., Yang R. and Suzuki A.; Met. Mater. Trans. A 33 (2002) 3137–3144.

[76] Kim H. S., Kim W. Y. and Lim S. H.; Scripta Mater. 54 (2006) 887–891.

[77] Plummer J. D: PhD Thesis "*On the physical aspects that control mechanical deformation in bulk metallic glasses*", Department of Materials Science and Engineering University of Sheffield (2012).

[78] Changli Z., Zhang X. and Cao P.; "*Mechanical and electrochemical characterization of Ti–12Mo–5Zr alloy for biomedical application*", J.Alloys and Compd. 509, (2011) 8235– 8238.

[79] Bertrand E., Gloriant T., Gordin D., Vasilescu E., Drob P., Vasilescu and C., Drob S. I.; J. Mech. Behav. Biomed. 3 (2010) 559–564.

Chapter 7

Defining Material Properties by Elastic Constant Systematics

7.1 Introduction

Elastic constants of materials and alloys are of interest because of the information they provide concerning the nature of the binding forces in solids. Elastic constants of some simple BCC metals have been extensively investigated, theoretically and experimentally, in a wide range of compositions and temperatures [1]. The relationship between the elastic properties and the importance of $C^{\prime}$ as an index of BCC-lattice stability is usually considered from the microscopic point of view of electronic structure (as characterised by the electron per atom ratio or e/a parameter).

Of interest here is a unified analysis of alloys transformable by stress-induced formation (SIM) via elastic constant systematics obtained by first principle calculations. Several β type alloys, such as Ti-Mo, that possess transforming (SIM) properties undergo a first order transformation above a certain composition range (in the case of β-type Ti alloy), revealing a martensitic transformation from β (disordered BCC) to an orthorhombic α′′ martensite phase. They are called SIM alloys because they are inherently metastable in nature and prone to transformation if additional energy, such as stress or hydrostatic pressure, is provided. They are, in some cases, reversible from α″ ↔ β phase in the absence of the additional energy, which is the basis for the continued search for the shape memory effect in β-type Ti alloy.

Although the shape memory effect has been reported in Ti-Mo alloy [2-5], Ti-Nb alloy [6-8] and Ti-V alloy [9], fundamental understanding is still insufficient in Ti-based shape memory alloy. The explanation in terms of the elastic moduli has not being significantly extended beyond the commonly encountered stability criteria.

Previously, in Chapters 4 and 6, we investigated the elastic constant of binary and multicomponent Ti-Mo alloys and interpreted the changes in moduli from the T-matrix solution of the elastic constants. The present section, as an extension, will systemise the specific case of the transformable (stressed induced martensitic) BCC Ti alloys in the context of continuum elastic theory uniquely determined by the three elastic constants — C_{11}, C_{12} and C_{44} — derived from theoretical and experimental data. In a cubic crystal, C_{44} corresponds physically to shear resistance on a (100) plane, $(C_{11} - C_{12})$ to shear resistance on a (110) plane, and $(C_{11} + 2C_{12})/3$ to the bulk modulus B representing resistance to volume change $\Delta V/V$ caused by hydrostatic pressure P: $\Delta V/V = P/B$. In addition, the shapes of the three characteristic acoustic surfaces of a cubic symmetry crystal depend only on the ratios of these elastic constants for satisfying the thermodynamic constraints — $C_{44} > 0$, $C_{11} > |C_{12}|$ and $C_{11} + 2C_{12} > 0$ [10].

To do this, we rely heavily on a Blackman diagram [11]. In 1938, Blackman introduced this diagram — which is a dimensionless plot of reduced elastic stiffness coefficient C_{12}/C_{11} versus C_{44}/C_{11} — to search for material with a high Debye temperature, which led to the surprising result that materials with similar chemical bondings fall into the same region of the diagram, despite large differences in their absolute stiffness coefficients. Recently, by incorporating important bonding conditions in its representations, the parameter has been used to provide illuminating descriptions of generalities of elastic behaviour in metallic glass [12].

We note that experimental and computation details pertaining to this aspect of the present work are given in Chapters 4, 5 and 6.

7.2 Results and discussions

Figure 7.1 shows a Blackman's diagram of BCC metals and alloys containing a range of calculated and experimental elastic property data from the literature in Table 7.1. The data represent a wide-range of BCC metallic alloys in terms of composition and behaviour. Lines (blue dash lines) radiating from the upper-left corner represent lines of constant Zener shear–deformation elastic anisotropy, $A = 2C_{44}/(C_{11} - C_{12})$, and the 45° dashed line denote $C_{12} = C_{44}$. They also correspond to the important central interatomic forces relationship in cubic SIM behaviours displayed a cluster over and into a small region (at lower $C_{12}/C_{11} \leq 0.4$ and $C_{44}/C_{11} \leq 0.5$) of the diagram, in very close proximity to the central interatomic forces line (Pc>0) and A≤0.5. This may indicate a similarity in interatomic bonding type (not strength). Other non-SIM alloys are also found at a well-defined area over the large C_{12}/C_{11}

and low C_{44}/C_{11} region bounded by A ≥ 0-1 ≥3. The other BCC metals cluster over larger but still well defined areas. We attribute the larger areas to differences in interatomic bonding within the same crystal structure. The Blackman diagram is therefore very useful for the present study on interatomic bonding in BCC metals and alloys.

First, we note the physical meaning of the cluster as an indication of near-same interatomic bonding, despite large differences in composition and size. A previous criterion [13] provides an insight into the close link between crystal structure and mechanical properties of solids, ascribing strong metallic non-directional bond-bending forces to materials with a positive value of Cauchy pressure (Pc>0), while the negative value is indicative of strong convalency, directional interatomic bond angularity and strong resistance to bond bending.

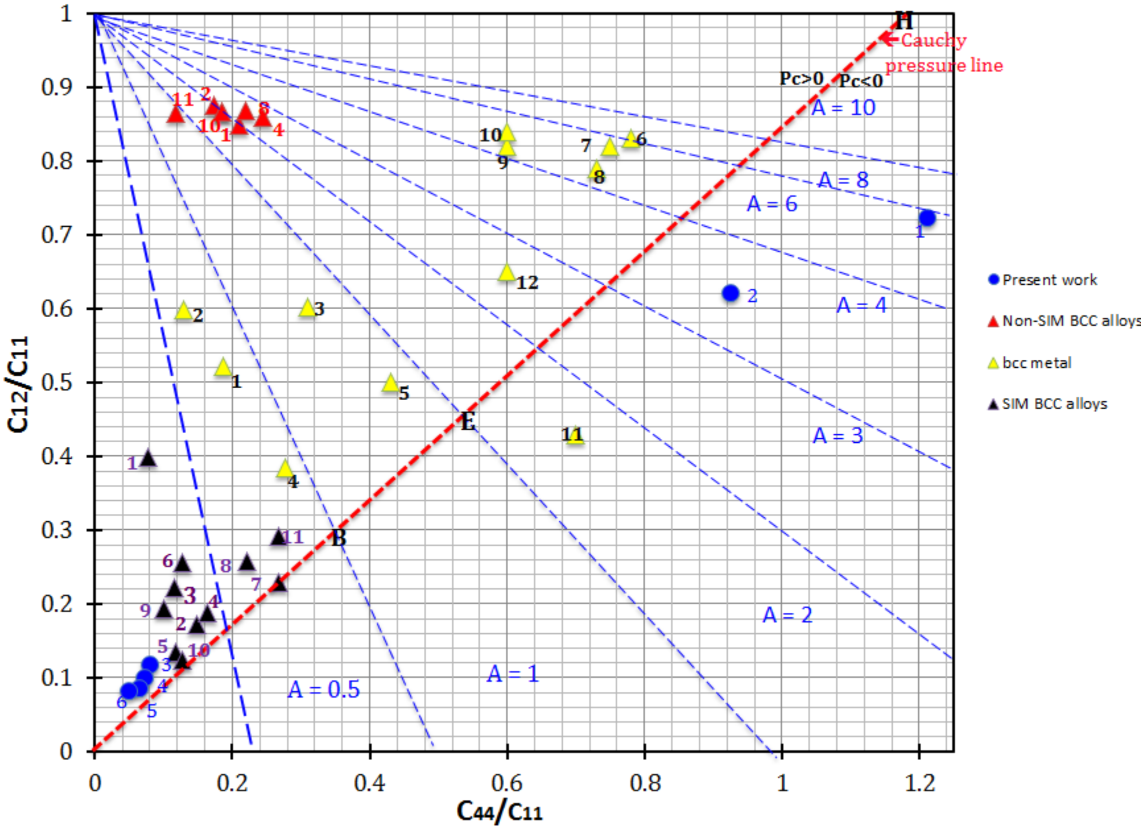

Figure 7.1: Blackman diagram displaying the congregation of some BCC alloys with respect to the interatomic bonding forces. Also indicated are elastic anisotropy (blue dash lines), $A = 2C_{44}/(C_{11} - C_{12})$ and the Cauchy pressure line, $C_{12} = C_{44}$. The identities of the elements/alloys are given in Table 7.1.

The position of the SIM alloy signifies its positive Cauchy pressure, suggesting a non-directionality bonding framework, while its close proximity to the Cauchy line is indicative of the inherently instability and inability to withstand high shear stress. Born and Huang [14] pointed out that the Cauchy relationship is unfavourable for lattice stability, and that lattices interacting with particularly large central forces tend to be unstable. Both C_{44} and $C^{'} = (C_{11} - C_{12})/2$ correspond physically to shear resistances and to phonons on a (100) plane in cubic a crystal. This may suggest the both low shear moduli (C_{12}/C_{11} and C_{44}/C_{11}) are implicit characteristic of the lattice instability exhibited by SIM alloys, leading to cooperative atomic movement during deformation. It has been suggested that that the physical origin is the smaller principal strains (< 3%) involved in $\beta \rightarrow \alpha''$ transformation, rather than those required to produce the HCP structure [1], coupled with identical specific volume of β and α'' phase.

It is also important to point out that we found a good degree of correlation between the calculated data of Ti-(10-23) Mo and the experimental SIM data. We do, however, attribute the presence of the lean alloy composition (Ti-(3-6) Mo) — i.e. alloys 1 and 2 — in the negative Cauchy region (Pc<0) to the imaginary cubic nature assigned during calculation to alloys of predominantly orthorhombic α'' martensitic phase. For this symmetry, immediate difficulties arise because the three cubic independent elastic – stiffness coefficients lose their important physical meaning.

Figure 7.2 shows a Blackman diagram FCC metals and alloys, to which the Cauchy condition and elastic anisotropy lines are also indicated. We found that FCC SIM alloys fall near the Cauchy line in small clusters similar to the BCC ones in Figure 7.2. It terms of the C_{12}/C_{11} vs C_{44}/C_{11} placement, the two groups are bound differently in the Blackman diagram. FCC alloy are bound by large C_{12}/C_{11} and moderate C_{44}/C_{11}. The high elastic anisotropy as observed in the FCC SIM alloys, however, led Zener to predict successfully low-temperature martensitic transformation in Li and Na to an FCC crystal [15]. This may suggest a similar conclusion. The non SIM alloys and the other FCC metals fall rather far apart into a well-defined relatively small area. This therefore suggests strongly different interatomic bonding, probably caused by their different electron configurations.

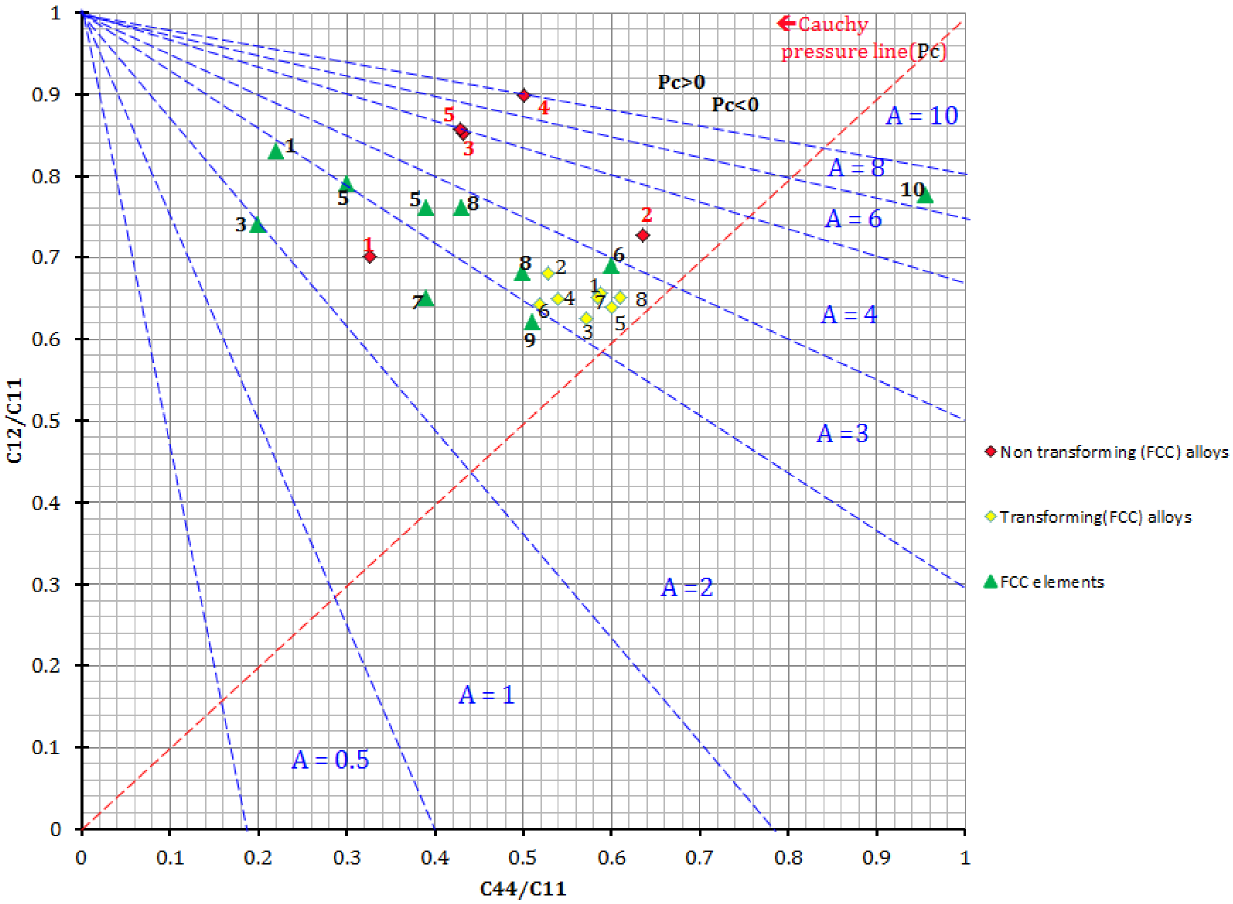

Figure 7.2: Blackman diagram showing a congregation of some FCC alloys with respect to the interatomic bonding forces. Also indicated are elastic anisotropy (blue dash lines), $A = 2C_{44}/(C_{11} - C_{12})$ and the Cauchy pressure line, $C_{12} = C_{44}$. The identities of the elements/alloys are given in Table 7.1.

Given the findings, it is important to plot both BCC and FCC SIM alloys together on the same Blackman diagram. Most materials fall into (Pc>0) however, and materials in the region Pc<0 are known to be exceptionally rare — with the exception of Barium (BCC metal, 9), which may be described as a free element never found in nature because of its high chemical reactivity due to its non-central interatomic force. Nguyen-Manh and colleagues concluded that negative Cauchy pressure in many –body repulsive terms can arise from an overlap of the free electron like *sp*-band electrons when compressed by the d-electrons in BCC [16]. Apart from δ-plutonium (BCC metal: 11), an s^1 electron material is known as the most anisotropic FCC element and all departures are towards the $C_{12} > C_{44}$ region.

By comparing the elastic properties of these phases in Figure 7.3 and Table 7.1, several trends become evident: first, the location of both FCC and BCC SIM alloys in the Blackman diagram. These are bound within the same axial distance of similar Poisson's ratio. In a Blackman diagram, the poisons ratio averages over all crystallographic directions. Pugh [17] established a relationship between Poisson ratio and ductility, while Koster-Franz [18] described its connection with interatomic bonding. As seen in Figure 7.3, their common indicators are similar to Poisons ratio regime (0.3 ≤0.324) and share a close proximity to the Cauchy pressure. The physical significance of this is that materials with similar Poison's ratios behave very similarly mechanically. Thus, a low poisons ratio primarily results in shape change and provides strong support for the high ductility and psuedoelasticity exhibited by SIM alloys.

7.3 Conclusions

We attest in this study that the Blackman diagram can be used as an effective tool to theoretically analyse predictions and experimental deductions of some basic important behaviours of alloys. We have demonstrated a SIM relation between the central interatomic forces and poisons ratio, and high ductility of SIM alloys.

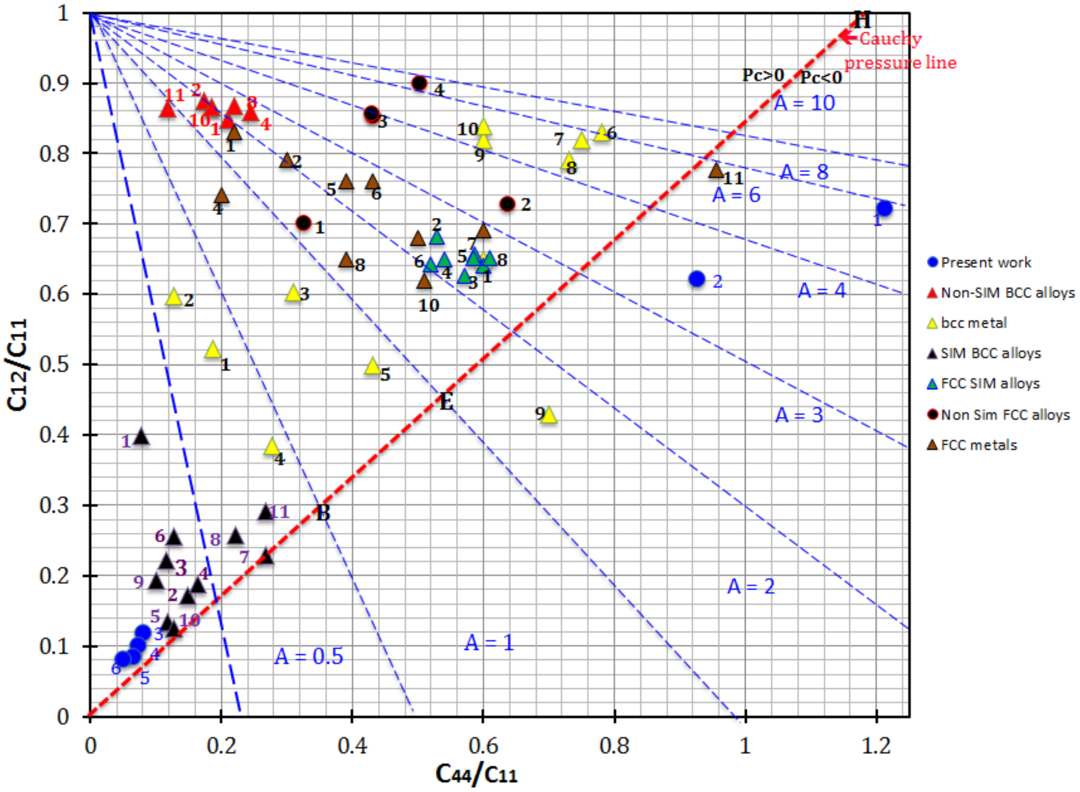

Figure 7.3: Blackman plot combining some BCC and FCC metals and alloys in one diagram, revealing the relationships between the two SIM alloys groups. The identities of the elements/alloys are given in Table 7.1.

7.4 References

[1] Fisher E. S., Westlake D. G., and Ockers S. T.; *Phys. Status Solidi A* 28 (1975)59 1-602

[2] Grosdidier T., and Philippe M. J.; Mater. Sci. Eng. A 291 (2000) 218-223.

[3] Ho F. W, JU. C. P., and Chern Lin J. H.; Biomaterials 24(199) 2115-2122.

[4] Hosoda H., Ohmatsu Y., and Miyazaki S.; Trans. MRS-J(26) (2001) 235-237.

[5] Hosoda H., Hosoda S., and Miyazaki S.; Trans. MRS-J(26) (2001) 243-246.

[6] Baker C.; Mater. Sci. J 5(1871) 92-100.

[7] Nitta K., Watanabe S., Masakashi N., Hosoda H., and Hosoda S.; Structural Biomaterials for the 21st century (TMS, 2001)25-34.

[8] Hosoda H., Fukui Y., Imamura T., Wakeshima S., Miyazaki S., and Inoue I.; Mater. Sci. Forum 426-432 (2003)3121-3123.

[9] Duerig T., Albrecht J., Richter D., and Fischer D.; Act. Metal. 30(1982) 2161-2172.

[10] Nye, J. F.; Physical Properties of Crystals (Oxford University Press, London, 1957), 32.

[11] Blackman M.; Proc. Roy. Soc. London 164, (1938) 62.

[12] Plummer J. D., and Todd I.; Applied Phys. Lett. 98(2011) 021907

[13] Pettifor; Mater.Sci& Tech. 8(1992), 345.

[14] Born M., and Huang H.; Dynamic Theory of crystal lattices (Oxford University Press, London, 1954), 152.

[15] Zener C.; Elasticity and Anaelasticity of Metals (University of Chicago Press, Chicago, 1948) 16.

[16] Soderlind P.; Adv.Phys. 47(1998), 959.

[17] Pugh S.; Philos. Mag. 45(1954), 823.

[18] Koster W., and Franz H.; Metall. Rev.6(1961)1.

[19] Ren X. *et al.*; Mag. 79(1999) 31-41.

[20] Hatcher N., Kontsevo Yu O., and Freeman A. J.; Phys.Rev.B 80(2009) 1-18.

[21] Li S. J., Cui T. C., Hao Y. L., and Yang R.; Acta Biomat 4 (2008) 305-17.

[22] Nobuhito S., Niinomi M., and Akahori T.; Mater. Trans. 45, No. 4 (2004) 1113–1119.

[23] Zhengjie L., Wan L., Xiaobing X., Weijie L., Qina J., and Zhang D.; Mater. Sci. and Eng. C 33 (2013) 4551–4561.

[24] Hou F. Q., Li S. J., Hao Y. L., and Yang R.; Scripta Mater. 63 (2010) 54–57.

[25] Tane M., Nakano T., Kuramoto S., Hara M., Niinomi M., Takesue N., Yano T., and Nakajima H.; Acta Mater. 59 (2011) 6975–6988.

[26] Kim H. Y., Ikehara Y., Kim. J. I., Hosoda H., and Miyaaki S.; Acta Metall.54 (2006) 2419.

[27] Talling R. J., Dashwood R. J., Jackson M., Kuramoto S., Dye D.; Scr. Mater. 59 (2008) 669.

[28] Hao Y., Li S., Sun B., Sui M., and Yang R.; Physical Rev. Letts. 98 (2008), 1-4.

[29] Paszkiewicz and Wolski; J. Phys. (Conference series) 104 (2008), 012038.

[30] Mañosa L *et al.*; Phys. Rev. B 49 (1994), 9969-9972.

[31] Zhou L., Cornely P., and Trivisonno J:Ultrasonic symposium (1990)1389-1329.

[32] Sedlak P., Seiner H., Landa M., Novak V., Sittner P., and Manosa Li; Acta Materialia 53 (2005) 3643–3661.

Table7.1: Elastic constant of some BCC and FCC metals and alloys.

	This work	**C11**	**C12**	**C12/C11**	**C44/C11**	**Ref.**
1	Ti-3Mo	159.3	115	0.72	1.21	
2	Ti-6Mo	111.3	69.07	0.62	0.93	
3	Ti-10Mo	167	19.6	0.12	0.081	
4	Ti-14Mo	179.2	17.9	0.10	0.074	
5	Ti-18Mo	192.6	16.3	0.085	0.066	
6	Ti-23Mo	197.5	16	0.081	0.051	
	Non-SIM (BCC)alloys					
1	Ti50Ni30Cu20	209	183	0.88	0.17	[19]
2	Ti-50Ni	165	140	0.85	0.21	[20]
3	Ti-29Nb-13Ta-4.6Zr	67.1	39.9	0.87	0.19	[21]
4	Ti-30Nb-10Ta-5Zr	128	92	0.86	0.24	[22]
5	Ti-35Nb	163.5	142	0.87	0.22	[23]
6	Ti-30Nb-5Ta-5Zr	70	30	0.87	0.185	[24]
7	Ti-32.7Nb-11.6Ta-4.49Zr-0.066O-0.052N	137	91.1	0.86	0.12	[25]
	Non SIM (FCC) alloys					
1	Ag-75Au	230	161.5	0.702	0.33	[19]
2	Cu-4.17Si	117	85.2	0.73	0.64	[19]
3	α-Ag-2.4Zn	190	162	0.85	0.43	[19]
4	α-Cu-9.98Al	199	179	0.89	0.50	[19]
5	α-Cu-22.7Zn	158.9	136.2	0.86	0.43	[19]
	SIM(BCC) alloys					
1	Ti-35.37Nb	130.2	52	0.40	0.078	[26]
2	Ti-35Nb-2Zr-0.7Ta	183	31.4	0.17	0.15	[25
3	Ti-35.4Nb-1.9Ta-2.8Zr-0.37O	122	27	0.22	0.11	[25]
4	Ti-24.1Nb-4Zr-8.06Sn-0.15O	140	26.3	0.19	0.16	[25]
5	Ti-35Nb-10Ta-4.6Zr-0.16O	102.5	36	0.16	0.12	[27]
6	Ti-23.9Nb-3.75Zr-8.01Sn-0.04O	157.2	36	0.26	0.127	[27]
7	Ti-24Nb-4Zr-7.9Sn-0.17O			0.23	0.22	[27]
8	Ti-24Nb-4Zr-7.6Sn-0.07O	122	31.4	0.26	0.21	[25]
9	Ti-35.2Nb-10.5Ta-4.97Zr-0.091O-0.014N	140	27	0.19	0.1	[27]
10	Ti-23.9Nb-3.8Zr-7.61Sn-0.08O	102.5	26.3	0.12	0.13	[27]
11	Ti-24Nb-4Zr-7.9Sn	157.2	46	0.29	0.27	[28]
	SIM(FCC) alloys					
1	Cu44.9- 50Zn	125	80	0.64	0.6	[19]
2	Au47.5-50Cd	142	96.77	0.68	0.53	[19]
3	Ag45-50Zn	132.8	83.16	0.63	0.57	[19]
4	γ-FeNi	209	183	0.65	0.54	[29]
5	CuAlNi	142.8	93.7	0.66	0.59	[30]

6	B2-NiTi	162	104	0.64	0.52	[31]
7	Cu2.726A11.122Ni 0.152	137	89.2	0.65	0.59	[32]
8	Cu2.742Al1.105Ni0.152	136	81.763	0.65	0.61	[32]

	BCC elements	C12/C11	C44/C114	Ref.
1	V	0.52	0.19	[29]
2	Nb	0.59	0.13	[29]
3	Ta	0.60	0.31	[29]
4	Mo	0.38	0.28	[29]
5	W	0.5	0.43	[29]
6	Li	0.83	0.78	[29]
7	Na	0.82	0.75	[29]
8	K	0.79	0.73	[29]
9	Ba	0.43	0.7	[29]
	FCC elements			[29]
2	Au	0.83	0.22	[29]
3	Pd	0.79	0.3	[29]
4	Pt	0.74	0.2	[29]
5	Ag	0.76	0.39	[29]
6	Cu	0.76	0.43	[29]
7	β-Co	0.69	0.6	[29]
8	α-Sr	0.65	0.39	[29]
9	γ-Fe	0.68	0.5	[29]
10	Ni	0.62	0.51	[29]
11	δ-Pu	0.78	0.96	[29]

Chapter 8

Conclusions and Further work

8.1 Conclusions

The results gathered from experiments described in this thesis suggest that the modelling solution approach (as carried out in the present work) can be used effectively to predict and study important properties of metallic alloys. Furthermore, it has been shown that first principle calculations (DFT) as implemented in the CASTEP code are a very effective technique in characterising the phase stability, formation energy, elastic properties and deformation behaviour of superelastic materials. The good agreement between the theoretical calculations and experimental verified data for thermodynamic stability, composition and elastic constant justifies the use of the approach for evaluating property in the present work.

In order to understand the intrinsic mechanism by which alloying elements influence thermodynamic phase stability, we compared the total electronic density of states (DOS) of α'' and β crystal structures. From this viewpoint, it is thought that the structural stability change in the Ti-Mo system is connected to the lowering of $N(E_F)$ due to hybridisation of the d- electronic states of the Mo atom. This provides for the increasing covalency in the bonding of the two atoms.

The structural properties relating to the α′′ orthorhombic phase transformation in Ti-Mo alloy system has been studied using optical microscope, SEM, EBSD and Rietveld refinement of XRD profiles. The formation of the orthorhombic phase has been ascribed to three main reasons: (a) in view of the eightfold coordination around each (Ti, Mo) atom with four additional neighbours at a slight greater distance. The formation of the α′′ in preference to α in Ti-Mo binary alloy beyond a certain Mo critical concentration could be a reflection of a tendency for Mo to retain the eightfold coordination obtained in BCC titanium; (b) atomic size difference can also lead to distortion of the crystal structure; and (c) assuming the major influence of atom size is ignored, the movement/shift of the atoms along y -atomic coordinate without breaking the group symmetry is another possible explanation. Additionally, the orthorhombicity in this alloy decreases as Mo content increases.

The trend of the Young's moduli of the samples followed a similar direction to the hardness, suggesting that α′′ might be responsible for the low hardness and Young's modulus, since both are structurally related properties. It is worth noting, however, that the Young's modulus of the Ti-6Mo was even lower than that of the Ti-6-4 alloy. This advantage of α″ orthorhombic structure can be exploited to further reduce the Young's modulus of future metallic biomaterials.

Based on the DFT-GGA electronic calculation, a number of metastable body centered cubic ternary and multicomponent alloys were experimentally and theoretically designed to correspond to the composition formula of Ti-5Mo +U (U=Nb, Zr, Ta, Sn, Ta+Sn, Nb+Sn and Sn+Zr) supercells at T= 0K. The trend in the electronic formation energy attests to the significant sensitivity of the binary Ti-Mo alloy system to phase stability and elastic moduli with micro-elemental addition, which indicates that DFT-GGA is favourable to the computational screening of relative phase stability and other p of alloys. Our newly designed Ti-Mo-Zr alloy exhibited the lowest Young's modulus, with 45 GPa (42.19GPa from theory), which is significantly lower and much closer to natural bone than the elastic modulus of conventional metallic implant materials (cp-Ti, near β and β Ti alloys), which vary between 121 and 57 GPa.

We have suggested by analysis of data in this study that the Blackman diagram can be used effectively to theoretically analyse predictions and make experimental deductions about the behaviours of alloys and by this have demonstrated a link between the central interatomic forces (Cauchy pressure) and the Poissons ratio with superelastic of SIM alloys.

8.2 Further works

Although the results of the present work suggest a link between cast material texture and the directionality of calculated Young's modulus of the alloys, further work is needed to obtain a more detailed understanding of the operative texture mechanisms. In particular, the significance of the role of the initial microstructure (1) on the elastic modulus, and (2) in inhibiting the emergence of textures requires investigation. Further higher resolution TEM work is recommended to establish the effect of texture on the elastic property of the alloys.

Furthermore, the results of this work have shown that the mechanical properties of binary Ti-Mo alloy systems are very sensitive to chemical composition. There is consequently a good scope to improve the alloys for specific applications. For example, the amount of transformation strain could be optimised through control of chemical composition or through control of specimen texture. A systematic approach is required to analyse the effect of alloying elements on the interplay between twinning, SIM and slip during subsequent loading.

It is envisaged that, with further theoretical research, SIM alloy can be designed using the elastic constant systematics from DFT. First principle calculations may be able to portray the shape memory effect of multicomponent Ti-Mo alloys akin to other Ni-Ti and Ti-Nb based alloys. This would broaden the portfolio of applications of these alloys even further, offering a more in-depth understanding of what physical and microstructural factors enable a material to exhibit the shape memory effect. This would suggest that further work is needed to redefine the composition window and other factors considered before alloys can be designed on first principles.